Development of aptasensors for detection of Shiga like toxin 1 (Stx1) and Shiga like toxin 2 (Stx2) from *Escherichia coli*

A thesis submitted in partial fulfilment for the award of the degree of

Doctor of Philosophy

by

Malaya Mili

Department of Biosciences and Bioengineering
Indian Institute of Technology Guwahati
Guwahati-781039, Assam, India

INDIAN INSTITUTE OF TECHNOLOGY GUWAHATI
Department of Biosciences and Bioengineering
Guwahati: 781039

STATEMENT

I do hereby declare that the matter embodied in this thesis entitled "Development of aptasensors for detection of Shiga like toxin 1 (Stx1) and Shiga like toxin 2 (Stx2) from *Escherichia coli*" is the result of investigations carried out by me in the Department of Biosciences and Bioengineering, Indian Institute of Technology Guwahati, Assam, India, under the guidance of Prof. Pranab Goswami.

In keeping with the general practice of reporting scientific observations, due acknowledgements have been made wherever the work described is based on the findings of other investigators.

Malaya Mili

January, 2026
Malaya Mili

INDIAN INSTITUTE OF TECHNOLOGY GUWAHATI
Department of Biosciences and Bioengineering
Guwahati: 781039

CERTIFICATE

It is certified that the work described in this thesis entitled "Development of aptasensors for detection of Shiga like toxin 1 (Stx1) and Shiga like toxin 2 (Stx2) from *Escherichia coli*", done by Malaya Mili (Roll No. 196106014) for the award of degree of Doctor of Philosophy is an authentic record of the results obtained from the research work carried out under my supervision in the Department of Biosciences and Bioengineering, Indian Institute of Technology Guwahati, India.

The results embodied in the thesis have not been submitted to any other University or Institute for the award of any degree.

Dr. Pranab Goswami

Professor (Higher Administrative Grade)

(Thesis supervisor)

Acknowledgement

As I bring this thesis to completion, I take a moment to acknowledge with deep gratitude all those who supported me on this long academic journey. Their thoughtful feedback, questions, and constant academic and personal support have profoundly influenced this work.

I would like to express my deepest gratitude to my Ph.D. supervisor, Prof. Pranab Goswami, for his constant guidance and mentorship throughout my doctoral journey. He taught me not only the technical aspects of research but also the values of patience, perseverance, and independent thinking. His encouragement, insightful ideas, and the freedom he gave me to explore my research were crucial in shaping this work. I am especially thankful for his trust in my abilities and for providing a well-equipped laboratory and a motivating work environment. Working under his supervision has been a truly enriching and formative experience.

I sincerely thank my doctoral committee, Prof. Ranjan Tamuli, Prof. Manish Kumar, and Dr. Kalyan Raidongia for their critical evaluation of my research work and their meaningful suggestions. Their constructive feedback and guidance significantly strengthened the quality of my work and helped shape it into a more rigorous and meaningful study. I also acknowledge all former and present Heads of the Department, faculty members, and staff of the Department of Biosciences and Bioengineering, IIT Guwahati, for maintaining excellent research facilities and for their constant support.

I am grateful to our collaborators, Prof. Sungbo Cho and Dr. Chinnadayyala Somasekhar Reddy, for their valuable contributions, insightful discussions, and support during the work.

I would like to thank the Central Instruments Facility (CIF) and the Computer and Communication Centre (CCC) at IIT Guwahati for providing access to various instruments and the high-end computational facilities.

I am thankful to my past and present lab members Phurpa, Smita, Lightson, Vinay, Pooja, Rafiqul, Rupinder, Dolly, Bhaskar, Arup, Kangkana, Nabajyoti, Aparupa, Mohit, Nagarajana, Monalisha, and Mugdha for sharing this journey with me through their support, laughter, love and shared struggles. Special thanks to my M. Tech junior Hritushree and B. Tech Junior Rahul, who helped me in my research work.

This acknowledgement would be incomplete without thanking my loved ones, Padmini Pegu, Dr. Pranjal Chowdhury, Dr. Banashree Baishya, and Gariyoshi Mahanta, whose constant support, shared cups of tea, relaxing hangouts and comforting conversations during stressful times helped me stay balanced and motivated.

I am eternally grateful to my parents and family, whose sacrifices, unwavering support, and constant encouragement have been the foundation of my academic journey and have shaped me into the person I am today.

Finally, I extend my sincere thanks to everyone who, directly or indirectly, contributed to the successful completion of this thesis.

Malaya Mili

January 2026.

Table of Contents

Abstract

Shiga toxin-producing *Escherichia coli* (STEC) are among the leading causes of foodborne illnesses worldwide, contributing to significant morbidity and mortality. The Shiga-like toxin 1 (Stx1) and Shiga-like toxin 2 (Stx2) expressed by STEC are the main virulence factors responsible for bloody diarrhoea, haemolytic uremic syndrome (HUS), and haemorrhagic colitis (HC). The severity of the diseases necessitates rapid, sensitive, portable, and low-cost diagnostic tools to strengthen on-field food safety monitoring, improve disease prognosis and guide timely intervention. Current detection methods typically involve culture-based identification, PCR-based molecular diagnostics and antibody-based immunoassays. These methods involve complex procedures, long assay times, and require advanced instrumentation as well as trained personnel. Moreover, antibody production is costly, prone to batch-to-batch variability, and antibodies often lose activity under fluctuations in temperature, pH, or storage conditions. These limitations hinder their applications in point-of-care settings, where the on-field conditions vary, and the standard storage conditions are not always feasible to maintain. Aptamers, owing to their high selectivity, strong thermal stability, low production costs, and ease of functionalization, are being increasingly recognised as ideal biorecognition elements for biosensing applications. In this thesis work, aptamer-based impedimetric biosensors for the detection of Stx1 and Stx2 were developed using interdigitated microelectrodes and their sensing performances were evaluated using electrochemical impedance spectroscopy (EIS). The aptasensor for Stx1 was fabricated using a highly selective aptamer developed via standard Systematic Evolution of Ligands by Exponential Enrichment (SELEX) method. The aptamer was characterized, and then immobilised on a chain-type interdigitated microelectrode to develop the aptasensor. The microelectrode was fabricated following advance techniques such as electron beam deposition, chemical wet etching and photolithography. The developed aptasensor exhibited a limit of detection (LOD) of 2.88 pM, a linear dynamic range of 10 - 450 pM and a sensitivity of 107.02 Ω/pM. To validate the practical application of the aptasensor it was tested in real sample using cow milk. The sensor showed the recovery in the range of 97.5% to 103.5%. In the next phase of the work an aptamer against Stx-2 was developed. In this part of the work, the aptamer was however, identified from a computationally designed aptamer library following a systematic in-silico approach comprising of generation of aptamer library, prediction of secondary and tertiary structures of the aptamers, molecular docking, and molecular dynamic simulation. The selected aptamer was validated using circular dichroism (CD) and isothermal titration calorimetry (ITC). The *in silico* designed aptamer for Stx2 was then used as the biorecognition element for the development of the Stx2 biosensor using a wave-type interdigitated microelectrode. The wave type microelectrode fabrication followed the same techniques described for the chain type electrode. The developed sensor exhibited an LOD of 4.63 pM, a linear range of 10 – 400 pM and a sensitivity of 97.03 Ω/pM. To validate the practical application of the aptasensor it was tested in real sample using cow milk. The sensor showed recovery in the range of 93.06% to 108.4%.

List of abbreviations

STEC	Shiga Toxin producing *E. coli*
HUS	Haemolytic Uremic Syndrome
HC	Haemorrhagic Colitis
WHO	World Health Organization
ECDC	European Centre for Disease Prevention and Control
PCR	Polymerase Chain Reaction
RT-PCR	Reverse Transcription Polymerase Chain Reaction
EIS	Electrochemical Impedance Spectroscopy
IDE	Interdigitated Microelectrodes
Gb3	Globotriaosylceramide
Stx	Shiga toxins
Stx1	Shiga like toxin 1
Stx2	Shiga like toxin 2
VTEC	Verotoxin-producing *E. coli*
ORF	Open Reading Frame
LD_{50}	Lethal Dose, 50%
TGN	Trans-Golgi Network
ER	Endoplasmic Reticulum
ISO	International Organization for Standardization
IMS	Immunomagnetic Separation
MALDI-TOF	Matrix-Assisted Laser Desorption/Ionization Time-of-Flight
EHEC	Enterohemorrhagic *E. coli*
LOD	Limit of Detection
LFA	Lateral Flow Assay

ELISA	Enzyme-Linked Immunosorbent Assay
LFITS	Lateral Flow Immunochromatographic Test Strips
AgNP	Silver Nanoparticle
SPR	Surface Plasmon Resonance
LSPR	Localized Surface Plasmon Resonance
Mn/Fe-MIL(53)	Manganese-Iron-doped Matériaux de l'Institut Lavoisier number 53
TMB	3,3',5,5'-Tetramethylbenzidine
SPRi	Surface Plasmon Resonance Imaging
SERS	Surface-Enhanced Raman Spectroscopy
SELEX	Systematic Evolution of Ligands by Exponential Enrichment
MDS	Molecular Dynamic Simulation
CV	Cyclic Voltammetry
DPV	Differential Pulse Voltammetry
EIS	Electrochemical Impedance Spectroscopy
R_s	Solution Resistance
R_{ct}	Charge Transfer Resistance
C_{dl}	Double Layer Capacitance
TCEP	Tris(2-Carboxyethyl) Phosphine Hydrochloride
ICE	Interdigitated Chain Type Electrode
MCH	1-Mercapto-6-Hexanol
$NaBH_4$	Sodium Borohydride
AFM	Atomic Force Microscopy
SAM	Self Assembled Monolayer
CPE	Constant Phase Element

PBS	Phosphate Buffered Saline
RSD	Relative Standard Deviation
RMSD	Root Mean Square Deviation
RMSF	Root Mean Square Fluctuations
R_g	Radius of Gyration
YASARA	Yet Another Scientific Artificial Reality Application
FFT	Fast Fourier Transform
PLIP	Protein–Ligand Interaction Profiler
MM/GBSA	Molecular Mechanics/Generalized Born
CD	Circular Dichroism
ITC	Isothermal Titration Calorimetry
IDWµE	Interdigitated Wave-type Microelectrodes

List of Symbols

°C	Degree Celsius
%	Percent
µM	Micromolar
mM	Millimolar
λ	Wavelength
kcal	Kilocalorie
kDa	Kilo Dalton
mg	Milligram
mL	Millilitre
M	Molar
A	Adenine
T	Thymine
G	Guanine
C	Cytosine

List of Figures

List of Tables

Chapter 1

Introduction and Review of Literature

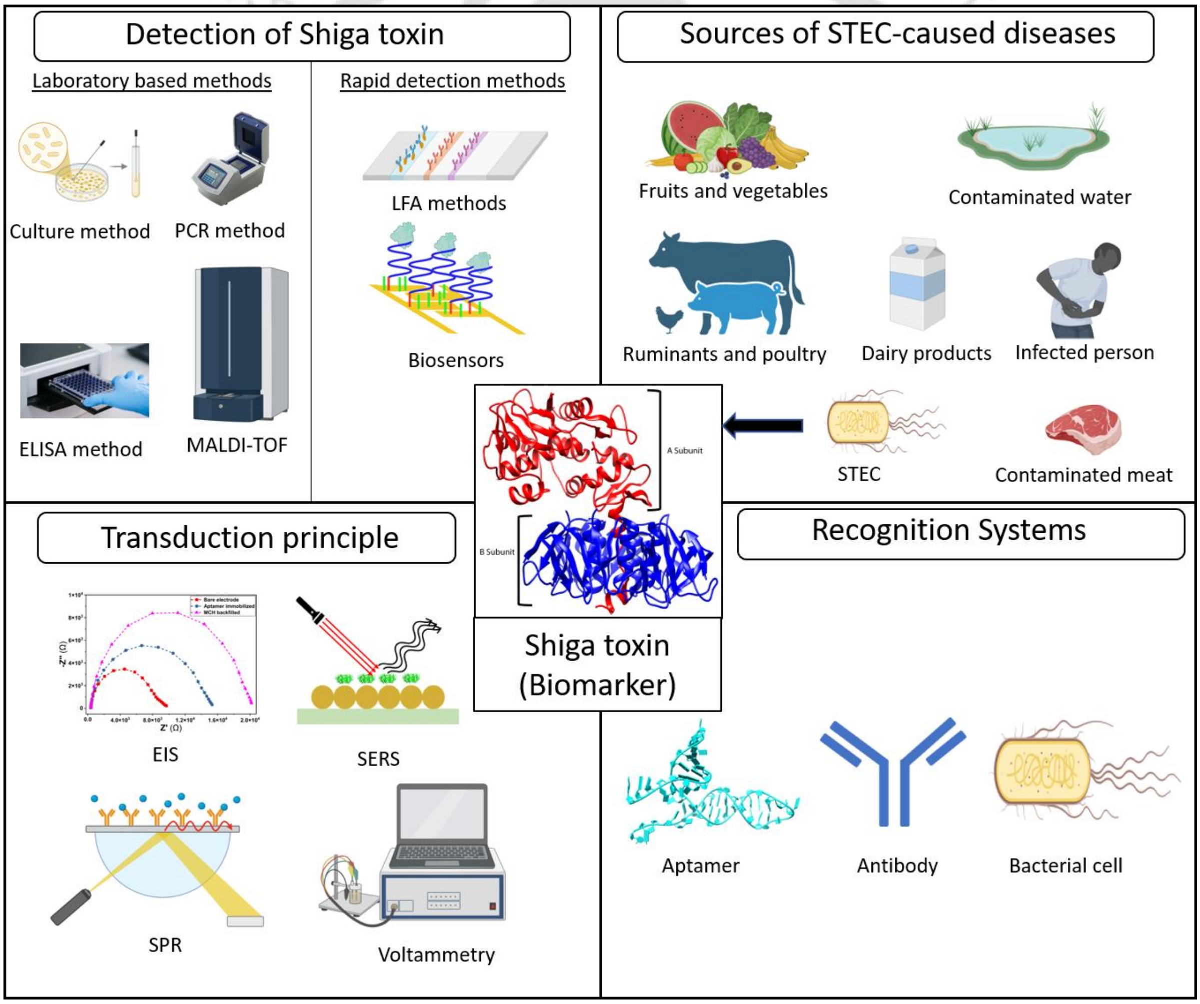

Introduction and Review of Literature

1.1. Introduction

Foodborne infectious diseases remain a major global public health concern, with *Escherichia coli (E. coli)* associated outbreaks contributing substantially to morbidity and mortality. Among pathogenic *E. coli* strains, Shiga toxin–producing *E. coli* (STEC) represent one of the most clinically severe groups, causing illnesses ranging from mild diarrhoea to life-threatening complications such as haemolytic uremic syndrome (HUS). Since its identification in the early 1980s, STEC has been responsible for more than 1343 outbreaks worldwide (Alhadlaq et al., 2024). According to the World Health Organization (WHO), foodborne STEC infections account for over one million cases annually across the globe (WHO Report, 2019). Recent surveillance data further underscore the growing burden of STEC infections; for example, the European Centre for Disease Prevention and Control (ECDC) reported 8,565 confirmed STEC cases in the European Union/European Economic Area in 2022, corresponding to a notification rate of 2.5 cases per 100,000 population, a 25% increase compared to 2021 (ECDC, 2024). Vulnerable populations, particularly children under five years of age and elderly individuals, are at increased risk of severe disease outcomes (Juarez et al., 2025).

The pathogenicity of STEC infections is primarily mediated by Shiga toxins, making their early and accurate detection critical for clinical diagnosis, outbreak management, and food safety surveillance. However, direct detection of Shiga toxins at the protein level remains challenging due to their low abundance in complex biological matrices and the inherent limitations of existing analytical techniques. Current diagnostic approaches include culture-based methods, cytotoxicity assays, polymerase chain reaction (PCR) targeting *Stx* genes, immunoassays, and mass spectrometry-based techniques. While these methods have significantly advanced STEC detection and characterization, each presents notable drawbacks. Culture-based methods are time-consuming and labour-intensive, PCR requires costly specialized instrumentation, cytotoxicity assays depend on cell culture facilities, and immunoassays rely on antibodies that may suffer from limited stability, batch-to-batch variability, and high production costs. These constraints highlight the urgent need for rapid, sensitive, and cost-effective toxin detection platforms, particularly those suitable for point-of-care and field applications.

In this context, biosensor technologies have emerged as promising alternatives to conventional diagnostic strategies (Goswami, 2020). Biosensors combine a biorecognition element with a transduction mechanism to convert molecular recognition events into measurable signals. Among various biosensor platforms, electrochemical biosensors have gained considerable attention due to their high sensitivity, low cost, operational simplicity, and compatibility with miniaturized and portable devices. Electrochemical techniques are especially attractive for toxin detection as they enable label-free analysis and real-time monitoring of biomolecular interactions. A critical determinant of biosensor performance is the selection of an appropriate biorecognition element. Although antibodies have been widely employed for Shiga toxin detection, their biological origin imposes limitations related to stability, reproducibility, and cost. In contrast, aptamers have emerged as robust alternatives owing to their high affinity and specificity, chemical stability, and ease of synthesis. Furthermore, aptamers can be readily functionalized with chemical groups such as thiols or amines, facilitating their integration into diverse sensing platforms (Mili et al., 2024).

Alongside biorecognition strategies, the choice of transduction technique plays a pivotal role in determining biosensor sensitivity and reliability. Electrochemical impedance spectroscopy (EIS) has emerged as a powerful label-free method for biosensing applications, as it sensitively monitors changes in interfacial electrical properties over a broad frequency range. This feature makes EIS particularly suitable for detecting large, non-electroactive biomolecules such as protein toxins. The performance of EIS-based sensors can be further enhanced through advanced electrode designs, including interdigitated microelectrodes (IDEs), which offer a high surface-to-volume ratio, compatibility with microfabrication technologies, low production costs, and ease of integration into compact sensing devices.

Given the significant public health burden posed by STEC infections and their widespread occurrence globally, including in the Indian subcontinent, this work aims to develop a rapid, reliable, and cost-effective diagnostic platform for STEC toxin detection. By leveraging advances in biosensor design and electrochemical sensing strategies, the present study seeks to improve existing diagnostic capabilities and contribute to more effective surveillance and control of STEC infections. Such an approach holds particular promise for low-resource settings, where conventional diagnostic infrastructures remain limited, thereby offering meaningful improvements in public health outcomes in regions most affected by STEC.

1.2. Review of literature

1.2.1. Shiga toxin producing *E. coli* (STEC)

STEC comprise a group of intestinal pathogenic *E. coli* responsible for severe gastrointestinal diseases, including bloody diarrhoea, haemorrhagic colitis (HC), and haemolytic uremic syndrome (HUS). These pathogens are considered zoonotic, as transmission can occur from infected animals to humans as well as through person-to-person contact (Kim et al., 2020). STEC have been isolated from a wide range of sources, including vegetables, fruits, dairy products, and their derivatives.

Human infections typically arise from the consumption of contaminated food, such as raw or undercooked meat, raw vegetables, dairy products derived from infected animals, or contaminated water.

Ruminants, particularly cattle, sheep, and goats, are regarded as the principal reservoirs of STEC. Owing to the absence of globotriaosylceramide (Gb3), the receptor for Shiga toxins, in their intestinal epithelium, these animals can harbour STEC in the large intestine without exhibiting clinical symptoms, thereby acting as asymptomatic shedders. In addition to ruminants, several other animals including pigs, horses, poultry (such as chickens, ducks, and turkeys), and companion animals like dogs and cats, have also been reported as potential sources of STEC infection (Kim et al., 2020).

The name Shiga toxin-producing *E. coli* was given due to the ability of these bacteria to produce the Shiga toxins, which are the primary virulence factor. Shiga toxins (Stx) were first discovered by Japanese scientist Kiyoshi Shiga in 1897 from *Shigella dysenteriae.* In the early 1980s, O'Brien and the group discovered a group of *E. coli* that produced a toxin similar to the Shiga toxin produced by *Shigella dysenteriae* and were subsequently named the Shiga toxin-producing *E. coli*. The Shiga toxins were also termed Verotoxins due to their ability to kill Vero cells in culture and the bacterial group as Verotoxin-producing *E. coli* (VTEC) (Johannes & Römer, 2010). Since its discovery, more than 400 serotypes of STEC have been reported worldwide. O157:H7 is one of the major serotypes responsible for foodborne illness due to STEC. Other than O157, six other non-O157 serogroups, known as the big six, consisting of O26, O45, O103, O111, O121, and O145, are considered the major serogroups of STEC responsible for HUS, HC worldwide. The non-O157 strains have been reported to cause 64% of the world's STEC infection (Fan et al., 2019).

1.2.2. Shiga toxin phage

STEC produces two major types of Shiga toxins: Shiga-like toxin 1 (Stx1) and Shiga-like toxin 2 (Stx2). They are encoded by diverse double-stranded DNA phages with a common head and tail structure. The structures range from icosahedral or elongated heads to diverse tail morphologies including contractile, non-contractile or short tails, with or without associated tail fibres. These phages displays sequence and genetic organizations similar to that of the lambda bacteriophages with genes arranged into distinct functional clusters responsible for recombination, early regulation, replication, late regulation, and lysis. The Stx genes are located towards the late regulatory region of the prophage. Their genome size ranges from 28.7 to 71.9 kb (Yang et al., 2020; Ohnishi et al., 2002; Krüger & Lucchesi, 2015; Yara et al., 2020) . The Stx phages belong to different families within the order *Caudovirales*, such as *Podoviridae*, *Siphoviridae*, and *Myoviridae*. A very large number of Stx phages identify the host receptors through a highly conserved tail spike protein. They identify the highly conserved protein *YaeT* on the target bacterial cell surface for adsorption. During the lysogenic phase, the Stx phage integrates into the bacterial chromosomal DNA, forming a prophage that replicates along with the bacterial genome and is transferred to the bacterial progeny. At this stage the *CI* repressor binds to the operator within the early regulatory region, thus silencing the transcription of the Stx phage genes. However, a small population of cells have been reported to express the Stx phage genes spontaneously(Riley et al., 2012). The phage integrase enzyme recognizes many insertion sites on the bacterial chromosome, such as *yehV* (Kristina et al., 2005), *wrbA* (Guy et al., 1999), *yecE* (Jürgen & Herbert, 2002), *sbcB* (Ohnishi et al., 2002), *ssrA* (Creuzburg et al., 2005), *prfC* (Creuzburg et al., 2005), *argW* (Creuzburg et al., 2005), the region between the *torS* and *torT* genes (Creuzburg et al., 2005), allowing them to integrate into the bacterial genome, even if few of the sites are blocked or deleted. Many *E. coli* strains naturally harbours multiple Stx prophages in their chromosome. During harsh environmental conditions, such as changes in pH, low iron availability, ionic conditions, antibiotic application, and exposure to DNA-damaging agents, the SOS response is triggered, inducing the activation of the prophage. The SOS response activates the *RecA*, which stimulates the autocleavage of the CI repressor on the early regulatory region operators. This leads to the transcription of the early promoters, resulting in the expression of the early anti-terminator genes, which allows the polymerase to read through the downstream terminators, leading to the expression of the late-phase anti-terminator genes. This facilitates the transcription at the late promoter and results in the expression of the Stx genes at the downstream of the late promoter. The activated prophage is excised from the bacterial chromosomal DNA and starts replicating as an extrachromosomal entity. During replication, the Stx proteins, along with various phage structural proteins, are expressed. The expression of the phage lytic proteins at the end of the induction process leads to the lysis of bacterial cells and the release and spreading of the Shiga toxins from the STEC infection (Rodriguez-Rubio et al., 2021). Along with the Shiga toxins, the Stx phages are also released during bacterial cell lysis, which further spreads to other bacteria present in the vicinity. The Stx phages have also been reported to integrate into organisms from other genera, as Stx genes have been recovered from *Enterobacter cloacae* (Paton & Paton, 1996), *Aeromonas spp.* (Palma-Martínez et al., 2016), *Shigella sonnei* (Tóth et al., 2016), *Citrobacter freundii* (Schmidt et al., 1993).

The expression of the Stx1 phage-encoded Stx1 protein is mediated by two independent promoters, resulting in two pathways of Stx1 expression. The late phage promoter, pR’ dependent expression follows the induction of the prophage, resulting in expression and release of Stx1 via phage mediated host cell lysis. In addition to the phage dependent mechanism, the Stx1 expression is also mediated by a Stx1 specific promoter. This promoter binds to Fur protein, which in turn form complex with iron. Thus, in the presence of iron, the transcription via the promoter is blocked, whereas in an iron deficient environment, the Stx1 proteins are expressed, without the lysis of the bacterial cell. In both the conditions comparable level of Stx1 is produced(Wagner et al., 2002). In contrast, the expression of Stx2 is strictly dependent upon the induction of the Stx2 prophage, leading to expression and release by host cell lysis.

1.2.3. Molecular characteristics of Shiga toxins

The Shiga toxin (Stx) expressed by *Shigella dysenteriae* and the Shiga like toxin 1 (Stx1) expressed by STEC share almost identical sequences, differing only in one amino acid at the 45th residue of the A subunit, while Stx1 and Stx2 share only 55% amino acid sequence similarity (Chan & Ng, 2016) and 58% nucleotide sequence similarity (Yokoyama et al., 2000). The Stx1 gene sequence contains 1257 bp, with 2 open reading frames (ORF). The first ORF with 948 nucleotide bp corresponds to the 315 amino acid long A subunit and the second ORF with 270 nucleotide bp coding for the 89 amino acid long B subunit. The Stx2 contains 1321 bp nucleotide, also with 2 ORF, where the 319 amino acid long A subunit is coded by a 960 nucleotide bp long ORF, and the 89 amino acid long B subunit is encoded by a 270 nucleotide bp long ORF (Yokoyama et al., 2000). While the translated sequence contains 315 and 319 amino acids for the A subunit of Stx1 and Stx2, respectively, the mature A subunits contain 293 and 297 amino acids for Stx1 and Stx2, respectively. This reduction in length of the mature A subunit is attributed the presence of 22 amino acid long N-terminal signal peptide. Similarly, the B subunit also contains 19-20 amino acid long N-terminal signal peptides (Menge, 2020), with the mature subunit being 69 and 71 amino acid long for Stx1 and Stx2, respectively. Once these translated sequences are transferred to the periplasmic space, the signal peptides are cleaved off by the signal peptidase enzymes.

Although Stx1 and Stx2 share limited similarity in their amino acid sequence, both of them exhibit similar structures and mechanisms of action. The Shiga toxin family exhibits an AB_5 holotoxin structure, consisting of one A subunit and five identical B subunits (**Figure 1.1**). The B subunits form a pentameric ring with a central pore around the C terminal of the A subunit. The A subunit is approximately 32 kDa and harbours the catalytically active site, with N-glycosidase activity. The cysteine amino acids present at the 242 and 261 positions of the A subunit of Stx1 form intramolecular disulfide bond, whereas for Stx2 the cysteines at positions 241 and 260 forms this disulfide bond. The glutamic acid at position 167 is the active site of the A subunit (Hovde et al., 1988). Each monomeric B subunit is around 7.7 kDa and it contains the receptor recognition units for binding with the target cells. They recognize the neutral glycosphingolipid globotriaosylceramide (Gb3 or CD77) receptor on the target cell surface. A subtype of Stx2, the Stx2e recognizes globotetraosylceramide (Gb4), containing an additional β [1–3]-linked *N*-acetylgalactosamine residue (Yosief et al., 2013).

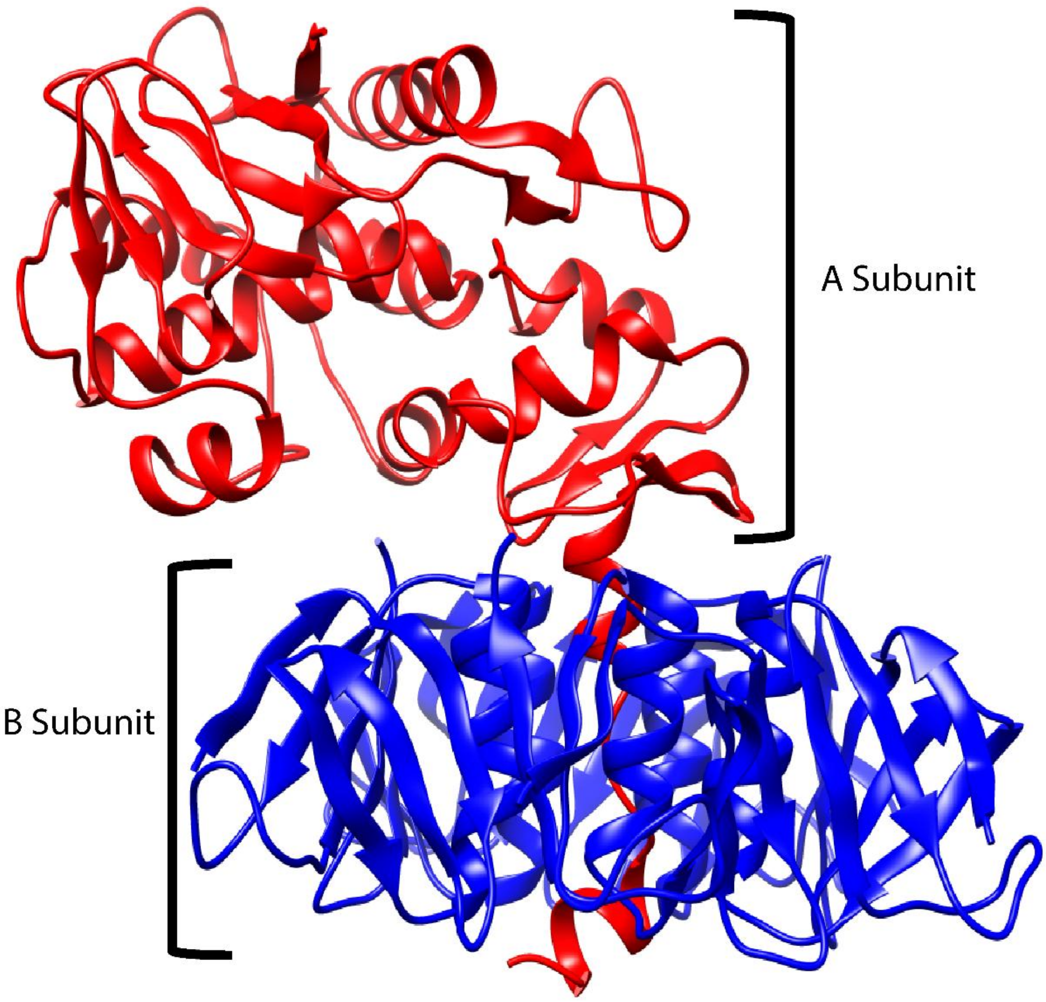

Figure 1.1: Ribbon diagram of Shiga-like toxin 2 (Stx2) displaying the A and B subunit (PDB ID – 1R4P). The A subunit is denoted in red and the B subunit is in blue.

Even in the absence of the A subunit, the B subunit monomers form the pentameric ring without any covalent bonds. They form an internal disulfide bond between the 4th and the 57th position cysteine residues (Seidah et al., 1986). The secondary structures of the B subunits are mainly composed of α-helix and *β*-sheets, with the α-helix assembling towards the inside of the pentameric ring forming a 11 Å wide pore, and the *β*-sheets positioned towards the outer part of the pentamer (Stein et al., 1992). While the central α-helix undergoes conformational changes during pH fluctuations, the outer *β*-sheets are highly stable. Each B subunit monomer contains 3 receptor binding sites, and all the 15 binding sites face the direction distal to the A subunit. Of the three binding sites per monomer, sites 1 and 2 demonstrate stronger binding affinity and contribute to enhanced cytotoxicity, whereas site 3 is responsible for lower-affinity interaction with Gb3 receptors (Bast et al., 1999). The multiple binding sites per monomer explain the high binding affinity of the toxin with the target cell (binding dissociation constant in the range of 10^{-9} M) (Fuchs et al., 1986). Although both Stx1 and Stx2 harbours 3 binding sites in each of their B subunit monomers, the site 2 of Stx2 is significantly different from that of Stx1 (Fraser et al., 1994). Stx1 exhibits 10 times more affinity for Gb3 receptor as compared to Stx2, but Stx2 is reported to be 400 times more lethal than Stx1. The LD_{50} of Stx2 is 400 times lower in mice than that of Stx1 (Tesh et al., 1993). The A and B subunits of the shiga toxins are expressed independently, following which their assembly occur at the cell membrane (Pellino et al., 2016).

1.2.4. Mechanism of action

During STEC infection, the Shiga toxins are released in the gut lumen of the gastrointestinal tract. The toxins traverse the intestinal epithelial barrier to reach the bloodstream, from which it travels to the different organs and targets the Gb3 expressing cells. In humans Gb3 is predominantly expressed in renal tubular cells and endothelial cells of kidney, gut, and brain, resulting in the tissue specific diseases manifestations during STEC infection (Paton & Paton, 2006). Once the Shiga toxins bind to the Gb3 receptor on the plasma membrane of the target cells, they enter the cell via endocytosis. They can be internalized via both clathrin-dependent or clathrin independent endocytosis (Sandvig et al., 1989) (Nichols et al., 2001). The bending of the plasma membrane is driven by the clustering of the glycosphingolipid via increasing toxin concentration. Further the invagination is processed by cellular factors including actin, dynamin, and plasma membrane cholesterol. Following the internalization of the toxins, they are sorted to the early and recycling endosomes. From there they avoid the late endocytic pathway, and are transported to the trans-Golgi network (TGN), and then to the endoplasmic reticulum (ER) in a retrograde manner. Clathrin and retromer molecules play a crucial role in sorting the toxins from early endosomes to the retrograde trafficking pathway, thereby avoiding the degradation of the toxins in the lysosome (Johannes & Römer, 2010) (**Figure 1.2**). When the toxin is localized in the early endosome, the A subunit is cleaved by a membrane associated endoprotease enzyme furin, at the site Arg251 – Met252 located in a protease sensitive loop around the positions 241 – 261 in the C- terminal of the A subunit, resulting in the cleavage of the A subunit into 27.5 kDa A1 fragment and 4.5 kDa A2 fragment. However, even after the cleavage, the A1 and the A2 fragments remain intact due to the disulfide bond formed between the Cys242 of the A1 fragment and the Cys261 of the A2 fragment. When the toxin reaches the ER lumen following the retrograde translocation, this disulfide bond is reduced, allowing the A1 fragment containing the active site to reach the ribosome in the cytoplasm (Garred et al., 1997). The A1 fragment binds to the ribosome and depurinates an adenine residue at 4324 position on the α-sarcin loop of the 28s ribosomal RNA (rRNA) of the eukaryotic ribosome. This halts the protein synthesis mechanism of the cell by preventing the binding of elongation factors to the ribosome and arresting translation chain elongation(Saxena et al., 1989).

Additionally, Shiga toxins damage the intestinal micro vessels, causing vasculitis which leads to mucosal injury resulting in bleeding and bloody diarrhoea. Bleeding further releases iron and other essential nutrients for the growth of the bacteria. Shiga toxin intoxication also results in the activation of ribotoxic stress as well as endoplasmic reticulum stress, which results from the accumulation of misfolded or unfolded proteins in the ER, leading to apoptosis of the cell. They also induce the release of pro-inflammatory cytokines in macrophages and monocytes, which upregulate the expression of Gb3 molecules on the epithelial cells triggering further progression of the disease. The Shiga toxin also activates the polymorphonuclear leukocytes resulting in the release of oxygen reactive metabolites, which causes injury to the endothelial cells (Johannes & Römer, 2010).

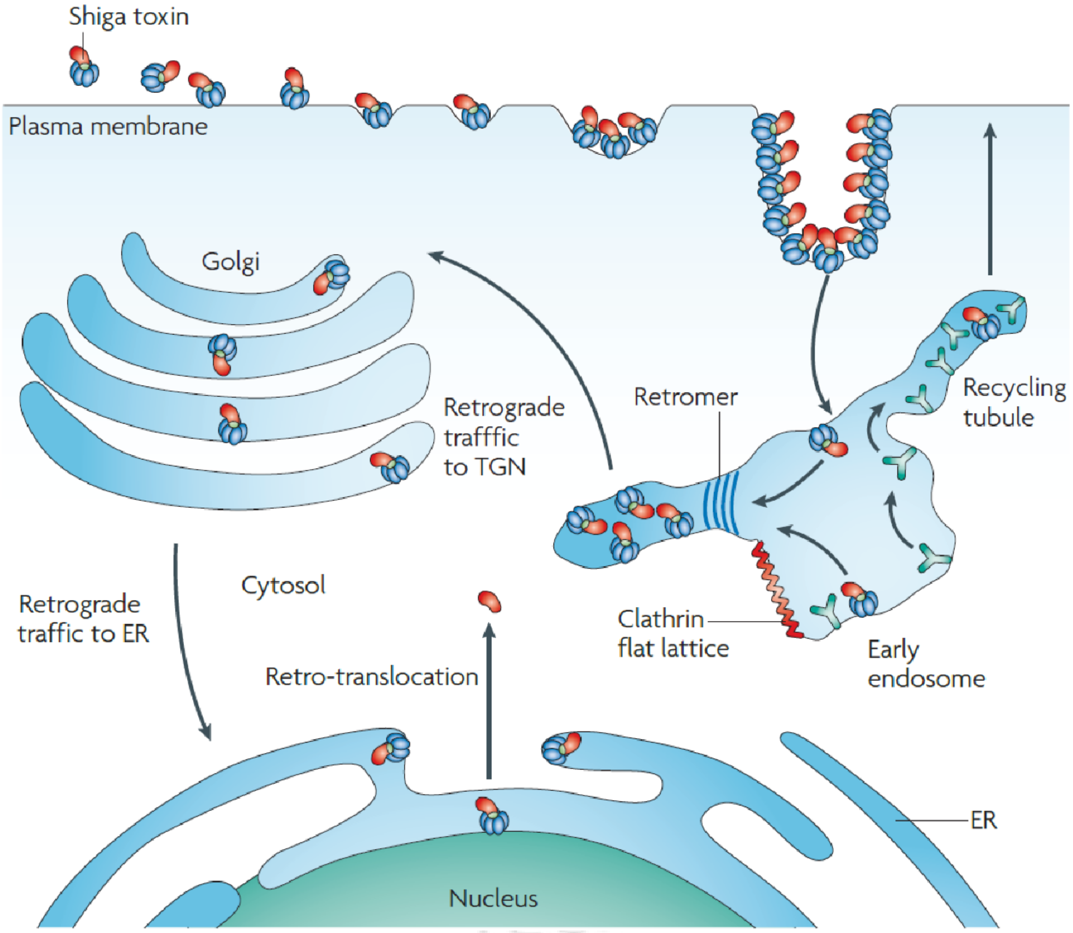

Figure 1.2: Mechanism of action of Shiga toxins illustrating retrograde trafficking (Johannes & Römer, 2010).

1.2.5. Subtypes of Shiga toxins.

Although the Shiga toxins from STEC share a common AB_5 structure, they are classified into two major groups, Stx1 and Stx2. Furthermore, based on the sequence identity and cellular toxicity, each of these groups are divided into various subtypes. The Stx1, also known as Stx1a, is considered the prototype for the Stx1 subtypes. Similarly, the Stx2, also known as Stx2a, is designated as the prototype for Stx2 subtypes. Stx1 is subdivided into 4 distinct subtypes, Stx1a (also known as Stx1), Stx1c, Stx1d, and Stx1e. These subtypes share sequences in the range of 95% - 98.3%. Compared to the prototype Stx1, the Stx1c subtype displays a 97.1% and 96.6% identity in the A and B subunit, respectively. In addition to the variation in the sequence, Stx1c exhibits differences in the antigenic properties, as it shows a reduced reactivity as compared to Stx1a in the reverse passive latex agglutination assay (VTEC-RPLA) (Wenlan et al., 2002). The Stx1d subtype has an overall sequence similarity of only 91%, with the A subunit and the B subunit exhibiting 93.7% and 92.1% sequence similarity, respectively. The Stx1d, is reported to be less cytotoxic as compared to its prototype Stx1 (Christine et al., 2003). The Stx1e subtype share only 87% amino acid sequence similarity in comparison to Stx1 (Skinner et al., 2016).

There are 15 subtypes reported for Stx2, from Stx2a to Stx2o. The Stx2 subgroups display higher heterogeneity in their nucleotide/amino acid sequences as compared to the Stx1 subtypes. The Stx2b subtype showed a 95.9% and 88.6% nucleotide sequence similarity in the A and B subunits, respectively, as compared to the Stx2d subtype (Paton et al., 1992). The Stx2c subtype exhibited a nucleotide sequence similarity in the range of 94.6% - 98.5% and 79% - 98.6% for the A and B subunit, respectively, compared to the other subtypes of Stx2, including Stx2a, Stx2d, and Stx2e (Schmitt et al., 1991). A nucleotide sequence similarity in the range of 94.5% - 99% and 81.5% - 96% for the A and B subunit was observed for Stx2d, in comparison with the sequences of the other subtypes (Yolande et al., 2001). The Stx2e subtype was found to exhibit cytotoxicity to Vero cells, but not to HeLa cells (Marques et al., 1987), further, it displayed a high nucleotide sequence similarity of 94% in the A subunit, but it showed a high heterogeneity in the B subunit sequence with a similarity of only 79% (Weinstein et al., 1988). The Stx2f subtype exhibits very low reactivity with commercial Stx2 immunoassay tests, further their sequence comparison with Stx2a displayed a very low similarity of 63.4% and 57.4% in the A and B subunit, respectively (Herbert et al., 2000). When compared to the other variants of Stx2, from Stx2a to Stx2f, the Stx2g variant displayed a sequence homology in the range of 63% - 94.9% and 76.7% - 90.7% in the A and B subunit, respectively (Leung et al., 2003). The Stx2h subtype share a sequence homology in the range of 69.7% - 92.9% in the A subunit and 67.2% - 91.3% in the B subunit, with any other Stx2 subtype (Bai et al., 2021). Lacher et al., 2016 first identified the Stx2i subtype in 2016 after isolating an unknown Stx2 subtype from a STEC infected shrimp. The Stx2j subtype was first identified in 2022 and it was found to be sharing the highest homology with Stx2h with 91.9% nucleotide sequence identity (Alexander et al., 2022). The Stx2k subtype share a sequence homology in the range of 46.3% -98.3% and 69.9% - 100% in the A and B subunit compared to other subtypes of Stx2 from Stx2a to Stx2i (Yang et al., 2020). Certain sequences that were earlier grouped as the

Stx2e subtype were reclassified as Stx2l due to their sufficient divergence from the established Stx2e subtype (Yang et al., 2022). The Stx2m subtype was first identified in 2021, and it shares a nucleotide sequence similarity in the range of 63.4% – 92.6%, and an amino acid sequence similarity of the range 72.4% – 93.8%, with the other subtypes of Stx2, from Stx2a to Stx2l (Bai et al., 2021). In 2023, Lindsey et al., 2023, identified and characterized the subtypes Stx2n and Stx2o. The Stx2n exhibit a nucleotide and amino acid sequence homology in the range of 72.2% – 94.6% and 83.9% – 95%, respectively with other Stx2 subtypes, while the Stx2o subtype displayed an amino acid sequence identity of 81.8% – 96.9% and a nucleotide sequence homology 70.4% – 94.1%.

Among the STEC infected clinical isolates, both Stx1 and Stx2 are found in equal frequencies. However, toxin belonging to the Stx2 family is associated with more severe human diseases, such as haemorrhagic colitis (HC) and HUS, while Stx1 intoxication is associated with mild or uncomplicated diarrhoea, with very few cases of HUS (Nüesch-Inderbinen et al., 2018). Among the Stx1 subtypes, Stx1a is the most predominant subtype in human infection as compared to the other subtypes (Melton-Celsa, 2014), and Stx1d is very rarely isolated from STEC infected human clinical samples (Wang et al., 2024). Furthermore, Stx1a is associated with more severe diseases as compared to the other subtypes of Stx1 (Bai et al., 2018).

Although, Stx2 is associated with more severe form of disease, out of the 15 subtypes, four subtypes viz., Stx2a, Stx2b, Stx2c, and Stx2d are more frequently associated with human disease. Infection with subtypes Stx2a, Stx2b, Stx2c, Stx2d, Stx2e, and Stx2f are associated with more severe form of disease as compared to the other subtypes, with Stx2a being the most potent among them in causing bloody diarrhoea and HUS (Wang et al., 2024).

1.3. Detection of STEC infection.

At present, there is no approved vaccine for humans against Shiga toxins or STEC infection (Liu et al., 2023). Treatment of patient with STEC infected HUS primarily involves supportive therapy, including fluid management, tracking and correcting electrolyte concentration, and controlling of blood pressure if needed (Harkins et al., 2020). The use of antibiotics is also conflicting, as some investigations indicate an increased risk of HUS (Wong et al., 2002), others have found no significant association, or even a potential benefit, depending on the class of antibiotic and treatment regimen employed (Bielaszewska et al., 2012) (Freedman et al., 2016). These therapeutic limitations emphasize the importance of accurate and early diagnosis to recommend appropriate medications, early intervention to reduce the risk of development of severe complications.

1.3.1. Laboratory-based diagnosis method

Current laboratory-based diagnosis of STEC infection and associated HUS includes a range of approaches, from culture-based identification of the causative organism and serotyping, to molecular detection of virulence genes such as *Stx1* and *Stx2* using PCR or qPCR. In addition, Shiga toxins can be directly detected using toxin-specific antibodies in enzyme immunoassays. These conventional methods are widely employed in public health laboratories and clinical microbiology settings.

1.3.1.1. Culture-based methods

The bacterial culture-based method is considered the gold standard in STEC diagnosis. Culture-based methods allow the isolation of viable organisms for identification and typing. It involves the plating of STEC infected samples on petri dishes containing specialized media that allow the selective growth of isolated colonies of the target organisms and support their identification in presence of other microorganisms. The media used for selective growth and isolation of *E. coli* O157 utilizes the differential characteristics unique to them and not available to other *E. coli* organisms, such as its inability to ferment sorbitol and absence of *β*-D-glucuronidase activity (Gill et al., 2014). Various media have been developed and used for the identification of different serotypes of STEC, such as Sorbitol MacConkey agar, Rainbow agar O157, CHROMagar, and Tryptone bile agar (Gill et al., 2014) (Verhaegen et al., 2015) (Parsons et al., 2016). Further selective growth is achieved with the use of antimicrobials, such as novobiocin and tellurite in appropriate concentrations with the media. Additional biochemical tests and serological tests are also performed for identification. According to the International Organization for Standardization (ISO), for detection of *E. coli* O157 from food sample, the samples are first enriched in selective media such as tryptone soy broth, infused with novobiocin and incubate at 41 °C – 42 °C. Following an incubation of 6 – 18 hours, immunomagnetic separation (IMS) is carried out using magnetic beads coated with O157 specific antibodies. The beads are plated on selective agar media such as Sorbitol MacConkey Agar with cefixime and tellurite or chromogenic media and incubated for 18 – 24 hours at 37 °C. The colonies from the plates are picked and streaked on non-selective agar plate, such as nutrient agar. Further slide agglutination test using *E. coli* O157 specific antiserum or indole formation tests are performed for confirmation (FSAI, 2019).

Although culture-based method allows for isolation and identification of viable microorganisms, they are highly time consuming, labour intensive, and may fail to recognize all serotypes of STEC due to the use of selective and differential culture media as they are used to target unique phenotypes, that may be absent in other serotypes. Moreover, culture identification of STEC does not confirm the presence of Shiga toxins, as it depends on the bacterial growth conditions and phage induction process.

1.3.1.2. Cytotoxic assay

Mammalian cell cytotoxicity assay-based methods are one of the first methods developed and used for the detection of Shiga toxins expressed by STEC. Unlike cell culture method or PCR based methods, the cytotoxicity assay directly measures the biological activity of the Shiga toxins. The Vero cell line extracted from the kidney of African green monkey is considered the gold standard, as they highly express Gb3 receptor on their cell surface and sensitive to Stx1 and Stx2 (Konowalchuk et al., 1977). In a typical Vero cell cytotoxicity assay, the culture supernatant from STEC infected sample or enriched sample are applied to Vero cells monolayers and their morphological changes are observed after 48 – 72 hours of sample application using microscope. In the presence of active Shiga toxins, the Vero cells appear round and shrivelled and found floating in the medium detached from the monolayer (Konowalchuk et al., 1977). In another cytotoxicity based method, the amount of Lactate dehydrogenase (LDH) released from lysed Vero cells following intoxication with Shiga toxins is measured for the screening of Shiga toxins (Roberts et al., 2001).

Despite their advantages, cytotoxic assay-based methods have notable limitations, such as they are labour intensive, time-consuming, need expert personnel, require cell culture facilities to perform.

1.3.1.3. PCR based detection of Stx genes

PCR based molecular detection is another method for direct detection of STEC from various samples. It involves the identification of the virulence genes encoding the Stx1 and Stx2 proteins along with genes such as *eae*, *intimin* gene, *hemolysin* gene, and *ehx4* gene. They are highly sensitive and specific and can perform multiplex assay to detect as well differentiate between multiple targets using different primers. However, the earliest method for identification of the *stx* genes involve the DNA hybridization method using ^{35}S-modified DNA probes (Willshaw et al., 1987) (Scotland et al., 1988). Following the DNA hybridization method, a very large number conventional PCR (Pollard et al., 1990) and real-time PCR based identification of *stx1* and *stx2* gene were developed (Bélanger et al., 2002) (Zhang et al., 2012). Several of RT-PCR based method for STEC detection have been commercialized, such as the GeneDisc STEC from Pall GeneDisc technologies (France), the Assurance GDS STEC from Biocontrol (Bellevue, WA), the Mericon VTEC stx1/2 from Qiagen (Switzerland), the LightMix Kit EHEC from Roche diagnostics (Switzerland), the iQ Check STEC VirX from from Biorad (France), the BAX system STEC suite screening assay from Dupont (Wilmington), the ABI custom Taqman VT1/VT2 assay from Applied biosystems (Carlsbad, CA). Generally, PCR or RT-PCR is incorporated with bacterial culture of the sample. The samples are first incubated on the agar media such as MacConkey Broth at 37 °C for 12 – 24 hours, following which DNA is isolated from the bacterial colonies and are tested for the presence of different STEC unique genes using PCR or RT-PCR.

Even though this method is highly sensitive and specific, it has certain limitations, these includes displaying of false negative or false positive results due to contamination in handling, errors in the amplification of the sequence due to the lack of exonuclease activity in Taq enzymes. Further it uses expensive instrumentation, needs expert operator, and it incurs high reagent costs (Liu et al., 2023).

1.3.1.4. MALDI-TOF based detection

MALDI-TOF mass spectrometry has been utilized in identification of the Shiga toxin proteins (Fagerquist & Sultan, 2010) as well as the STEC and differentiating their subtypes (Mclean et al., 2018). This method provides a highly sensitive and specific detection for Stx and STEC. It relies on the generation of mass spectrometry profile of the protein or the STEC and then comparing it with database containing already existing MS spectra of various organisms. This method depends on the evaluation of the spectra of highly expressed proteins of the bacteria, which represents the genetic makeup of the microorganism, leading to its identification (Elbehiry et al., 2022). For the analysis, the sample is allowed to grow on nutrient media, and a single colony is picked and mixed with the organic matrix, which co-crystallized with the sample after it dries and solidifies. Following the mixing with the matrix, the matrix-sample complex is irradiated with laser light. The laser energy is absorbed by the matrix, resulting in soft desorption and converting the matrix-sample complex to gaseous state. During desorption, charge transfer takes place due to the ion-molecule interaction between the uncharged neutral sample molecules and protonated matrix ions, the metal cations, electrons, and protons, resulting in ionization of the sample molecules. These ions are then accelerated through the time of flight analyzer using a set voltage and their mass to charge (m/z) ratio is analyzed based on the time taken by the ion to traverse the analyzer to reach the detector. The spectra of the analyzed sample is prepared by plotting the m/z ratio on the x-axis, and the intensity on the y-axis (Li et al., 2022). The resulting spectra is then matched with the library of spectra present with the device. The device library contains the spectra unique to the sample organism, and by comparing the spectra in the database, the identification of the unknown microorganism can be deduced. Mclean et al. have used MALDI-MS to identify and differentiate between the *E. coli* O157:H7 and other STEC along with differentiating within its serotype. They have used α-Cyano-4-hydroxycinnamic acid (CHCA) as the matrix and Bruker Biotyper software along with a custom mass spectra processing workflow to identify and differentiate the organisms (Mclean et al., 2018). Elabbasy et al, also identified pathogenic non-O157 STEC from carcasses of beef and samples from slaughterhouses using MALDI-TOF mass spectrometry. They have utilized the MALDI Biotyper 3 software for the analysis of the spectra (Elabbasy et al., 2021). Kubo et al, also used MALDI-TOF to rapidly detect STEC. They have used CHCA as the matrix for the sample preparation and identified using MALDI Biotyper RTC software and ClinProTools were used for the differentiation between STEC and non STEC organisms (Kubo et al., 2021). Fagerquist et al. have utilized MALDI-TOF MS based method for the identification of the Shiga toxins expressed by the STEC. They have used the targeted top-down proteomic strategy, which involves the MS/MS analysis of the mature proteins, without digesting the protein. The sample was prepared using Sinapinic acid as the matrix, and the MALDI-TOF MS displayed the peak for Stx1 B subunit and the Stx2 B subunit (Fagerquist et al., 2019). In another work, they have identified the A2 fragment of the A subunit of Stx2, by expressing the protein in the presence of furin enzyme, which cleaves the A subunit of Stx2 into two subunits. Following the expression of the toxin, it was identified using the top down MALDI-TOF-TOF-MS/MS technique for identification. CHCA and Sinapinic acid was used as the matrix for sample preparation (Fagerquist & Sultan, 2010).

Overall, MALDI-TOF MS, due to their ability to identify highly conserved proteins expressed by the organisms, have demonstrated to identify and differentiate between different strains of STEC as well as to differentiate between different serotypes. The ability to differentiate between strains and serotypes is highly beneficial for physicians to recommend proper treatment. However, the instrument used is very expensive, and bulky, also it requires an expert to handle the machine. Additionally, if there is a lack of MS spectra of a new organism in the database, it might lead to misidentification of the pathogen.

1.3.1.5. Immunoassays

The immunoassay-based detection relies on the antigen-antibody interaction to detect, identify, and quantify the target molecule. Owing to their specificity, operational simplicity and compatibility with the routine diagnostic methods, they are widely used for the detection of Shiga toxins. Many commercially approved immunoassays for the detection of Shiga toxins have been developed for use in clinical laboratory settings. The Premier Enterohemorrhagic *E. coli* (EHEC) microwell immunoassay developed by Meridian Bioscience Inc., uses a monoclonal antibody developed against Stx1 and Stx2 and exhibited a sensitivity and specificity of 83.9% and 99.8%, respectively (Staples et al., 2012). Another commercially available Shiga toxin detection immunoassay, the ProSpect Shiga toxin *E. coli* microplate assay, was evaluated by Gavin et al. The assay uses anti-Stx1 and anti-Stx2 rabbit polyclonal antibodies as the capture antibody and a horseradish-peroxidase enzyme conjugated anti Stx1 and anti-Stx2 mouse monoclonal antibody as the detection antibody. After the reaction, the reaction mixture was analyzed spectrophotometrically at 450 nm. The assay demonstrated a sensitivity of 100% for *E. coli* O157 from stool samples, and a positive predictive value of 93% for the combined O157 and non-O157 serotypes (Gavin et al., 2004). Chui et al., evaluated the performance of the Shiga toxin check and Shiga toxin quick check immunoassay developed by TechLab Inc., for the detection of Stx1 and Stx2. Both the immunoassay exhibited a Limit of detection (LOD) of 7.0 × 10^5 CFU/reaction, with a sensitivity in the range of 70% – 85% and a selectivity in the range of 98.2% to 100% (Chui et al., 2015). Doupath Verotoxin test developed by Merck is another immunochromatographic assay used for detection of Stx1 and Stx2, by immobilizing anti-Stx antibodies on a membrane. Additionally, a commercially available immunoassay for detection of Stx1 and Stx2, ImmunoCard STAT developed by Meridian Bioscience exhibited no cross reactivity along with a sensitivity and selectivity of 35% and 99%, respectively (Chui et al., 2015).

The specificity, sensitivity, operational simplicity, and commercial availability have facilitated the widespread adoption of immunoassays for the detection Shiga toxins. However, the use of antibodies leads to low stability if exposed to different environments, high production costs. Moreover, the immunoassays require enrichment of the sample in culture, leading to a longer time to perform.

The laboratory-based methods for detection of Shiga toxins and identification of STEC involving culture based, considered the gold standard, along with PCR based, MALDI-TOF based, and immunoassays are widely used due to their specificity, high sensitivity, ability to differentiate between different subtypes and serotypes of STEC as well as between shiga toxins. However, these methods are time consuming, involves high costs, require trained personnel to handle, require specialized equipment and laboratory settings to perform. Consequently, there is a need for development of rapid, sensitive, specific, low cost, portable sensor to be used in resource limiting settings, for the detection of Shiga toxins.

1.3.2. Rapid detection methods

To address the limitations associated with the laboratory-based detection of STEC and Shiga toxins, rapid detection methodologies are being developed. These approaches are developed to decrease the turnaround time for the detection, reduce the cost, minimal sample preparation, easy to handle, and to be deployable at resource limiting settings.

1.3.2.1. Lateral flow assay-based detection

Lateral flow assay (LFA) is one of the most widely adopted rapid detection technologies for detection of Shiga toxins due to their simple, rapid, cost-effective, and portable nature. These assays enable the qualitative or semi-quantitative detection of Shiga toxins. As LFA does not involve complex machinery, they can be handled without the need for any expert personnel, making them suitable for preliminary screening in clinical, food safety, and point of care settings. LFA are mostly paper and nitrocellulose membrane-based platforms, which rely on the capillary driven flow and the interaction between the recognition element and target molecule to generate visible signals. A typical LFA test strip consists of four components, the sample pad, absorbent pad, conjugate pad, and the nitrocellulose membrane. The biorecognition elements are immobilized on the nitrocellulose membrane (Moyano et al., 2020). Ching et al., developed an LFA based colorimetric sensor for the detection Stx1 and six Stx2 subtypes using monoclonal antibodies that interact with epitopes common to both Stx1 and Stx2. They have used a sandwich Enzyme-Linked Immunosorbent Assay (ELISA) format, where the antibody Stx2-1 was used as the capture antibody and was immobilized on an immunopore SP membrane, and the gold-conjugated antibody Stx2-2 was used as the detector antibody.

Target	Biorecognition Element	Assay format	LOD	Reference
Stx1 and Stx2	Monoclonal antibodies	Sandwich LFA	0.1 ng mL^{-1}	Ching et al., 2015
Stx2 (Two format of LFA)	Monoclonal antibodies	Sandwich LFA	5 ng mL^{-1} and 25 ng mL^{-1}	Lu et al., 2020
Stx1 and Stx2	Monoclonal antibodies	Sandwich LFA	1 ng mL^{-1}	Wei et al., 2020
Stx1 and Stx2	Polyclonal and Monoclonal antibodies	Sandwich LFA		Wang et al., 2016

Table 1.1: - Prominent LFA-based systems for Shiga toxin detection and analytical performance.

The LFA exhibited an LOD of 0.1 ng mL^{-1} (Ching et al., 2015). Lu et al. developed two lateral flow immunochromatographic test strips (LFITS) for the rapid detection of Shiga toxin type 2 (Stx2), employing colloidal gold nanoparticles and CdTe quantum dots as colorimetric and fluorimetric signal labels, respectively. The assay was based on a sandwich immunoassay format, in which an anti-Stx2 monoclonal antibody (Ab1) was immobilized on the nitrocellulose membrane as the capture antibody, while a second anti-Stx2 antibody (Ab2) conjugated to either gold nanoparticles or CdTe quantum dots served as the detector probe. The gold nanoparticle-based LFITS enabled visual detection by the naked eye with a limit of detection of 25 ng mL^{-1}, whereas the quantum dot-based LFITS achieved enhanced sensitivity with a visual detection limit of 5 ng mL^{-1} under UV illumination. Both formats demonstrated good selectivity, stability, and rapid assay times, highlighting their potential for PoC detection of Stx2 (Lu et al., 2020). A comprehensive overview of lateral flow assay–based detection strategies reported for Shiga toxins is provided in **Table 1.1**. Despite their simplicity and rapid response, most reported LFA-based methods for Shiga toxin detection rely on antibody–antigen interactions and remain limited by moderate sensitivity, antibody stability issue, batch-to-batch variability, which restricted quantitative detection, underscoring the need for an alternative recognition elements and improved transduction strategies.

1.3.2.2. Biosensors

Biosensors are analytical devices that integrate a biorecognition elements with a transducer to enable specific and sensitive detection of target analytes by converting the biochemical signal to a detectable electrical or other suitable signal (Goswami, 2020). In comparison to laboratory-based detection techniques such as culture-based method, PCR based method, cytotoxicity assay, MALDI-TOF based methods, biosensors offer several advantages, including reduced assay time, portability, low cost, can be handled without an expert, and the potential for real-time on-site application. These properties make biosensors a better alternative for applications in food safety, environmental monitoring, and clinical diagnosis, where rapid decision-making is critical. A typical biosensor consists of five components, the biorecognition element, transducer, amplifier, processor and the display (**Figure 1.3**). The biorecognition element including aptamer, protein, antibody, antigen, enzymes, and bacterial cells are the commonly used component that interacts with the target molecules providing specificity to the biosensor. The transducer which is placed in close contact with the biorecognition element converts the signal generated due to the interaction of target and the biorecognition element into a quantitative or semi-quantitative signal. The amplifier component amplifies the signal converted by the transducer and it also removes the background noise that may arise from the transducer by subtracting the baseline signals. A processor processes the input signal received and convert it to a digital form for display. Further the display unit displays the processed data in its recognizable format. Based on the type of transducer, biosensors can be categorized into electrochemical, optical, piezoelectric, and

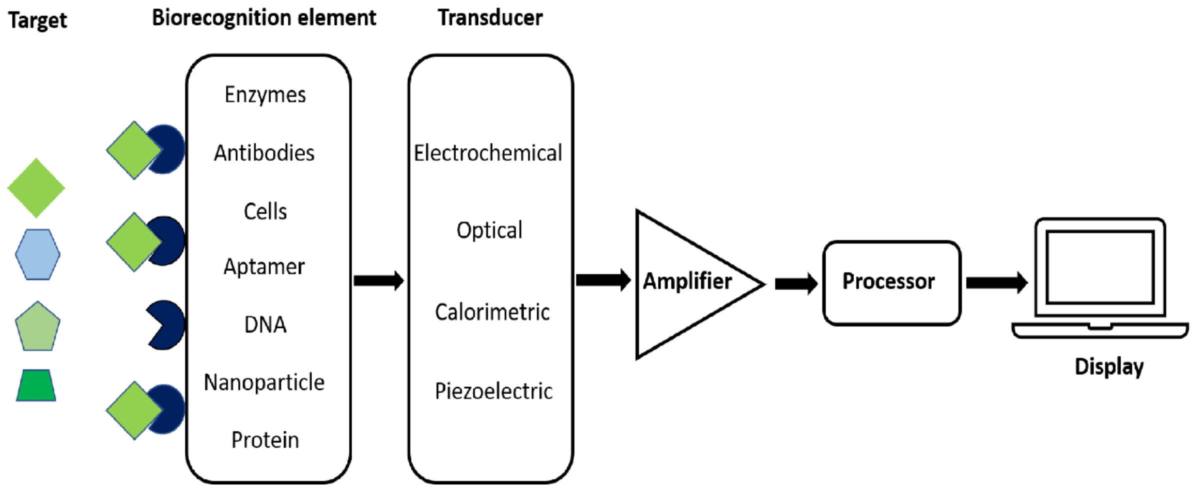

Figure 1.3: General configuration of a biosensor.

calorimetric biosensors. A survey of the existing literature indicates that the majority of biosensor-based strategies developed for the detection of Shiga toxins are predominantly based on optical and electrochemical transduction principles. These two approaches have attracted the greatest attention due to their high analytical sensitivity, adaptability to diverse biorecognition elements, and suitability for both laboratory-based and portable detection platforms. Consequently, the following sections focus on electrochemical and optical biosensors reported for Shiga toxin detection, with particular emphasis on their sensing mechanisms, biorecognition strategies, and analytical performance characteristics.

1.3.2.2.1. Electrochemical biosensors for the detection of Shiga toxins

Electrochemical biosensors constitute one of the most widely explored classes of biosensing platforms due to their high sensitivity, simplicity, and compatibility with miniaturized and portable electronic systems. These biosensors operate by converting the specific biorecognition event occurring between the biorecognition element and the target molecule into a measurable electrical signal, typically in the form of current, potential, or impedance changes (Kalita et al., 2023). Based on the transduction mechanism used in electrochemical biosensors, they can be classified into amperometry, voltammetry, potentiometry and electrochemical impedance spectroscopy (EIS), each offering distinct advantages and information about the interaction between the target and the biorecognition element. Amperometric and voltammetric biosensors rely on the measurement of current generated by redox reactions at the electrode surface, offering high sensitivity and wide linear detection ranges. While Amperometric biosensors quantify the target concentration by measuring the current generated from a redox reaction at a constant potential, voltammetric transducers scan across a potential window to identify and quantify the target concentration via current-voltage profiles. Potentiometric sensors measure changes in potential under mostly near-zero current conditions, while impedance-based biosensors monitor alterations in interfacial properties such as charge transfer resistance and double-layer capacitance. Among these, electrochemical impedance spectroscopy (EIS) has gained increasing attention owing to its high sensitivity, label-free detection of biomolecular interactions by monitoring interfacial impedance changes, commonly using an external redox probe, without the need for enzymatic or nanoparticle labelling. Several electrochemical biosensing strategies have been reported for the detection of Shiga toxins, employing diverse recognition elements and assay formats. Patel *et al.*, developed a silver nanoparticle (AgNP)-based electrochemical biosensor for the detection of Shiga toxin-1 using commercially available screen-printed carbon electrodes in which a sandwich immunoassay format was employed, wherein Shiga toxin-1 was captured using antibody-functionalized magnetic beads and subsequently labelled with antibody-conjugated AgNPs. Following immunomagnetic separation, the AgNP labels were chemically dissolved in nitric acid, and the released silver ions were quantified using anodic stripping voltammetry. The sensor exhibited an LOD of 2 ng mL^{-1} for Shiga toxin-1 in phosphate-buffered saline with an assay time of less than three hours (Patel et al., 2023). An alternative electrochemical biosensing strategy was reported by Kaur *et al.*, who used aptamers as the biorecognition element with voltammetric detection for the sensitive identification of Stx1 and Stx2. In this study, aptamers were immobilized onto a chitosan-functionalized tungsten diselenide (WSe_2) nanosheet-modified electrode to fabricate a label-free electrochemical aptasensor. Toxin binding at the aptamer-modified electrode surface was transduced using square-wave voltammetry, resulting in a concentration-dependent decrease in current signal. The developed aptasensor demonstrated a wide dynamic range (50 pg mL^{-1} to 100 ng mL^{-1}) with LOD of 44.5 pg mL^{-1} and 41.3 pg mL^{-1} for Stx1 and Stx2, respectively (Kaur et al., 2020).

1.3.2.2.2. Optical biosensors for detection of Shiga toxin

Optical biosensors translate the interaction between a target analyte and a specific biorecognition element into a measurable optical signal. These signals typically arise from changes in optical properties such as absorbance, fluorescence intensity, refractive index, scattering, or Raman signatures. Owing to their inherent sensitivity, non-invasive signal transduction, and capability for real-time monitoring, optical biosensors have been widely applied for the detection of a broad range of biomolecules, including proteins, nucleic acids, and small-molecule toxins. In a typical optical biosensor, the recognition element such as an antibody or aptamer is immobilized on an optically active substrate, and binding with the target molecule leads to a change in the local optical environment that can be quantitatively measured. Depending on the transduction principle, these changes may arise from alterations in refractive index at a metal surface, variation in fluorescence emission, nanoparticle aggregation-induced colour shifts, or enhanced Raman scattering. Based on their transduction principle the optical biosensors can be classified into surface plasmon resonance (SPR) based sensors, fluorescence-based sensors, colorimetric assays, interferometric techniques, and surface-enhanced Raman scattering (SERS) based sensors. An optical biosensing strategy based on localized surface plasmon resonance (LSPR) was reported by Nagatsuka *et al.*, who developed glycan-functionalized plasmonic chips for the detection of Shiga toxin by mimicking its natural host-cell recognition mechanism. In this work, gold nanoparticles of varying diameters were immobilized on glass substrates and functionalized with synthetic globotriaosylceramide (Gb3) oligosaccharides, which serve as the native cellular receptors for Shiga toxin. Binding of the toxin to the Gb3-coated nanoparticles induced changes in the local refractive index at the nanoparticle surface, which were monitored as LSPR signal variations using a portable optical setup. The developed sensor exhibited an LOD of 10 ng mL^{-1} with an assay time of 20 minutes (Nagatsuka et al., 2013). Ren *et al.*, developed a dual-mode aptamer-based biosensor integrating colorimetric and SERS detection for the sensitive determination of Stx2. In this work, a high-affinity DNA aptamer specific to Stx2 was employed as the biorecognition element and combined with a multifunctional signal probe composed of bimetallic Manganese-Iron-doped Matériaux de l'Institut Lavoisier number 53 (Mn/Fe-MIL(53)) metal–organic framework decorated with gold nanostars (Mn/Fe-MIL(53)@AuNSs). The sensing mechanism relied on an aptamer–cDNA hybridization strategy coupled with magnetic bead separation, where target binding triggered the release of the Mn/Fe-MIL(53)@AuNSs probe into the supernatant. The released probe catalyzed the H_2O_2-mediated oxidation of 3,3',5,5'-Tetramethylbenzidine (TMB), enabling visual colorimetric detection, while simultaneously generating a strong SERS signal through the embedded Raman reporter (4-mercaptobenzoic acid) and plasmonic gold nanostars. The colorimetric mode achieved an LOD of 26 pg mL^{-1} within a dynamic range of 0.05 – 500 ng mL^{-1} and for the SERS mode the sensor achieved an LOD of 0.82 ng mL^{-1} and a dynamic range of 5 – 1000 ng mL^{-1} (Ren et al., 2024). Another optical biosensing approach was developed by Wang et al., using a surface plasmon resonance imaging (SPRi)–based immunosensor platform. In this study, multiple monoclonal and polyclonal antibodies against Shiga toxin subtypes were microarray-spotted onto a gold-coated SPRi biochip, enabling high-throughput and multiplex detection within a flow-cell format. Detection was achieved by monitoring changes in reflectivity (ΔR) arising from toxin–antibody binding at the gold surface, allowing real-time, label-free analysis of Stx1a and Stx2a toxoids. In the direct label-free format, the SPRi assay achieved limits of detection in the range of 50–100 ng mL^{-1}, with polyclonal antibodies providing higher sensitivity than monoclonal counterparts. To overcome sensitivity limitations associated with the relatively small molecular mass of Shiga toxins, the authors further implemented a gold nanoparticle–amplified sandwich immunoassay, which enhanced the SPRi signal by nearly two orders of magnitude and improved the detection limit to the picogram per millilitre level, while maintaining a total assay time of less than 20 minutes (Wang et al., 2020). An alternative optical biosensing strategy targeting Shiga toxin–producing *E. coli* biomarkers was reported by Lamoureux *et al.*, who developed a planar optical waveguide–based biosensor for the sensitive detection of Shiga toxin and lipopolysaccharides in complex food matrices. The platform exploits evanescent field–based fluorescence sensing, in which biorecognition events occurring at the waveguide surface are selectively excited and detected with minimal background interference. For Shiga toxin detection, the authors employed a sandwich immunoassay format using a biotinylated lipid bilayer–functionalized waveguide surface, with a biotinylated monoclonal antibody against the Stx2 A subunit serving as the capture element and a fluorescently labelled polyclonal antibody against the B subunit as the reporter. Binding of the toxin resulted in a concentration-dependent fluorescence signal, enabling label-based optical detection with a signal-to-noise ratio of approximately five for Stx2 at 100 µg mL^{-1} (Lamoureux et al., 2015). **Table 1.2** contains the optical sensors developed for detection of Shiga toxins.

Target	Optical Principle	Biorecognition Element	LOD	Reference
Stx1 & Stx2	SPR imaging	Antibodies	50 ng mL^{-1}	Wang et al., 2020
Stx1	LSPR	Gb3	10 ng mL^{-1}	Nagatsuka et al., 2013
Stx2	Colorimetric	Aptamer	26 pg mL^{-1}	Ren et al., 2024
Stx2	SERS	Aptamer	0.82 ng mL^{-1}	Ren et al., 2024
Stx2	Planar optical waveguide	Antibodies		Lamoureux et al., 2015
Stx1 & Stx2a	SERS	Antibodies	0.007 ng mL^{-1}	Milano et al., 2025
Stx1 & Stx2	SERS	Adsorption based	15 pM	D'Avino et al., 2025
Stx2	SERS	Antibodies	1.4 nM	Rippa et al., 2022

Table 1.2: Prominent optical-based sensors for Shiga toxin detection and their analytical performance.

1.4. Biorecognition element

The biorecognition element is a critical determinant of biosensor performance, as it governs specificity toward the target analyte and directly influences sensitivity, reproducibility, and applicability in complex sample matrices. In biosensors developed for Shiga toxin detection, the majority of reported platforms have employed either antibodies or aptamers as recognition elements. These affinity ligands provide selective interaction with the toxin and enable its transduction into a measurable signal through electrochemical or optical readout mechanisms.

1.4.1. Antibody based biorecognition

Antibodies have historically been the most widely used biorecognition elements in Shiga toxin biosensors. Their high binding affinity and epitope specificity have enabled the development of both electrochemical immunosensors and optical immunoassays, often employing sandwich-type configurations to enhance selectivity and signal intensity. In such systems, monoclonal antibodies are typically used as capture probes due to their defined specificity, while polyclonal antibodies are frequently employed as detection probes to amplify the analytical signal.

Despite their extensive application, antibody-based biosensors exhibit several inherent limitations that restrict their broader adoption. Antibodies, as discussed above, are sensitive to environmental conditions such as temperature, pH, and ionic strength, which can lead to denaturation and loss of binding activity. Their performance is also highly dependent on surface immobilization orientation and density, factors that can vary significantly between sensor preparations. In addition, batch-to-batch variability, limited shelf life, and relatively high production costs pose challenges for reproducibility and large-scale deployment. These constraints become particularly significant in applications requiring long-term stability, repeated use, or operation in complex matrices such as food samples or biological fluids.

1.4.2. Aptamer based biorecognition

Aptamers are short, single-stranded DNA or RNA oligonucleotides, and polypeptides (rarely used) that can selectively bind target molecules through the formation of well-defined three-dimensional structures. Selected in vitro through systematic evolution processes such as Systematic Evolution of Ligands by Exponential Enrichment (SELEX), nucleic acid aptamers have emerged as versatile biorecognition elements for biosensing applications (Tuerk & Gold, 1990) (Ellington & Szostak, 1990). Unlike antibodies, which rely on biological production systems, aptamers are chemically synthesized, allowing precise control over sequence composition, structure, and functional modification.

Aptamer–target recognition is governed by a combination of non-covalent interactions, including hydrogen bonding, electrostatic interactions, π–π stacking, van der Waals forces, and shape complementarity (Zhang et al., 2023). Upon binding to their target, aptamers may undergo conformational rearrangements that stabilize the aptamer–target complex. These structural changes form the basis of many sensing strategies, as they can be readily transduced into measurable signals through changes in interfacial properties, molecular displacement events, or signal reporter proximity (Shraim et al., 2022). Depending on the nature of the target, aptamer binding can occur through different interaction modes. For protein targets, aptamers typically recognize surface-exposed epitopes or structural motifs via folded secondary and tertiary structures. In some cases, aptamer binding results in a significant conformational transition, while in others, binding is dominated by surface adsorption and localized electrostatic interactions. These diverse binding modes provide flexibility in sensor design, enabling both direct binding assays and competitive or displacement-based formats.

A key advantage of aptamers lies in their chemical stability and robustness under a wide range of environmental conditions. Aptamers generally exhibit greater resistance to temperature fluctuations, pH variations, and organic solvents compared to antibodies, making them well suited for biosensing applications involving complex sample matrices. In addition, aptamers can be readily modified with functional groups, redox labels, or spacers without significantly compromising binding affinity, facilitating their integration with diverse transduction platforms (Mili et al., 2024). Another important advantage of aptamers is their reproducibility and batch-to-batch consistency. As fully synthetic molecules, aptamers can be produced with high purity and minimal variability, addressing a major limitation associated with antibody-based recognition. Furthermore, aptamers often allow regeneration of sensor surfaces through controlled denaturation and refolding, enabling repeated use of sensing platforms.

1.5. Generation of aptamer via SELEX

The SELEX process involves iterative rounds of selection and amplification, during which oligonucleotide sequences capable of binding the target molecule are progressively enriched from a large, randomized nucleic acid library. Since its introduction, SELEX has been successfully applied to a broad range of targets, including small molecules, proteins, cells, and toxins, and remains the benchmark method for aptamer discovery (Chen et al., 2016).

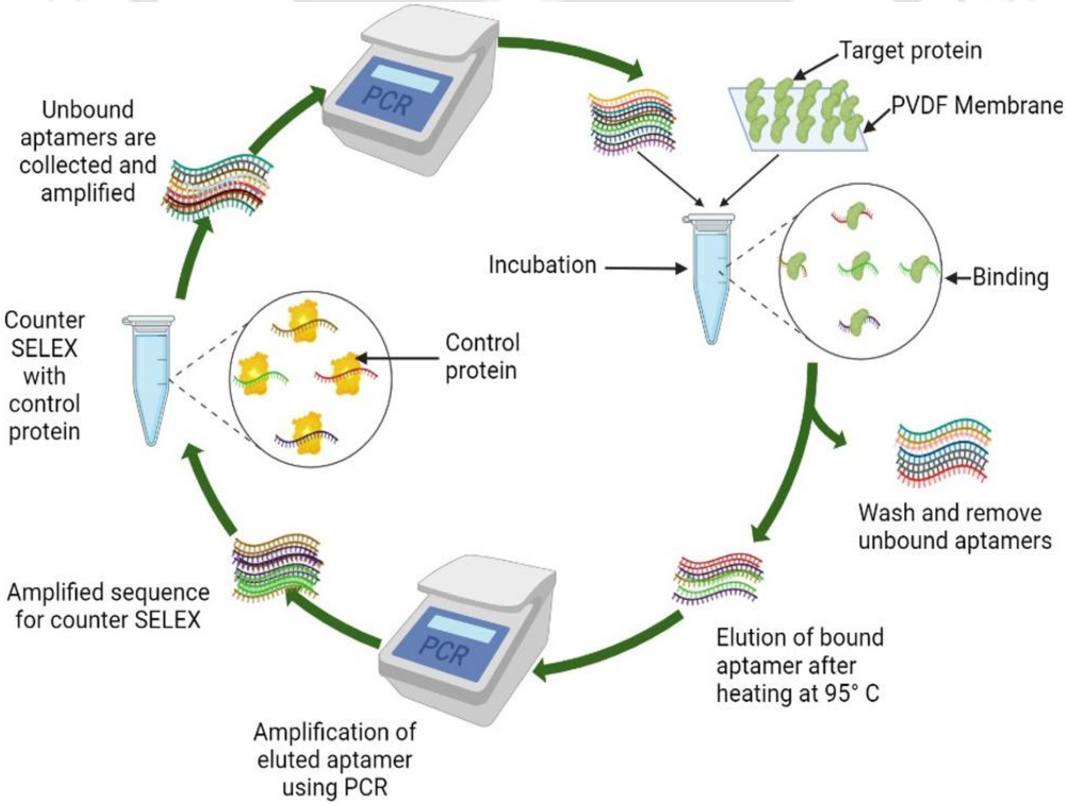

Figure 1.4: General configuration of SELEX cycle. (Created using biorender.com).

A typical SELEX workflow begins with a single-stranded DNA or RNA library containing a randomized central region flanked by fixed primer-binding sites. This library is incubated with the target molecule, allowing binding between single stranded oligonucleotides and the target molecule. Following incubation, bound sequences are separated from unbound or weakly bound sequences using partitioning techniques such as affinity chromatography, magnetic separation, or membrane filtration. The bound sequences are then recovered and amplified, typically by PCR for DNA aptamers or by reverse transcription followed by PCR for RNA aptamers. The amplified pool is converted back to single-stranded form and subjected to subsequent rounds of selection. With each successive SELEX round, selection stringency is increased by adjusting parameters such as target concentration, incubation time, washing conditions, or buffer composition. These adjustments promote enrichment of sequences with higher binding affinity and specificity. After multiple rounds, often ranging from 8 to 15, the enriched pool is cloned or sequenced, and individual aptamer candidates are characterized for their binding properties using biochemical or biophysical assays (**Figure 1.4**).

SELEX offers several advantages as an aptamer selection method. It is performed entirely in vitro, allowing precise control over selection conditions and eliminating the need for animal immunization. Aptamers selected via SELEX often exhibit comparable affinity and selectivity to antibodies, while offering advantages such as chemical stability, ease of synthesis, and batch-to-batch reproducibility. These attributes make SELEX-derived aptamers particularly attractive for biosensing applications.

Despite its success, SELEX also presents several limitations. The process is inherently time-consuming and experimentally demanding, requiring multiple iterative rounds of selection and amplification. Additionally, amplification via PCR can introduce bias into the evolving pool, favouring sequences that amplify more efficiently rather than those with superior binding affinity. Such bias can result in loss of potentially high-affinity candidates during the enrichment process (Takahashi et al., 2016). Furthermore, SELEX typically requires purified and structurally stable target molecules, which may not always be readily available for complex protein toxins.

To address the experimental complexity associated with conventional SELEX, numerous variants of the selection process have been developed with the aim of improving efficiency, specificity, and selection speed. Counter-SELEX and negative selection strategies are commonly incorporated to eliminate sequences that bind non-target molecules, thereby enhancing selectivity and reducing downstream screening efforts (Bachu et al., 2024). Capillary electrophoresis SELEX (CE-SELEX) minimizes the number of selection rounds by exploiting mobility differences between bound and unbound oligonucleotides, enabling rapid enrichment of high-affinity binders without immobilization of the target (Takahashi et al., 2016). Cell-SELEX allows aptamer selection against native targets presented on cell surfaces, eliminating the need for purified target proteins and preserving physiological conformation (Chen et al., 2016). To further reduce experimental time and reagent consumption, microfluidic SELEX and bead-based SELEX platforms integrate binding, partitioning, and washing steps into miniaturized systems, allowing automated and high-throughput selection (Lin et al., 2014). More recently, real-time and label-free SELEX approaches, such as biolayer interferometry-based SELEX, enable direct monitoring of binding events during selection, reducing the number of iterative rounds required (Lin et al., 2014). Although, these SELEX variants streamline the selection process and mitigate some limitations of conventional SELEX, however, they do not fully eliminate experimental complexity or amplification-associated biases, underscoring the need for complementary computational strategies for aptamer development.

1.6. Computational approach for aptamer selection and design

The development of high-affinity aptamers has traditionally relied on the SELEX process, which involves iterative rounds of binding, partitioning, and amplification to enrich target-specific sequences from large random libraries as mentioned above. Although SELEX has been successfully applied to a wide range of targets, it is inherently time-consuming, resource-intensive, and experimentally demanding. Moreover, amplification steps, particularly PCR, can introduce systematic biases that favour sequences with higher amplification efficiency rather than superior binding affinity, potentially leading to the loss of promising candidates (DeRosa et al., 2023). These limitations have driven growing interest in computational approaches as complementary or alternative strategies for aptamer selection and optimization.

Computational methods offer the ability to explore large sequence spaces *in-silico*, reduce experimental burden, and provide molecular-level insight into aptamer–target interactions. By enabling early-stage screening of candidate sequences based on structural stability and predicted binding behaviour, computational workflows can significantly narrow down the number of sequences that require experimental synthesis and validation. This rational filtering is especially advantageous for challenging protein targets, such as bacterial toxins, where high specificity and affinity are essential and experimental screening can be costly and laborious.

1.6.1. *In-Silico* selection strategies for aptamer development

Current computational approaches for aptamer development generally follow a multistep workflow that integrates sequence generation, structural prediction, interaction analysis, and dynamic stability assessment. One of the most widely employed initial strategies involves secondary structure prediction, in which candidate aptamer sequences are evaluated based on their folding behaviour and thermodynamic stability. Computational tools based on nearest-neighbour thermodynamic models estimate the Gibbs free energy (ΔG) of folding, enabling prioritization of sequences that form stable yet structurally defined secondary conformations (Zuker, 2003). Such thermodynamic stability is widely regarded as a prerequisite for reliable target recognition and reproducible biosensor performance.

Following structural screening, molecular docking techniques are used to predict the binding orientation and interaction interface between the aptamer and the target molecule. Docking simulations provide insight into potential binding sites, dominant non-covalent interactions, and relative binding strengths by scoring multiple aptamer–target conformations. For protein targets, docking analysis can further identify surface regions that are particularly favourable for nucleic acid binding, thereby guiding rational selection of promising aptamer candidates (Yan et al., 2017).

To overcome the inherently static nature of docking predictions, molecular dynamics (MD) simulations are increasingly incorporated into aptamer design workflows. MD simulations allow evaluation of the temporal stability of aptamer–target complexes under solvated, physiologically relevant conditions. Parameters such as conformational fluctuations, interaction persistence, hydrogen-bond occupancy, and binding free-energy trends are commonly analysed to assess whether a docked complex remains stable over time. This dynamic perspective is especially important for nucleic acid–protein interactions, where molecular flexibility plays a critical role in binding.

One of the earliest and most comprehensive frameworks for computationally guided aptamer selection was proposed by Chushak and Stone, who demonstrated that *in-silico* screening could be used to dramatically reduce the aptamer sequence search space prior to experimental validation. The proposed strategy employs a multilevel screening pipeline**,** beginning with secondary structure–based selection. In this first step, large libraries of randomly generated RNA sequences are evaluated using thermodynamic folding algorithms, and sequences are filtered based on their predicted ΔG of secondary structure formation. Aptamers previously shown to bind small molecules were found to exhibit significantly lower free energies compared to random sequences of the same length, supporting the use of ΔG as a criterion to enrich structurally stable yet conformationally flexible candidates. Structural motif analysis is then applied to favour sequences containing accessible loop and bulge regions that are critical for molecular recognition. Three-dimensional structure prediction followed by molecular docking is subsequently used to evaluate aptamer–ligand interactions, enabling ranking of candidates based on binding propensity. This multilevel computational pipeline established the feasibility of ΔG-guided structural screening combined with docking as a rational framework for de novo aptamer design (Chushak & Stone, 2009).

Several computational strategies reported to date have focused primarily on the optimization of existing aptamer sequences, rather than on their de novo generation. These approaches commonly involve truncation of non-essential regions, systematic point mutation analysis, or affinity refinement of previously identified aptamers in order to enhance binding performance or reduce sequence length while preserving target specificity. More recently, hybrid methodologies that integrate computational screening with experimental validation or limited selection cycles have been proposed to accelerate aptamer development while maintaining experimental reliability. Such studies illustrate how *in-silico* tools can be used to rationally guide aptamer improvement and reduce experimental effort.

Bell *et al.* reported a structure-based computational framework in which a SELEX-derived RNA aptamer was refined through molecular docking and MD simulations. Predicted secondary and tertiary structures were docked against the target protein to identify favourable binding orientations, followed by MD simulations to evaluate interaction stability under solvated conditions. Free-energy analysis and interaction mapping enabled identification of nucleotide positions critical for binding, guiding rational point mutations to enhance affinity. The computational predictions were subsequently validated experimentally using isothermal titration calorimetry, exemplifying a hybrid optimization strategy that combines *in-silico* refinement with experimental confirmation (Bell et al., 2020).

A related optimization-focused approach was described by Hu *et al.*, who employed three-dimensional aptamer modelling, rigid docking, and MD simulations to investigate the binding mechanism of an aptamer–toxin complex. Rather than generating new aptamer sequences, the study aimed to identify key structural motifs and interaction hotspots responsible for binding stability. MD simulations were used to analyze hydrogen-bond persistence, electrostatic interactions, and conformational flexibility, enabling discrimination between essential and dispensable regions of the aptamer. This mechanistic insight supported rational truncation of the sequence while retaining binding specificity, which was subsequently verified experimentally (Hu et al., 2019).

Extending these concepts toward broader sequence screening, Thevendran et al., proposed a hybrid *in-silico* selection strategy that combines virtual library generation with thermodynamic filtering, rigid docking, and MD-based validation. Candidate DNA aptamers were initially screened based on predicted folding stability and secondary-structure features before being docked against the target protein. High-ranking complexes were then subjected to MD simulations to assess interaction stability and binding persistence, allowing prioritization of a limited number of sequences for experimental testing. This hierarchical workflow demonstrates how computational screening can substantially reduce the experimental search space while retaining confidence through downstream validation (Thevendran et al., 2023).

Collectively, these studies illustrate that computational approaches, ranging from de novo sequence screening to optimization of existing aptamers provide a powerful framework for rational aptamer development. By integrating thermodynamic screening, molecular docking, and dynamic simulation with experimental validation, such strategies offer an efficient route to identify high-affinity aptamers while mitigating key limitations associated with conventional SELEX-based selection.

1.7. Electrochemical transduction principles and electrode engineering

The effectiveness of a biosensor depends not only on the affinity and specificity of the biorecognition element but also on the capability of the transduction platform to convert molecular recognition events into measurable signals. In electrochemical biosensors, transduction is achieved by monitoring changes in electrical parameters at the electrode–electrolyte interface induced by analyte binding. Owing to their high sensitivity, simplicity, and compatibility with miniaturized systems, electrochemical transducers have been widely employed for toxin detection and are particularly well suited for label-free biosensing applications (Kalita et al., 2023).

Electrochemical transduction techniques commonly used in biosensors include cyclic voltammetry (CV), differential pulse voltammetry (DPV), amperometry, and electrochemical impedance spectroscopy (EIS). EIS offers several advantages over other electrochemical techniques when applied to biosensing applications. Owing to its ability to probe over a wide range of frequencies EIS can simultaneously assess multiple interfacial electrochemical processes on the electrode surface. Additionally, EIS operates under near steady-state conditions using small-amplitude alternating perturbations, thereby minimizing disruption of the sensing interface. The technique is highly sensitive to subtle changes in interfacial properties such as charge transfer resistance, capacitance, and dielectric constant, which are directly influenced by biomolecular binding events. These characteristics make EIS particularly well suited for label-free detection of biomolecular interactions, including aptamer–target binding, where signal generation relies on modulation of the electrode–electrolyte interface rather than direct electrochemical reactions.

1.7.1. Electrochemical impedance spectroscopy (EIS)

EIS measures the response of an electrochemical system to a small alternating potential applied over a wide range of frequencies. The wide range of frequencies allows the analysis of the all the electrochemical processes occurring on the electrode surface with varying time constants. The low frequencies are used to analyze the slow processes and high frequency are used to analyze the fast-electrochemical processes. The measured impedance represents the opposition of the system to charge and mass transport processes and is typically expressed as a complex quantity comprising both resistive and capacitive components. The impedance spectrum reflects contributions from solution resistance (R_s), charge transfer resistance (R_{ct}), double layer capacitance (C_{dl}), and diffusion processes. The solution resistance originates from ionic transport within the electrolyte and is largely unaffected by modifications at the electrode surface. At the interface, the accumulation of ions leads to the formation of an electrical double layer, consisting of a compact layer adjacent to the electrode and a diffuse layer extending into the solution, which collectively contributes to the interfacial capacitive behaviour. In the presence of a reversible redox couple such as ferri/ferrocyanide, electron exchange between the electrode and the redox species is controlled by the charge transfer resistance, representing the kinetic barrier to interfacial electron transfer. At lower frequencies, mass transport of redox species to and from the electrode surface becomes significant, contributing an additional impedance component that is commonly described by a Warburg diffusion response. In EIS, the measured impedance spectrum is modelled using an equivalent electrical circuit. Each circuit element represents a specific process, and fitting the experimental data to this model enables extraction of parameters such as solution resistance, charge transfer resistance, and interfacial capacitance. Impedance measurements are commonly classified into two types: faradaic and non-faradaic (Yang et al., 2004). Faradaic impedance measurements rely on the presence of a redox-active species in solution, whereas non-faradaic measurements are conducted without the use of any redox probe.

In biosensing applications, EIS is particularly sensitive to changes occurring at the electrode surface, as biomolecular interaction events lead to changes in the interfacial properties of the electrode. Immobilization of a biorecognition element, such as an aptamer, introduces a molecular layer that alters the electrical double layer structure and impedes access of redox species to the electrode surface. This results in measurable changes in interfacial capacitance and charge transfer resistance, which can be quantitatively monitored using impedance analysis.

To enhance sensitivity, EIS measurements are frequently performed in the presence of a reversible redox probe, most commonly the ferri/ferrocyanide couple $[Fe(CN)_6]3-/4^-$. This redox system exhibits rapid and well-defined electron-transfer kinetics, making it highly responsive to surface modifications. Even minor perturbations at the electrode interface can significantly influence electron transfer of the redox probe, leading to amplified impedance responses. The use of such a redox mediator therefore improves signal-to-noise ratio and enables reliable transduction of molecular recognition events into measurable electrical signals (Zhang et al., 2025).

In aptamer-based EIS sensors, the negatively charged phosphate backbone of the immobilized aptamer creates electrostatic repulsion toward negatively charged redox probes, while also introducing steric hindrance at the electrode surface. Binding of the target protein results in additional blocking of the electrode surface, altered surface charge distribution, and modification of the local dielectric environment. These effects collectively reduce the rate of electron transfer between the redox species and the electrode, observed as an increase in charge transfer resistance (R_{ct}). Because these impedance changes directly reflect target binding, EIS enables label-free detection of aptamer–target interactions under mild experimental conditions that preserve native biomolecular structure.

Overall, EIS provides a comprehensive and highly sensitive means of characterizing interfacial electrochemical processes and detecting biomolecular interactions. Its ability to deconvolute resistive, capacitive, and diffusional contributions makes it particularly well suited for aptamer-based biosensors, where detection relies on subtle yet quantifiable changes at the electrode–electrolyte interface.

1.7.2. Interdigitated microelectrodes as electrochemical transducers

Interdigitated microelectrodes (IDEs) are planar electrode structures composed of two interlocking arrays of micro-scale electrode fingers separated by narrow gaps, and the alternating electrode fingers are connected together. This geometry generates strong localized electric fields across the inter-electrode spacing, making IDEs highly sensitive to changes in the electrical properties of the medium within the gaps. As a result, IDEs are particularly effective for impedance-based sensing, where detection relies on modulation of interfacial charge transfer and dielectric properties.

Compared to conventional macroelectrodes, IDEs offer several advantages for biosensing applications. The high surface-to-volume ratio, low ohmic drop, rapid attainment of steady-state conditions and reduced diffusion distances enhance sensitivity toward surface-confined biomolecular interactions (Amatore et al., 1983) (Ciszkowska & Stojek, 1999) (Maruyama et al., 2006). In addition, the planar configuration of IDEs facilitates uniform surface functionalization and controlled immobilization of aptamers, contributing to improved reproducibility and signal stability. Additionally, the use of IDEs avoids the incorporation of a reference electrode and allows for the convenient measurement of steady-state current responses, which are comparatively easier to detect than those from conventional multi-electrode configurations (Nebling et al., 2004) (Liu et al., 2004). IDEs can be fabricated using standard microfabrication techniques, enabling precise control over electrode dimensions and compatibility with compact, low-cost sensing platforms.

1.7.3. Influence of IDE Geometry on Sensor Performance

The performance of interdigitated electrode array microelectrodes (IDAM) is strongly influenced by their geometric and material design parameters. Key factors include the number, width, height, and length of the electrodes, as well as the spacing between adjacent fingers. Early studies primarily emphasized the ratio between electrode width and gap as the main determinant of sensitivity. However, later work showed that electrode height and material also significantly affect device performance (Min & Baeumner, 2004). Increasing the number of electrode fingers does not substantially improve the signal-to-noise ratio, since both the signal and background noise increase proportionally with electrode area (Štulík et al., 2000). In contrast, reducing the electrode width enhances sensitivity, which is attributed to more efficient diffusion of electroactive species around narrower electrodes. These parameters determine the distribution and intensity of the electric field and directly affect sensitivity to interfacial changes induced by target binding. Consequently, optimization of IDE geometry has emerged as an effective strategy for enhancing sensor performance without modifying the biorecognition chemistry.

Conventional rectangular IDE designs often suffer from non-uniform electric field distribution, with pronounced field intensification at sharp edges and corners (Sherif et al., 2023) (Islam & Wu, 2023). This edge effect leads to spatially heterogeneous sensing regions, which can compromise measurement reproducibility and limit sensitivity, particularly in impedance-based detection schemes. Such non-uniformity can mask subtle interfacial changes associated with low-abundance biomolecular interactions, thereby constraining analytical performance in biosensing application (Le et al., 2019).

To overcome these limitations, non-conventional IDE geometries, including chain-shaped and wave-shaped electrode designs, have been introduced. Chain-shaped IDEs minimize sharp edges and distribute the electric field more evenly along the electrode surface, leading to improved homogeneity of the sensing region. This geometry has been shown to enhance impedance sensitivity by promoting uniform modulation of charge transfer resistance upon target binding, resulting in lower detection limits and improved signal-to-noise ratios in protein detection assays (Le et al., 2020). Similarly, wave-shaped IDEs eliminate abrupt geometric discontinuities and generate smoother electric field profiles, which reduce localized field concentration and enhance measurement reliability. Such designs have been reported to provide more consistent capacitive and impedimetric responses, particularly in label-free sensing configurations (Park et al., 2020) (Chinnadayyala et al., 2019). Beyond electric field uniformity, advanced IDE geometries also increase the effective electrode–electrolyte interaction area without proportionally increasing device footprint. This improved coupling between the electrode surface and the surrounding electrolyte amplifies impedance changes associated with biomolecular recognition events, making these geometries especially advantageous for EIS based biosensors. Collectively, these findings underscore electrode architecture as a critical design variable in IDE-based biosensing platforms, where rational geometric optimization can significantly enhance sensitivity and reproducibility without altering the underlying biorecognition chemistry.

1.8. Research gap

Despite extensive research on Shiga toxin–producing *Escherichia coli* (STEC), significant gaps remain in the development of rapid, sensitive, and field-deployable sensing platforms for the detection of Shiga toxins. Conventional laboratory-based diagnostic techniques, including culture-based assays, cytotoxicity tests, PCR-based detection of *stx* genes, and immunoassays are limited by long turnaround times, inability to directly quantify toxin activity, dependence on sophisticated instrumentation and trained personnel, and reliance on antibodies with restricted thermal and chemical stability. Collectively, these limitations underscore the urgent need for direct, sensitive, specific, and rapid point-of-care devices for Shiga toxin detection.

To address these challenges, biosensor-based approaches have emerged as promising alternatives. However, the performance of such sensing platforms critically depends on the choice of biorecognition element. Conventional antibody-based recognition systems suffer from drawbacks such as batch-to-batch variability, limited operational stability, and relatively high production costs. In contrast, aptamer-based biosensors offer several advantages, including high selectivity, chemical stability, ease of synthesis, and cost-effectiveness. Despite these benefits, relatively few studies have explored aptamer-based strategies for Shiga toxin detection, particularly those employing electrochemical transduction methods.

Among electrochemical techniques, EIS has gained prominence as a powerful, highly sensitive method for monitoring biomolecular interactions. Nevertheless, its application in aptamer-based Shiga toxin sensing remains limited. Moreover, interdigitated microelectrodes (IDEs) are well established as highly sensitive transducers for impedance-based biosensing; however, systematic studies evaluating the influence of IDE geometry on Shiga toxin detection performance are scarce. In particular, comparative investigations of non-conventional IDE designs, such as chain-shaped and wave-shaped geometries, in the context of aptamer-based toxin sensing are largely absent from the literature.

In parallel, the discovery of aptamers targeting Shiga toxins has predominantly relied on conventional SELEX, which is inherently time-consuming and prone to amplification bias. Although computational approaches for aptamer optimization, primarily involving truncation or mutation of existing sequences have been reported, fully de novo computational design of aptamers against Shiga toxin subunits remains largely unexplored.

1.9. Objective of the thesis

In view of the identified gaps and challenges, the primary objective of the present work is the development of aptamer-based electrochemical biosensors for the sensitive and specific detection of Shiga toxins. The study encompasses the expression and purification of Shiga toxin subunits, the generation of toxin-specific aptamers using both conventional SELEX and *de novo* computational design approaches, and the integration of these aptamers into electrochemical impedance-based sensing platforms. Interdigitated microelectrodes, including chain-shaped and wave-shaped designs, were employed for the development of the aptasensor platforms. The performance of the developed aptasensors was systematically evaluated by analyzing key parameters such as limit of detection, dynamic range, reproducibility, and interference effects. Furthermore, the efficiency of the aptasensors was assessed using real samples to evaluate their practical applicability.

The work presented in this thesis is organized into the following chapters, comprising five experimental chapters in addition to the introductory chapter entitled *"Introduction and Literature Review."* The final chapter, *"Conclusion and Future Outlook,"* summarizes the major conclusions of the study and outlines perspectives and future directions related to the present investigation.

Chapter 1: ***Introduction and literature review***

This chapter provides a comprehensive overview of Shiga toxins, covering essential aspects including their sources, mechanisms of action, and significant impact on global public health. Current diagnostic approaches for the detection of Shiga toxin–producing bacteria and their role in infection management are critically reviewed. In addition, emerging diagnostic strategies, particularly biosensor-based approaches are discussed, with emphasis on biorecognition elements, various transduction mechanisms, and sensing platforms, including interdigitated electrode systems. Through these discussions, the chapter identifies key gaps and challenges in existing Shiga toxin diagnostic research. Overall, Chapter 1 establishes the foundational background for understanding the complexities associated with Shiga toxin detection and underscores the need for continued research and innovation in this field.

Chapter 2: *Cloning, expression, and purification of Stx1B and Stx2B.*

This chapter describes the cloning, heterologous expression, and purification of the Shiga toxin 1 B (Stx1B) and Shiga toxin 2 B subunits (Stx2B), which serve as the molecular targets for subsequent aptamer selection and biosensor development. The chapter outlines the selection of gene sequences, construction of recombinant expression vectors, optimization of expression conditions in suitable *E. coli* host strains, and purification of the recombinant proteins using affinity-based methods. In addition, the chapter details the biochemical and structural characterization approaches employed to confirm protein identity and structural integrity, thereby establishing a reliable source of well-characterized toxin subunits for downstream computational, biophysical, and sensing studies.

Chapter 3: ***Development and characterization of Stx1B-specific aptamers using SELEX.***

This chapter focuses on the generation of Stx1B-specific DNA aptamers using the Systematic Evolution of Ligands by Exponential Enrichment (SELEX) process. The chapter describes the processing of a randomized ssDNA library, iterative rounds of positive selection against immobilized Stx1B, and the incorporation of negative selection steps to improve selectivity by eliminating sequences with affinity toward Stx2B and the solid support. It outlines the enrichment strategy across multiple SELEX cycles, followed by cloning, transformation, and sequencing of enriched aptamer candidates. The chapter further details sequence analysis approaches used to identify dominant and recurring aptamer motifs, establishing a set of candidate aptamers for subsequent biophysical evaluation and integration into electrochemical biosensing platforms.

Chapter 4: ***Development of an aptasensor for Stx1 using chain-shaped interdigitated electrodes.***

Chapter 4 describes the fabrication and characterization of an aptamer-based impedimetric biosensor for the detection of Shiga toxin 1 (Stx1). The chapter details the integration of the SELEX-derived aptamer as the biorecognition element onto a gold interdigitated chain-type microelectrode using a thiol-based self-assembled monolayer strategy. It further outlines the EIS based sensing approach employed for the toxin detection, including electrode functionalization, and data analysis. In addition, the chapter addresses the evaluation of sensor selectivity, stability, reproducibility, and applicability in complex matrices through real-sample testing, thereby establishing the feasibility of the developed platform for practical toxin detection.

Chapter 5: ***In-silico*** **design of ssDNA aptamers targeting Stx2B.**

Chapter 5 focuses on the *de novo* design and selection of DNA aptamers targeting the B subunit of Shiga toxin 2 (Stx2B) using computational approaches. The chapter outlines a systematic *in-silico* workflow involving virtual ssDNA library generation, thermodynamic screening based on predicted folding free energy, secondary and tertiary structure prediction, and molecular docking to evaluate aptamer–target interactions. Comparative docking against structurally related toxin subunits was employed to assess target specificity and minimize cross-reactivity. The chapter further describes the application of molecular dynamics simulations and binding free energy calculations to evaluate the stability, flexibility, and interaction persistence of shortlisted aptamer–protein complexes. In addition, the chapter details the experimental validation strategy used to corroborate computational predictions through biophysical techniques, establishing a robust framework for integrating *in-silico* aptamer design with downstream biosensor development.

Chapter 6: Development of an aptasensor for Stx2 using wave-type interdigitated electrodes.

This chapter presents the development of an aptamer-based impedimetric biosensor for the detection of Shiga toxin 2 (Stx2) using the *in-silico* designed aptamer and a gold interdigitated wave-type microelectrode (IDWµE). The chapter details the immobilization of the thiol-modified aptamer onto the electrode surface through Au–S chemistry, followed by surface passivation to reduce nonspecific interactions. It describes the EIS based sensing strategy employed to monitor aptamer–toxin binding, including sensor fabrication, measurement protocol, and signal transduction mechanism. In addition, the chapter addresses the evaluation of sensor selectivity, stability, reproducibility, and applicability in complex sample matrices, thereby demonstrating the integration of computationally designed aptamers with optimized electrochemical transduction platforms for practical toxin detection.

Chapter 7: Conclusions and future outlook

Chapter 7 presents the overall conclusion of the thesis by integrating the key outcomes of each chapter. The chapter summarizes the expression of recombinant Stx1B and Stx2B, and the development of high affinity aptamers using both SELEX and *in-silico* methods and the validation of the generated aptamers by developing sensors to detect Stx1 and Stx2 using chain-type and wave-type interdigitated microelectrodes. Additionally, the chapter also outlines the future direction of the work, including integration of the developed biosensor with portable device to be usable as a point of care device, multiplexed toxin detection and optimization of the *in-silico* aptamer design method.

Chapter 2

Cloning, expression, purification, and characterisation of Shiga-like toxin 1 and Shiga-like toxin 2

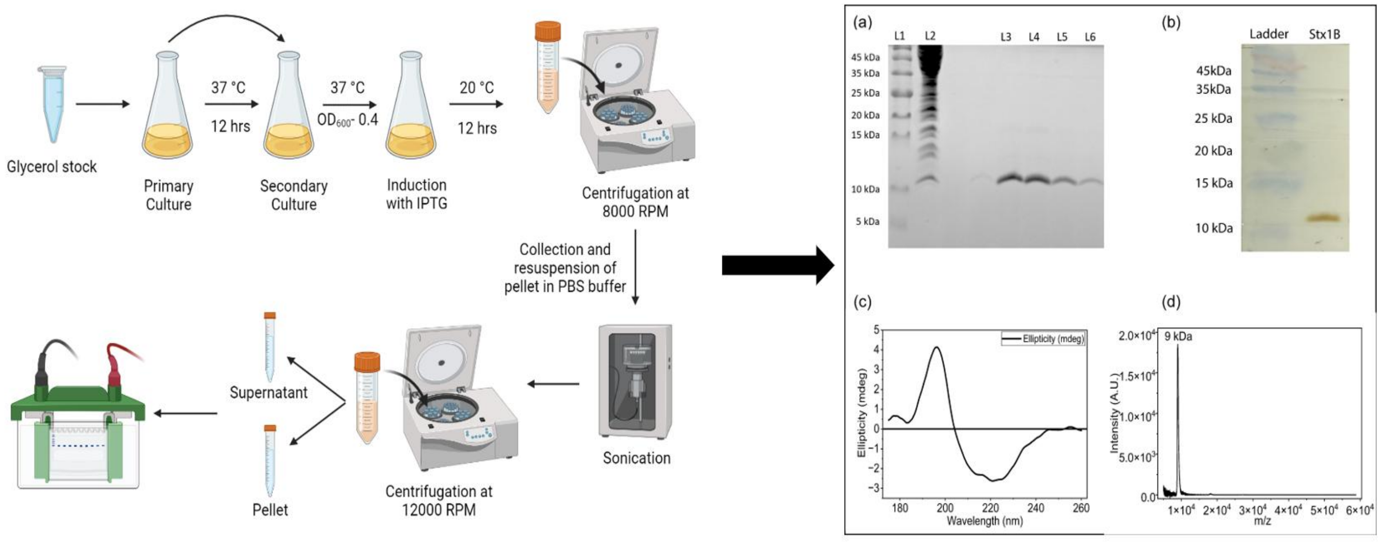

Left Panel – Expression of proteins. Right panel – Characterization of proteins using (a) SDS-PAGE, (b) Western blot, (c) CD, and (d) MALDI-TOF

Cloning, expression, purification, and characterisation of Shiga-like toxin 1 and Shiga-like toxin 2.

2.1. Overview

Shiga toxins (Stx1 and Stx2), produced by Shiga toxin producing *Escherichia coli* (STEC), are among the principal toxins responsible for foodborne illnesses. These toxins cause diseases such as haemorrhagic colitis (HC) and bloody diarrhoea, which may progress to severe complications, including haemolytic uremic syndrome (HUS). Both Stx1 and Stx2 are AB_5 holotoxins composed of a single A subunit and five identical B subunits. The A subunit has an approximate molecular weight of 32 kDa, while each B subunit has a molecular weight of approximately 7–8 kDa.

The A subunit contains the catalytic domain responsible for N-glycosidase activity, whereas the B subunit mediates receptor recognition and binding. Stx1 and Stx2 share 56.90% and 56.98% amino acid sequence similarity in their A and B subunits, respectively. Owing to its non-toxic nature and its presence in a 5:1 ratio relative to the A subunit, the B subunit represents an attractive biomarker candidate. Aptamers developed against the B subunit therefore hold significant potential for diagnostic and future therapeutic applications.

In this study, the B subunits of both toxins were utilized for aptamer development, as described in subsequent sections. This chapter focuses on the cloning, expression, purification, and characterization of Stx1B and Stx2B proteins. Both proteins were expressed with a C-terminal 6×His tag to facilitate purification.

2.2. Experimental section

2.2.1. Materials

The coding sequences of Stx1B and Stx2B (accession number AE005174) were curated from NCBI and commercially synthesized in the pGEM-T vector from Biomatik (Canada). Primers were synthesized from Bioserve Biotechnologies Pvt. Ltd, India. Emerald Amp® GT PCR Master mix was procured from DSS Takara Bio India Pvt. Ltd (India). Luria Bertani (LB) Agar, LB Broth, calcium chloride ($CaCl_2$), magnesium chloride ($MgCl_2.6H_2O$), potassium chloride (KCl), ethylene diamine tetra acetic acid (EDTA), and tris base were purchased from Himedia (India). Restriction enzymes were purchased from New England Biolabs (USA). pET-28 vectors were obtained from Novagen (India). The Ni-NTA His Trap FF column for the purification of His-tagged proteins was purchased from Cytiva (UK). Anti-His antibody and HRP-conjugated secondary antibody were purchased from Realgene Labs and Bibiotech India, respectively. Anti-Shiga toxin 1 B subunit antibody was procured from Merck (Germany). PVDF membrane was purchased from Amersham

(UK). The 3,3’-diaminobenzidine (DAB) was purchased from Amresco (USA). G2P Spin Clean Plasmid Prep kit was purchased from Gene to Protein (G2P) Pvt. Ltd (India). All other chemicals used were of analytical grade, and all the buffers used were prepared with deionized water (18.2MΩ.cm) (Millipore Co., USA).

2.2.2. Bacterial culture

Different strains of *E. coli* bacteria (DH5α, BL21(DE3) pLysS, Rosetta (DE3) were used for the cloning and expression of the proteins. The bacterial strains were cultured and grown using Luria-Bertani broth and Luria-Bertani agar. The primary culture of the bacteria was grown at 37 °C and 180 rpm in shaking mode using a shaker incubator with suitable antibiotics (Kanamycin, Ampicillin, and chloramphenicol). For the expression of the proteins, the secondary culture of bacteria was grown at an optimized temperature. Glycerol stock of the plasmid transformed *E. coli* strains was prepared and stored at -80 °C for future use.

2.2.3. Nucleic acid quantification

The success and reproducibility of the cloning process are strongly dependent on the quantity and quality of the nucleic acids involved. The quantity of DNA was determined using a UV-VIS nanodrop spectrophotometer. The amount of nucleotide was measured by the absorbance at $\lambda_{260\ nm}$. Before measuring the nucleotide, the blank was set with nuclease-free water and measured at $\lambda_{260\ nm}$. To check the purity of the nucleotides, the ratio of absorbance at A260/A280 nm and A260/A230 was measured. A pure nucleotide shows the ratio of A260/A280, a value of ~ 1.8, indicating no protein contamination. Additionally, an A260/A230 ratio of ~ 2.0-2.2 suggests the absence of salt, phenol, or organic contamination. A fixed conversion factor of 50 $\mu g\ ml^{-1}$ and 33 $\mu g\ ml^{-1}$ was used to measure the concentration of double-stranded DNA and single-stranded DNA, respectively. The concentration of the DNA was calculated using the equation-

DNA Concentration = A_{260} × Dilution factor × conversion factor (50 $\mu g\ ml^{-1}$ for dsDNA and 33 $\mu g\ ml^{-1}$ for ssDNA).

2.2.4. Protein quantification

The amount of the expressed proteins was measured using the Bradford assay. Coomassie Brilliant Blue G-250 (CBB-250) was used as the colorimetric dye, which binds to proteins under acidic conditions and shifts the absorbance maxima to $\lambda_{595\ nm}$. A standard calibration plot was constructed using Bovine Serum Albumin (BSA) as a standard protein, with the value of absorbance at $\lambda_{595\ nm}$ on the Y-axis and the corresponding known concentration of BSA on the X-axis. This calibration plot was used to measure the concentration of purified Stx1B and Stx2B.

2.2.5. Agarose gel electrophoresis

To analyze the DNA samples, agarose gel electrophoresis was performed using gels with concentrations ranging from 0.8% to 2%. The agarose gels were prepared in 1X Tris-Acetate-EDTA (TAE) buffer by heating it in a microwave oven to dissolve the agarose. For visualization of the DNA, 0.5 mg/mL ethidium bromide was added when the temperature of the agarose solution dropped to 45–50 °C. The DNA samples were mixed with 6X DNA loading dye and loaded into the wells on the agarose gel. Electrophoresis was performed in 1X TAE buffer at 80 V until the desired separation of the DNA fragment was achieved. The gel was visualized under a UV transilluminator to observe the DNA bands, and documentation for future reference was performed using the ChemiDoc XRS+ Imaging System (BIO-RAD, USA).

2.2.6. Primer designing

The nucleotide sequences of *Stx1B* and *Stx2B* were curated from the NCBI database and commercially synthesized. To amplify the sequences for further downstream processing, primers were designed using the NCBI Primer Design Tool. The designed primers were flanked by NcoI and XhoI restriction sites to generate cohesive ends.

2.2.7. Polymerase Chain Reaction (PCR)

PCR was performed to amplify the *Stx1B* and *Stx2B* genes for cloning into the pET28 vector. Based on the melting temperature (T_m) of both the forward and reverse primers, the annealing temperature of the PCR reaction was set. Emerald Amp® GT PCR Master mix was used along with 20 – 30 ng DNA and 0.5 µM of primers to set up the reaction in 0.2 ml PCR tubes. Further, the PCR amplicons were visualized in 1.5% agarose gels. The PCR reaction mixture and conditions are mentioned in the appendix (Table A1 and A2). The primers used are given in Table A3.

2.2.8. Purification of PCR amplicons

The amplified PCR products were purified from the enzymes, buffers, or excess dNTPs for downstream usage using the G2P PCR cleanup kit. One volume of the PCR product was mixed with one volume of binding buffer and loaded onto a silica membrane spin column, which was then centrifuged at 10,000 g for 5 minutes. The flow-through was discarded, and the silica membrane spin column was washed by adding 600 µL of washing buffer and then centrifuged at 10,000 g for 2 minutes. The flow-through was discarded and dry spun to remove any residual wash buffer. Finally, the silica spin column is transferred to a 1.5 mL centrifuge tube, and the amplified DNA is eluted using 50 µL of elution buffer.

2.2.9. Restriction digestion of *Stx1B* and *Stx2B*

The purified PCR amplicons of *Stx1B* and *Stx2B* sequences were double-digested with NcoI and XhoI to create cohesive ends complementary to the pET28a (+) vectors. The composition of the reaction mixture, as presented in the appendix, was set and incubated at 37 °C for 1 hour, as per the manufacturer's guidelines (Table A4).

2.2.10. Elution of digested amplicons from agarose gel

The double-digested PCR amplicons were analyzed on a 2% agarose gel, and the specific bands were eluted from the gel using the G2P gel extraction kit, following the manufacturer's procedure. The bands corresponding to the PCR amplified amplicons were excised from the agarose gel using a surgical blade. The excised gel was weighed, and 3 volumes of gel solubilization buffer were added for every 1 volume of gel. The mixture was then incubated at 50 °C for 10 minutes. The solubilized gel mixture is loaded onto a silica membrane spin column and centrifuged at 10000 g for 5 minutes. Furthermore, the silica membrane spin column was washed twice with 500 µL washing buffer by centrifuging at 10,000 g for 3 minutes. The column was dry-spun for an additional 3 minutes to remove any residual wash buffer. Finally, the silica membrane spin column was transferred to a 1.5 mL centrifuge tube, and the silica membrane-bound double-digested PCR amplicons were eluted using elution buffer.

2.2.11. Ligation of double-digested PCR amplicons with double-digested pET28a (+) vectors

Multiple vector-to-insert ratios were tested for the ligation of PCR amplicons of *Stx1B* and *Stx2B* with the pET28a (+) vectors. Based on the size and concentration of the insert and the vector, the volumes for the different ratios were calculated using NEBiocalculator and prepared as mentioned in the appendix (Table A5). The total reaction volume, including the vector, insert, and ligase enzyme, was adjusted to 20 µl with nuclease-free water. The reaction was incubated at 4 °C overnight. After ligation, 5 µl of the ligated mixture was transformed into competent cells and plated on agar plates containing kanamycin antibiotics. The plates were incubated at 37 °C for 12 – 16 hours.

2.2.12. Plasmid isolation

The recombinant plasmid containing the *Stx1B* and *Stx2B* gene sequence was isolated from the *E. coli* DH5α strain using a commercial plasmid isolation kit from Gene to Protein (G2P) company, following the manufacturer's protocol. A single transformed white colony was picked from the LB agar plate and inoculated into 5 mL of LB broth in a test tube. The culture was then incubated for 12-16 hours at 37 °C and 180 rpm in a shaking incubator. The bacterial culture was harvested by centrifuging at 10000 g for 5 minutes. The supernatant was discarded, and the cell pellet was collected and resuspended in 250 µl of resuspension buffer. The cells were lysed by adding 250 µl of lysis buffer and incubated for 15 minutes at room temperature. Subsequently, 500 µL of neutralization buffer was added, and the mixture was gently mixed by inverting to ensure complete neutralization. The resultant lysate was centrifuged at 12000 g for 5 minutes. The supernatant was then carefully extracted and loaded onto a silica membrane spin column, which was centrifuged at 10000 g for 3 minutes. The flow-through was discarded, and the silica membrane column was washed with 500 µL of washed buffer twice to remove contaminants. The column was dry spun at 12000 g for an additional 5 minutes. Finally, the plasmid was eluted from the silica membrane column using 50 µL of elution buffer and transferred to a fresh microcentrifuge tube by centrifuging at 10,000 g for 2 minutes.

2.2.13. Preparation of competent cells

Competent cells were prepared from the glycerol stock of different strains of *E. coli* bacteria {DH5α, BL21(DE3) PLysS, Rosetta DE3}. The cells were revived by inoculating them in 5 mL of LB broth (primary culture) inside a test tube and incubated at 37 °C for 12-16 hours with vigorous agitation. A secondary culture was prepared by inoculating 10% of the primary culture into a new 5 ml LB broth and growing it under the same conditions until the culture reached an optical density (O.D.) of 0.4–0.6 at 600 nm. Following that, the bacterial cell cultures were centrifuged at 5000 rpm for 5 minutes at 4 °C, and the supernatant was discarded. The transformation and storage solution (TSS solution) was used to resuspend the bacterial cell pellet. Further aliquots of 100 µl cells were prepared and stored at -80 °C for future use.

2.2.14. Transformation of competent cells

The competent cells were taken out of the -80 °C freezer and allowed to thaw on ice for 10 minutes. To the 100 µL competent cells, 50–100 ng of ligated DNA, amounting to less than 10 µL in volume, was added. The mixture was gently mixed by pipetting or flicking the microcentrifuge tubes and then incubated on ice for 30 minutes. The cells were then subjected to heat shock at 42 °C in a water bath. *E. coli* DH5α, BL21(DE3) PLysS, and Rosetta DE3 were subjected to 60, 75, and 90 seconds of heat shock, respectively. The cells were then immediately transferred to ice and incubated for 3 minutes. Following this, 900 µL of LB broth was added and the mixture was incubated at 37 °C for 1 hour. Meanwhile, LB agar plates supplemented with the required antibiotics corresponding to the antibiotic resistance gene present on the recombinant plasmid were prepared by spreading X-gal and IPTG for blue-white screening of the transformed bacterial clones. Following this, 50 µl of the transformed cells were spread on LB agar plates. The plates were incubated at 37 °C overnight. The white colonies from the agar plates were picked up with sterile pipette tips and allowed to grow in LB broth containing the appropriate antibiotics. Their glycerol stocks were then prepared and stored at –80 °C for future use.

2.2.15. Cloning of *Stx1B* and *Stx2B*

The coding sequences of *Stx1B* and *Stx2B* were curated from the NCBI database and commercially synthesized in the pGEMT vector. For the expression of the proteins, both sequences were cloned into the pET28a (+) plasmid. The sequences were PCR amplified using primers with NcoI and XhoI restriction sites at the 3' and 5' ends, thereby generating *Stx1B* and *Stx2B* sequences with the restriction sites. The sequences and the pET28a (+) plasmid were then double-digested with the NcoI and XhoI restriction enzymes to create cohesive ends. The double-digested plasmid and the gene sequence were ligated using the T4 DNA ligase enzyme. The recombinant plasmids were then used to transform the *E. coli* DH5α competent cells, and the blue-white screening method was employed to screen the positive colonies. The recombinant clones were further confirmed by isolating the plasmid DNA and performing PCR with specific primers, as well as by Sanger sequencing of the recombinant plasmids. The confirmed recombinant Stx1B clones were then transformed into *E. coli* BL21(DE3) pLysS and the recombinant Stx2B clones were transformed into *E. coli* Rosetta DE3 cells were used for the expression of the recombinant proteins.

2.2.16. Sanger sequence analysis of recombinant plasmids

Sequencing was performed through Bioserve company, Hyderabad. Sequencing of the sample was performed using an ABI 3730 (48-capillary) electrophoresis instrument, following the Sanger sequencing protocol.

2.2.17. Expression of His tagged Stx1B and Stx2B

For the expression of Stx1B protein, the *E. coli* BL21(DE3) pLysS/pET28a/Stx1B clone was taken out from -80 °C and inoculated in 5 ml LB broth containing kanamycin and chloramphenicol as antibiotics. The primary culture was grown at 37 °C for 12 – 16 hours at 180 rpm. Subsequently, 2.5 ml of the primary culture was inoculated into 250 ml of new LB broth to initiate the secondary culture, and was grown at 37 °C till it reached an OD of 0.6 – 0.8 at 600 nm. For the expression of the recombinant protein, the culture was induced with 0.2 mM Isopropyl β-D-thiogalactopyranoside (IPTG) and further incubated at 16 °C for 18 hours. For expression of Stx2B protein, the primary and secondary culture of *E. coli* Rosetta DE3/ pET28a/Stx2B clone was grown following the same procedure as that used for *E. coli* BL21(DE3) pLysS/pET28a/Stx1B clone. However, it was induced with 0.2 mM IPTG and incubated at 37 °C for 8 hours. The cells were then centrifuged at 8000 g for 10 minutes, and the pellet was resuspended in 1× PBS (pH 7.4). Furthermore, the cells were sonicated using an ultrasonic processor (Hielscher) with a 25% amplitude and 0.5 cycles, maintaining continuous ice cooling until the lysate appeared clearer. The lysate was then centrifuged at 13000 g for 30 minutes at 4 °C, and the supernatant was collected for further processing.

2.2.18. Purification of His tagged Stx1B and Stx2B

For the purification of the protein, the His Trap FF column was prepared by passing 5 column volumes of binding buffer at a rate of 1 ml min^{-1}. Following the binding buffer, the supernatant containing the proteins was passed at a rate of 0.5 ml min^{-1}, and then the column was stored at 4 °C for 30 minutes. Subsequently, the column was washed with 5 column volumes of washing buffer, and finally, the protein was eluted using a gradient elution buffers at a flow rate of 0.5 ml min^{-1} and collected using microcentrifuge tubes. The composition of the solutions used in protein purification is listed in the appendix (Table A6).

2.2.19. Sodium Dodecyl Sulphate Polyacrylamide Gel Electrophoresis (SDS-PAGE)

The purified proteins, obtained using Ni-NTA affinity chromatography, were analyzed using Tricine SDS-PAGE (Schägger, 2006). 1 – 2 µg of purified recombinant protein was mixed with the reducing sample buffer and denatured by heating the mixture at 95 °C for 5 minutes in a water bath. The sample, along with the pre-stained protein ladder, was loaded onto the SDS-PAGE gel. The electrophoresis was performed using a discontinuous buffer system with a 4% stacking gel and a 16% separating gel, both with a thickness of 0.75 mm, at a constant voltage of 140 mV, on a MiniVE vertical gel electrophoresis system (GE Healthcare, India). The gels were stained with Coomassie blue stain, and the separated protein bands were visible to the naked eye after destaining the gel with destain buffer. The documentation for future reference was created using the ChemiDoc XRS+ Imaging System (BIO-RAD, USA).

2.2.20. Western blot

The purified recombinant protein was confirmed with western blotting using an anti-His antibody. The recombinant proteins were resolved using 16% tricine SDS-PAGE in a MiniVE vertical electrophoresis unit at 140 mV. The resolved protein on the gel was electroblotted to a Polyvinylidene fluoride (PVDF) membrane using a blot module (GE Healthcare) at a constant voltage of 25 V for 4 hours at 4 °C. The transfer of the protein to the PVDF membrane was confirmed by staining with Ponceau S reagent. Later, the membrane was washed with washing buffer [PBS, pH 7.4 with 0.1% Tween 20 (PBST)] to remove the Ponceau S reagent. To prevent non-specific adsorption, the membrane was blocked with a blocking buffer containing 3% BSA for 2 hours. The blocking buffer is drained off, and the membrane is washed three times with PBST buffer. An optimized concentration of monoclonal anti-His antibody, used as the primary antibody, was incubated with the membrane at 4 °C overnight. The membrane was then washed with PBST buffer and treated with HRP-modified anti-mouse IgG secondary antibody diluted in PBS buffer for 1 hour at room temperature. Further, the membrane was washed with PBS three times, and a solution containing 500 µl of 1%, 3,3'- Diaminobenzidine tetrahydrochloride hydrate (DAB) in 4.5 ml of PBS supplemented with 50 µl hydrogen peroxide was used to develop the membrane. The image of the blot was captured using the ChemiDoc XRS+ Imaging System from Bio-Rad.

2.2.21. Circular Dichroism Spectroscopy

Circular dichroism (CD) was used to study the secondary structure of the recombinant protein. The experiment was performed using a Jasco J-815 spectropolarimeter (Japan), with a 0.2 cm path length Suprasil quartz cuvette at room temperature. The spectrum was recorded from 190 nm to 260 nm at a scan rate of 100 nm min^{-1}, with a spectral bandwidth of 1 nm. The spectra were accumulated 5 times, and the average of the accumulations was considered. Further, the spectrum was corrected for baseline, and the data were smoothed with a Savitsky-Golay filter with the Jasco spectra analysis software. The secondary structure analysis was performed using the Dichroweb web server.

2.2.22. Matrix-Assisted Laser Desorption Ionization-Time Of Flight mass spectrometry (MALDI-TOF)

The accurate molecular masses of the recombinant Stx1B and Stx2B proteins were analysed using MALDI-MS analysis. Sinapinic acid was used as the matrix for the analysis. The matrix solution was prepared in a saturated concentration using a solvent mixture of acetonitrile and water containing 0.1% trifluoroacetic acid (TFA). The proteins were mixed with a saturated solution of Sinapinic acid, and the spectra were collected in positive mode, with each spectrum being an average of 100 shots to improve the signal-to-noise ratio.

2.3. Results and Discussions

2.3.1. Stx1B and Stx2B sequence alignment and comparison

Multiple sequence alignment of Stx1B and Stx2B was performed using Clustal Omega. The amino acid sequences of Stx1B (accession number NP_311000) and Stx2B (accession number BCA73239) were curated from the National Centre for Biotechnology Information (NCBI)

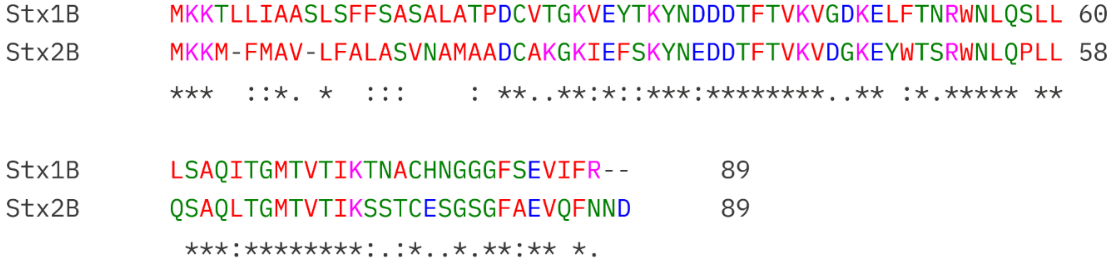

```
Stx1B      MKKTLLIAASLSFFSASALATPDCVTGKVEYTKYNDDDTFTVKVGDKELFTNRWNLQSLL 60
Stx2B      MKKM-FMAV-LFALASVNAMAADCAKGKIEFSKYNEDDTFTVKVDGKEYWTSRWNLQPLL 58
           ***  ::*. *  :::    : **..**:*::***:********..** :*.***** **

Stx1B      LSAQITGMTVTIKTNACHNGGGFSEVIFR--      89
Stx2B      QSAQLTGMTVTIKSSTCESGSGFAEVQFNND      89
            ***:********:.:*..*.**:** *.
```

Figure 2.1 - Sequence alignment of Stx1B and Stx2B using Clustal Omega.

database. The sequence alignment between Stx1B and Stx2B revealed ~56% sequence identity (**Figure 2.1**), indicating a moderate level of sequence similarity between the two proteins.

2.3.2. Cloning of *Stx1B* and *Stx2B*

The gene sequences encoding the Stx1B and Stx2B proteins were amplified from the synthesized plasmid using specific primers designed to incorporate NcoI and XhoI restriction sites. The agarose gel image of the amplified product displayed a single band at approximately 280 bp, matching the expected amplicon size **(Figure 2.2a)**. The amplified sequences and the pET28 (a) vector were digested using NcoI and XhoI restriction enzymes.

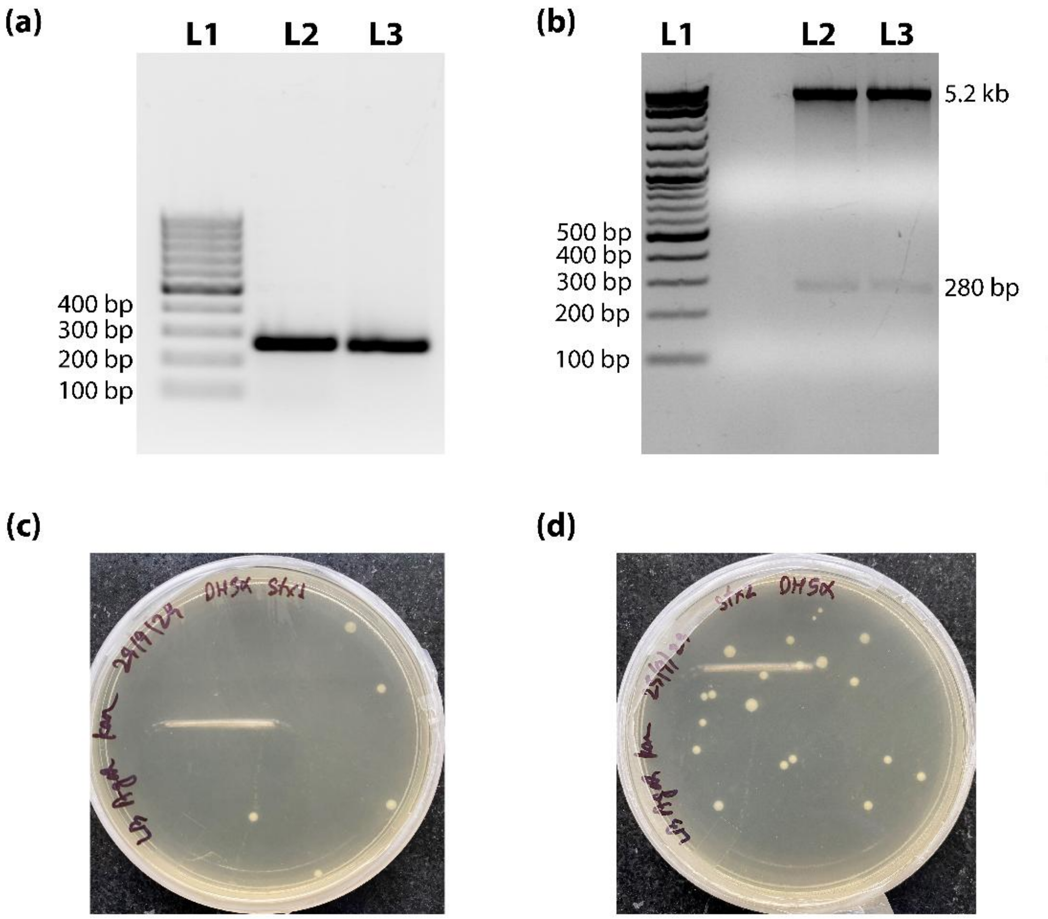

Figure 2.2: (a) PCR amplification of L2- *Stx1B*, L3- *Stx2B*, observed in 1% agarose gel; (b) Restriction digestion of recombinant L2- *Stx1B*, L3- Stx2B; Blue-white screening of transformed colonies (c) Stx1B, (d) Stx2B.

Following the purification and ligation of the digested sequences and the vector, the recombinant plasmids were transformed into *E. coli* DH5α cells, and blue-white screening was adopted for identifying the transformed colonies **(Figure 2.2c and 2.2d)**. The white colonies representing the transformed colonies were picked, and colony PCR was performed to confirm the presence of the insert in the recombinant plasmid. The screened colonies produced a band of the correct size in the agarose gel, indicating a successful ligation of the insert and the vector. Double-digestion of the isolated recombinant plasmid with NcoI and XhoI restriction enzymes yielded two bands corresponding to the vector backbone and the released insert (**Figure 2.2b**). Furthermore, the successful cloning was confirmed by Sanger sequencing, which verified the sequence of the recombinant pET28(a)_*Stx1B* and pET28(a)_ *Stx2B* with no mutations, frameshifts, or truncations.

2.3.3. Expression of Stx1B and Stx2B

Stx1B protein was expressed by inducing the pET28(a)_*Stx1B* transformed *E. coli* BL21(DE3) pLysS cultures with 0.2 mM IPTG at 16 °C. Initially, small-scale trials were conducted to optimize the temperature (37 °C, 25 °C, and 16 °C) and IPTG concentration (0.2, and 0.8) for the soluble expression of the protein. Analysis of the expression profile of Stx1B at 37 °C using SDS-PAGE resulted in strong overexpression of the protein. However, the majority of the protein was present in the pellet fraction, indicating the formation of inclusion bodies (**Figure 2.3a**). However, decreasing the temperature from 37 °C to 25 °C, then to 16 °C, gradually improved the solubility of the protein. The variation in IPTG concentration did not result in any significant difference in protein expression levels. Both low (0.2 mM) and high (0.8 mM) IPTG induction resulted in comparable expression yields.

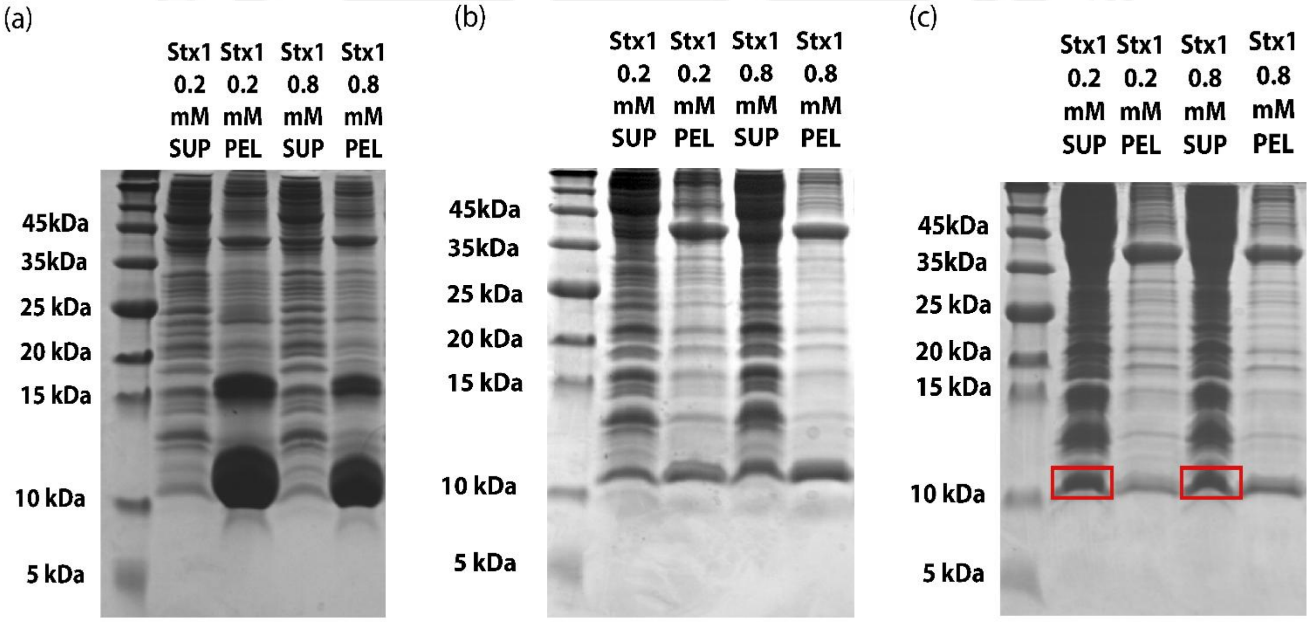

Figure 2.3- Expression of Stx1B at (a) 37 °C, (b) 25 °C, (c) 16 °C.

For expression of Stx2B, the recombinant pET28(a)_*Stx2B* vector was transformed into *E. coli* Rosetta DE3 cells. The protein was strongly expressed in the soluble fraction at 37 °C and did not require extensive optimization. However, induction with a lower IPTG concentration (0.2 mM) resulted in slightly increased expression compared to induction with a high concentration of IPTG (0.8 mM) (**Figure 2.4**).

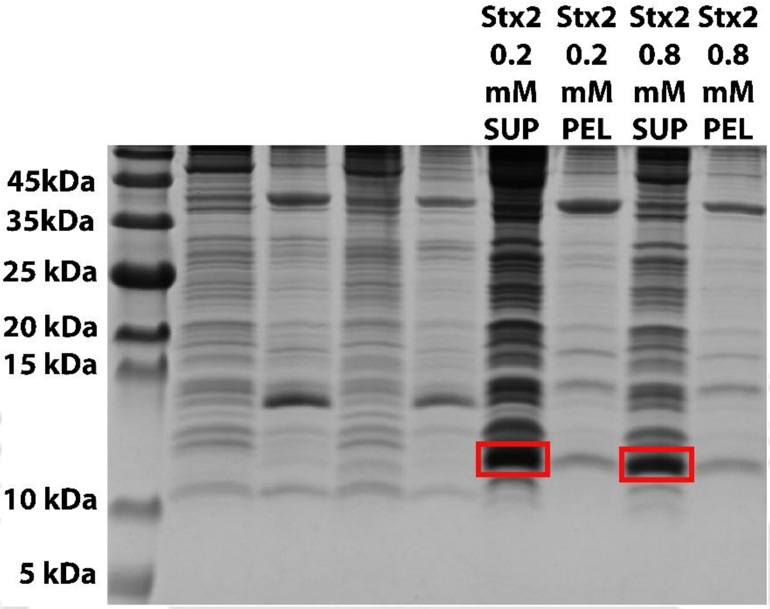

Figure 2.4 - Expression of Stx2B at 37 °C

2.3.4. Purification of Stx1B and Stx2B

Following optimization of the expression parameters of Stx1B and Stx2B on a small scale, the bacterial cultures were grown on a large scale (500 mL) for purification. The cells were harvested using centrifugation, and the pellets were resuspended in 1× PBS buffer and then lysed using sonication. The soluble fraction of the cell lysate following sonication were applied to the His Trap FF column for purification. Because of the presence of the 6× histidine tag at the C-terminal, the

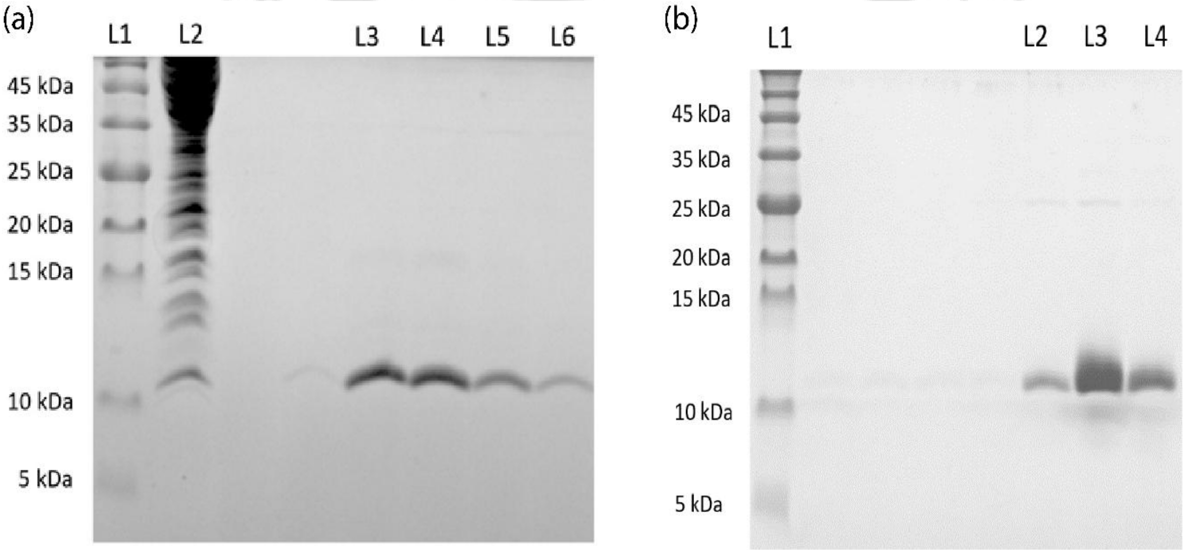

Figure 2.5 - (a) L1 -ladder, L2- cell lysate, L3-L6- purified Stx1B, (b) L1- ladder, L2-L4- purified Stx2B.

proteins strongly bind to the Ni-NTA resin in the column. Impurities binding to the column were removed using the wash buffer, and the bound proteins were eluted using the elution buffer. The eluted fraction displayed a single band on the SDS-PAGE indicating a successful purification of the proteins (**Figure 2.5**).

2.3.5. Characterization of Stx1B and Stx2B.

Western blot analysis of Stx1B was performed using an anti-Stx1B antibody and an anti-His antibody for the Stx2B protein. Clear immunoreactive bands were observed on the blots confirming the integrity of the expressed proteins (**Figure 2.6a and 2.6b**). Further, the molecular weight of Stx1B and Stx2B was confirmed to be 9 kDa and 8.8 kDa, using MALDI-TOF analysis (**Figure 2.7a and 2.7b**). CD analysis revealed the Stx1B contained 11.2% α helix, 43% *β* sheets, and 45.8% random coils, whereas the Stx2B consists of 13% α helix, 39% *β* sheets, and 48% random coils (**Figure 2.7c and 2.7d**).

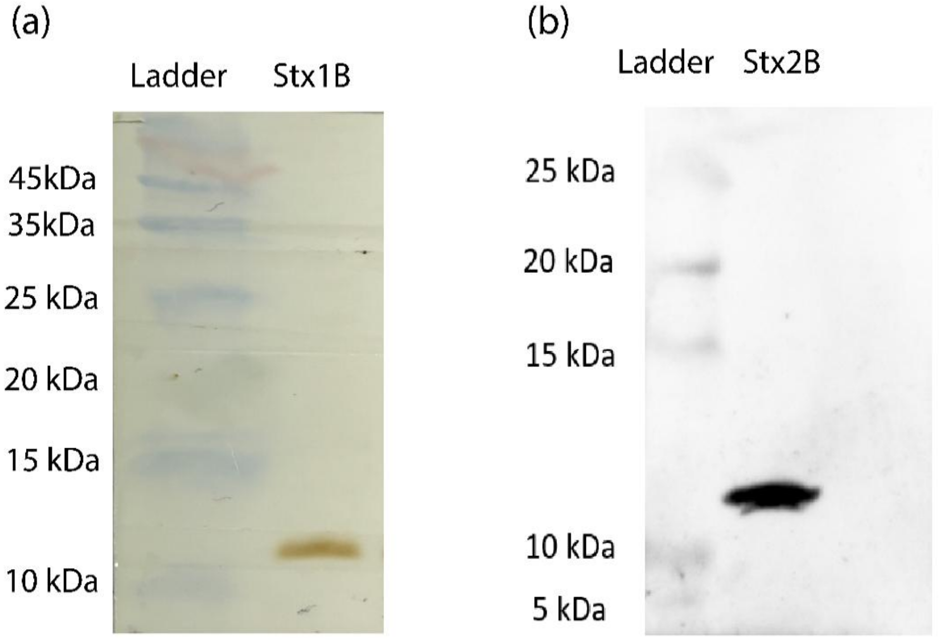

Figure 2.6 - Western blot analysis of (a) Stx1B using anti Stx1B antibody, and (b) Stx2B using anti-His antibody.

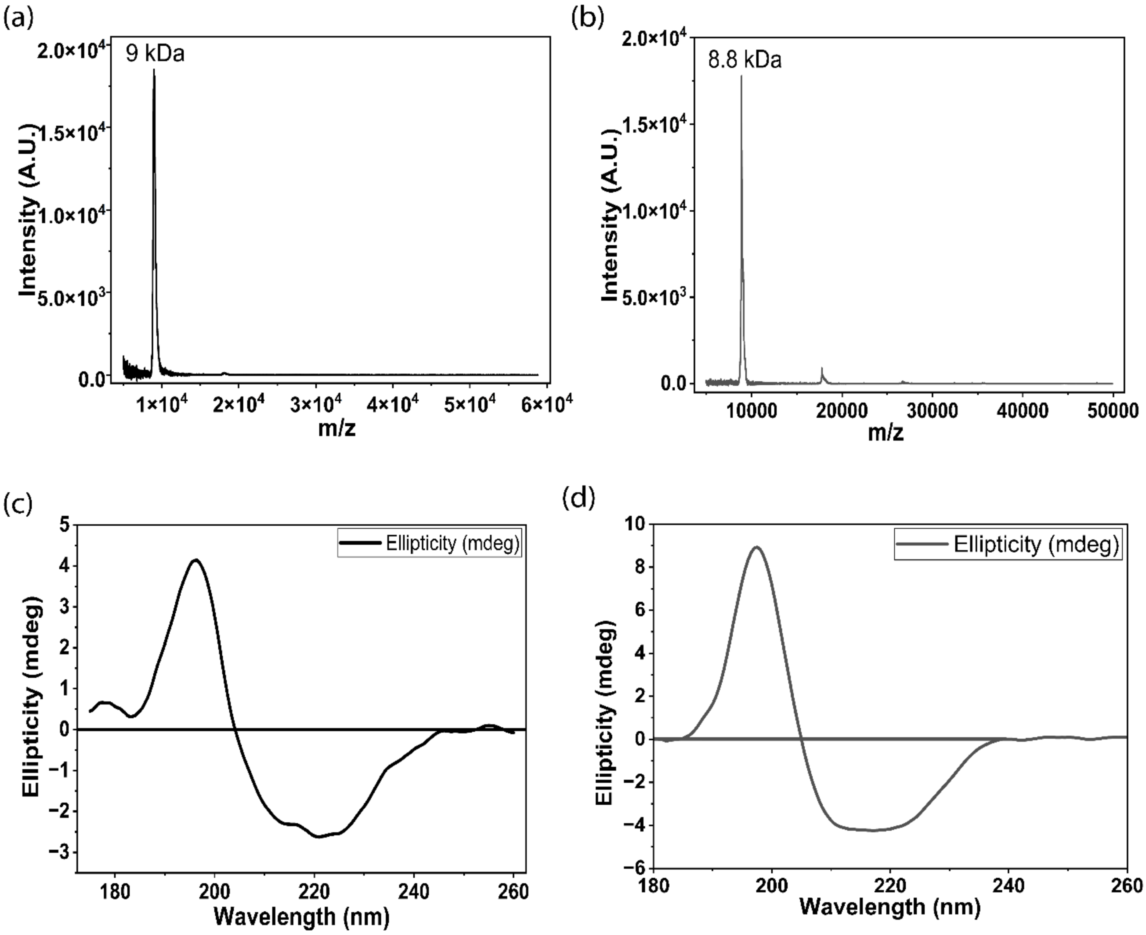

Figure 2.7 - MALDI-TOF analysis of (a) Stx1B, (b) Stx2B. Circular Dichroism analysis of (c) Stx1B, and (d) Stx2B.

2.4. Conclusion

The coding sequences of *Stx1B* and *Stx2B* genes were synthesized commercially, and they were cloned into pET28 (a) expression vector for protein expression. The recombinant pET28 (a)_*Stx1B* was transformed into *E. coli* BL21 (DE3) pLysS cells, and the pET28 (a)_*Stx2B* vector was cloned into *E. coli* (DE3) Rosetta cells. The parameters of the protein expression were optimized and the Stx1B was expressed at 16 °C with 0.2 mM IPTG induction and Stx2B was expressed at 37 °C with 0.2 mM IPTG induction. The expressed proteins were purified with Ni-NTA columns utilizing the 6×His tag expressed with the proteins. Further, the proteins were characterized using western blot, MALDI-TOF, and circular dichroism. The study successfully, cloned, expressed, purified, and characterized the target proteins Stx1B and Stx2B.

Chapter 3

Development of Stx1B specific aptamers by SELEX and their characterisation

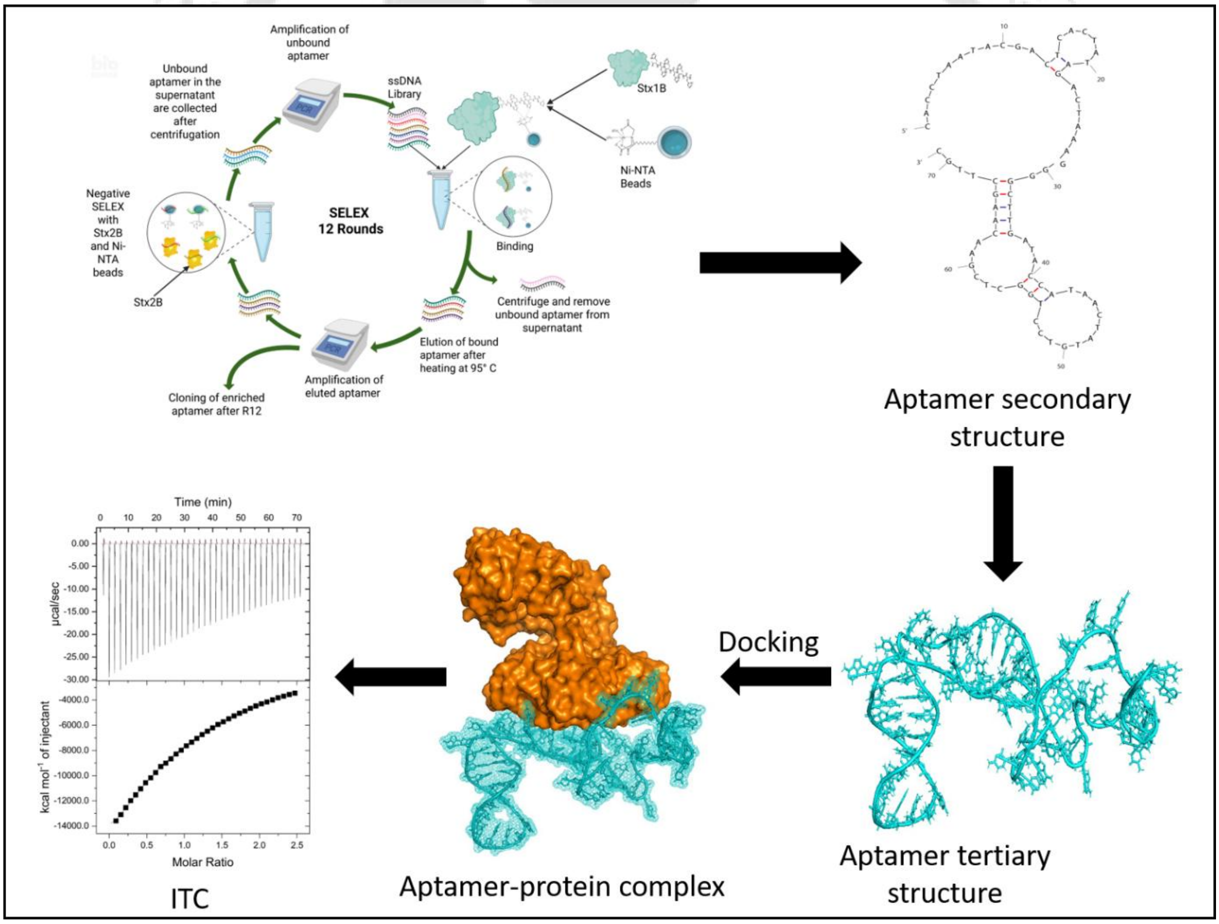

Development of Stx1B specific aptamers by SELEX and their characterisation

3.1. Overview

Nucleic acid aptamers are short, single-stranded oligonucleotide molecules (DNA or RNA) that can fold into well-defined three-dimensional conformations, enabling them to bind selectively and with high affinity to a wide range of targets, including proteins, small molecules, toxins, and whole cells. Owing to their unique structural adaptability, aptamers have emerged as powerful molecular recognition elements in biosensing, diagnostics, and therapeutic applications. Unlike linear oligonucleotides, aptamers adopt secondary and tertiary structures such as stems, loops, bulges, and pseudoknots, which collectively contribute to target recognition through shape complementarity and non-covalent interactions (Mili et al., 2024).

In comparison to antibodies, aptamers offer several advantages. They can be generated entirely through in vitro processes, eliminating the need for animal immunization and reducing batch-to-batch variability. Aptamers exhibit high chemical stability, retain functionality over a broad range of pH and temperature conditions, and can be easily modified with functional groups for immobilization or signal transduction without compromising binding performance. These attributes make aptamers particularly attractive alternatives to antibodies for applications requiring robustness, reproducibility, and cost-effective large-scale production (Goswami, 2020).

The selection of target-specific aptamers is commonly achieved through Systematic Evolution of Ligands by Exponential Enrichment (SELEX), an iterative in vitro selection process. SELEX begins with a large combinatorial oligonucleotide library containing random sequences, from which aptamers with affinity toward a target molecule are progressively enriched over multiple selection cycles. Each round typically involves incubation of the library with the target, partitioning of bound from unbound sequences, recovery of target-bound oligonucleotides, and their amplification to generate the input library for the subsequent cycle. To further enhance specificity, counter-selection or negative SELEX steps may be incorporated to eliminate sequences that bind to non-target molecules or selection matrices.

In this chapter, the development of aptamers specific to the B subunit of Shiga toxin 1 (Stx1B) using the SELEX strategy is presented. The chapter describes the SELEX methodology used and the systematic implementation of positive and negative selection cycles to enhance target specificity. For the selection process, the recombinant His-tagged Stx1B protein was immobilized onto Ni-NTA beads, enabling efficient target presentation and facile partitioning of bound and unbound oligonucleotides. Centrifugation-based separation was employed to remove non-binding sequences and recover target-bound aptamers during each selection cycle. The chapter further describes the cloning, screening, and sequence analysis of enriched aptamer candidates, as well as the physicochemical approaches adopted to assess aptamer–target interactions. Collectively, this chapter establishes a systematic and reproducible framework for the generation and validation of Stx1B-specific aptamers as robust biorecognition elements for subsequent biosensor development.

3.2. Experimental procedures

3.2.1. Materials

Biotinylated reverse primer, forward primers, and ssDNA library with the sequence CACCTAATACGACTCACTATAG-N30-CTGGCTCGAACAAGCTTGC, for SELEX were procured from IDT (USA). 5’-SH-$(CH_2)_6$-CACCTAATACGACTCACTATAGACTAAAGGGGCTTGATACCATAACTATGTCCTGG-CTCGAACAAGCTTGC-3' (thiol-modified) sequence was procured from Eurofins (Sweden). Streptavidin magnetic particles were purchased from Roche (Germany). Ni-NTA agarose beads were procured from Qiagen (Netherlands). Emerald Amp® GT PCR Master mix was procured from DSS Takara Bio (India). All the reagents used were of analytical reagent grade, and the buffers were prepared using deionized water (18.2 MΩ.cm) (Millipore Co., USA).

3.2.2. Selection of aptamers using SELEX

The SELEX procedure was performed using His-tag–mediated immobilization of the recombinant Stx1B and Stx2B proteins onto Ni-NTA agarose beads (**Figure 3.1**). Prior to immobilization, the Ni-NTA agarose beads were washed three times with Ni-NTA binding buffer composed of 200 mM NaH_2PO_4, 500 mM NaCl, and 5 mM imidazole (pH 7.4). For protein immobilization, 100 µL of 10 µM His-tagged protein was incubated with 100 µL of Ni-NTA agarose beads in binding buffer for 30 min at room temperature under gentle agitation on a rocker platform at 30 rpm. Following incubation, the protein-bound beads were washed three times with SELEX binding buffer (50 mM sodium phosphate, 50 mM NaCl, 5 mM KCl, and 2.5 mM $MgCl_2$) to remove unbound protein and were finally resuspended in the same buffer for subsequent selection steps.

Prior to each SELEX cycle, 10 µM of ssDNA library was prepared by heating in 50 µL of SELEX binding buffer at 95 °C for 10 min, followed by immediate cooling on ice for 10 min to facilitate proper folding. The initial two selection rounds were designed as negative SELEX to eliminate non-specific binders. In the first round, the ssDNA library was incubated with Ni-NTA agarose beads alone for 1 h at room temperature with gentle mixing (30 rpm), allowing sequences with affinity toward the matrix to bind. Separation of bound and unbound sequences was achieved by centrifugation at 1500 × g for 2 min, after which the supernatant containing unbound aptamers was collected and amplified by PCR for use in the subsequent cycle (The primers used and the PCR conditions are given in appendix Table A7 and A8). In the second negative SELEX cycle, Ni-NTA bead-immobilized Stx2B was employed as a counter-target due to its close structural similarity to Stx1B. The ssDNA library was incubated with Stx2B-bound beads for 1 h under identical conditions. Following centrifugation, the supernatant containing non-binding sequences was collected and amplified for use in the next round.

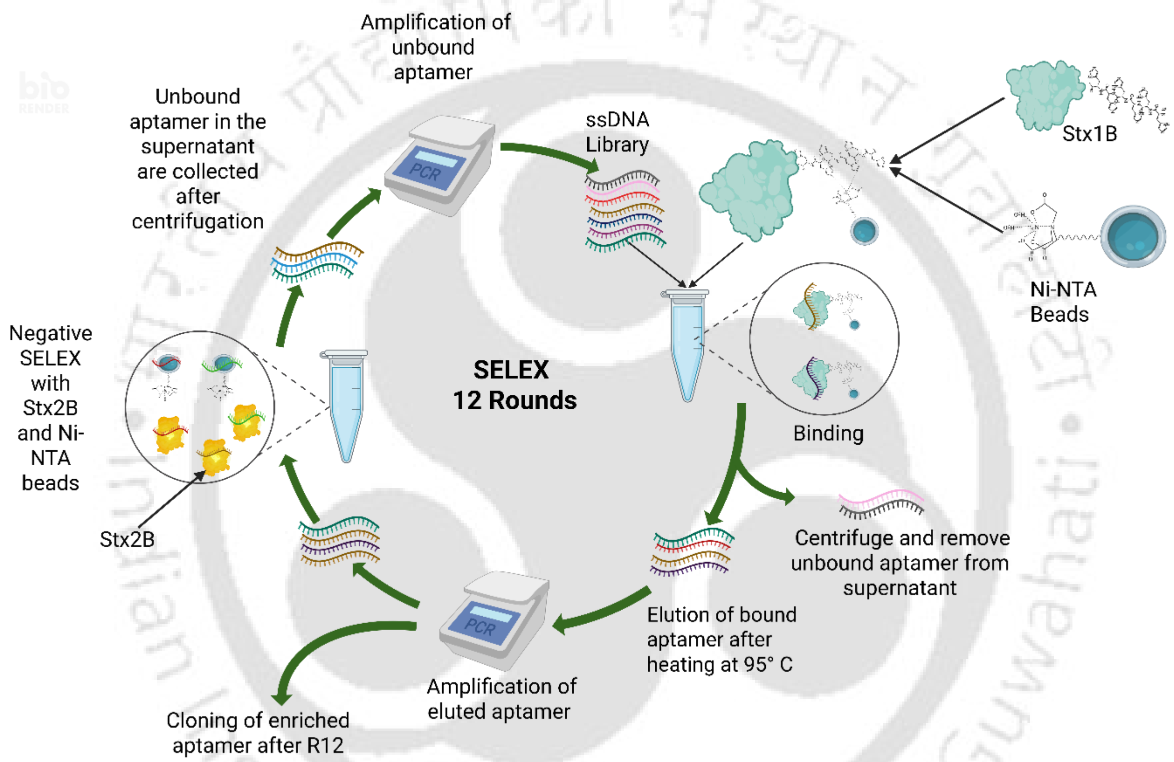

Figure 3.1: Schematic representation of the SELEX process used for aptamer selection. (Created in https://BioRender.com)

From the third cycle onward, positive SELEX was initiated using Ni-NTA bead-bound Stx1B as the target. The curated ssDNA library was incubated with immobilized Stx1B for 1 h at room temperature with gentle agitation. After incubation, centrifugation was performed to separate unbound sequences, and the pellet containing Stx1B-bound aptamers was retained. Bound aptamers were eluted by resuspending the pellet in SELEX binding buffer and heating at 95 °C for 10 min, followed by centrifugation at 1500 × g for 2 min. The supernatant containing the eluted aptamers was collected and amplified by PCR to generate the input library for the subsequent SELEX cycle.

To further enhance selectivity, additional negative selection steps were incorporated during the SELEX process. Ni-NTA beads were used as counter-targets in cycles 1 and 7, while Stx2B was employed in cycles 2 and 8. In total, 12 rounds of SELEX were conducted, comprising four negative and eight positive selection cycles. To progressively increase selection stringency, the incubation time during positive SELEX was gradually reduced from 60 min (rounds 3 and 4) to 45 min (rounds 5 and 6), 30 min (rounds 9 and 10), and finally 15 min (rounds 11 and 12). Conversely, the incubation duration for negative SELEX was increased from 60 min in rounds 1 and 2 to 90 min in rounds 7 and 8 . Following completion of the twelfth SELEX cycle, the final PCR amplicons were subjected to cloning for downstream sequence analysis.

3.2.3. Cloning of enriched aptamer sequences.

Following the completion of twelve SELEX cycles, the enriched ssDNA pool was amplified by PCR to obtain sufficient quantities of the selected sequences. The PCR products were purified using a commercial PCR purification kit (Gene2Protein, India) to remove residual primers, nucleotides, and enzymes. The purified amplicons were subsequently cloned into the pGEM-T vector using a TA cloning strategy, exploiting the single 3′-adenine overhangs generated during PCR amplification.

The recombinant plasmids were then introduced into *E. coli* DH5α competent cells via transformation. Transformed cells were plated onto LB agar plates supplemented with kanamycin, X-gal, and isopropyl β-D-1-thiogalactopyranoside (IPTG) to facilitate blue–white screening of recombinant colonies. White colonies, indicative of successful insertion of the aptamer sequences, were selectively picked and cultured in LB medium containing kanamycin. Plasmid DNA was isolated from the overnight cultures using a plasmid isolation kit (Gene2Protein, India) and subsequently subjected to Sanger sequencing for identification and characterization of the cloned aptamer inserts.

3.2.4. Prediction of aptamer structures and docking

The secondary and tertiary structures of the selected aptamer sequences were predicted using computational approaches and subsequently docked with Stx1 to elucidate potential binding sites and interacting residues. Secondary structure prediction was performed using the Mfold web server under conditions of 25 °C and 150 mM Na^+ concentration. This platform generates the most energetically favourable folding conformations of ssDNA sequences along with their corresponding Gibbs free energy (ΔG) values. The predicted secondary structures were converted into dot–bracket notation and utilized as input for three-dimensional structure modelling. Tertiary structure prediction of the aptamers was carried out using the 3dRNA/DNA web server based on the secondary structure constraints. The resulting three-dimensional aptamer models were docked with the crystal structure of Stx1 using the HDOCK server under default docking parameters. To analyze the molecular basis of aptamer–protein interactions, the docked complexes were further examined using the Protein–Ligand Interaction Profiler (PLIP) web server, which identifies and characterizes the non-covalent interactions involved in complex formation.

3.2.5. Isothermal Titration Calorimetry

The interaction between the aptamer and the target protein was evaluated using isothermal titration calorimetry (ITC) with an iTC200 microcalorimeter (GE Healthcare, India). Both the protein and aptamer samples were prepared in the same binding buffer comprising 50 mM sodium phosphate, 50 mM NaCl, 5 mM KCl, and 2.5 mM $MgCl_2$ to minimize heat effects arising from buffer mismatch. The protein solution, at a concentration of 20 µM, was loaded into the injection syringe, while the aptamer solution at 1.5 µM was placed in the sample cell. The titration protocol consisted of an initial injection of 0.4 µL, followed by 39 successive injections of 1 µL each at intervals of 120 s, with continuous stirring at 600 rpm to ensure proper mixing. The resulting thermograms were processed and analyzed using Origin software to extract the binding parameters.

3.3. Results and Discussions

3.3.1. Development of aptamers specific to Stx1B

A total of twelve iterative rounds of SELEX were conducted to enrich ssDNA sequences with high affinity and specificity toward the Stx1B protein. These rounds consisted of four negative selection cycles and eight positive selection cycles. Negative SELEX was strategically incorporated at defined stages of the selection process using Ni-NTA agarose beads and the structurally homologous Stx2B protein as counter-targets. This approach was employed to eliminate ssDNA sequences exhibiting non-specific binding to the immobilization matrix or cross-reactivity toward closely related toxin subunits. Following each negative selection step, the unbound ssDNA sequences were recovered and carried forward for subsequent positive selection against Stx1B, thereby progressively refining the specificity of the aptamer pool.

At the end of each SELEX cycle, PCR amplification of the recovered ssDNA library was performed to monitor the success of sequence recovery and amplification. The PCR products were analyzed by agarose gel electrophoresis, and the band intensities corresponding to the expected amplicon size were recorded (**Figure 3.2**). The presence of amplified products after every round confirmed the effective partitioning, recovery, and amplification of ssDNA throughout the SELEX process. Notably, a comparatively high band intensity was observed following the first round of selection

(R1), which can be attributed to the high concentration and diversity of the initial ssDNA library, encompassing a wide range of sequences, including weakly binding and non-specific candidates.

During the early SELEX rounds, a reduction in band intensity was observed, reflecting the removal of non-binding or weakly interacting sequences through repeated washing and counter-selection steps. As the selection cycles progressed, a gradual increase in the intensity of the amplified ssDNA bands became evident, indicating enrichment of sequences with improved binding affinity toward the target protein. In the later rounds of SELEX, the band intensities reached a plateau and remained relatively constant, suggesting that the aptamer pool had reached a state of convergence with no substantial further enrichment. Based on this stabilization of the amplification profile, the SELEX process was terminated after twelve rounds.

The enriched ssDNA pool obtained from the final positive selection cycle was subsequently subjected to cloning to enable individual sequence identification. The amplified products were cloned and transformed into *E. coli* DH5α competent cells, and the transformed cells were plated on selective agar plates. From these plates, twenty colonies were randomly selected to ensure representative sampling of the enriched library. Plasmids were isolated from each selected colony and screened by PCR to confirm the presence of the aptamer insert. Seventeen colonies were found to contain inserts of the expected size, indicating successful cloning of the enriched ssDNA sequences.

The plasmids from PCR-positive clones were further analyzed by DNA sequencing to determine the nucleotide sequences of the selected aptamer candidates. The obtained sequences were subjected to multiple sequence alignment to identify recurring or dominant motifs within the enriched pool. This analysis revealed that certain sequences appeared more frequently than others, suggesting preferential enrichment during the SELEX process (**Table 3.1**). Among the identified sequences, the sequences from colony no. 3 and colony no. 12 exhibited the highest representation, appearing four and two times, respectively. The repeated occurrence of these sequences within the enriched pool indicates their selective amplification during successive SELEX rounds and suggests a potential advantage in target recognition. Based on their relative abundance and enrichment profile, these aptamer candidates were selected for further structural and binding characterization. These aptamer candidates were renamed as sT3 and sT12 for the sequences from colony no. 3 and colony no. 12, respectively. The secondary structures of the selected aptamer candidates, sT3 and sT12, were computationally predicted, yielding ΔG values of –3.98 kcal/mol and –7.15 kcal/mol, respectively, indicating the formation of thermodynamically stable folded conformations (**Figure 3.3**). Based on these predicted secondary structures, three-dimensional models of both aptamers were generated and subsequently docked with the crystal structure of Shiga toxin 1 (PDB ID: 1R4Q) using the HDOCK server. Docking analysis revealed that both aptamer candidates preferentially associate with the B subunit of Stx1 (**Figure 3.4**), suggesting that the selected sequences recognize regions relevant to toxin binding or assembly.

Further examination of the docked complexes using the Protein–Ligand Interaction Profiler (PLIP) web server provided insights into the molecular interactions underlying aptamer–protein recognition. The analysis identified multiple non-covalent interactions, including hydrogen bonds, electrostatic interactions, and hydrophobic contacts, which collectively contribute to stabilization of the aptamer–protein complexes. A summary of the key interacting residues and interaction types is presented in **Table 3.3**. Although sT12 exhibited a more negative ΔG value at the secondary structure level, both aptamers demonstrated specific and well-defined interaction interfaces with the Stx1B subunit in the docking models.

Colony No.	Sequence (5’-3’)	ΔG (kcal/mol)
1	CACCTAATACGACTCACTATAGAACACTTAAGTCGGCTCTCAGACCGGAACCCTGGCTCGAACAAGCTTGC	-6.396
2	CACCTAATACGACTCACTATAGTTTACTCTCGGTAGAACTCATCGCTATTACCTGGCTCGAACAAGCTTGC	-4.076
3	CACCTAATACGACTCACTATAGACTAAAGGGGCTTGATACCATAACTATGTCCTGGCTCGAACAAGCTTGC	-4.023
4	CACCTAATACGACTCACTATAGGCAGATCATACGTCTCTATTCATAAGCAAACTGGCTCGAACAAGCTTGC	-4.513
5	CACCTAATACGACTCACTATAGCGCGCTGCCTGAACCGAACCATACCGTATCCTGGCTCGAACAAGCTTGC	-5.357
6	CACCTAATACGACTCACTATAGTAAATTGGTGGGTGTAAAGGCGCTCTAGGTCTGGCTCGAACAAGCTTGC	-5.951
7	CACCTAATACGACTCACTATAGGTGCTTTATCAGATATTTACCCCATTCTTTCTGGCTCGAACAAGCTTGC	-5.928
8	CACCTAATACGACTCACTATAGACTAAAGGGGCTTGATACCATAACTATGTCCTGGCTCGAACAAGCTTGC	-4.023
9	CACCTAATACGACTCACTATAGTGCCTTCGACGATCACGCTAAATTGGGTGCCTGGCTCGAACAAGCTTGC	-7.621

10	CACCTAATACGACTCACTATAGACTAAAGGGGCTTGATACCATAACTATGTCCTGGCTCGAACAAGCTTGC	-4.023
11	CACCTAATACGACTCACTATAGGTGTTGCTTGGGCTGCATGGGTATATAACGCTGGCTCGAACAAGCTTGC	-8.226
12	CACCTAATACGACTCACTATAGTTGGCGCTGTATAGTCGAAGTAGTTACATCCTGGCTCGAACAAGCTTGC	-7.15
13	CACCTAATACGACTCACTATAGATTGAGCAACCGAGCGACCCCTATAGTAGTCTGGCTCGAACAAGCTTGC	-8.375
14	CACCTAATACGACTCACTATAGCCCAAGTAATGCTCGTGAATCTCTCCATAGCTGGCTCGAACAAGCTTGC	-5.158
15	CACCTAATACGACTCACTATAGACTAAAGGGGCTTGATACCATAACTATGTCCTGGCTCGAACAAGCTTGC	-4.023
16	CACCTAATACGACTCACTATAGATCAGCTTAGTCATATGAAGTAAATTGTGACTGGCTCGAACAAGCTTGC	-4.936
17	CACCTAATACGACTCACTATAGTTGGCGCTGTATAGTCGAAGTAGTTACATCCTGGCTCGAACAAGCTTGC	-7.15

Table 3.1: Aptamer sequences obtained from the colonies after sanger sequencing.

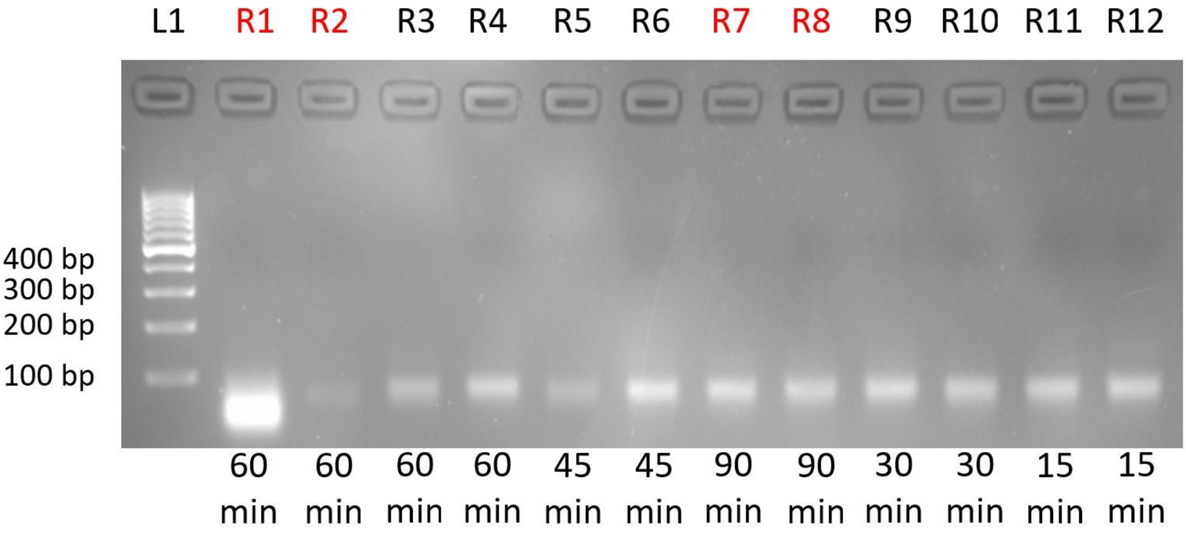

Figure 3.2: Amplified bands at the end of each SELEX round. The red rounds represent the negative SELEX. The incubation time for each round is indicated at the bottom of the gel.

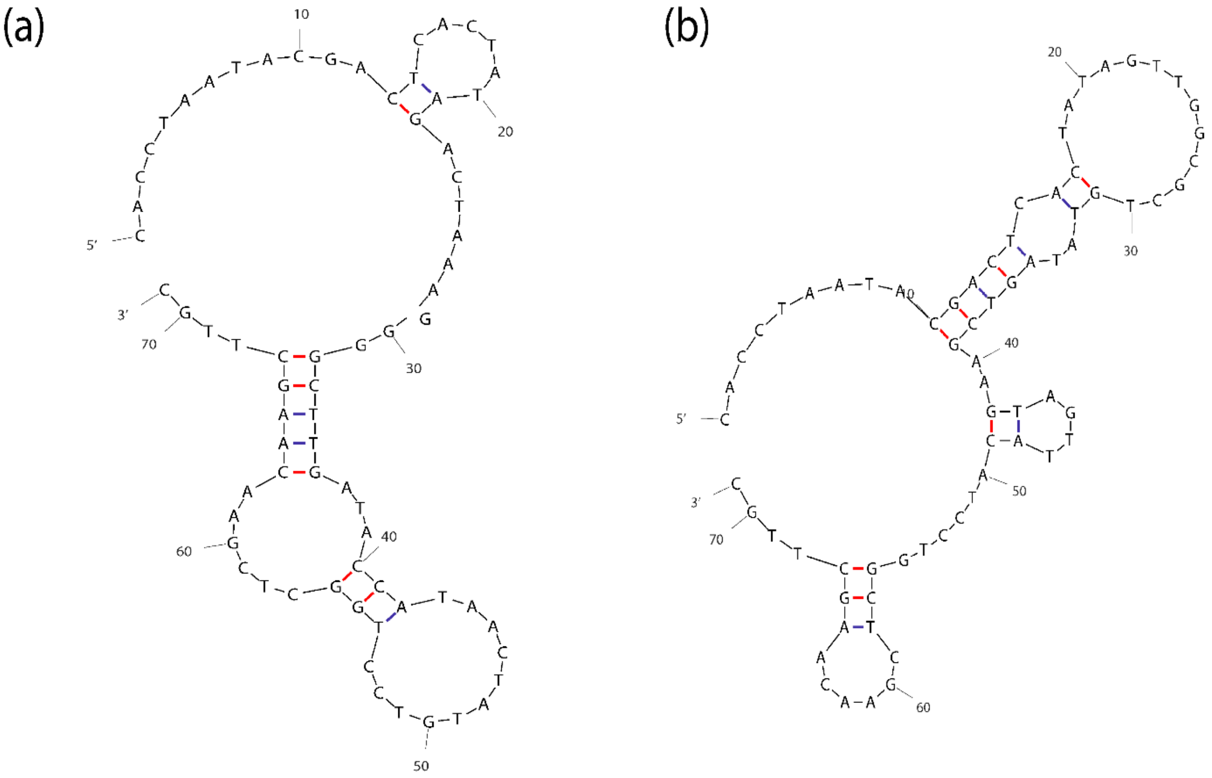

Figure 3.3: Secondary structures of selected aptamer candidates (a) sT3, (b) sT12.

Sequence Name	Sequence (5’-3’)
sT3	CACCTAATACGACTCACTATAGACTAAAGGGGCTTGATACCATAACTAT GTCCTGGCTCGAACAAGCTTGC
sT12	CACCTAATACGACTCACTATAGTTGGCGCTGTATAGTCGAAGTAGTTAC ATCCTGGCTCGAACAAGCTTGC

Table 3.2: Aptamer sequences of sT3 and sT12.

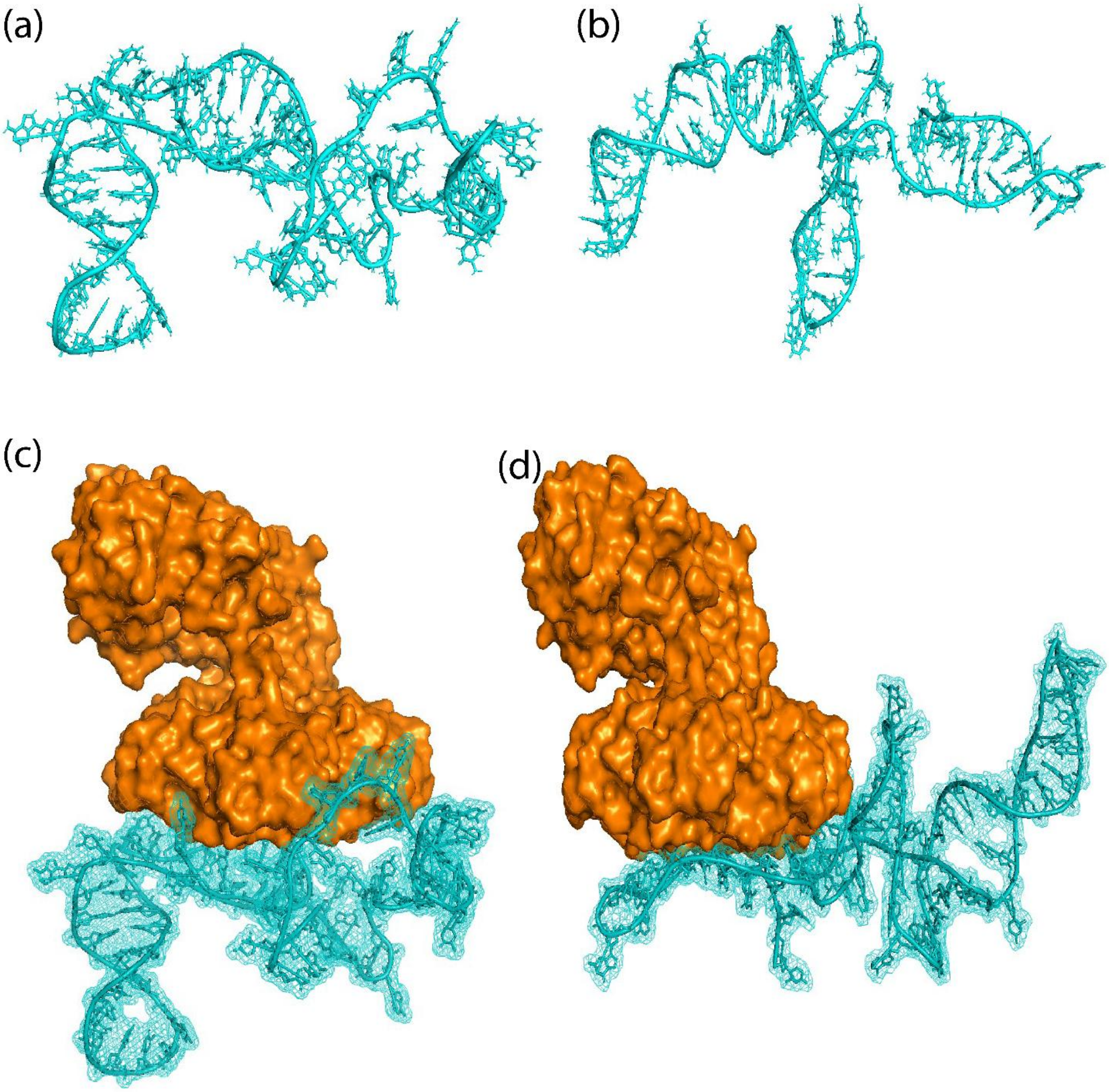

Figure 3.4: Tertiary structures of (a) sT3, (b) sT12 and docked structures of (c) sT3-Stx1 and (d) sT3-Stx1.

Aptamer-Protein complex	H bonds (Protein residue: Aptamer residue)	Hydrophobic bond (Protein residue: Aptamer residue)	π-Cation (Protein residue: Aptamer residue)	π-Stackings (Protein residue: Aptamer residue)	Salt Bridges (Protein residue: Aptamer residue)
sT3-Stx1	THR1:G11 ASP3:A9 ASP3:C10 ASP16:T58 ASP16:T59 ASP16:G60 ASN32:A61 TRP34:A62 TRP34:A64 ASN35:A65 ASN35:C63 LYS53:A9 ASN59:T8 THR290:A64	TRP34:T69 PHE30:C71	LYS53:A9	TRP34:A62 PHE30:C71	ASP18:G60 HIS58:T8
sT12-Stx1	ASN15:A2 ASP17:C3 ASP18:T58 ASN32:T54 ASN32:C57 ARG33:T54 ARG33:T5 TRP34:T69 THR54:T5 ASN55:T5 GLY62:T5 SER64:T54	ASP17:C3	TRP34:G66	TRP34:A64 TRP34:A65 HIS58:A50	ASP18:G55 ARG33:T58

Table 3.3: Interaction profile of the aptamers with Stx1.

3.3.2. Prediction of binding affinity between aptamer and protein.

Isothermal titration calorimetry (ITC) was employed to quantitatively assess the binding interactions between the selected aptamer candidates and the Stx1B subunit. The calorimetric profiles for both aptamers displayed distinct exothermic heat changes upon titration, indicative of favourable binding events. The resulting binding isotherms were best described using a one-site binding model, suggesting a single predominant interaction interface between the aptamer and the target protein. For the sT3 aptamer, the fitting yielded a binding stoichiometry of N = 0.896 ± 0.019 and a dissociation constant (K_d) of 273 ± 0.03 nM, reflecting a strong and well-defined interaction with Stx1B. In comparison, the sT12 aptamer exhibited a stoichiometry of N = 0.878 ± 0.175 and a substantially weaker binding affinity, with a K_d value of 6.80 ± 0.56 µM (**Figure 3.5**). The near-unity stoichiometry values observed for both aptamers are consistent with a one-to-one binding mode and align well with the interaction models predicted through molecular docking.

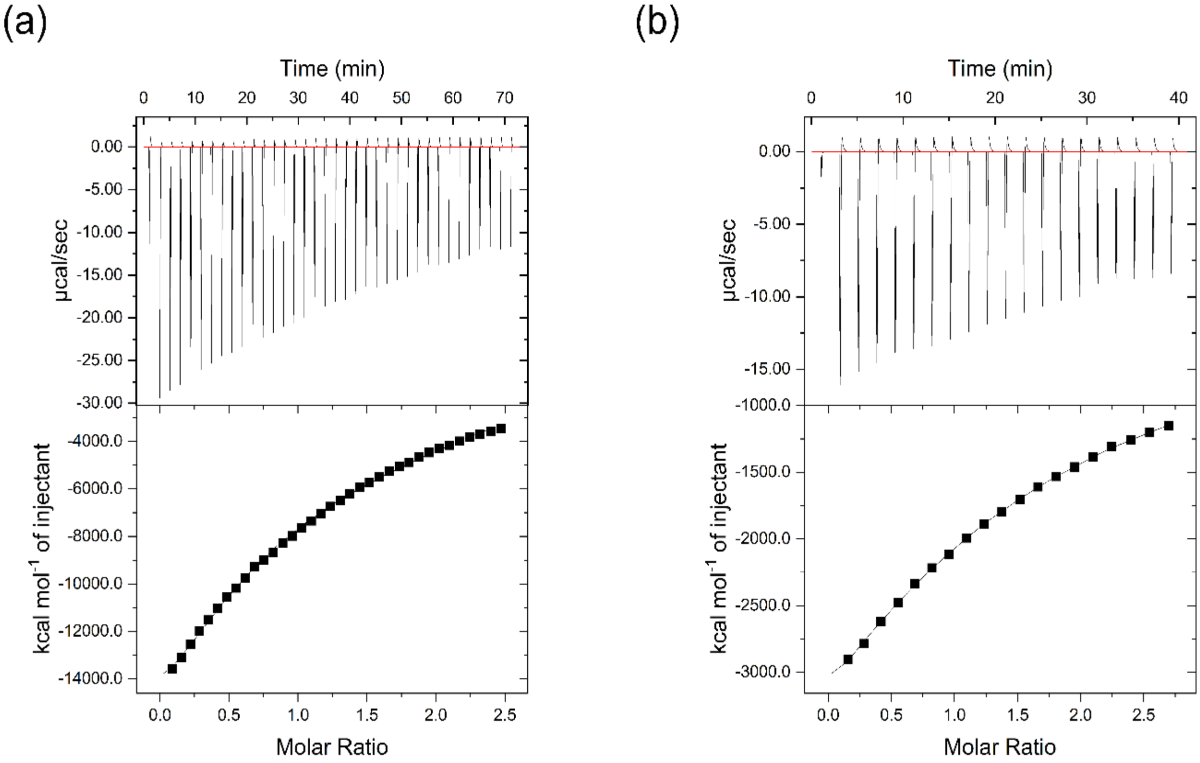

Figure 3.5: ITC thermogram of (a) sT3-Stx1 complex (b) sT12-Stx1 complex.

These quantitative binding data are in agreement with the SELEX enrichment and sequence frequency analyses, wherein sT3 emerged as the most frequently represented sequence within the enriched pool. Furthermore, despite sT12 exhibiting a more negative predicted secondary structure free energy, the ITC results demonstrate that sT3 possesses a significantly higher binding affinity toward Stx1B. Based on its superior binding affinity, consistent stoichiometry, and dominant enrichment during the SELEX process, sT3 was identified as the most promising aptamer candidate for further investigation.

3.4. Conclusion.

This chapter describes the systematic development and characterization of ssDNA aptamers specific to the B subunit of Shiga toxin 1 (Stx1B) using the SELEX strategy. A rational selection workflow was implemented, combining His-tag–mediated immobilization of the target protein on Ni-NTA agarose beads with centrifugation-based partitioning to enable efficient separation of bound and unbound sequences. The inclusion of negative SELEX steps using both Ni-NTA beads and the structurally related Stx2B subunit played a critical role in eliminating non-specific and cross-reactive sequences, thereby enhancing the selectivity of the enriched aptamer pool.

Progressive enrichment of target-binding sequences was monitored across twelve SELEX cycles through PCR amplification, revealing convergence of the ssDNA library toward a limited number of dominant candidates. Cloning and sequencing of the final enriched pool enabled identification of recurring sequences, indicating successful selection pressure and enrichment. Among the isolated candidates, sT3 and sT12 emerged as the most frequently represented aptamers and were therefore selected for detailed characterization.

Computational analyses provided structural insights into the selected aptamers, including prediction of secondary and tertiary structures and molecular interactions with Stx1. Docking and interaction profiling demonstrated that both aptamers interact specifically with the Stx1B subunit through defined non-covalent interactions, supporting their potential as selective recognition elements. Experimental validation using ITC further confirmed aptamer–protein binding in solution and enabled quantitative comparison of binding affinities. The ITC results revealed a marked difference in binding strength between the two candidates, highlighting sT3 as the superior binder despite differences in predicted folding stability.

Overall, this chapter establishes a robust and reproducible framework for the generation, screening, and validation of Stx1B-specific aptamers by integrating SELEX, molecular biology techniques, computational modelling, and thermodynamic analysis. The findings demonstrate the effectiveness of the applied selection strategy and provide a well-characterized aptamer candidate against Stx1.

Chapter 4

Development of aptasensor for Stx1 using chain-shaped interdigitated electrodes

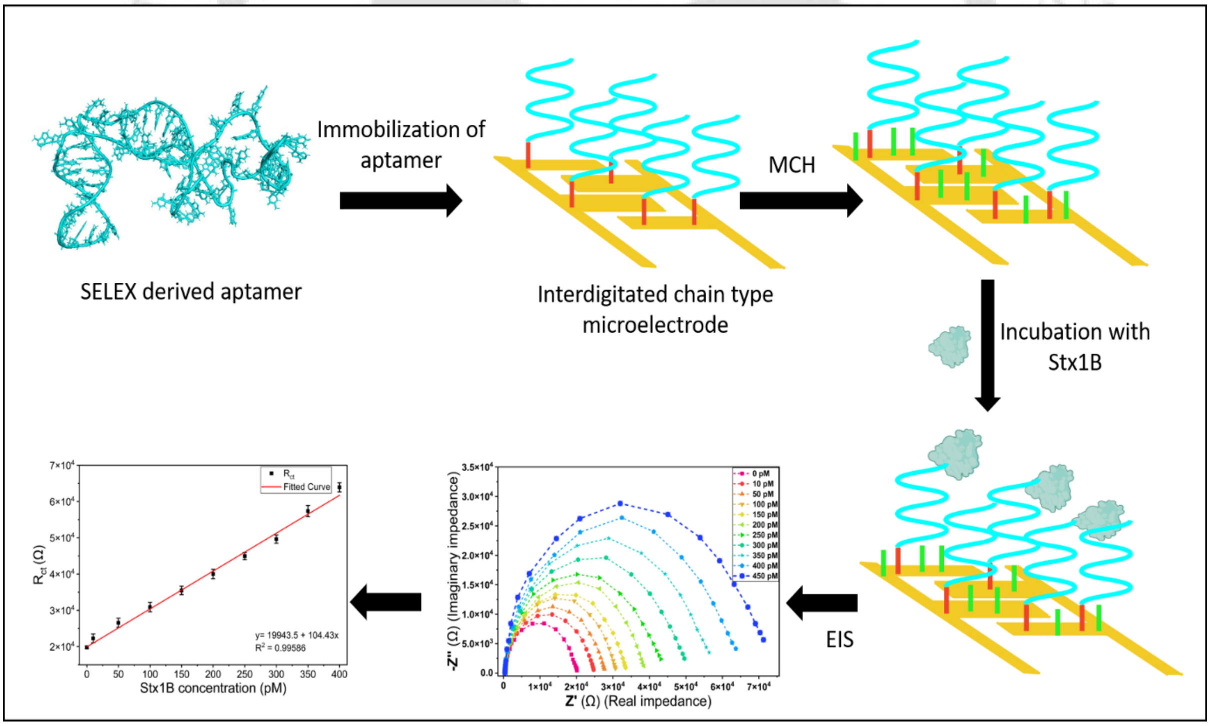

Development of aptasensor for Stx1 using chain-shaped interdigitated electrodes.

4.1. Overview

Electrochemical biosensors have emerged as powerful analytical platforms for the rapid and sensitive detection of biomolecular targets due to their simplicity, low cost, and compatibility with miniaturized systems. Among various electrochemical transduction techniques, impedimetric sensing based on electrochemical impedance spectroscopy (EIS) is particularly attractive as it enables label-free detection by monitoring changes at the electrode–electrolyte interface resulting from biomolecular recognition events. The performance of such biosensors critically depends on the choice of the biorecognition element and the efficiency of its immobilization onto the electrode surface.

Building upon the aptamer developed and characterized in the previous chapter, this chapter focuses on the fabrication of an aptamer-based impedimetric biosensor for the detection of Shiga toxin 1. The chapter describes the functionalization of a gold interdigitated chain-type microelectrode using a self-assembled monolayer approach, enabling stable and oriented immobilization of a thiol-modified sT3 aptamer. Surface passivation strategies employed to minimize non-specific adsorption and improve sensing reliability are also discussed.

Furthermore, this chapter outlines the principles of electrochemical impedance spectroscopy used to transduce the aptamer–toxin interaction into a measurable electrical signal. The experimental conditions for impedance measurements, including the use of a redox probe and appropriate buffer systems, are detailed. In addition, the chapter addresses the evaluation of key analytical performance parameters of the developed aptasensor, including sensitivity, specificity, stability, reproducibility, and applicability to complex sample matrices. Collectively, this chapter demonstrates the integration of a SELEX-derived aptamer with an impedimetric sensing platform, establishing a foundation for sensitive and reliable electrochemical detection of Stx1.

4.2. Experimental

4.2.1. Materials

Thiol modified sT3 aptamer with the sequence 5’-SH-$(CH_2)_6$-CACCTAATACGACTCACTATAGACTAAAGGGGCTTGATACCATAACTATGTCCTGGCTCGAACAAGCTTGC-3'was purchased from Eurofins (Sweden). Tris(2-carboxyethyl) phosphine hydrochloride (TCEP) was procured from Invitrogen, India. Sodium Borohydride ($NaBH_4$), Potassium ferrocyanide and Potassium ferricyanide were purchased from Himedia, India. Commercial milk was purchased from Amul, India. All the reagents used were of analytical reagent grade, and the buffers were prepared using deionized water (18.2 MΩ.cm).

4.2.2. Immobilization of thiol modified aptamer on Interdigitated chain type microelectrodes

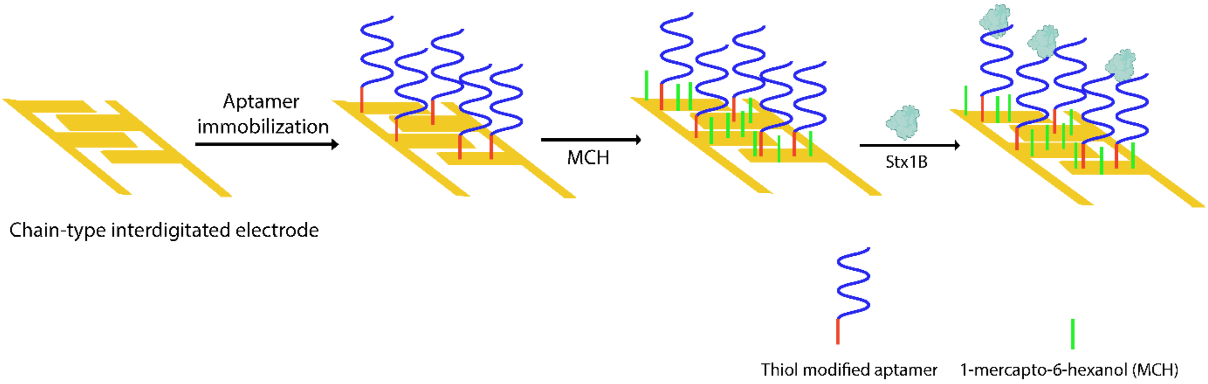

Figure 4.1: Schematic of thiol-modified aptamer immobilization on ICE.

The interdigitated Chain type electrode (ICE) employed in this study was received from Prof. Sungbo Cho, Gachon University, Republic of Korea based on a collaborative work. The thiol-functionalized aptamer was immobilized onto the gold-based ICE through covalent Au–S bonding. Prior to immobilization, tris(2-carboxyethyl) phosphine hydrochloride (TCEP) was employed to reduce the protective disulfide linkage present on the thiol-modified aptamer, thereby generating free thiol (–SH) groups. The aptamer was treated with TCEP at a molar ratio of 1:100 (aptamer: TCEP) and incubated at room temperature for 1.5 h to ensure complete reduction of the disulfide bonds. Following reduction, the thiol modified aptamer was purified using ethanol precipitation to remove excess reducing agent and by-products. The steps involved in the preparation of the aptamer -immobilized ICE is shown in **Figure 4.1**. Briefly, before aptamer attachment, the ICE surface was cleaned by treatment with 0.5 M $NaBH_4$, thoroughly rinsed with deionized (DI) water, and dried under a gentle stream of argon gas. The cleaned electrode, with the gold finger region defining the sensing area, was then immersed in the solution of reduced thiol-modified aptamer and incubated overnight at 4 °C to facilitate self-assembled monolayer formation. After immobilization, the electrode surface was rinsed with binding buffer to remove unbound or weakly adsorbed aptamer molecules and subsequently backfilled with 1-mercapto-6-hexanol (MCH) to passivate the remaining bare gold sites. Finally, the modified electrodes were rinsed with DI water and stored at 4 °C until further use.

4.2.3. Surface characterization of ICE.

The surface morphology of the ICE was investigated by field emission scanning electron microscope (FESEM) (Sigma, Zeiss, Germany) using an accelerating voltage of 5 kV. The sensing array of the ICE was captured using FESEM, depicting the interdigitated electrode fingers and the contact pads at different magnification. The successful immobilization of aptamers on the electrode surface was verified using atomic force microscopy (AFM), which enables assessment of changes in surface morphology and roughness resulting from surface modification. AFM measurements were carried out using a Cypher S atomic force microscope (Oxford Instruments, USA), and images were acquired in non-contact mode over a scan area of 1 × 1 μm^2 for both bare and aptamer-modified electrodes.

4.2.4. Electrochemical Impedance Spectroscopy (EIS) study

EIS was employed to monitor changes at the electrode interface following successive surface modification steps and to serve as the transduction technique to generate response signal for the developed aptasensor. EIS measurements were conducted using a potentiostat (Zennium, Zahner, Germany), and variations in charge transfer resistance (R_{ct}) were used as the primary response signal to evaluate interfacial charge transfer processes. The impedance measurements were performed in a pseudo-reference electrode configuration, wherein one arm of the interdigitated chain-type electrode functioned as the working electrode, while the opposite arm served as both the counter and pseudo-reference electrode.

A redox probe solution consisting of 5 mM $K_3Fe(CN)_6/K_4Fe(CN)_6$ prepared in 1× PBS (pH 7.4) was used for all measurements. An alternating current (AC) perturbation of 5 mV was applied without any direct current (DC) bias over a frequency range of 1 Hz to 100 kHz, with five frequency points recorded per decade. For each measurement, the sensing region of the electrode was immersed in a well of a 96-well plate containing 350 µL of the redox probe solution.

4.2.5. Real sample analysis.

The practical applicability of the developed aptasensor was evaluated using real sample analysis. Commercial milk samples (Amul, India) were spiked with known concentrations of Stx1B prior to analysis. To minimize matrix interference, the spiked milk samples were centrifuged at 12,000 × g for 15 min at 4 °C, after which the upper lipid layer was carefully removed. The sensor response data obtained from the processed milk samples were fitted in the calibration equation discerned from the calibration curve generated under buffer conditions. The recovery efficiency and relative standard deviation (RSD) were subsequently calculated to assess the accuracy and reproducibility of the biosensor.

4.2.6. Statistical analysis.

All the experiments were performed with a minimum of three independent replicates, and the mean of the measured data was presented with standard deviation. Origin Pro software was used to analyze and generate graphical data. The limit of detection (LOD) of the developed sensor was calculated using the formula, LOD = 3× Standard deviation of Blank/ sensitivity (slope of the calibration curve) (Chinnadayyala et al., 2019).

4.3. Results and discussions

4.3.1. Development of aptamer-immobilized interdigitated electrode

In this study, a chain-shaped interdigitated electrode (ICE), characterized by the absence of sharp edges, was employed. In conventional rectangular interdigitated electrode arrays, electric field intensities are typically concentrated at the sharp edges of the electrode fingers, leading to a non-uniform electric field distribution across the sensing area. Such edge effects can result in localized signal dominance and reduced reliability in impedance-based measurements (Park et al., 2020). In contrast, the chain-shaped electrode geometry minimizes edge-induced field intensification, thereby promoting improved signal uniformity and measurement reliability.

The ICE was initially characterized by FESEM, which confirmed the presence of well-defined interdigitated chain-type electrode fingers with a 5 µm spacing and width, as well as contact pads for the working electrode and the reference electrode **(Figure 4.2)**. This configuration is expected to generate a more homogeneous electric field within the sensing region, facilitating uniform interaction between the electrode surface and the immobilized aptamer layer and thereby enhancing the overall electrochemical sensing performance.

The sT3 aptamer was thiol-functionalized and immobilized onto the surface of the chain-shaped interdigitated gold microelectrode using a self-assembled monolayer (SAM)-based strategy. Following immobilization, changes in the surface morphology of the electrode were examined by atomic force microscopy (AFM). The bare electrode surface exhibited a mean roughness of 1.004 nm and a maximum roughness of 15.54 nm. Upon aptamer immobilization, these values decreased to 0.774 nm and 12.67 nm, respectively, indicating the formation of a more uniform and compact surface layer. The observed reduction in surface roughness confirms the successful formation of a densely packed aptamer-based SAM on the gold electrode surface (**Figure 4.3 a, b).**

The developed ICE was connected to a potentiostat through a custom adapter, as illustrated in Fig. 4.2b. Electrochemical impedance spectroscopy (EIS) was subsequently employed to monitor interfacial changes arising from aptamer immobilization and the subsequent backfilling step.

Impedance measurements were performed using a redox probe solution containing 5 mM $K_3Fe(CN)_6/K_4Fe(CN)_6$ prepared in 1× PBS (pH 7.4), and spectra were recorded after each surface modification step.

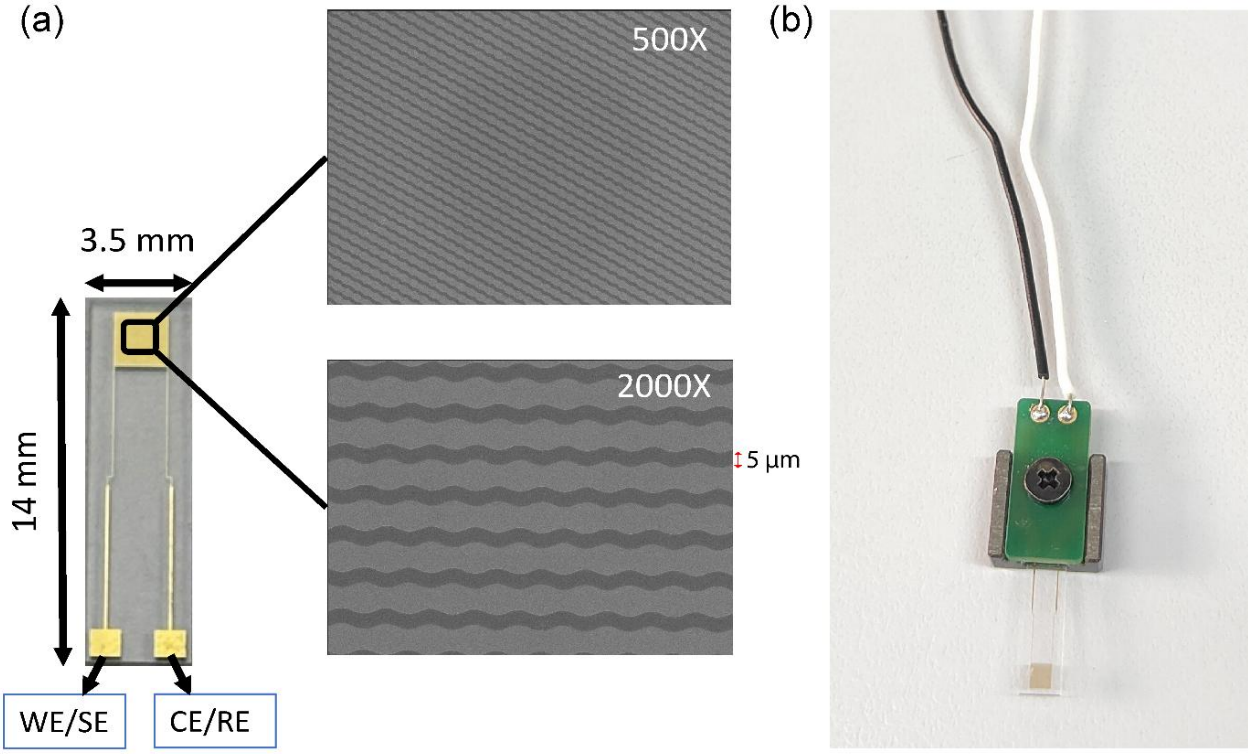

Figure 4.2: (a) FESEM image of ICE with 500X and 2000X magnification. (b)Adapter for connecting the ICE with the potentiostat.

The EIS data were represented as Bode plots (**Figure 4.3c, 4.3d**) and fitted using Zahner analysis software with an appropriate equivalent circuit model. The impedance spectra were best described using a Randles-type circuit consisting of a solution resistance (R_s) in series with a parallel combination of a constant phase element (CPE) and a charge transfer resistance (R_{ct}), followed by a finite-length diffusion element represented by a Nernst diffusion component (Z_N) (**Figure 4.3e**). Distinct frequency-dependent regions corresponding to different electrochemical processes were evident in the Bode plots (**Figure 4.3c**). The high-frequency region above 10 kHz was associated with the solution resistance (R_s), while the upper mid-frequency region corresponded to the double-layer capacitance (C_{dl}). The lower mid-frequency region, centred around approximately 500 Hz, was dominated by the charge transfer resistance (R_{ct}), and the low-frequency region reflected diffusion-controlled processes represented by the Nernst diffusion element (Z_N). The eelectrochemical parameters extracted from fitting the impedance spectra following each surface modification step are summarized in **Table 4.1**.

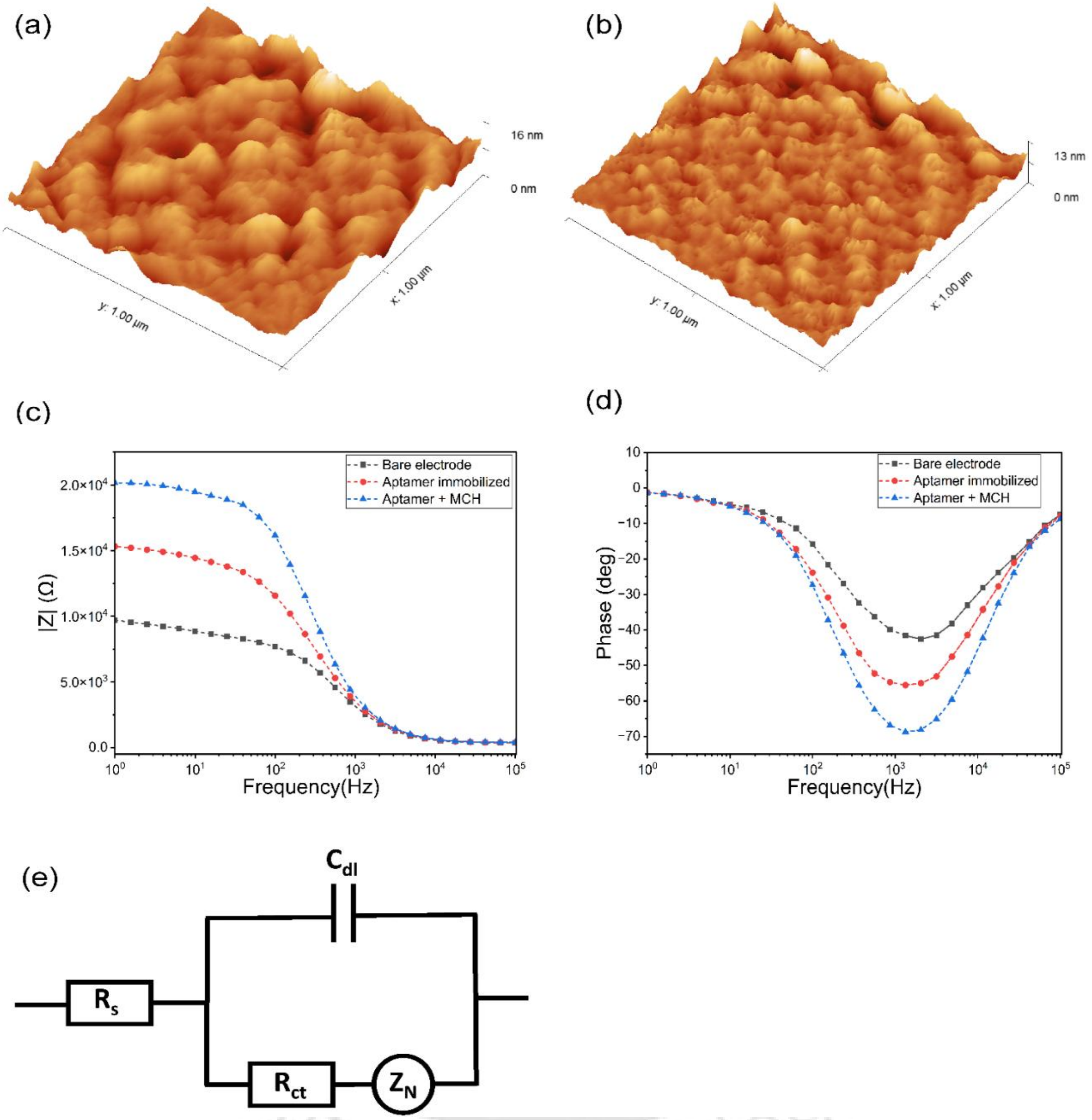

Figure 4.3: AFM image of the (a) bare electrode, (b) aptamer immobilized electrode. Bode plot of the (c) impedance magnitude (|Z|), and (d) phase at different modification stages of the ICE surface. (e) Randle's equivalent circuit for the EIS plots.

A progressive increase in the overall impedance magnitude (|Z|) was observed following aptamer immobilization, confirming the successful formation of a thiol-modified aptamer-functionalized SAM on the electrode surface **(Figure 4.3c)**. Immobilization occurs through the formation of strong Au–S covalent bonds, in which sulfur atoms from the thiol groups coordinatively bind to gold atoms, resulting in a stable and well-defined aptamer layer. The immobilized aptamer layer introduces steric hindrance and, due to the negatively charged phosphate backbone of the DNA, electrostatically repels the negatively charged $[Fe(CN)_6]^{3-/4-}$ redox species, thereby increasing interfacial resistance. Subsequent backfilling with 6-mercapto-1-hexanol (MCH) further passivates unoccupied gold sites, minimizes non-specific adsorption, promotes upright orientation of the immobilized aptamers, and regulates aptamer surface density. The additional MCH layer further restricts access of the redox probe to the electrode surface, leading to a further increase in |Z| **(Figure 4.3c)**.

Electrodes	R_s (Ω)	CPE		R_{ct} (kΩ)	Z_N	
		Y_0 (nS·s$^{\alpha}$)	α		DW (KDW)	k (1/s)
Bare	362	89.1	928	7.78	6.53	26.6
Aptamer immobilized	361	86.7	934	12.3	8.16	24.5
MCH back filled aptamer immobilized	382	71.0	936	18.8	4.61	14.9
Y_0 - CPE admittance, α - Phase shift factor, DW - Warburg Constant, k - Electron Transfer Rate Constant						

Table 4.1: Fitted EIS parameters for bare, aptamer-immobilized, and MCH-blocked electrode.

Consistent with these observations, the charge transfer resistance (R_{ct}), which reflects the resistance to electron transfer between the redox species and the electrode surface, increased systematically following each modification step. This stepwise increase in R_{ct} confirms the successful immobilization of the aptamer and effective backfilling with MCH. Consequently, R_{ct} was selected as the primary analytical parameter to monitor surface modification and to quantify target-induced changes during sensing experiments.

4.3.2. Application of aptamer-immobilized electrode for sensing Stx1.

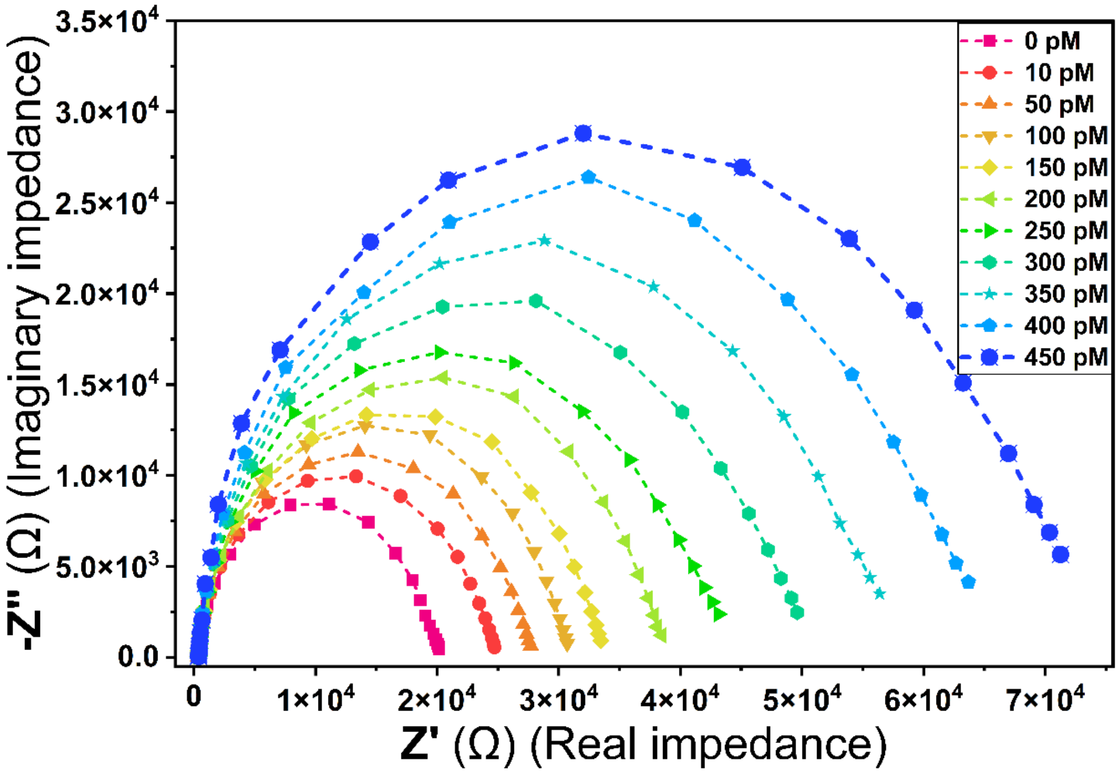

Figure 4.4: EIS spectra of the aptasensor with increasing concentration of Stx1B.

The sensing performance of the developed aptasensor was evaluated by incubating it with increasing concentrations of Stx1B, followed by electrochemical impedance measurements in the presence of a redox probe solution containing 5 mM $K_3Fe(CN)_6/K_4Fe(CN)_6$ prepared in 1× PBS (pH 7.4). The resulting impedance spectra were represented as Nyquist plots (**Figure 4.4**). A progressive increase in the diameter of the semi-circular region was observed with increasing Stx1B concentration, indicating a corresponding increase in the charge transfer resistance (R_{ct}).

This increase in R_{ct} arises from impeded electron transfer at the electrode–electrolyte interface due to the binding of Stx1B to the immobilized aptamer layer. The formation of the aptamer–target complex increases surface coverage and steric hindrance, thereby restricting the access of the redox probe molecules to the electrode surface. At an optimal aptamer packing density, the predominantly upright orientation of the immobilized aptamers facilitates efficient target recognition while maximizing the blocking effect upon target binding, resulting in enhanced sensor sensitivity. As the concentration of Stx1B increases, greater target occupancy on the electrode surface further amplifies this blocking effect, leading to a more pronounced suppression of redox probe diffusion and electron transfer.

A linear relationship between R_{ct} and Stx1B concentration was observed over the range of 10 pM to 450 pM, described by the regression equation y = 19817.44 + 107.02x with a correlation coefficient of 0.99 (**Figure 4.5**). The limit of detection (LOD) of the aptasensor was calculated to be 2.88 pM (n = 3) using the equation LOD = 3 × SD/sensitivity, where SD denotes the standard deviation of the R_{ct} values obtained for the blank measurements and the sensitivity corresponds to the slope of the calibration curve.

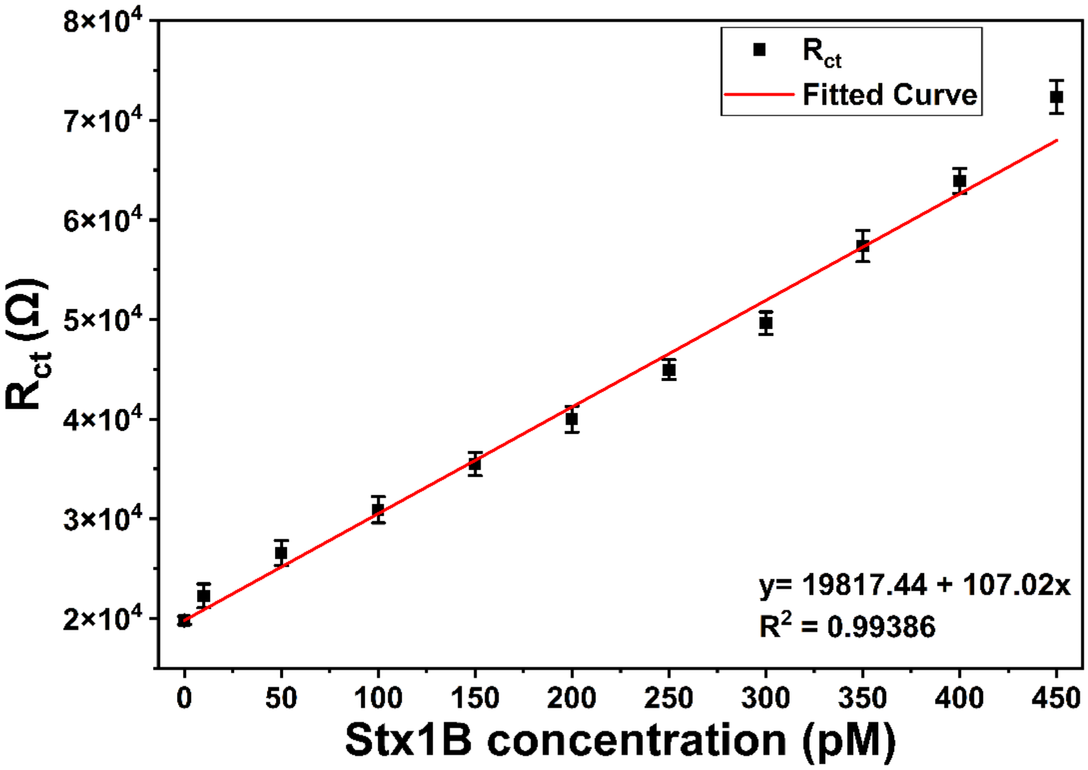

Figure 4.5: Linear calibration plot using the R_{ct} versus concentration of Stx1B

4.3.3. Performance evaluation of the developed aptasensor.

The selectivity of the developed aptasensor was examined to evaluate its ability to discriminate the target analyte from structurally related and non-specific molecules. To assess specificity, the aptasensor was individually incubated with the target molecule and selected non-target species, including a structurally similar toxin subunit and an unrelated protein. Specifically, the sensor was exposed to 250 pM Stx1B, 400 pM Stx2B, and 300 pM bovine serum albumin (BSA) for 20 min, followed by electrochemical impedance measurements in a redox probe solution containing 5 mM $K_3Fe(CN)_6/K_4Fe(CN)_6$ prepared in 1× PBS (pH 7.4). The charge transfer resistance (R_{ct}) values obtained after equivalent circuit fitting were analyzed to determine the sensor response. To account for baseline contributions, normalized impedance changes were calculated using ΔR_{ct} = (R_a −

R_o)/R_o, where R_o represents the R_{ct} of the aptamer-modified electrode and R_a corresponds to the R_{ct} measured after incubation with each analyte.

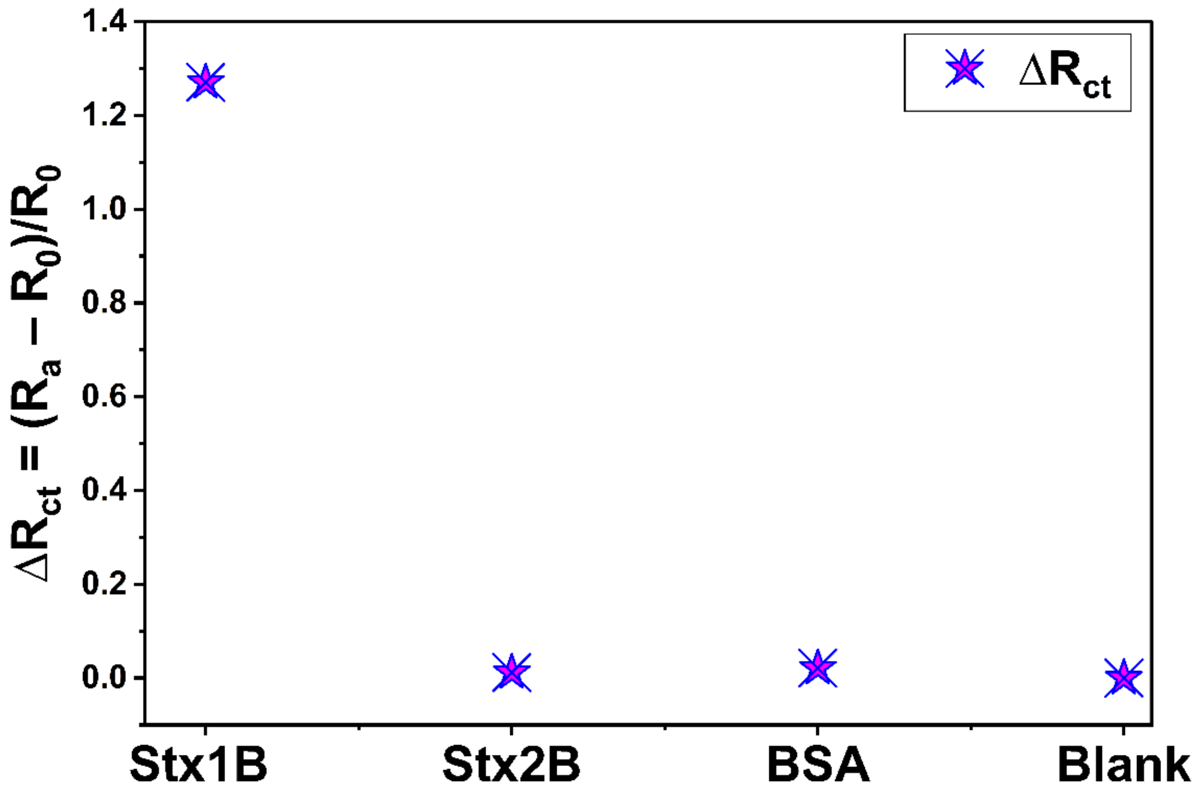

Figure 4.6: Selectivity analysis of the developed aptasensor.

As illustrated in **Figure 4.6**, a pronounced increase in ΔR_{ct} was observed exclusively for the target molecule, Stx1B, whereas negligible changes were recorded for Stx2B and BSA relative to the blank aptasensor. This selective response confirms the high specificity of the aptamer–Stx1B interaction and demonstrates the effective discrimination capability of the developed aptasensor. The operational stability of the biosensor, an essential parameter for reliable and practical application, was also investigated. To assess stability, impedance measurements were performed at five-day intervals over a period of 25 days, during which the aptasensor was stored in 1× PBS (pH 7.4) at 4 °C. The EIS spectra and corresponding R_{ct} values exhibited minimal variation throughout the storage period, and the biosensor retained 97.6% of its initial response after 25 days, as shown in **Figure 4.7**. This high degree of stability can be attributed to the robust Au–S covalent linkage formed between the thiol-modified aptamer and the gold electrode surface. In addition, the reproducibility of the aptasensor fabrication was evaluated by measuring the EIS responses of five independently prepared aptasensors following incubation with 300 pM Stx1B. The relative standard deviation (RSD) of the R_{ct} values was calculated to be 3.9%, indicating good reproducibility and consistency in electrode preparation and surface functionalization (**Figure 4.8** and **Figure 4.9**).

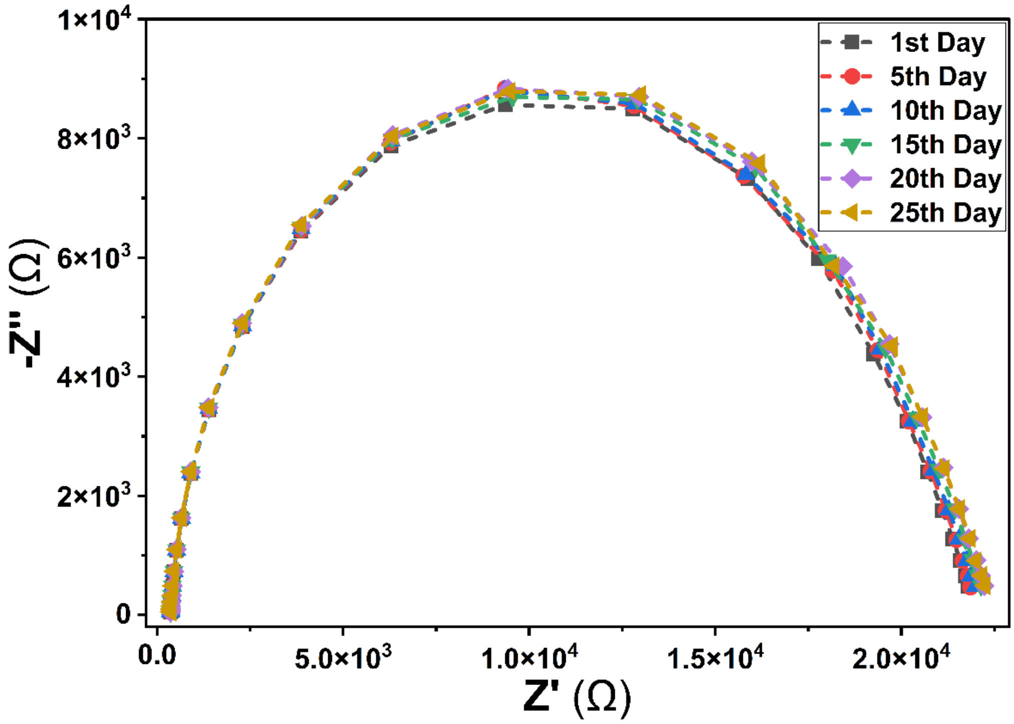

Figure 4.7: Stability analysis of the developed aptasensor over 25 days.

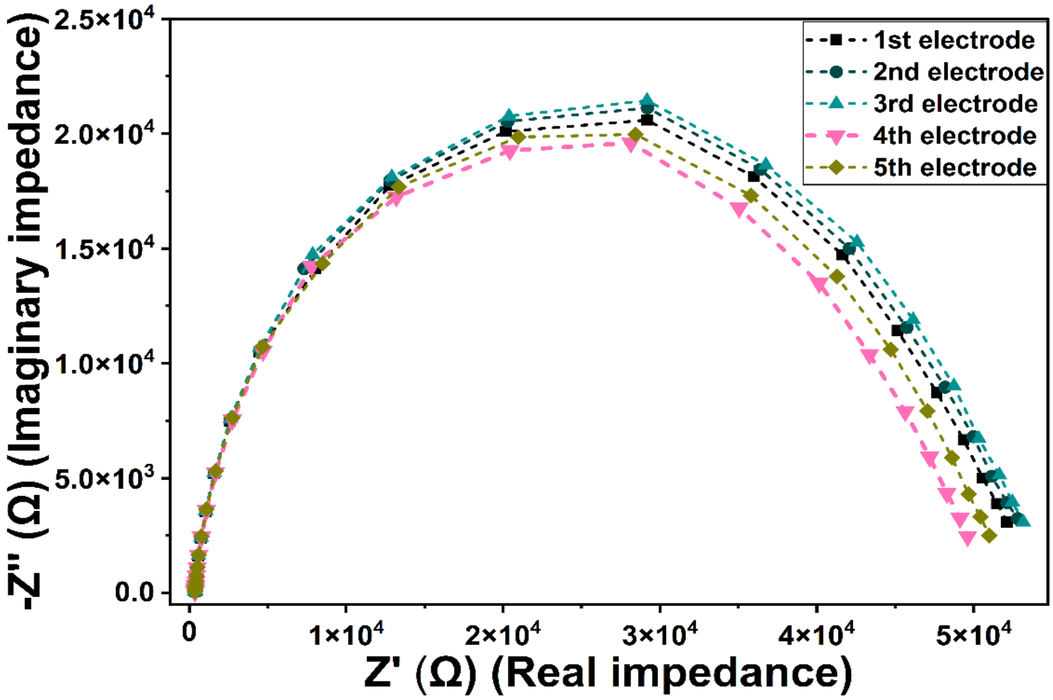

Figure 4.8: Reproducibility analysis using five independently prepared aptasensors.

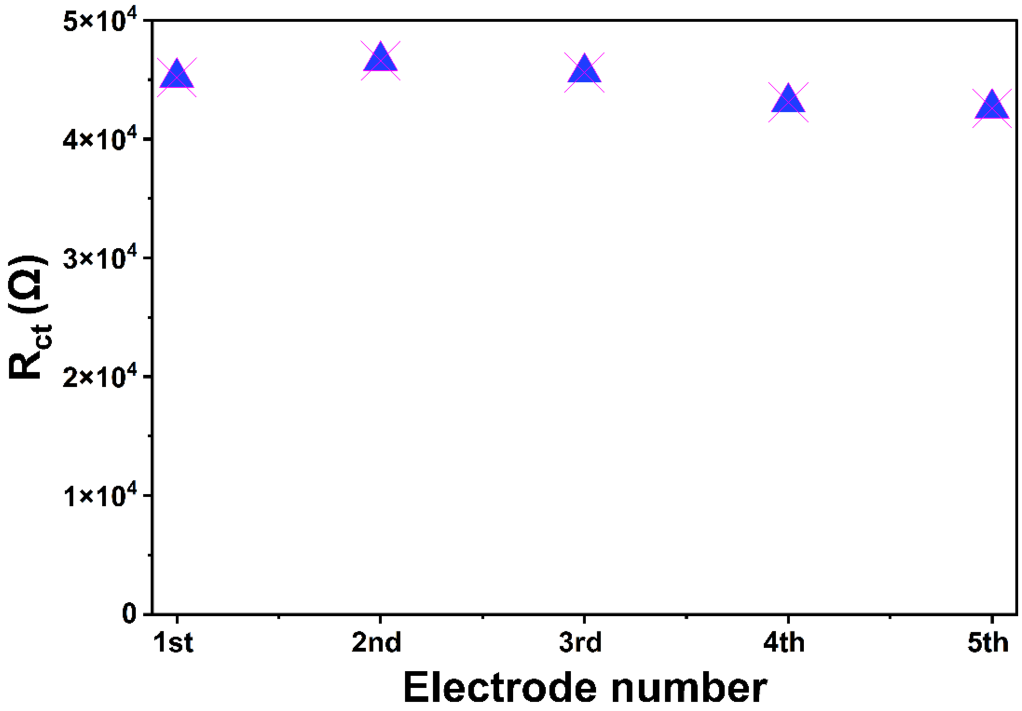

Figure 4.9: The R_{ct} values of the independently prepared electrodes.

4.3.4. Real sample analysis with the developed aptasensor.

The practical applicability of the developed aptasensor under real-sample conditions was evaluated through recovery studies using milk samples spiked with known concentrations of Stx1B. To reduce potential matrix effects arising from milk components such as lipids and proteins, the spiked samples were subjected to centrifugation to remove the upper fat layer prior to analysis. The processed milk samples were then incubated with the aptasensor for 20 min, followed by electrochemical impedance measurements in a redox probe solution containing 5 mM $K_3Fe(CN)_6/K_4Fe(CN)_6$ prepared in 1× PBS (pH 7.4).

Spiked	Detected	Recovery %	RSD%
10 pM	10.35 pM	103.5	0.97
200 pM	197.6 pM	98.8	1.66
400 pM	390 pM	97.5	1.98

Table 4.2: Recovery of the target protein from spiked milk samples.

The concentration of Stx1B in the milk samples was determined from the measured R_{ct} values using the calibration curve established under buffer conditions. The calculated recovery values ranged from 97.5% to 103.5%, demonstrating the capability of the aptasensor to accurately quantify Stx1B in complex sample matrices (**Table 4.2**). The close agreement between the responses obtained from spiked milk samples and those measured in buffer further indicates effective mitigation of matrix interference and confirms the suitability of the developed aptasensor for real-sample analysis.

4.4. Conclusion.

This chapter presents the successful development and comprehensive evaluation of an aptamer-based impedimetric biosensor for the detection of the Shiga like toxin 1 (Stx1). The sensing platform was constructed by immobilizing a SELEX-derived, thiol-modified sT3 aptamer onto a gold interdigitated chain-type microelectrode using a SAM strategy. Surface modification and functionalization were systematically characterized using AFM and EIS, confirming the formation of a uniform and stable aptamer layer on the electrode surface. EIS was effectively employed as a label-free transduction mechanism to monitor interfacial changes arising from aptamer immobilization, surface passivation, and target binding. The progressive increase in charge transfer resistance observed after each modification step validated the successful assembly of the sensing interface and supported the selection of R_{ct} as the primary analytical parameter for signal quantification. The developed aptasensor exhibited a concentration-dependent impedance response upon exposure to Stx1B, demonstrating its capability to sensitively transduce specific aptamer–toxin interactions. The selectivity of the aptasensor was confirmed through discrimination studies using structurally related and non-specific proteins, highlighting the high specificity of the sT3 aptamer toward Stx1B. Furthermore, the sensor demonstrated excellent operational stability, retaining its response over an extended storage period, and good reproducibility across independently fabricated electrodes. Real-sample analysis using spiked milk samples further validated the practical applicability of the sensing platform, with recovery values indicating minimal matrix interference and reliable detection in complex food matrices.

Overall, this chapter establishes a robust impedimetric aptasensing strategy by integrating a high-affinity aptamer with an ICE architecture. The systematic design, characterization, and validation of the sensing platform provide a strong foundation for the sensitive and selective detection of Shiga toxin and underscore the potential of aptamer-based electrochemical biosensors for food safety and public health monitoring applications.

Chapter 5

In-silico Designing of ssDNA aptamer against Stx2B

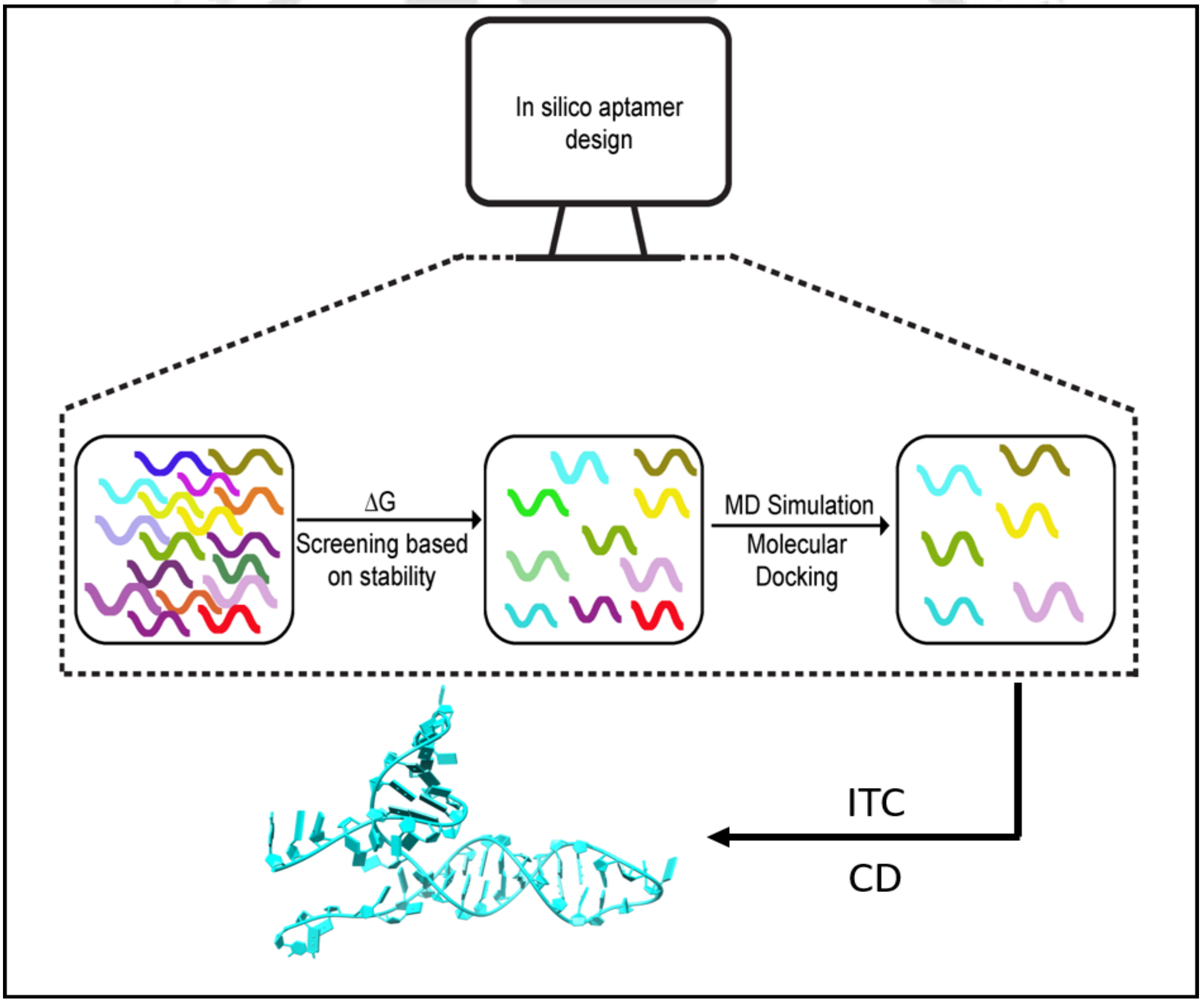

In-silico Designing of ssDNA aptamer against Stx2B

5.1. Overview

The identification of high-affinity and target-specific aptamers represents a crucial step in the development of aptamer-based biosensors. Aptamers are conventionally generated through an in vitro selection process known as Systematic Evolution of Ligands by Exponential Enrichment (SELEX), which consists of iterative cycles of target binding, partitioning of bound and unbound sequences, and enzymatic amplification. Although SELEX has been successfully employed for a broad spectrum of targets, including proteins and toxins, the methodology is intrinsically time-consuming, labor-intensive, and resource-intensive. Moreover, PCR-based amplification steps may introduce sequence-dependent biases, which can result in the preferential enrichment of certain sequences and the potential loss of rare yet high-affinity aptamer candidates.

Advances in computational biology and molecular modelling have led to the emergence of *in-silico* approaches as powerful complementary tools for aptamer selection and design. Computational strategies enable rational exploration of large nucleic acid sequence spaces, early elimination of structurally unfavourable candidates, and molecular-level insight into aptamer–target interactions. Instead of depending only on experimental SELEX procedure, *in-silico* approaches allow systematic screening of aptamer candidates based on their predicted structure, binding interactions, and stability. As a result, computational design has become an increasingly attractive strategy for speeding up aptamer discovery while reducing experimental effort.

A foundational contribution to this field was made by Chushak and Stone, who proposed one of the earliest structured frameworks for *in-silico* aptamer selection. The work established a conceptual foundation for de novo computational aptamer design and highlighted the value of integrating thermodynamic screening with docking-based interaction analysis (Chushak & Stone, 2009). At the core of most *in-silico* aptamer design workflows is the prediction of aptamer structure and stability. Aptamers derive their binding function from well-defined secondary and tertiary conformations, and their ability to adopt stable yet flexible structures is essential for effective molecular recognition (Brown et al., 2024). Computational tools based on nearest-neighbour thermodynamic models allow prediction of secondary structure and estimation of folding free energy, providing a quantitative basis for evaluating structural stability. Early-stage ΔG-based screening enables elimination of unstable or poorly folded sequences before proceeding to more computationally intensive analyses.

Following structural screening, molecular docking techniques are employed to predict the binding orientation, interaction interface, and non-covalent contacts between the folded aptamer and the target molecule. Docking provides insight into hydrogen bonding, electrostatic interactions, π–π stacking, and shape complementarity, which collectively govern aptamer–target recognition. For protein toxins, docking analysis is particularly informative, as it can identify favourable binding regions on biologically relevant domains, such as receptor-binding subunits. However, docking inherently provides a static representation of the interaction and does not fully account for molecular flexibility or solvent effects.

To address these limitations, molecular dynamics (MD) simulations are increasingly incorporated into computational aptamer design pipelines. MD simulations enable time-dependent evaluation of aptamer–target complexes under solvated, physiologically relevant conditions. By monitoring parameters such as root mean square deviation (RMSD), root mean square fluctuations (RMSF), number of hydrogen bonds formed and radius of gyration (R_g), MD simulations provide critical insight into the dynamic behaviour of aptamer–protein interactions. This dynamic assessment provides information about the stability, compactness of the aptamer-protein complex.

Although several computational studies have reported optimization of existing aptamers through truncation or point mutation, fully de novo computational design, starting from a random sequence library without prior experimental selection, remains relatively underexplored, particularly for protein toxins. Moreover, many reported computational studies stop at theoretical validation, with limited demonstration of experimental binding or integration into practical sensing platforms. Bridging this gap requires a holistic strategy that combines rational *in-silico* design with experimental validation and device-level implementation.

In this context, the present chapter describes a comprehensive *in-silico* framework for the de novo design of a DNA aptamer targeting the B subunit of Shiga toxin 2 (Stx2-B). The B subunit was selected as the molecular target due to its critical role in receptor binding and toxin internalization, making it a biologically relevant and accessible recognition site. The computational strategy employed in this work integrates virtual library generation, ΔG-based thermodynamic screening, molecular docking to evaluate aptamer–target interactions, and molecular dynamics simulations to assess binding stability under dynamic conditions. Following the computational screening the top-ranked aptamers were subjected to experimental validation using circular dichroism (CD) and isothermal titration calorimetry (ITC) to confirm binding behaviour and structural characteristics. Furthermore, the computationally designed aptamer was subsequently employed as the biorecognition element in an electrochemical impedance-based biosensor, demonstrating the translational relevance of the *in-silico* design strategy.

Overall, this chapter establishes rational workflow for *in-silico* de novo aptamer selection, and provides molecular level insight into aptamer–toxin recognition. By integrating thermodynamic screening, docking, and molecular dynamics simulations with experimental validation, the *in-silico* strategy presented here developed a highly specific aptamer against Shiga toxin 2.

5.2. Methodology

5.2.1. Construction of ssDNA library and structure prediction of ssDNA sequences

A randomized single-stranded DNA (ssDNA) library was generated using a custom Python script. Each sequence was 52 nucleotides in length and designed to contain an equal proportion of adenine (A), thymine (T), guanine (G), and cytosine (C). The thermodynamic stability of the generated sequences was evaluated using the Zipfold application available within the DINAMelt web server, which enables simultaneous prediction of minimum free energy (ΔG) values for large sequence sets (https://www.unafold.org/Dinamelt/applications/zipfold.php). Predictions were performed at a sodium ion concentration of 150 mM and a temperature of 25 °C.

Secondary structure prediction of the ssDNA sequences was carried out using the Mfold web server under the same ionic strength and temperature conditions applied for ΔG calculations (https://www.unafold.org/mfold/applications/dna-folding-form.php) (Zuker, 2003). Three-dimensional structures of the ssDNA candidates were subsequently generated using the 3dRNA/DNA web server, which requires the nucleotide sequence, corresponding secondary structure in dot-bracket notation, and specification of the molecule type as input parameters(http://biophy.hust.edu.cn/new/3dRNA/create) (Zhang et al., 2024). Structural modelling was conducted using the default pipeline of the server, with loop regions constructed using the bi-residue loop building approach. The resulting structures were energy-minimized using the ff14SB force field within a generalized Born (GB) implicit solvent model implemented by the server.

To obtain secondary structure representations in dot-bracket format compatible with downstream applications, the RNAComposer web server (https://rnacomposer.cs.put.poznan.pl/tools) (Sarzynska et al., 2023) was employed using the connectivity table (CT) files generated by Mfold. The crystallographic structure of Shiga toxin 2 (Stx2) was retrieved from the RCSB Protein Data Bank (PDB ID: 1R4P) (Fraser et al., 2004). Prior to docking studies, non-essential ligands and ions were removed from the protein structure using UCSF Chimera, followed by energy minimization using the YASARA energy minimization server to obtain a relaxed protein conformation (http://www.yasara.org/minimizationserver.htm) (Pettersen et al., 2004) (Krieger et al., 2009).

5.2.2. Molecular docking study

Molecular docking studies were conducted using the HDOCK web server, which supports both protein–protein and protein–nucleic acid docking (Yan et al., 2017). The energy-minimized three-dimensional structure of the target protein was used as the receptor, while the predicted three-dimensional structures of the ssDNA sequences were treated as ligands. Docking was performed using a template-free approach based on Fast Fourier Transform (FFT) algorithms to explore global binding conformations. Following docking, the resulting protein–aptamer complexes were subjected to interaction analysis using the Protein–Ligand Interaction Profiler (PLIP) web server (https://plip-tool.biotec.tu-dresden.de/plip-web/plip/index) (Adasme et al., 2021). The docked structures in PDB format were uploaded to the PLIP platform, which systematically identifies and categorizes non-covalent interactions between the protein and the aptamer. This analysis provided detailed insights into the nature of molecular interactions contributing to complex formation.

5.2.3. Molecular Dynamics Simulation study

Molecular dynamics (MD) simulations of the protein–aptamer complexes were performed using GROMACS version 2022 (Abraham et al., 2015). The AMBER99SB force field was used to model the protein, whereas the AMBER94 force field parameters were applied to the nucleic acid component. Each complex was positioned at the centre of a cubic simulation box with a minimum distance of 1 nm from the box edges and solvated using the TIP3P explicit water model. System neutrality was achieved by the addition of sodium counterions. Long-range electrostatic interactions were treated using the Particle Mesh Ewald (PME) approach, while short-range electrostatic and van der Waals interactions were calculated using the Verlet cut-off scheme with a cut-off distance of 15 Å. Prior to production runs, the system was energy-minimized using the steepest descent algorithm for 5000 steps to eliminate unfavourable contacts and relax the structure. Equilibration was carried out in two stages under position restraints. Initially, the system was equilibrated for 100 ps in the canonical (NVT) ensemble at 300 K using the modified Berendsen thermostat, followed by equilibration for 100 ps in the isothermal–isobaric (NPT) ensemble at 1 bar employing the Parrinello–Rahman barostat. After completion of the equilibration steps, positional restraints were removed, and the system was subjected to a production MD simulation for 100 ns, corresponding to 5×10^7 simulation steps.

5.2.4. Binding Free Energy calculation

The binding free energies of the aptamer–protein complexes obtained from molecular dynamics simulations were estimated using the Molecular Mechanics/Generalized Born Surface Area (MM/GBSA) approach implemented through the gmx_MMPBSA tool (Valdés-Tresanco et al., 2021). MM/GBSA is a widely used computational method for evaluating the binding energetics of protein–protein and protein–nucleic acid complexes, as well as for assessing complex stability, identifying key binding residues through energy decomposition analysis, and predicting interaction hotspots. The binding free energy (ΔG_{BIND}) of the complex was calculated according to the following relationship:

$$\Delta G_{\mathrm{BIND}} = (G_{\mathrm{COM}}) - (G_{\mathrm{REC}}) - (G_{\mathrm{LIG}}),$$

where G_{COM} corresponds to the total free energy of the aptamer–protein complex, G_{REC} represents the free energy of the receptor (Stx2B), and G_{LIG} denotes the free energy of the aptamer ligand. Each of these energy terms was computed as the sum of molecular mechanics energy contributions in the gas phase (ΔE_{MM}) and solvation free energy components (ΔG_{SOL}).

The ΔE_{MM} term accounts for interaction energies calculated under vacuum conditions and includes contributions from van der Waals and electrostatic interactions. The solvation free energy (ΔG_{SOL}) reflects the energetic changes associated with transferring the system from the gas phase into a solvent environment and comprises both polar and non-polar solvation components. To ensure statistical reliability, binding free energy calculations were performed using 500 representative snapshots extracted from the final 20 ns of the molecular dynamic trajectory.

5.2.5. Principle component analysis (PCA) and free energy landscape analysis (FEL)

Principal component analysis (PCA) and free energy landscape (FEL) analysis were performed to investigate the conformational dynamics and the stability of the protein-aptamer complexes during the MD simulation. The trajectories were fitted by least-squares minimization to remove overall rotational and translational motions. The covariance matrix was constructed using the Cα atoms of the protein along with the aptamer atoms, and the corresponding eigenvalues and eigenvectors were calculated using the *gmx covar* module implemented in GROMACS 2022. The principal components (PC1 and PC2) were extracted using *gmx anaeig*. The free energy landscape was subsequently constructed using the PC1 and PC2 projections, and the resulting PCA projections and FEL maps were processed and visualized using python scripts.

5.2.6. Circular dichroism spectroscopy study

To investigate the interaction between the computationally designed aptamers and the target protein, circular dichroism (CD) spectroscopy was performed using a Jasco J-815 CD spectrometer (Japan). CD spectra were recorded over a wavelength range of 200–320 nm after incubating the aptamer with increasing concentrations of Stx2B. Measurements were carried out at room temperature using a 2 mm path-length quartz cuvette, with a scan rate of 1 nm s^{-1}, and each spectrum was obtained as an average of three accumulations. Background spectra of the buffer were recorded under identical conditions and subtracted from the corresponding spectra of the aptamer–protein complexes.

Prior to binding studies, the aptamer (10 µM) was thermally denatured by heating at 95 °C for 10 min and subsequently allowed to refold by incubation at room temperature for 30 min in a thermocycler. The refolded aptamer solution was then incubated with Stx2B for 1 h at room temperature before CD measurements were performed. Changes in the CD spectral profiles were analyzed to assess conformational alterations associated with aptamer–protein interaction.

5.2.7. Isothermal Titration Calorimetry study

The binding affinity between the aptamer and Stx2B was quantified using isothermal titration calorimetry (ITC). Measurements were performed on an iTC200 microcalorimeter (GE Healthcare, UK) using a binding buffer composed of 50 mM phosphate buffer supplemented with 50 mM NaCl, 5 mM KCl, and 2.5 mM $MgCl_2$ at pH 7.4. Stx2B at a concentration of 20 µM was placed in the sample cell, while the aptamer solution (1.5 µM) was loaded into the syringe.

The titration protocol consisted of an initial injection of 0.4 µL, followed by 39 successive injections of 1 µL each into the reaction cell. All experiments were carried out at 25 °C with a constant stirring speed of 600 rpm, and a spacing of 120 s was maintained between consecutive injections to allow the system to reach equilibrium. The resulting heat changes associated with each injection were recorded and analyzed to determine the thermodynamic parameters governing aptamer–protein binding.

5.3. Results and discussions

5.3.1. Structure prediction of ssDNA and docking study.

A virtual single-stranded DNA (ssDNA) library consisting of 5,000 randomly generated sequences, each 52 nucleotides in length, was constructed for *in-silico* screening. The sequences were ranked based on their predicted ΔG values, and the 100 candidates exhibiting the most favorable (lowest) ΔG values were shortlisted for subsequent analysis (**Table 5.1**). Folding free energy is a widely accepted indicator of secondary-structure stability and therefore serves as a primary thermodynamic criterion for identifying structurally stable and potentially high-affinity aptamers from both computationally and experimentally generated libraries. This concept has been experimentally validated by Chushak and Stone (2009), who demonstrated that experimentally confirmed aptamers consistently possess significantly lower folding free energies compared to random sequences of identical length, thereby substantiating ΔG-based thermodynamic screening as a rational strategy for enriching structurally viable candidates. Importantly, validation against known aptamer–ligand complexes revealed that native aptamers ranked among the top-scoring sequences, while the proposed computational pipeline effectively reduced the search space by several orders of magnitude.

The secondary (**Figure 5.1)** and tertiary structures **(Figure 5.2**) of the selected sequences were then generated. Following the generation of the tertiary structures of the top 100 aptamer candidates, they were subjected to molecular docking to further refine selection based on target specificity and binding preference. Docking was performed against both Stx2 and Stx1, with Stx1 included as a structurally similar negative control to assess cross-reactivity. Importantly, aptamer selection was not based solely on favourable docking scores toward Stx2, instead, emphasis was placed on selective recognition of the B subunit of Stx2. Aptamers that exhibited binding to the Stx2 B subunit but showed equal or stronger docking affinity toward Stx1 were excluded, as such behaviour indicated poor target discrimination. Only those sequences that demonstrated preferential binding to the B subunit of Stx2, coupled with superior docking scores relative to Stx1, were retained for further analysis (**Figure 5.3**). Application of this dual-selection criterion, target specificity and comparative docking performance, resulted in the identification of six high-confidence aptamer candidates viz., A330, A673, A4209, A3351, A2814, and A4536. This stringent filtering strategy ensured that the shortlisted aptamers were not only energetically favourable binders but also exhibited selectivity toward Stx2, which is essential for reliable toxin-specific biosensing.

Sequence numbers	Sequence	ΔG values kcal/mol	Tm (°C)
A2919	GCGCTCAGAATGAGCGTGGAGCGGGTCCGACCCGCGAAGATGCTTATGCAGT	-16.466	77.3
A276	AGCTACTCTTCTACTATACCCAGTAGAAGAGTACATGGCGAACTGTCGCCGG	-16.189	77.9
A3049	TGATATCGGGCCGCGCACGAAGATCAGCCATCGTGCGCCCACACCCGATCTG	-14.768	80.7

A330	AGCACTAGGCGACTTGTCGCTTGAATGAGCAGCTATCTGCTCGTTCACCGGC	-15.262	76.9
A4327	CTAGGCTTCCGCCGGCTTCTTTGGGCGCGGAAGCGGCGTAGTAGGCCACGCC	-15.143	74
A1148	AAATTCTAAAAGCTTCTCGAGCTTGTGTGCCTGACGCTTTGGCGTAGGCACC	-14.183	72.2
A2823	CGTGTACAAGTTGATCGTTACGCCCCGTCAAGCGTCGGCGCGTACGCCGACG	-13.547	85
A4288	GACCAACGATCGCGCCGATGTCTGTGCACGGCGGAAGTCGGTCGCGGCGTTA	-11.857	74.3
A186	GGTACGTAGCCCCATACCCTGGCAATGGTATGGGCACCCACGGGCTACGATA	-12.004	74.9
A2882	CGCAACAATAGGCGCTACCGTTTGCGGAGGTTTACCCGCGTAAAGGTAGCGT	-12.676	74.2
A1257	ATAGCAGCCGAAAAGGTGTGCGTACTGTGCGCAGGAGGCTTCGGCTGGACCT	-11.755	75.2
A3698	GGACCGTGCGCCGACGACGTAAAGGGTGATTGGCGCACCCGTTATCGGCGTG	-11.988	74.9
A427	CAAACTGCAGCTGCAGCGCCACTACGTGCGCTGGGGCTTCCAGCTTTTCCTA	-11.783	78.8
A2511	AACCGTCGAAAATGGGATCCGTCCACGCGATCCCAGCTTCCCCAAAGGAAGC	-12.806	71.4
A4409	AAGTTGCACGTCAGGAGACGGGCTTGCAACTAGGACAATAGGTGTCATCACT	-12.264	72.5
A3351	AAGGCATCCAATGAACCTCGGCCAATCCGTAGTGGGCCGTTTTCGGCTCACA	-12.771	72.8
A446	TAGAGCATGGGGACCACCGACCGCCCTCGGCAATCGTCGAGGTGGAGGCGGA	-11.427	80.3
A556	ATGGGCGGTACGCCCATTGAGACAACTTATGTGTGCTACCAGCCTAAATGAT	-12.144	80.6
A1434	CATGCAGCCACTATCTTGGGGCTACGGTGCGCATGTTCGCAGGAGCATGCGA	-11.673	79.7
A3649	GCGCAGCCCAATGGTTTCACATTGGGCTAGGGTTCGCAGGTCTTCGCAAGAA	-11.947	79.8
A47	ACTTTCTGAAGTGTCCGGGTGCGCCGCAGGCGTATGCAGCCGAGCCTCTAGG	-11.841	68.8
A2737	GGGAGCCTGTGGCTGAACCCCTATGGGTCGCGGCACGCGTTTGCACCATACT	-11.821	82
A3808	TGGCTTCCGCTGGGGAGCCAATACCCGTTTCTACCACGAAGCTTGGTCGTGG	-11.722	78.6
A1853	CCGCAATGCACAGCAATGTGCCTATATTGTGGAAGCTTTCGAGCCCATCTCC	-11.294	72
A3516	GGGTTATCGTGGCGGCCTACCTCTATCGTCTGGTAGGACGCTTCGGCTCAGC	-10.96	82
A4899	CCTCCATTGGGGGCTCGGAAATTCCAGTCCGGGCCCCATCAGGCCGGCATAT	-11.182	92.1
A1264	GGTAAGGGGTGAGTGAGTCTCGTGCAGAGACTCGCGCACTTTAAACGAAGGT	-11.241	77.7
A4093	ATCATACCCCCTCCGATGACTGGGGGTTGCGGAACGCCGAGGGCAGACGCAC	-12.149	73.8
A4296	GATGACCGTCGTGTTCAGCACACGGAGGCGCACTTGTCAAGTTACAAGACGC	-11.901	64.2
A673	CCCGCCTCACGGGTGGGGCGTCAGTGAAAGGCTTAGGCCAGCCCGGCCCTAA	-11.221	81.1
A2034	GGGCTGTACGGCCCATGACTGCAAGATTGCACCCGCGTTATGCGAGACGGTA	-11.957	73.4
A2596	GCGGCACTGGCGAGAACGCCCGTTACAGTGCCCGGACCGCCTGTCAGGTGTG	-11.245	70.1
A3946	GAGGGCGTGGCGATTCCTCATCGCCACTTATCTAGGACACTAGCGCAGGAGC	-11.964	73
A411	CGCTTGCGCATGCAGACAAGCAGGCATAAGGTCGGGTGACGAACTAGTGCCT	-10.992	96.3
A1957	ACCAGCACATGTGCACTCACCCCACGGGAAAGCAAGACGGGGTGAGTTTTAG	-11.367	78

A2507	TACCTGACTCTTCAATGGAACTGCTATACGCGCAGCGTAATGCAGTCGAGTA	-10.71	90.2
A2675	GCGCCCTACGTGGGACTTGGCCACGTTGGGAAGCTAACGCATGACCTTTTGC	-11.492	73.7
A4750	TGCCGGCCTCGCTGGCCATCACGCGAGGGCCAATGGGCCATTGTCGTCTAGT	-10.648	74.1
A925	GTAGCGGCCCTGGTTACCATATATTAAAGTAGATTCCAGGGACGCAAGTACC	-10.915	86
A2637	GCCCGAGTTTCGTACTCGGGATACTAATATTGCGCGACCAGTGCCTCTGAGG	-11.276	77
A2455	GGATCCGTCAGATCCTTACACCGTACATGCGGATCTGACGAAATTCTTGAAC	-11.111	79.9
A3398	TCCTCGTCACATGGCAAACGCGCCTACTAATCTGGTGGTTTTGCCATGCTCC	-10.676	72.4
A4330	GCTTTCCGTATGCGCCGATACCGACCTGCGCAGACGGGATCATCGGGTTCTT	-10.791	85.8
A676	TCCCAAACCGCACCCCCTCAACTCGGGTGGCGCGTCTCGCTAGACCGCGCAT	-11.433	67.5
A1647	TAGGCGGCTCGCGATCAATTCGCGGACGCGCACGGTTATCGTCGGCACTCAT	-10.621	75.6
A2355	TAGGCGTTCCGCGACGCAGGGGCCGCGGGAGTCGACCGCAACTCACGAAGGC	-10.885	68.6
A2814	TACGCGGATGACCCCTTTAACGCCGGGTACAACCGGGAGAAGGACCCGGATC	-11.203	73.9
A109	ACTGCTGCCTAGCAGGGAATACTTGGACCTTTCCGGCGCGCAATCGCGTTTA	-11.652	66.5
A510	CCACGAGCGAATTCGGCGCACTGGCGCCATCGACTCGGCGCGCTTCTGAACT	-10.866	67.6
A1717	AGCGTCTCTCAGGGAGACGGCGTGAGAGCATACTGCGATGTAGTGCAGAGAC	-11.217	73.1
A2686	TGATCTTTGACGCGCTACGGTCGAGCGTTGCGCGCCCCTAAGCTGCTTATTT	-10.933	84
A375	CTACCAGGATTAATGCGCTCCCGAAGCTCGGAGGCGTGAAAACGCAAGCGAT	-11.385	69.4
A3121	GCGAACGAGGTGAGCCTCGAACGCGACCTCGGCCCGGGGGTCACTGCCAATT	-10.578	71.5
A3831	CCATTCGGGGGTGTGACCCGAATGGGAAATTATATGAATCTTGATAATGGGA	-10.845	69.4
A4368	TACAGTTCAAAACGGGCCCATCGCCCGAGCAGCATGGGGCGACATGTGGACG	-10.046	74.4
A4949	ATTCGAGCTTTTACTGCTTCCACAGCAGTTGAGAAATAGCGCGCTTGCGACT	-9.704	78.7
A4974	CTTAGGAAGTACGCCGAATCTGGCCTAAATTTGTGGCACAGGGTCGGCTATA	-9.18	71.3
A1020	AACAAGCGTTCGGAAACTCCGGGGCAGCACGCATCACTTGCCTAACGGCGAG	-8.865	68.7
A1333	AATATTGCTAACGTTCAGCTCTCGATGAGCAGCGTGTGGAACACGGCCCGAA	-9.977	73.7
A1816	AAGGCGTGTCTCGGCAAAATTTGCCGAATACGTGTGCTTCTCGGATCCGGCC	-10.213	64.8
A2318	TTTGTACATGTTGATAAACATCGTTGGGCGAACATGTGTTTAGCCCTGACTG	-9.41	70.4
A2446	CCCGCAAGTTCGCCTCTGCCATAGAGGGGTACCGCCGGTACGCGGCTAGCTG	-9.982	72.7
A2982	AGCGCACGTATCACCGCGCGGCTGGAAGGGCTGCGTCGCATAGCGCCCCAGT	-8.817	66.7
A3033	GGGGTGTAGAACGCCCCGGGCATACGGTTTCTGTGTATCTTAGAATCCCGTT	-9.187	66.2
A3511	TAGCGCACGGCAGGCGCCAGGCGTCCCATCTCACACCCCTAGCGGTGTAGAT	-9.326	70.8
A4826	TGCAGTGCCGTGCTGGAGACGCACTAACAAGCACTAGGGTGCTTACCCAACA	-9.382	75.9
A224	CCATCGCCGCATCCCGTAAGCGGGGTTTAAGAACCGCTTTCGCTCAGTGCGC	-10.161	66.8

A325	GCTGCGTGTGTTGTTCGTAGACACCCCCTTGGGGTAATCAGCGGAGCTTGGC	-8.903	75.3
A553	TGCGCAGCGCTTGCCAGTGCACTCCACTTTTCCAGCGCTAGCCACGCGACTG	-8.303	66.5
A2123	CAGAAAACGTCCGCGTTTCCGACCGGACACGGTGGGGACATTGTTGTGAACG	-9.466	67.3
A2914	GGAGCAAGTCGGGGTCGATTGCTGCCTACAAGGGCGACGCGCCAAAGTCCCT	-9.737	66.2
A2929	CACAGGTTGCAACTTCTGTAGTGCCTATAAATAGGCGGGCGGCTGTTGCCTT	-9.948	67.1
A3690	AAACGGACGGCGGACGGTTTCACCCGAGTGCCGCACTGTCGCCTCAGGAGAC	-9.084	67.7
A3723	ATTCGCGTCGAATTTACGGCCCCACTAACGGGGCAGACACCGCTTAGGCAAT	-9.965	67
A4209	GGGACACTCTTGTAAGCCCTCGCGGTCGGGGGGGTGCCACCCTCGCGGTGT	-9.084	69.7
A4319	AAGGACACGCATACGCCTGTGTGCGCGTCATTACAGGTTGCACCTCGAACTA	-8.625	73.7
A4536	CCGGGGCCTCGAAGCAATAGGCCGGGAGGTCTTTCCAGGCCTAATTAACCGG	-9.505	72.5
A4958	GGCGTTGCCATTTCGGCGAGGCGCCTTAGAGGGGAACGGCGCATCACCTTCT	-9.582	74.8
A4962	GACCCTGGGAATTAGGGCTCCCAGATACGGCAAGCGTCATGGCGGCACTAAC	-9.764	69.3
A76	AAGTGGCGACTCTGTCAGAAAAATAAGGCAACGGTGTTGCCACTTCTAATCA	-8.602	73.3
A1496	CCGGGACTCCTCTGTGGTGTAGAGACACGAGCGCGTTCCGGCGTGGGCCGAA	-9.258	71.6
A2828	CAGACGAGTGTCACAGGCATCTTTGCCCTATCTGTCCGTCAACAGAGACAGA	-9.933	64
A2906	CGTCCACGGTACAGAAAGTGTAGAAAGTCCGTGGGGCGTGCTGGACGGGTCA	-9.119	65.1
A4279	GGCGCTCAGCCATTCGCTGAACGCCGCCTCCCAACACTCCACTAGGTAATCA	-9.209	72.2
A4405	ACTTAAACAAAGGGGTTTTCTACATCAGTGTCGGAACGACACCCGGCTCCGT	-10.149	65
A4595	GACGCTATGACCCAGTGCGTGGGCAACTGGTTCCGTAGCGACCGGCCGCAGT	-9.691	63.3
A499	TAGCGGACCCGCAGTTCTCTACTGTCCGCTAAACCGTACTCATCCGTACCTG	-9.233	63.8
A527	TCCGAAAGAGGTTGTACTGGGCTCAATACATAATGTCGTCTGTCGACATTAC	-9.038	72.5
A543	TCTGTAGAAGTTATACAGATACCGCGATTCCGGCACTCTGGCGTCGCAACCT	-9.237	64.1
A748	CACTACGGCATATGCCACGGCACCTCGTGGCCGATAGGGAGGTCTACGGCCT	-9.706	74.9
A750	GTCTCGAGGCCGCGCTACTTCTCCATGTGCGGCTGCGTTGTTGGCGGCTTTC	-9.222	78
A1277	GATGGCACTCCAAGGGCAAGCACTTAGAGGCTCGGAACGAGCGTTTAGGATC	-8.453	70
A1304	CTATTACTGTAGCAAGGTCTAGACGTCGCCGTCAACGGATTGGTTGACGGTC	-9.413	78.9
A2100	CGCCTCCTACCCCCTGGGAAGTCAGGGAACAGGAGGTAGAGAAAGAATACAC	-8.937	72.1
A2552	CAGATGGGGTTGCGTACAAGAGGAACGCGCTAACGCGTACCTTGGTAAAGAT	-8.657	98.5
A3045	GCTCACACTGCACCTATGCGGCGACTCAGCTTCCCAATGCTGATTCGTAGCA	-8.781	73
A3069	TTCCGAACCAACTCGTGGTTGCACCGGCTATCACCCCAGGCCGCAGCAACGT	-9.699	6.5
A3106	TGATGAGCGGGCATGCGTTGGACTACGCCTGAGCCCGAGGCCTTCTTTTCTT	-8.949	74.3
A3246	AGGTCCACGATTAGATAGCAACACGACTTGTCGTGATCGTCGAGCGGGCCAC	-8.417	66.9

A3257	CCTAGCTACTGCCTGACGTCGTTAGCGGCGGAACAGTAGCGGCTCGCAATTC	-8.378	71.2

Table 5.1 - 100 ssDNA sequences with the least ΔG values.

The binding modes and interaction profiles of these aptamers with Stx2B were examined in detail (**Table 5.2**). Docking analysis indicated that aptamer–Stx2B recognition is governed by a combination of electrostatic and hydrophobic interactions, complemented by hydrogen bonding and salt bridge formation, collectively contributing to complex stabilization.

The repeated involvement of specific amino acid residues across multiple aptamer–protein complexes indicates that these residues play a key role in mediating aptamer binding to Stx2B. Notably, residues TRP29D, TRP29E, TRP29F, TRP33C, TRP33D, TRP33E, and TRP33F were consistently engaged in π–π stacking and hydrophobic interactions. In addition, ARG32C, ARG32D, ARG32E, and ARG32F frequently participated in salt bridge formation and hydrogen bonding. Several lysine residues also contributed persistently to aptamer recognition, with LYS12B, LYS12F, LYS52C, LYS52D, LYS52F, and LYS297A forming multiple salt bridges with different aptamer candidates. The recurrent participation of these amino acids suggests the presence of a conserved interaction hotspot on Stx2B that is critical for aptamer binding. To further validate these interactions and assess the dynamic stability of the aptamer–protein complexes, MD simulations were subsequently carried out, as described in the following section.

5.3.2. Molecular Dynamics (MD) Simulation study on aptamer-protein interactions.

MD simulations provided detailed insight into the dynamic stability and binding behaviour of the aptamer–Stx2B complexes. Analysis of RMSD, RMSF, radius of gyration (R_g), and intermolecular hydrogen bonding collectively revealed clear differences in the structural integrity and interaction strength of the six candidate aptamers. Among these, the A330–Stx2B complex consistently exhibited the most stable behaviour throughout the 100 ns simulation, indicating a robust and persistent binding mode.

RMSD analysis demonstrated that the A330–Stx2B complex underwent minimal structural deviation after equilibration, suggesting that the docked binding conformation was dynamically stable and maintained over time (**Figure 5.4**). In contrast, complexes such as A4209–Stx2B showed larger RMSD fluctuations, reflecting ongoing conformational rearrangements that are typically associated with weaker or less favourable binding interactions. The comparatively low RMSD and narrow distribution observed for A330–Stx2B indicate that this aptamer forms a wellaccommodated binding interface with Stx2B, resisting large-scale structural perturbations during simulation.

RMSF analysis further highlighted differences in flexibility among the aptamer candidates. While the protein backbone remained largely rigid across all complexes (atoms 0-9700), variations in aptamer flexibility were evident and sequence dependent (atoms 9700-11400). A330 displayed the lowest overall fluctuation among the aptamers with a highest peak of 1.18 nm. In contrast, higher RMSF values observed for other sequences indicating increased flexibility, which may reduce binding persistence and compromise interaction specificity (**Figure 5.5**). Reduced flexibility at the binding interface is often indicative of stronger and more specific molecular recognition, supporting the selection of A330 as the most favourable candidate.

The radius of gyration analysis provided additional evidence for the superior stability of the A330–Stx2B complex. A consistently lower and stable Rg value indicates that the complex remains compact throughout the simulation, reflecting efficient packing of the aptamer against the protein surface **(Figure 5.6**). In contrast, complexes such as A3351–Stx2B exhibited an increase in Rg over time, suggesting partial unfolding or reorientation of the aptamer relative to the protein. Such structural expansion is commonly associated with suboptimal binding and reduced interaction stability. The compact nature of the A330–Stx2B complex is therefore consistent with a tightly bound and energetically favourable interaction.

Intermolecular hydrogen bond analysis further reinforced the preferential binding of A330 to Stx2B. Hydrogen bonds play a critical role in stabilizing nucleic acid–protein complexes, and a higher number of persistent hydrogen bonds generally correlates with stronger binding affinity. The progressive increase in hydrogen bond formation observed for A330 over the course of the simulation suggests gradual optimization of the binding interface, leading to enhanced complex stability (**Figure 5.7**). In contrast, other aptamer candidates formed fewer and less persistent hydrogen bonds, indicating weaker or more transient interactions with the target protein.

The Molecular Mechanics/Generalized Born Surface Area (MM/GBSA) binding free energy calculations provided quantitative support for the qualitative trends observed in the MD simulation analyses. The substantially more favourable binding free energy predicted for A330–Stx2B compared to other complexes reflects the cumulative contributions of stable electrostatic interactions, van der Waals contacts, and solvation effects. The agreement between RMSD, RMSF, Rg, hydrogen bond analysis, and binding free energy calculations strengthens the confidence in A330 as the most suitable aptamer for Stx2B recognition (**Table 5.3)**.

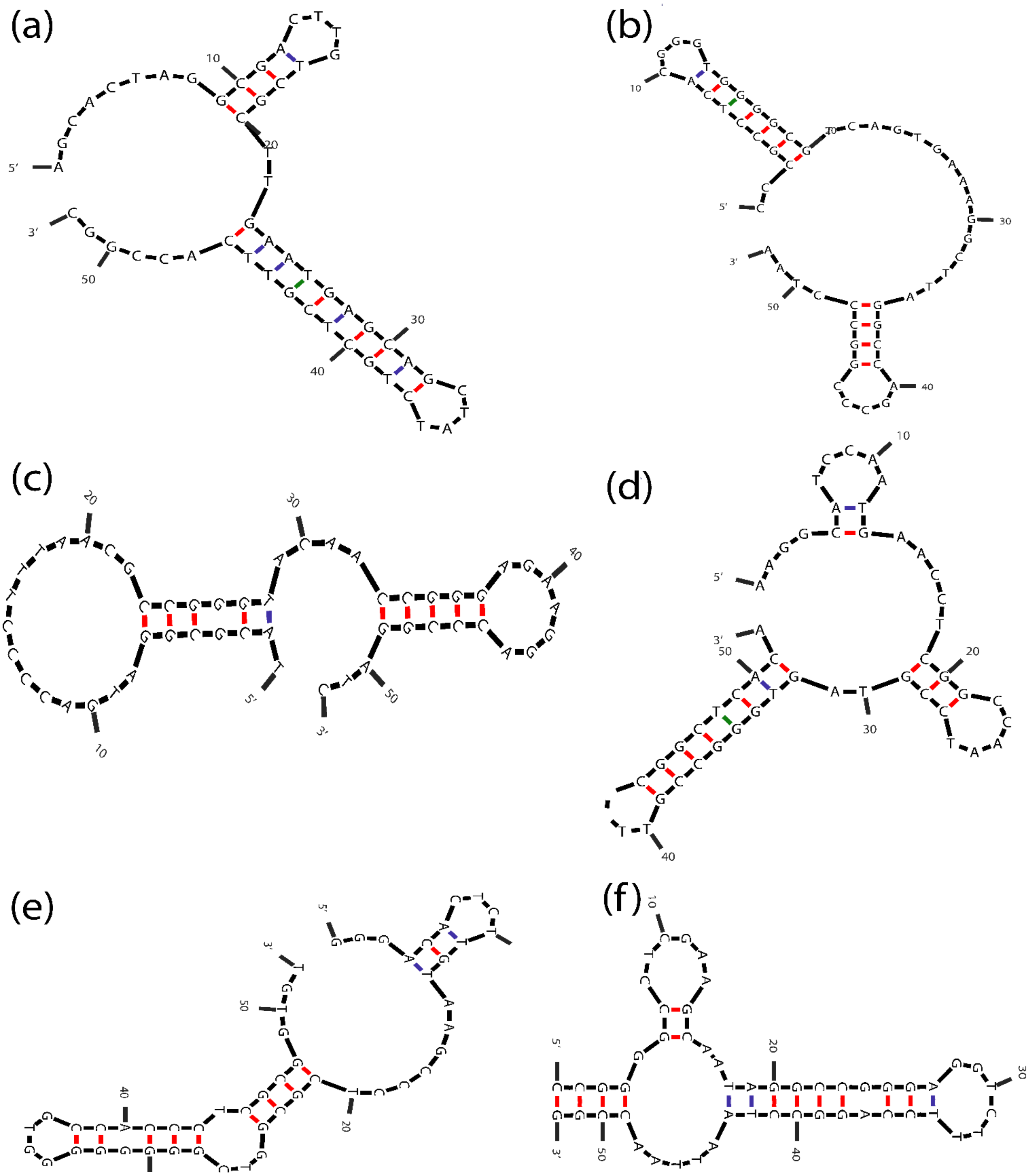

Figure 5.1: Representation of secondary structures of ssDNA sequences (a) A330, (b) A673, (c) A2814, (d) A3351, (e) A4209, and (f) A4536.

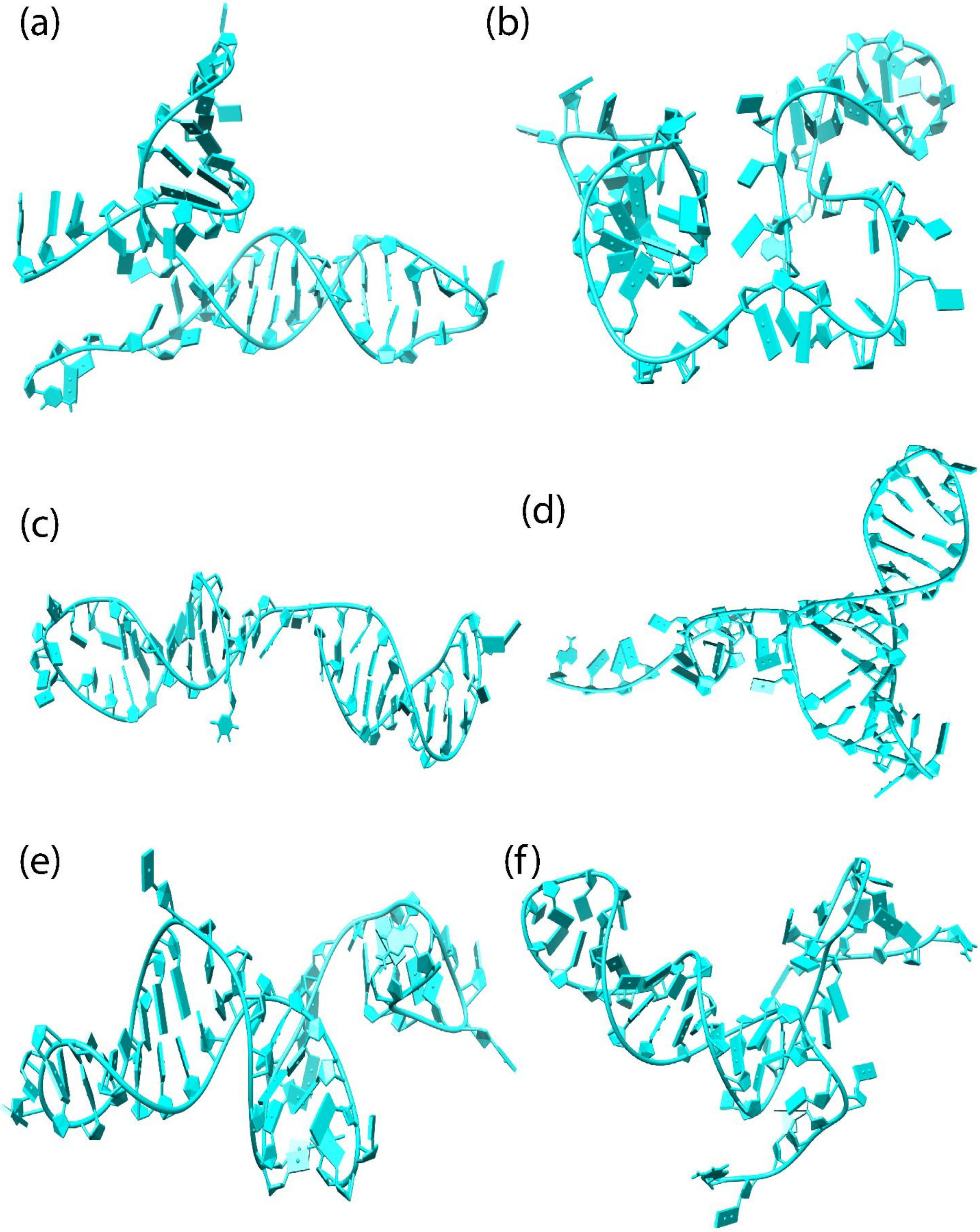

Figure 5.2: Representation of tertiary structure of ssDNA sequences (a) A330, (b) A673, (c) A2814, (d) A3351, (e) A4209, (f) A4536.

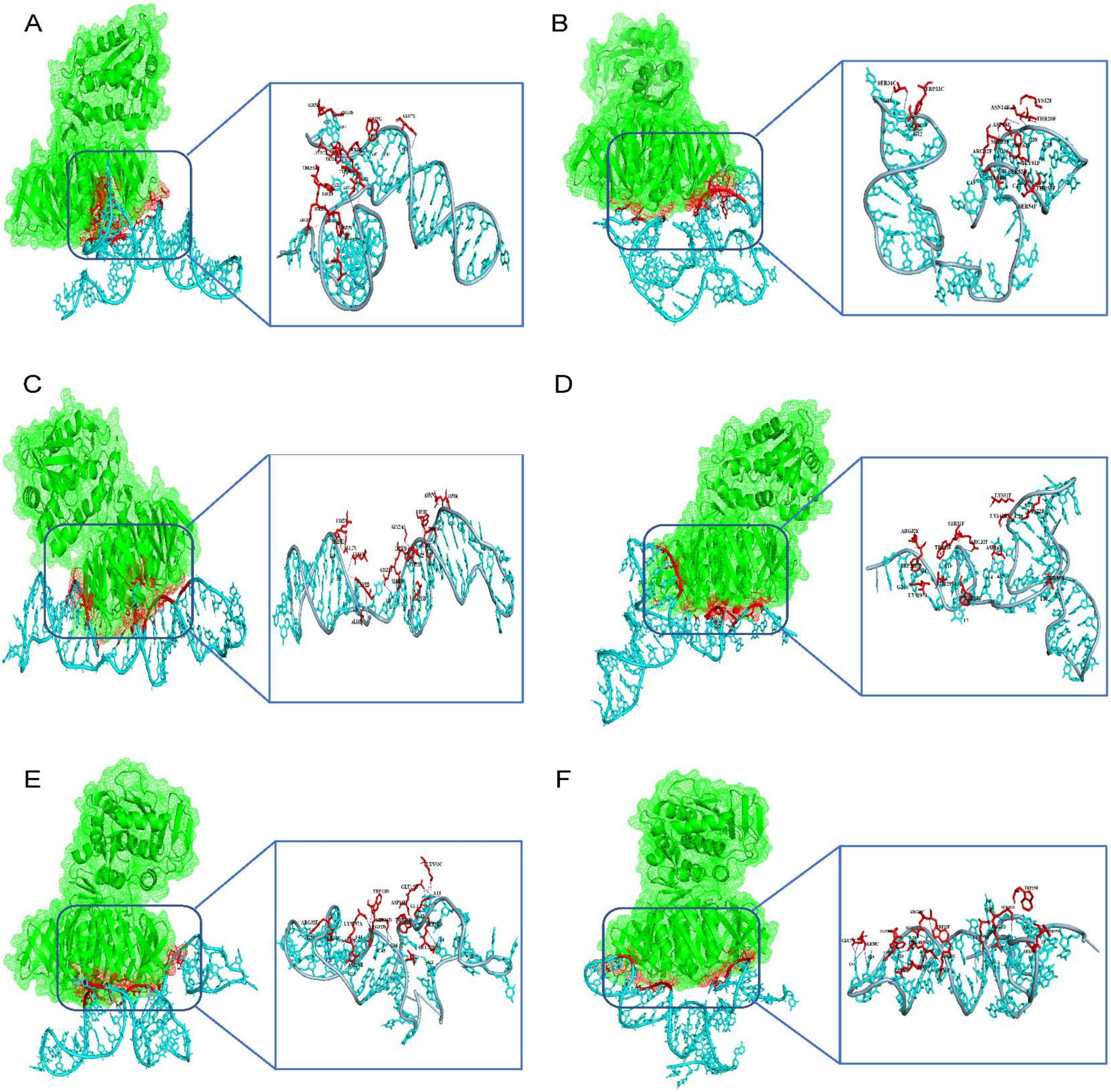

Figure 5.3 - Docked structures of the aptamer candidate with Stx2. (A) A330-Stx2 (B) A673-Stx2 (C) A2814-Stx2 (D) A3351-Stx2 (E) A4209-Stx2 (F) A4536-Stx2. Stx2 is marked in green and the aptamer is marked in cyan. The red patches indicate the aptamer protein interacting residues. The inset displays the magnified view of the interacting residues.

Aptamer candidates	H-bonds: Hydrophobic bond: π-Cation: π-Stackings: Salt Bridges	Interacting regions Nucleotide cluster: amino acid cluster
A330	11:5:0:2:6	**T15-G16**: GLU57F, GLY59F **C20-T22-G23**: ARG32E, TRP33E/F, THR295A. **T45-C46-A47-G50-G51**: TRP29E, SER31E/D, LYS297A, ARG32D (**Fig. 3A)**
A673	15:1:1:0:5	**G11-G12**: SER31C, TRP33C, ASP17C **G36-C38-C39:** ASP16F, LYS12F, ASN14F, THR20F **C47-C48-C49**: SER53F, SER54F, THR55F, GLY61F, PHE62F, ARG32F (**Fig. 3B**)
A2814	16: 1:0:0:4	**T9-G10**: ASP16C. ASP17C. **C24-G25-A29**: TRP33D, TYR13D, TRP33C, SER31C, ARG32D, SER31D, and ARG32D. **G49-A50-T51**: GLU27E, LYS22E, GLN66D, LYS52D, ALA1D. (**Fig. 3C)**
A3351	8:1:0:2:5	**G4-T7-A10**: ARG32F, TRP33C, TRP33E, TRP33F. **C27-C28**: LYS12B, LYS22B, LYS52F. (**Fig. 3D**)
A4209	17:2:2:0:5	**A14-A15**: GLU15D, LYS52C, ASP16D, TRP29D. **G25-T26-G28-G29**: ASP16E, ASP17E, SER31E, ARG32E. **C45-G46:** ARG32D, TRP33D, LYS297A, SER31D. (**Fig. 3E**)
A4536	20:1:0:0:3	**C7-C8-T9:** SER31D, ARG32D, TRP29D. **G24-G25-G26:** ASP17F, SER31F, TRP33F, ARG32F. **G29-T30-T33:** GLU57F, SER58F, ASP16F, THR18F, LYS12F. (**Fig. 3F**)

Table 5.2: - Interactions profile of aptamers with Stx2-B proteins.

PCA of the MD trajectories revealed distinct conformational distributions for each aptamer-protein complex. The projections along PC1 and PC2 showed that the A330-Stx2B complex occupies a relatively compact and confined region, indicating restricted conformational motion and enhanced structural stability (**Figure 5.8**). In contrast A4209-Stx2B and A4536-Stx2B exhibited a broader and more dispersed distribution indicating flexibility and sampling of multiple conformational states. The complexes A673-Stx2B, A2814-Stx2B, and A3351-Stx2B displayed intermediate behaviour with moderate spreading of conformational space.

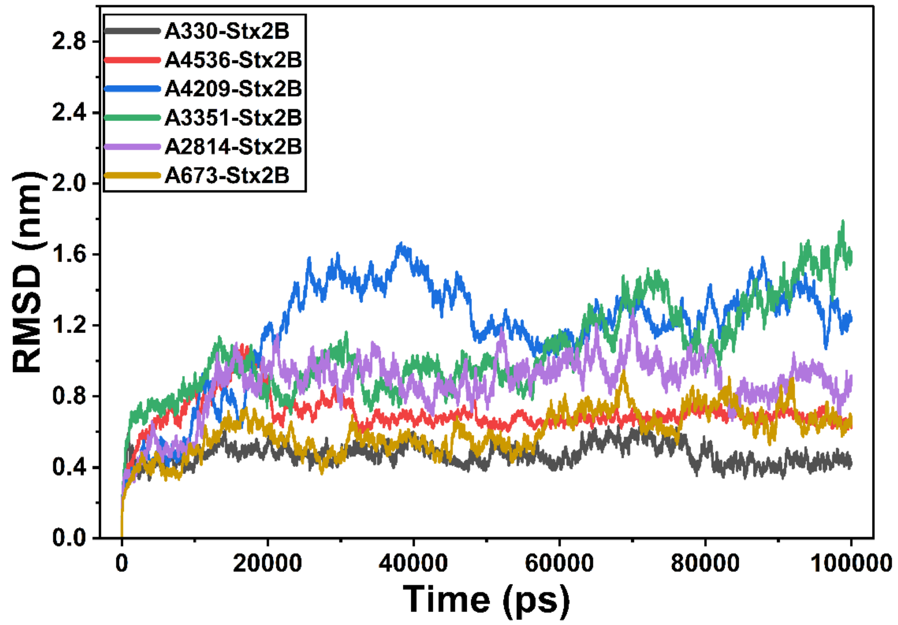

Figure 5.4: RMSD plots of aptamer–Stx2B complexes over the course of 100 ns MD simulations.

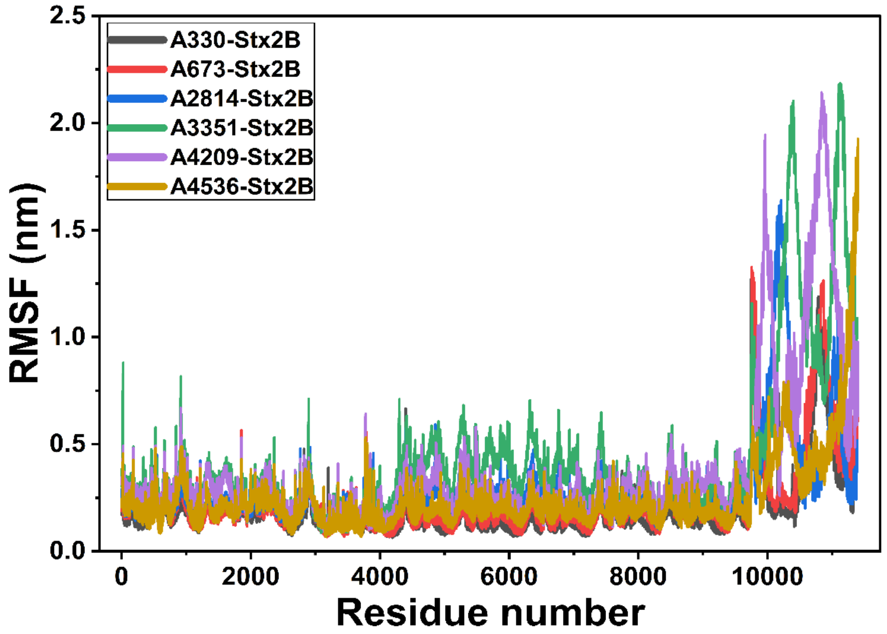

Figure 5.5: RMSF plots of aptamer-Stx2B complexes over the course of 100 ns MD simulations.

The FEL analysis further supports these observations. The A330-Stx2B complex exhibits a well-defined and continuous low-energy basin, indicating a stable and energetically favourable conformational state. In contrast, A4536-Stx2B and A4209-Stx2B displayed fragmented energy landscape with multiple shallow minima, reflecting conformational heterogeneity and reduced stability (**Figure 5.9**). These observations are consistent with the RMSD, RMSF, radius of gyration, hydrogen bond, and MM/GBSA analyses, further confirming that A330 exhibits superior structural stability, reduced flexibility at the binding interface, enhanced intermolecular interactions, and the strongest predicted binding affinity toward Stx2B. These findings provided a strong rationale for selecting A330 for subsequent experimental validation and biosensor development, bridging computational predictions with practical application.

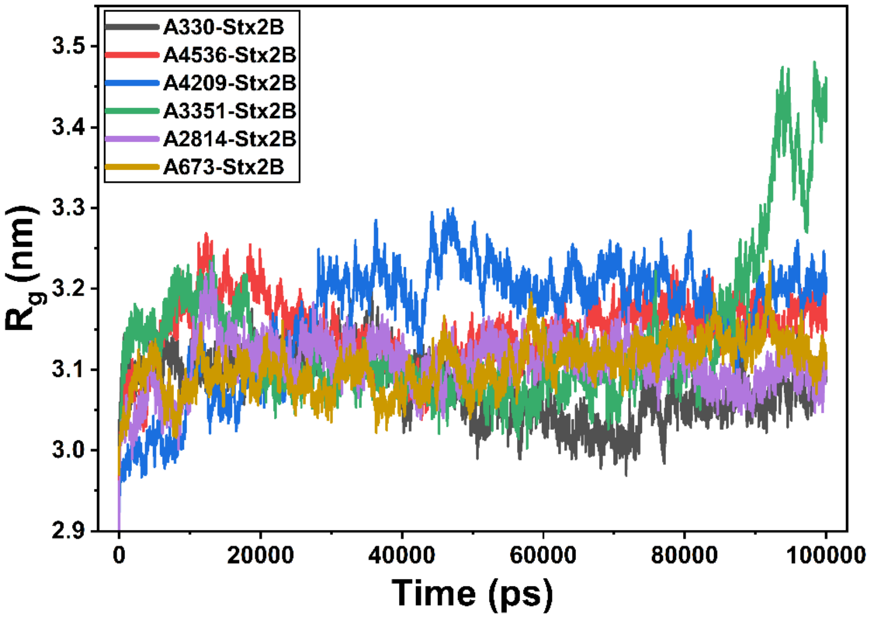

Figure 5.6: Radius of gyration plots of aptamer–Stx2B complexes over the course of 100 ns MD simulations

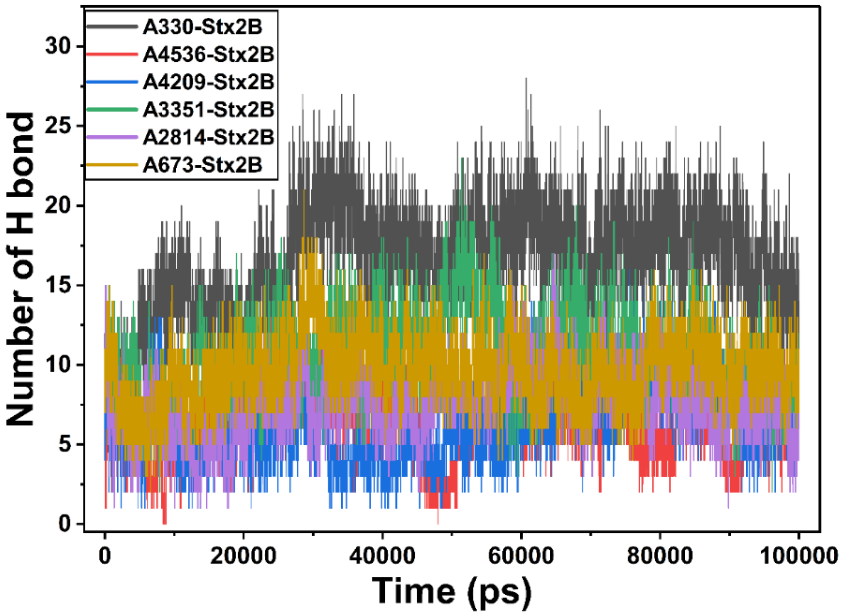

Figure 5.7: Hydrogen bond plot of aptamer–Stx2B complexes over the course of 100 ns MD simulations.

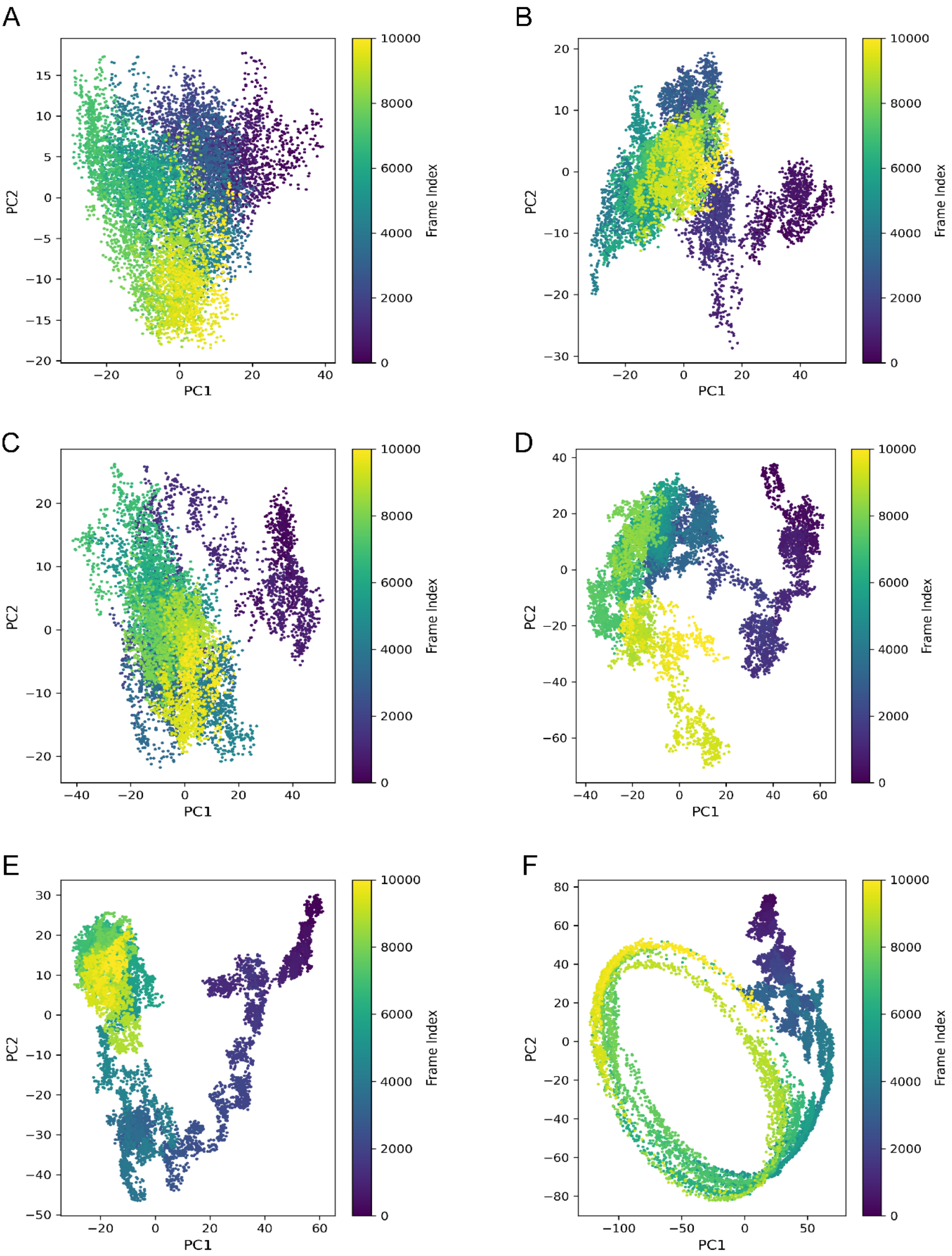

Figure 5.8: Principal component analysis (PCA) plots of the MD trajectories of (A) A330-Stx2 (B) A673-Stx2 (C) A2814-Stx2 (D) A3351-Stx2 (E) A4209-Stx2 (F) A4536-Stx2.

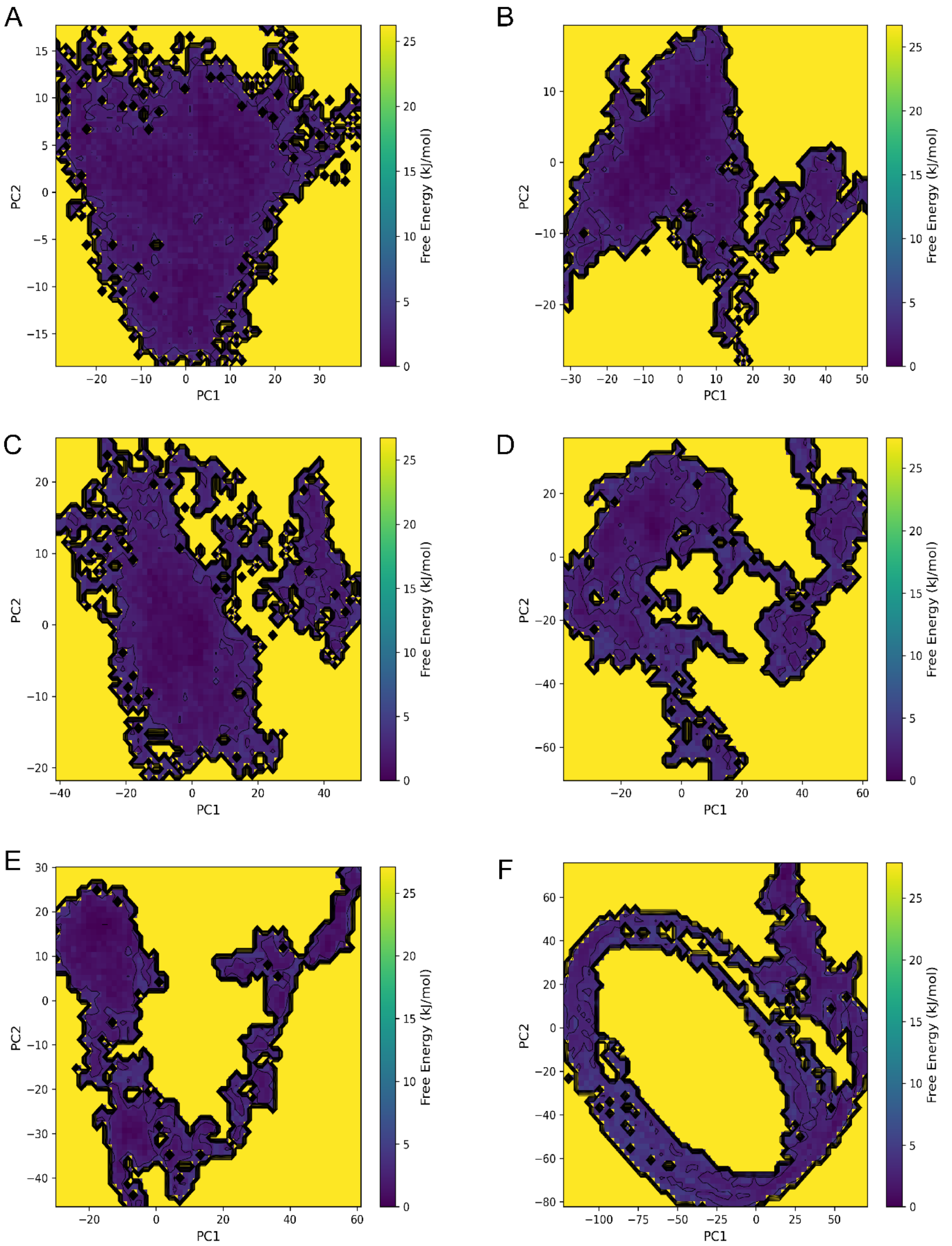

Figure 5.9: Free energy landscape (FEL) of (A) A330-Stx2 (B) A673-Stx2 (C) A2814-Stx2 (D) A3351-Stx2 (E) A4209-Stx2 (F) A4536-Stx2.

Aptamer Protein complex	Average RMSD value	Average R_g value	Average H-bond number	Binding free energy (kcal/mol)
A330-Stx2B	0.47	3.07	16.4	-97.01 ± 0.45
A673-Stx2B	0.62	3.10	9.6	-70.47 ± 0.41
A4209-Stx2B	1.25	3.16	6.3	-35.71 ± 0.35
A3351-Stx2B	1.09	3.13	10.4	-28.72 ± 0.40
A2814-Stx2B	0.91	3.10	7.4	-22.95 ±0.31
A4536-Stx2B	0.71	3.14	6.1	-20.93 ± 0.44

Table 5.3- Average structural and energetic parameters obtained from MD simulation of aptamer protein complex.

5.3.3. Experimental Validation of Computationally Designed Aptamers

5.3.3.1. Circular Dichroism (CD) study analysis

The CD spectroscopy was used as an initial experimental approach to evaluate the interaction between Stx2B and the top three *in-silico* designed aptamer candidates viz., A330, A673, and A4209, selected based on docking and molecular dynamics analyses. Among these candidates, aptamers A673 and A4209 exhibited no significant alteration in their secondary structure upon addition of Stx2B (**Figure 5.11** and **Figure 5.12**). In contrast, the interaction between A330 and Stx2B resulted in a pronounced change in ellipticity in the CD spectra (**Figure 5.10**).

The CD spectrum of A330 displayed characteristic features of B-form DNA, with a positive band near 280 nm and a negative band around 250 nm (Kypr et al., 2009). Upon incubation with increasing concentrations of Stx2B, a marked enhancement in the intensity of these spectral

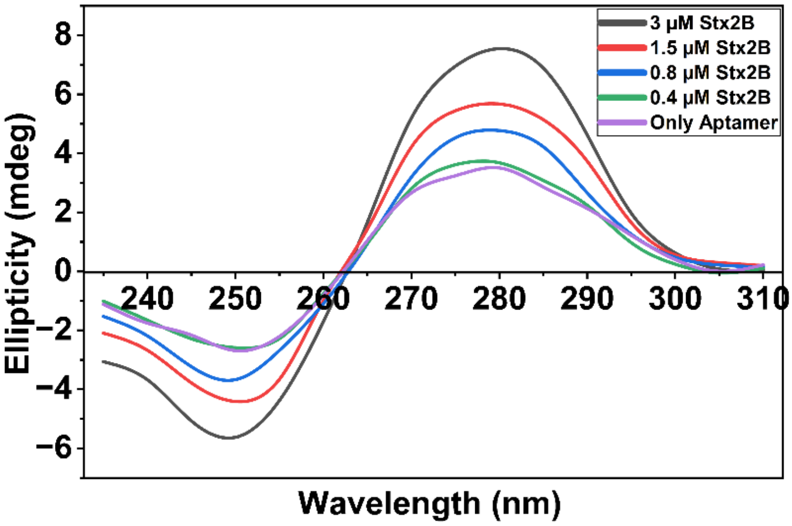

Figure 5.10: - CD analysis of Stx2-A330 interaction.

features were observed, indicating a binding-induced conformational response. These observations provide experimental evidence of a specific interaction between A330 and Stx2B, supporting its selection as the most promising aptamer candidate for further biophysical and sensor-based validation. While CD spectroscopy provided qualitative evidence of binding-induced conformational changes, ITC was employed to quantitatively determine the binding affinity and thermodynamic profile of the A330–Stx2B interaction.

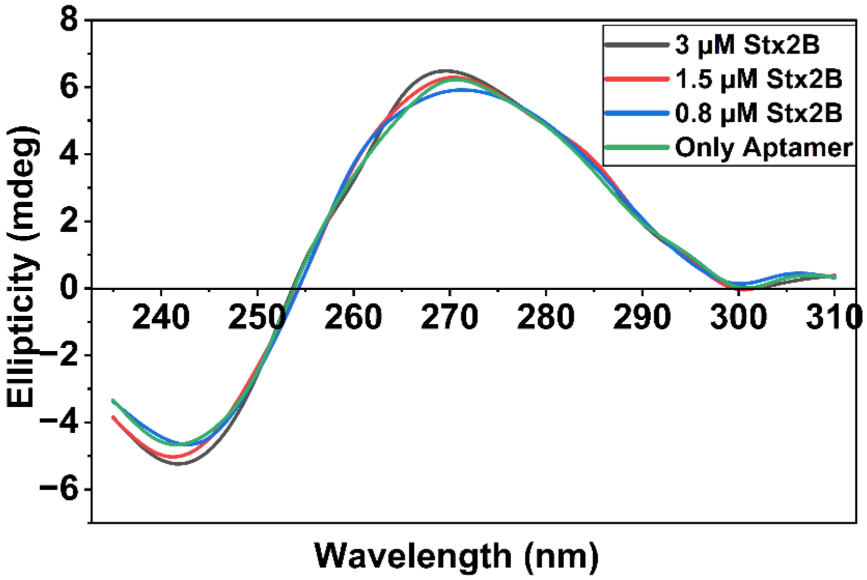

Figure 5.11: - CD analysis of Stx2-A673 interaction.

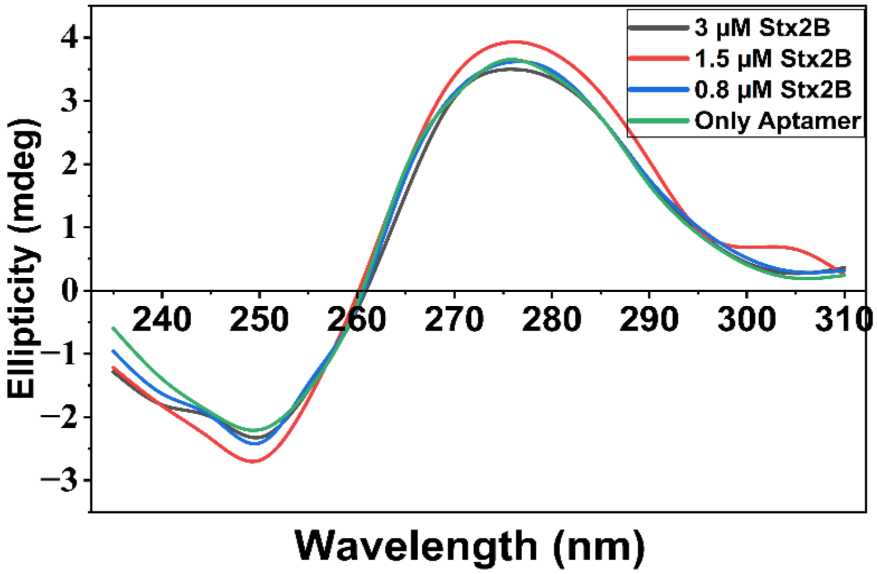

Figure 5.12: - CD analysis of Stx2-A4209 interaction.

5.3.3.2. Isothermal Titration Calorimetry (ITC) study

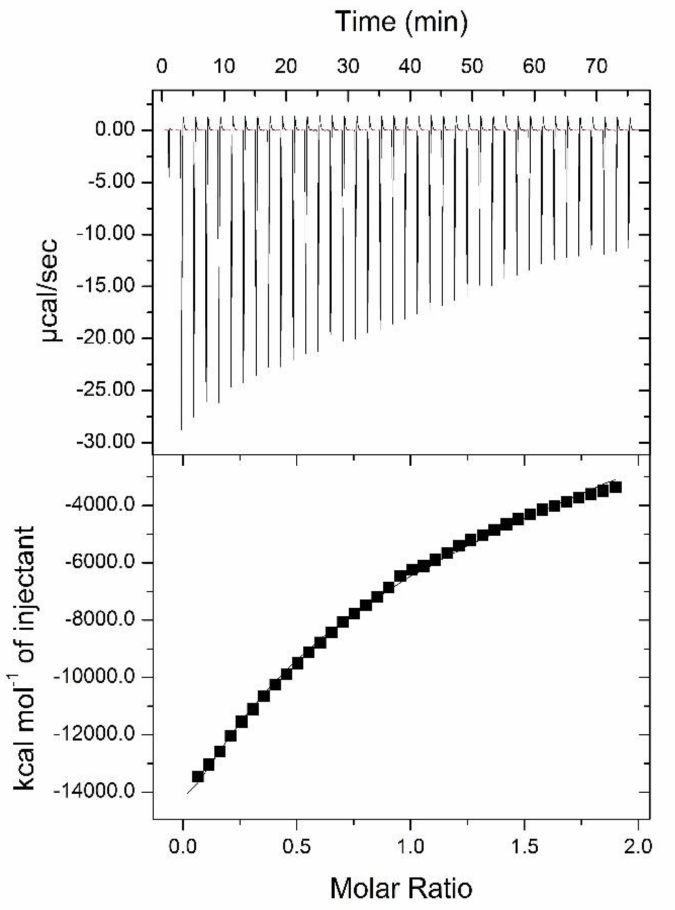

Figure 5.13- ITC thermogram of A330-Stx2B.

ITC, widely regarded as a benchmark technique for obtaining complete thermodynamic profiles of receptor–ligand interactions, was employed to determine the binding affinity between aptamer A330 and Stx2B. The measurements were conducted in solution under label-free conditions. ITC analysis indicated an exothermic binding interaction, yielding a dissociation constant (K_d) of 459 ± 7 nM (**Figure 5.13**). Taken together with the computational and CD spectroscopy results, these findings led to the selection of aptamer A330 for subsequent fabrication of an aptamer-based sensor using an interdigitated microelectrode platform for Stx2B detection as discussed in the next chapter.

To further validate the rationale behind the ΔG-based pre-screening strategy, a small subset of ssDNA sequences exhibiting comparatively high predicted ΔG value was also subjected to molecular docking and molecular dynamics simulations. Three representative sequences Seq3570 (ΔG = −0.229 kcal/mol), Seq3987 (ΔG = −0.797 kcal/mol), and Seq4286 (ΔG = −1.364 kcal/mol), were selected from the initial pool of 5000 sequences and analyzed using the same computational workflow applied to the low ΔG candidates.

Although these high-ΔG value sequences exhibited docking scores comparable to several low-ΔG aptamers, their dynamic behaviour during MD simulations revealed pronounced instability. The corresponding aptamer–protein complexes displayed substantially higher RMSD values of 2.85 nm, 1.61 nm, and 1.22 nm for Seq3570-Stx2, Seq3987-Stx2, and Seq4268-Stx2, respectively, indicating significant structural deviation over the simulation period (**Figure 5.14**). Consistent with this observation, RMSF analysis revealed elevated residue-level fluctuations of 4.30 nm, 3.11 nm, and 3.11 nm, for Seq3570-Stx2, Seq3987-Stx2, and Seq4268-Stx2 respectively, suggesting increased conformational flexibility of the aptamer scaffolds (**Figure 5.15**).

Seq3570 formed a negligible average number of hydrogen bonds (0.23), while Seq3987 and Seq4286 formed hydrogen bonds (15.60 and 15.01, respectively) comparable to those observed with the low-ΔG aptamer candidates **(Figure 5.16**). Collectively, these results indicate that although docking scores alone may suggest favourable binding, thermodynamically unstable sequences fail to maintain persistent interactions under dynamic conditions. This comparative analysis highlights the importance of ΔG-based thermodynamic filtering combined with MD-based stability assessment for identifying robust and biologically relevant aptamer–protein interactions.

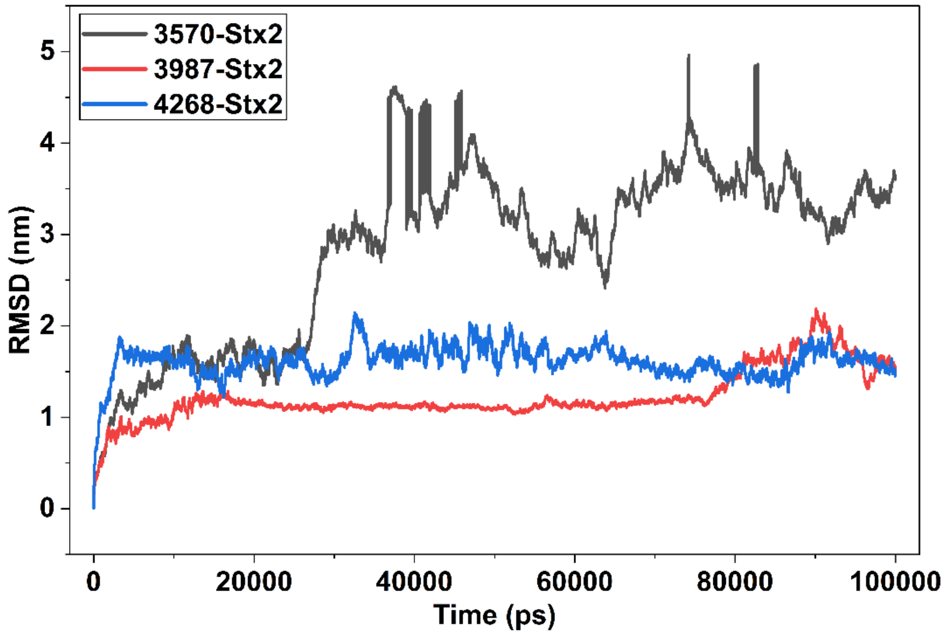

Figure 5.14: RMSD plots of less stable aptamer and Stx2 complexes with over the course of 100 ns MD simulations.

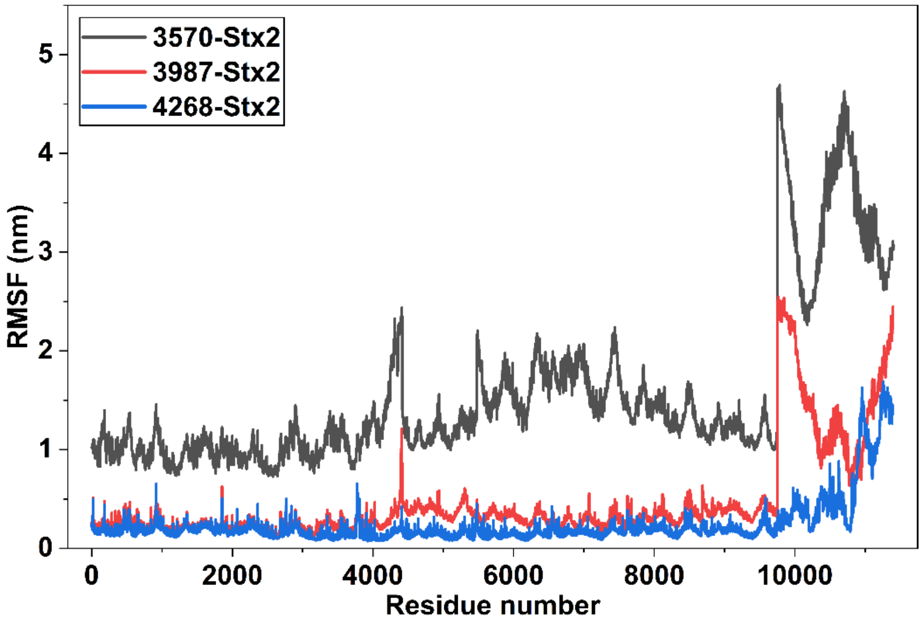

Figure 5.15: RMSF plots of less stable aptamer and Stx2 complexes with over the course of 100 ns MD simulations.

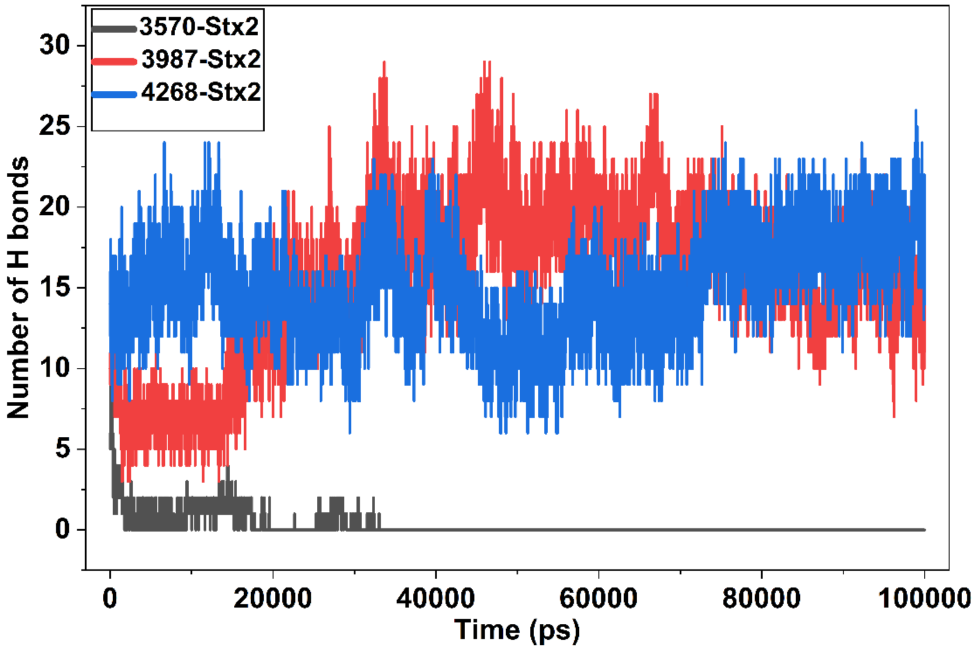

Figure 5.16: H Bond plots of less stable aptamer and Stx2 complexes with over the course of 100 ns MD simulations.

5.4. Conclusion

This chapter presented a comprehensive *in-silico* strategy for the de novo design and selection of DNA aptamers targeting the B subunit of Shiga toxin 2 (Stx2B). By integrating thermodynamic screening, molecular docking, MD simulations, and binding free energy calculations, a rational and systematic workflow was established to efficiently narrowing a large virtual sequence space to a small number of high-confidence aptamer candidates. This multilevel computational approach enabled early elimination of structurally unstable or non-specific sequences and provided molecular-level insight into aptamer–protein recognition mechanisms.

Thermodynamic filtering based on ΔG value ensured selection of sequences capable of forming stable secondary structures, while comparative docking against Stx2 and the structurally related Stx1 served as a critical specificity filter. This dual docking criterion allowed discrimination between general binders and sequences exhibiting preferential recognition of the Stx2 B subunit, thereby strengthening target selectivity at an early stage. Subsequent MD simulations and MM/GBSA binding free energy analyses further validated the stability, compactness, and energetic favourability of the shortlisted aptamer–protein complexes under dynamic conditions.

Among the candidates evaluated, aptamer A330 consistently demonstrated superior performance across all computational metrics, including reduced structural deviation, lower flexibility at the binding interface, enhanced intermolecular hydrogen bonding, and the most favourable predicted binding free energy. These computational findings were further corroborated through experimental validation using CD spectroscopy and ITC analyses, which confirmed binding-induced conformational changes and quantified a nanomolar-range binding affinity for the A330–Stx2B interaction.

Overall, this chapter establishes the effectiveness of integrating *in-silico* design with experimental validation for aptamer development, particularly for challenging protein toxin targets. The strategy adopted here not only reduced experimental complexity and selection bias associated with conventional SELEX but also ensured specificity and binding robustness prior to sensor fabrication. The successful identification of aptamer A330 provided a strong molecular foundation for its subsequent integration into an electrochemical impedance–based biosensing platform, which is described in the following chapter.

Chapter 6

Development of aptasensor for Stx2 using wave-type interdigitated electrode

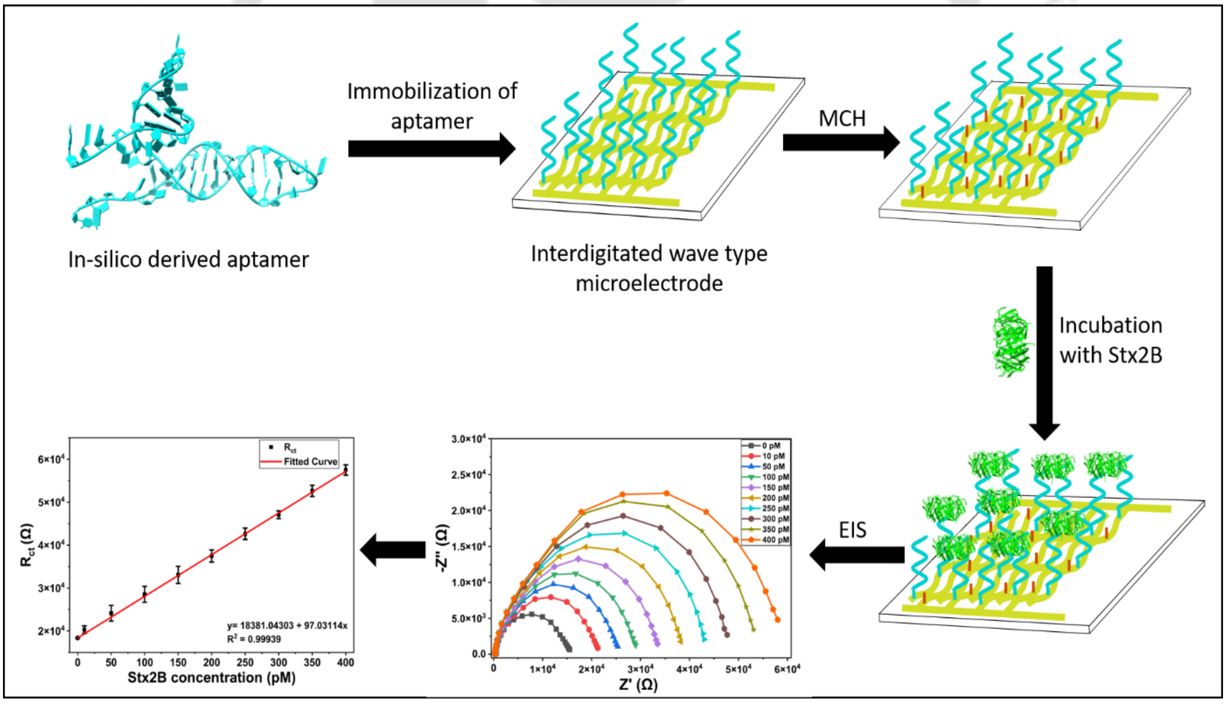

Development of aptasensor for Stx2 using wave-type interdigitated electrode.

6.1. Overview

This chapter presents the development of an electrochemical aptasensor for the detection of Shiga toxin 2 (Stx2), employing the *in-silico* designed aptamer A330 (developed in the preceding chapter) as the biorecognition element and a microfabricated interdigitated electrode platform as the transducer. The chapter details the design, fabrication, and surface functionalization of the sensing interface, along with the establishment of an electrochemical detection strategy for toxin analysis.

A wave-type interdigitated gold microelectrode was selected for its favorable electrochemical properties and enhanced effective surface area, enabling efficient signal transduction. The aptamer was chemically modified to allow stable and oriented immobilization on the gold surface via thiol–gold chemistry, followed by surface passivation with a suitable blocking agent to suppress nonspecific adsorption.

Electrochemical impedance spectroscopy was employed to monitor interfacial changes at the electrode–solution interface. The sensing principle relies on toxin-induced modulation of charge-transfer resistance of a redox probe upon specific binding of Stx2 to the immobilized aptamer. The chapter further evaluates key analytical performance parameters, including selectivity, stability, reproducibility, and applicability in complex matrices using spiked food samples. Overall, this chapter provides a systematic development and validation of an electrochemical aptasensing platform for Stx2 detection, demonstrating its potential for food safety and related analytical applications.

6.2. Experimental

6.2.1. Materials

The *in-silico* developed aptamer, A330, with thiol modification (SH-$(CH_2)_6$-5'-AGCACTAGGCGACTTGTCGCTTGAATGAGCAGCTATCTGCTCGTTCACCGGC) was purchased from Eurofins (Sweden). Tris(2-carboxyethyl) phosphine hydrochloride (TCEP) was procured from Invitrogen, India. Sodium Borohydride ($NaBH_4$), Potassium ferrocyanide and Potassium ferricyanide were purchased from Himedia, India. Commercial milk was purchased from Amul, India. All the reagents used were of analytical reagent grade, and the buffers were prepared using deionized water, MilliQ (18.2 MΩ.cm) (Millipore Co., USA).

6.2.2. Functionalization of interdigitated wave type microelectrode (IDWμE) with thiol modified aptamer.

As a part of a collaborative study, Prof. Sungbo Cho from Gachon University, Republic of Korea, provided the interdigitated wave type microelectrode (IDWμE) utilized in this study. The IDWμE was fabricated on a glass slide of dimensions 3.5 mm × 14 mm with an interelectrode spacing of 7 μm through photolithographic patterning and chemical wet etching (**Figure 6.1**). Prior to gold deposition, a 25 μm thick titanium layer was deposited onto the glass substrate to improve metal adhesion, followed by the deposition of a 50 μm thick gold layer as the conductive electrode material.

Prior to aptamer immobilization, the electrode surface was cleaned by treatment with 0.5 M sodium borohydride for 10 minutes, followed by thorough rinsing with deionized water and drying. To activate the thiol functionality, the disulfide-protected aptamers were reduced using tris(2-carboxyethyl) phosphine hydrochloride (TCEP). Briefly, a 100 μM aptamer solution was incubated with 10 mM TCEP at room temperature for 1.5 hours. Excess TCEP was subsequently removed by ethanol precipitation. The reduced aptamers were then diluted to a final concentration of 1 μM using binding buffer.

For immobilization, 5 μL of the reduced aptamer solution was drop-cast onto the active sensing region of the electrode and incubated in a humidified chamber at 4°C for 12 hours to allow stable attachment. Following immobilization, the electrode surface was rinsed with binding buffer to remove loosely bound aptamers. Surface passivation was then carried out by incubating the electrode with 1 mM 6-mercapto-1-hexanol (MCH) at room temperature for 2 hours. Finally, the electrodes were thoroughly washed with deionized water and stored in a humidified chamber at 4°C until further use.

6.2.3. Surface analysis of IDWμE.

Field emission scanning electron microscope (FESEM) (Sigma, Ziess, Germany) was utilized to acquire high resolution image of the IDWμE surface with different magnification and to analyze its morphological features using an accelerated voltage of 5 kV. Furthermore, Atomic force microscopy (AFM) was employed to examine the topographical variations of the electrode surface before and after aptamer modification. Imaging was performed using a Cypher S AFM system (Oxford Instruments, USA) operated in non-contact mode, with scans acquired over a surface area of 1 × 1 μm². In addition, X-ray photoelectron spectroscopy (XPS) was utilized to verify and characterize the immobilization of the thiol-functionalized aptamer on the electrode surface. XPS provides information on both elemental composition and chemical states of surface-bound species.

The measurements were conducted using a VersaProbe III XPS instrument (Physical Instruments, PHI, Japan). High-resolution spectra corresponding to Au 4f, S 2p, C 1s, N 1s, and P 2p were collected from the modified electrode surface.

6.2.4. Electrochemical impedance spectroscopy analysis.

Electrochemical impedance spectroscopy (EIS) measurements were conducted in 1× phosphate-buffered saline (PBS, pH 7.4) containing 5 mM $K_3Fe(CN)_6$/$K_4Fe(CN)_6$ as the redox couple. The experiments were performed using a Zennium electrochemical workstation (Zahner, Germany) in a two-electrode configuration, where one set of the interdigitated microelectrode functioned as the working electrode and the opposing set served as both the counter and pseudo-reference electrode. A sinusoidal perturbation of 5 mV was applied, and impedance data were collected over a frequency range of 1 Hz to 100 kHz, with five measurement points recorded per decade. The obtained impedance spectra were analyzed and fitted using Zahner analysis software. All measurements were carried out in a 96-well plate format using a solution volume of 350 µL, with electrical connections established through a custom-fabricated adapter.

6.2.5. Real sample analysis.

To verify the real-life practical usability of the aptasensor, cow milk was used as a sample. The commercially purchased milk (Amul, India) was spiked with different concentrations of Stx2B. The upper-fat layer of the milk was removed after centrifuging at 12000 rpm for 15 minutes at 4 °C. The solution at the bottom was filtered through a 0.22 µm filter membrane and diluted 10 times with 1× PBS, pH 7.4. It was then incubated with the developed aptasensor for 20 minutes, allowing all the available Stx2B to react with the sensor. After incubation, EIS measurements were carried out in 5 mM $K_4Fe(CN)_6$/$K_3Fe(CN)_6$ in 1×PBS solution.

6.2.6. Statistical analysis.

All experiments were performed in triplicate, and the data are reported as mean values with corresponding standard deviations represented as error bars. Statistical analysis was carried out using OriginPro software. The limit of detection (LOD) of the aptasensor was determined based on the relationship: LOD = 3 × (standard deviation of the blank signal) /sensitivity (Singh et al., 2019).

6.3. Results and discussions.

6.3.1. Characterization of IDWµE.

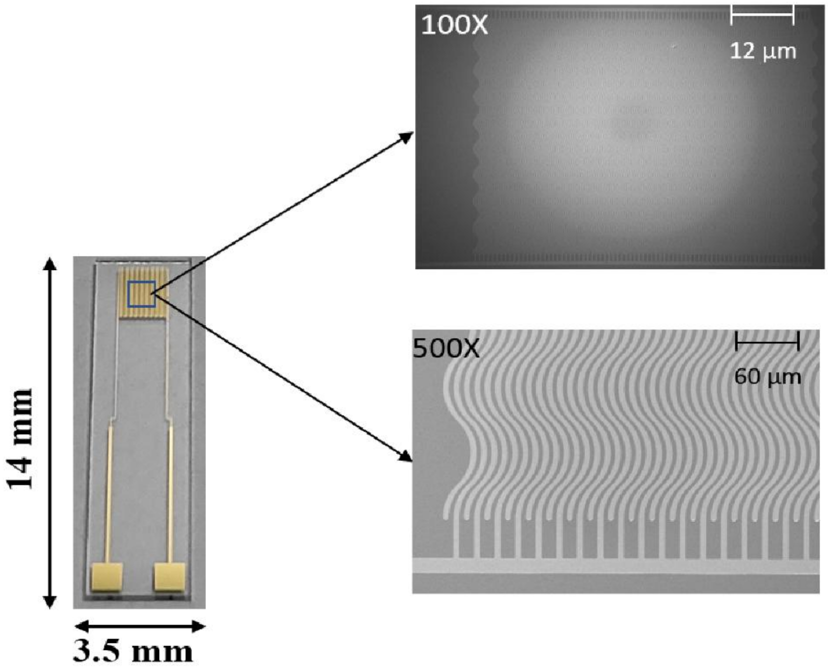

Figure 6.1: Photograph and FESEM image of IDWµE with 100× and 500× magnification.

Interdigitated wave-type microelectrodes (IDWµE) were employed in this work owing to the increased electrochemically active surface area provided by the wave-shaped geometry compared to conventional straight interdigitated electrodes, which is known to enhance sensing performance. Additionally, in traditional rectangular interdigitated electrode designs, the electric field is predominantly concentrated at the edges of the electrode fingers, resulting in a non-uniform electric field distribution and potential localized signal dominance. In contrast, the wave-type electrode architecture mitigates edge effects by promoting a more homogeneous electric field distribution across the electrode surface, thereby contributing to improved and more uniform electrochemical signal transduction (Park et al., 2020). The fabricated IDWµE comprises contact pads, transmission lines, and gold micro-fingers, as confirmed by the FESEM micrographs shown in **Figure 6.1**.

AFM analysis performed in non-contact mode before and after surface modification provided clear evidence of successful aptamer self-assembled monolayer (SAM) formation on the electrode surface. The unmodified electrode exhibited an average surface roughness of 1.221 nm and a maximum roughness of 14 nm (**Figure 6.2a**). Following aptamer immobilization via drop casting of the thiol-functionalized aptamer, these values decreased to 0.865 nm and 11.3 nm, respectively

(**Figure 6.2b**). This reduction in surface roughness indicates the formation of a smoother and more homogeneous surface layer, consistent with successful SAM formation on the electrode.

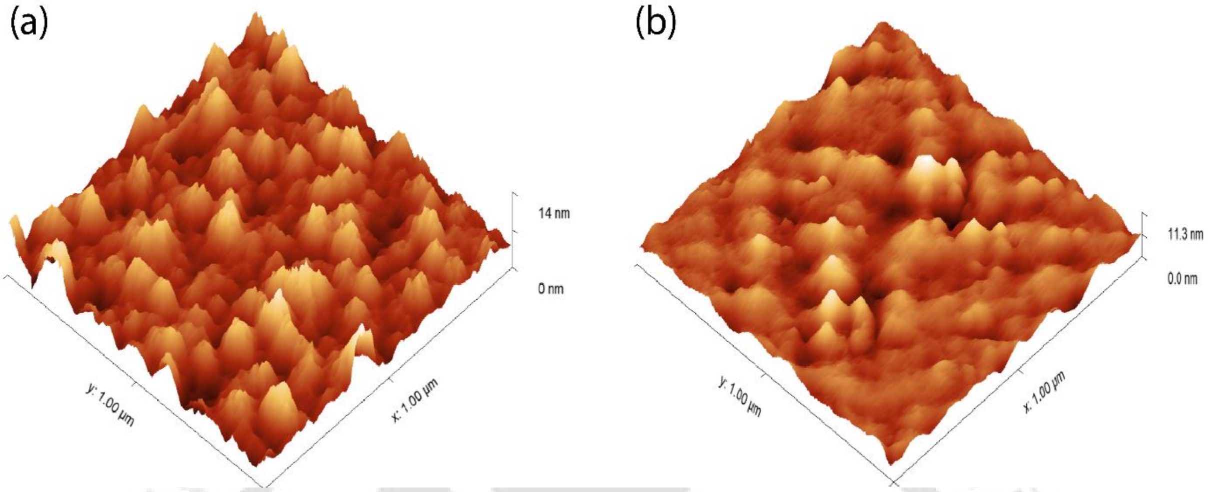

Figure 6.2: AFM image of (a) bare electrode (b) aptamer immobilized electrode.

To further confirm the immobilization of the thiol-modified aptamer, X-ray photoelectron spectroscopy (XPS) analysis was carried out. High-resolution spectra corresponding to carbon (C 1s), nitrogen (N 1s), phosphorus (P 2p), and sulfur (S 2p) were acquired from the modified electrode surface (**Figure 6.3**). The N 1s spectrum displayed a characteristic peak at 400.3 eV, attributable to the nitrogen-containing nucleobases of the aptamer (Vega-Figueroa et al., 2018). Deconvolution of the S 2p high-resolution spectrum revealed three distinct peaks at 162.5 eV, 163.8 eV, and 164.6 eV. The peak observed at 162.5 eV corresponds to the formation of Au–S bonds between the thiol groups of the aptamer and the gold electrode surface, confirming covalent attachment (Mirsaleh-Kohan et al., 2010). The remaining peaks at 163.8 eV and 164.6 eV are associated with unbound sulfur species, likely arising from weakly adsorbed or physisorbed thiol molecules (Lee et al., 2005).

The C 1s high-resolution spectrum was deconvoluted into four components. The peak at 284.80 eV is attributed to C–C and C–H bonds originating from the aptamer backbone and alkyl linkers, while the peaks at 286.17 eV and 286.78 eV correspond to C–N and C–O bonds associated with nucleobases and sugar moieties. An additional peak at 288.27 eV was assigned to N–C=O bonding environments, further supporting aptamer immobilization (Longo et al., 2015) (Peruzzi et al., 2021). Moreover, the P 2p spectrum exhibited a peak at 133 eV, which is characteristic of phosphate groups present in oligonucleotides (Vega-Figueroa et al., 2018). Collectively, the XPS results provide strong evidence for the successful immobilization of the thiolated aptamer onto the gold electrode surface.

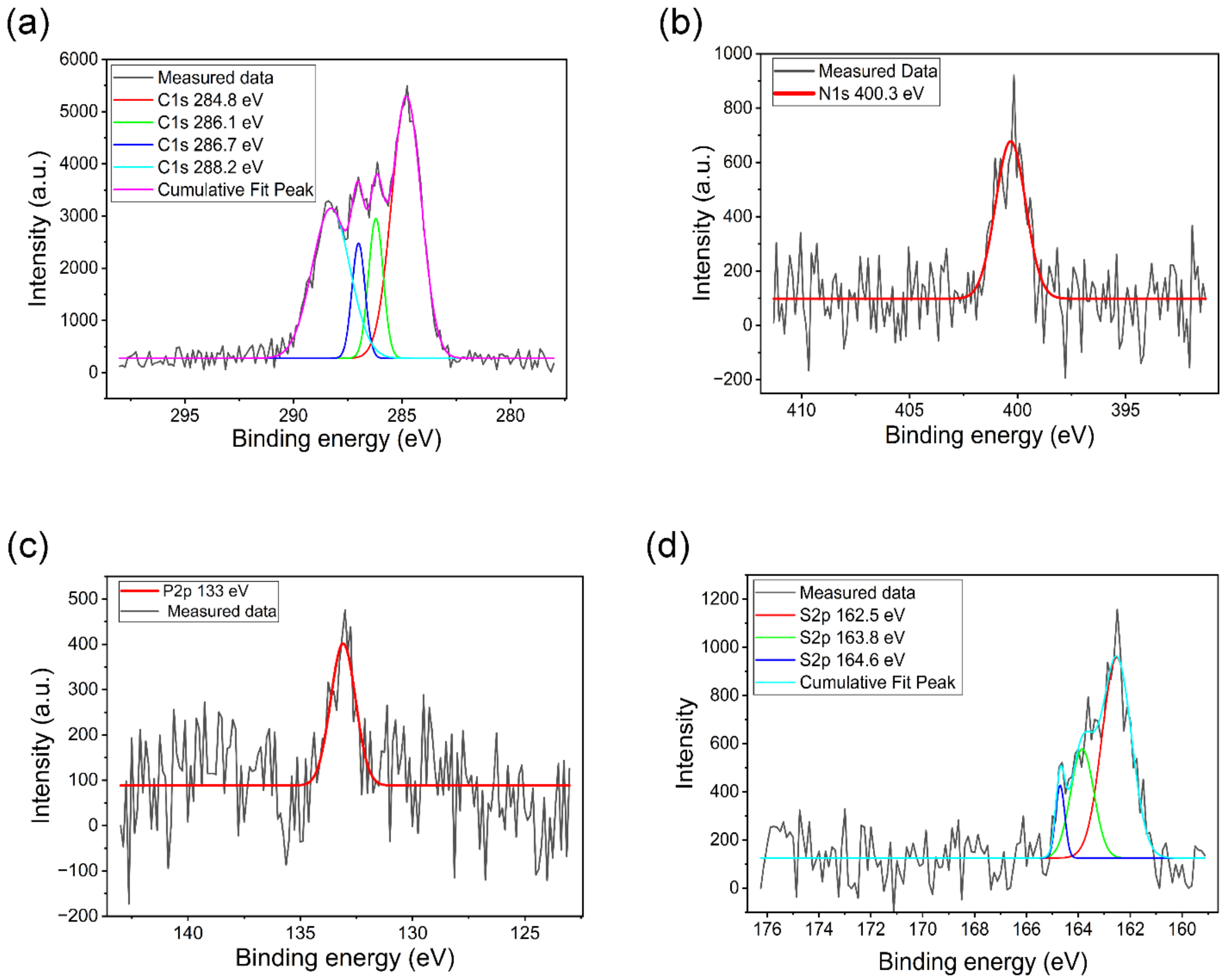

Figure 6.3: High resolution XPS spectra of the aptamer modified electrode. (a) C1s, (b) N1s, (c) P2p, (d) S2p.

6.3.2. Electrochemical impedance study of modified electrode.

The modified electrode was connected to a potentiostat (Zennium, Zahner, Germany) using a homemade adapter and was characterized using EIS technique after every step of modification. EIS measurements were performed in 1× phosphate-buffered saline (PBS) containing 5 mM $K_4Fe(CN)_6/K_3Fe(CN)_6$ as the redox couple, over a frequency range from 100 kHz to 1 Hz. The impedance data were represented as Nyquist plots, and the charge transfer resistance (R_{ct}), corresponding to the diameter of the semi-circular portion of the plot, was extracted following each surface modification step by fitting the spectra to an appropriate equivalent electrical circuit.

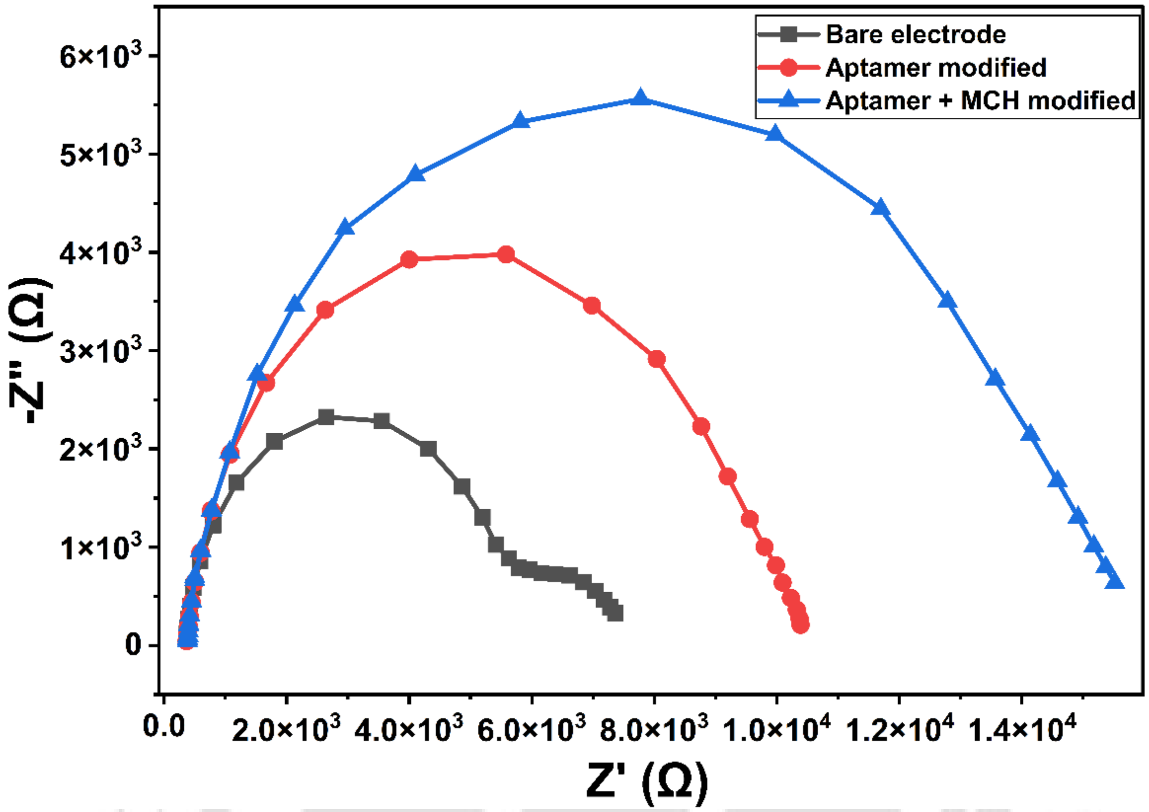

Figure 6.4: Nyquist plot of different modification stage of the IDWμE.

The experimental impedance spectra were adequately described using a Randles equivalent circuit model comprising the solution resistance (R_s), a constant phase element (CPE) representing the non-ideal double-layer capacitance (C_{dl}), the charge transfer resistance (R_{ct}), and a finite-length diffusion element modelled as a Nernst diffusion component (Z_N) (*Zahner Analysis Software*, 2023). The inclusion of the Nernst diffusion element is associated with the confined diffusion of the redox species between the closely spaced fingers of the interdigitated wave-type microelectrodes, which gives rise to an additional semi-circular feature at lower frequencies (Lai et al., 2019). The highest Z_N value was observed for the unmodified electrode surface. Following aptamer immobilization and subsequent surface passivation with 6-mercapto-1-hexanol (MCH), a decrease in the Z_N contribution was observed, while the R_{ct} component became the dominant feature of the impedance response. The charge transfer resistance of the bare electrode was initially measured to be 5.08 kΩ, which increased to 8.88 kΩ after aptamer attachment and further rose to 15.8 kΩ upon MCH backfilling. The progressive increase in R_{ct} observed after each surface modification step confirms the successful immobilization of the thiol-functionalized aptamer and effective surface blocking by MCH (**Figure 6.4**).

The increase in R_{ct} following aptamer immobilization can be attributed to electrostatic repulsion between the negatively charged phosphate backbone of the single-stranded DNA and the negatively charged $K_4Fe(CN)_6/K_3Fe(CN)_6$ redox couple, as well as steric hindrance introduced by the aptamer layer, both of which restrict redox probe access to the electrode surface. Subsequent MCH backfilling further passivates the remaining exposed gold surface, thereby imposing an additional diffusion barrier to the redox species. The fitted values of the individual Randles circuit elements obtained from the impedance analysis are summarized in **Table 6.1**.

The systematic increase in R_{ct} observed for the aptamer-functionalized IDWµE following successive surface modifications established charge transfer resistance as a reliable sensing parameter for the detection of Stx2B using the developed aptasensor platform.

Electrodes	R_s (Ω)	CPE		R_{ct} (kΩ)	Z_N	
		Y_0 (nS·s$^{\alpha}$)	α		DW (KDW)	k (1/s)
Bare	344	46.5	0.940	5.08	10	28.7
Aptamer Immobilized	357	109	0.926	8.88	6.22	28.8
MCH back filled aptamer immobilized	358	283	0.838	15.8	6.91	21.9
Y_0 - CPE admittance, α - Phase shift factor, DW - Warburg Constant, k - Electron Transfer Rate Constant						

Table 6.1: Fitted parameters of the Randles equivalent circuit model against the experimentally measured impedance spectra shown in Fig. 6.4.

6.3.3. Sensing of Stx2 using developed aptasensor.

To assess the analytical response of the developed aptasensor, the fabricated platform was incubated with varying concentrations of Stx2B for 20 minutes, followed by electrochemical impedance spectroscopy measurements. A progressive increase in the charge transfer resistance

(R_{ct}) was observed with increasing concentrations of Stx2B (**Figure 6.5**). This rise in R_{ct} can be attributed to the specific interaction between Stx2B and the immobilized aptamer, which results in the formation of an insulating biomolecular layer on the electrode surface, thereby hindering the diffusion of the redox probe toward the IDWµE interface.

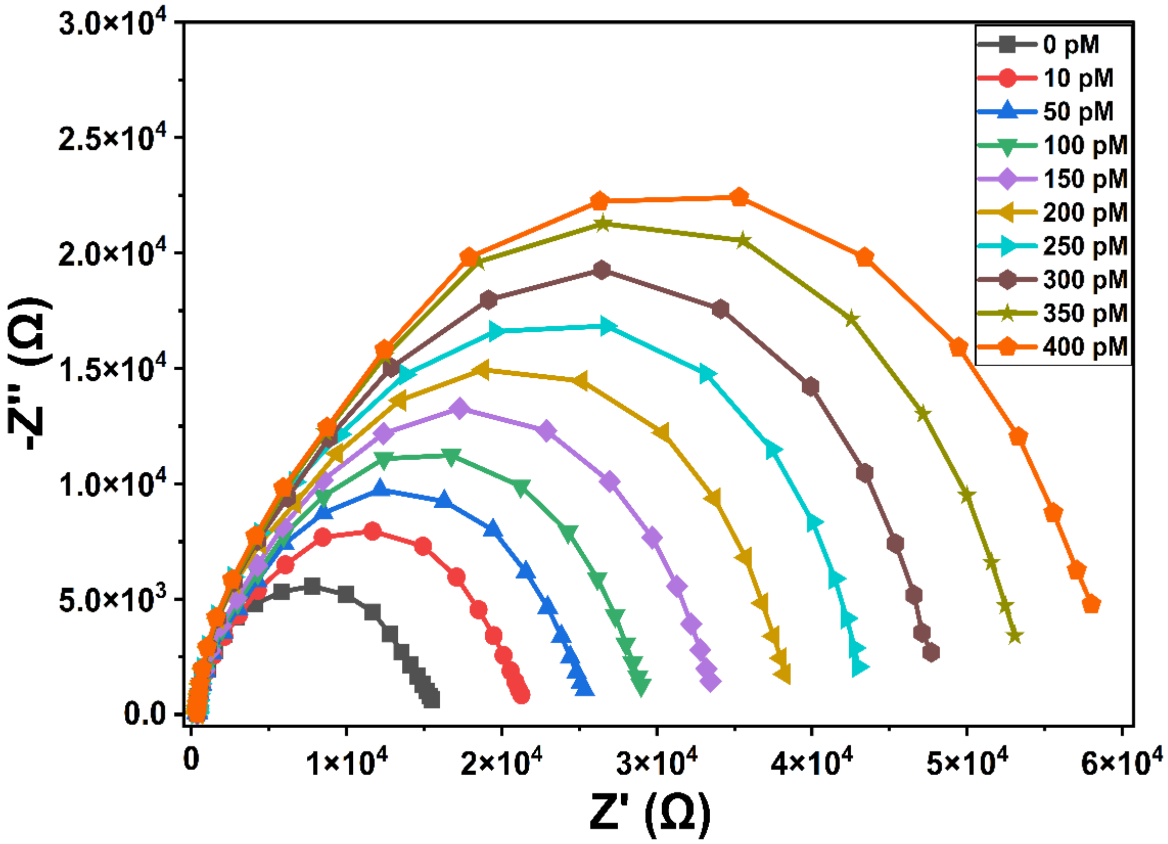

Figure 6.5: Nyquist plot of aptamer-modified electrode with increasing concentration of Stx2B.

A calibration plot was constructed by correlating the R_{ct} values with the corresponding concentrations of Stx2B, yielding a linear relationship described by the equation y = 18381.04 + 97.03x, with a correlation coefficient (R^2) of 0.99 across a concentration range of 10 pM to 400 pM (**Figure 6.6**). The limit of detection (LOD) of the sensor was determined to be 4.63 pM using the standard equation LOD = 3 × (standard deviation of the blank signal)/sensitivity, where the standard deviation was calculated from the R_{ct} values obtained in the absence of Stx2B (n = 3), and the sensitivity corresponds to the slope of the calibration curve.

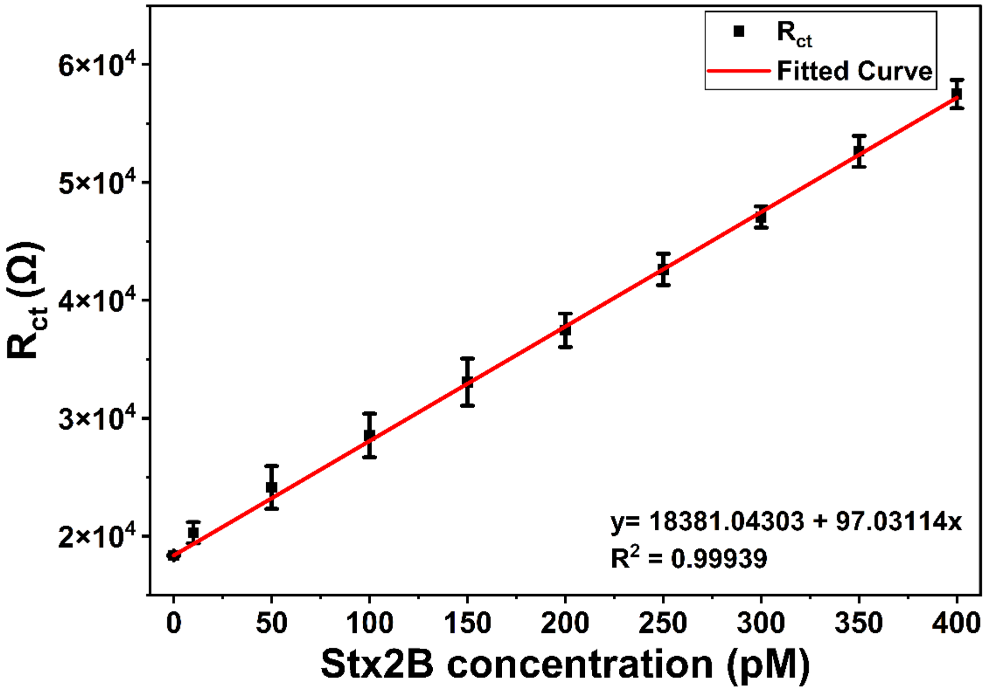

Figure 6.6: Linear calibration plot of R_{ct} over increasing concentration of Stx2B.

6.3.4. Evaluation of the developed aptasensor.

The performance of the developed aptasensor was systematically evaluated to establish its analytical reliability and practical applicability for Stx2B detection. Key performance parameters, including specificity, reproducibility, and long-term stability, were investigated using EIS. These studies were conducted to validate the selectivity, consistency, and robustness of the aptasensor under controlled experimental conditions.

The specificity of the developed aptasensor was examined through interference studies using a structurally related toxin subunit, Stx1B, and a non-related protein, BSA. The aptasensor was individually incubated with equal concentrations (150 pM) of Stx2B, Stx1B, and BSA for 20 minutes under identical experimental conditions. EIS measurements were subsequently performed in 1× PBS (pH 7.4) containing 5 mM $K_4Fe(CN)_6/K_3Fe(CN)_6$ over a frequency range of 1 Hz to 100 kHz. As shown in **Figure 6.7**, no significant changes in the impedance spectra were observed when the aptasensor was exposed to Stx1B or BSA. Analysis of the corresponding charge transfer resistance (R_{ct}) values further confirmed a negligible response toward these non-target analytes compared to Stx2B. The aptasensor exhibited a markedly higher R_{ct} value in the presence of Stx2B (35.2 kΩ) relative to Stx1B (15 kΩ), BSA (14.4 kΩ), and the blank sensor (14 kΩ). Statistical analysis demonstrated that the response toward Stx2B was highly significant compared to all other groups, while the difference between Stx1B and the blank was marginally significant and that between BSA and the blank was not statistically significant ($p > 0.05$). These results confirm the high selectivity of the developed aptasensor toward Stx2B (**Figure 6.8**).

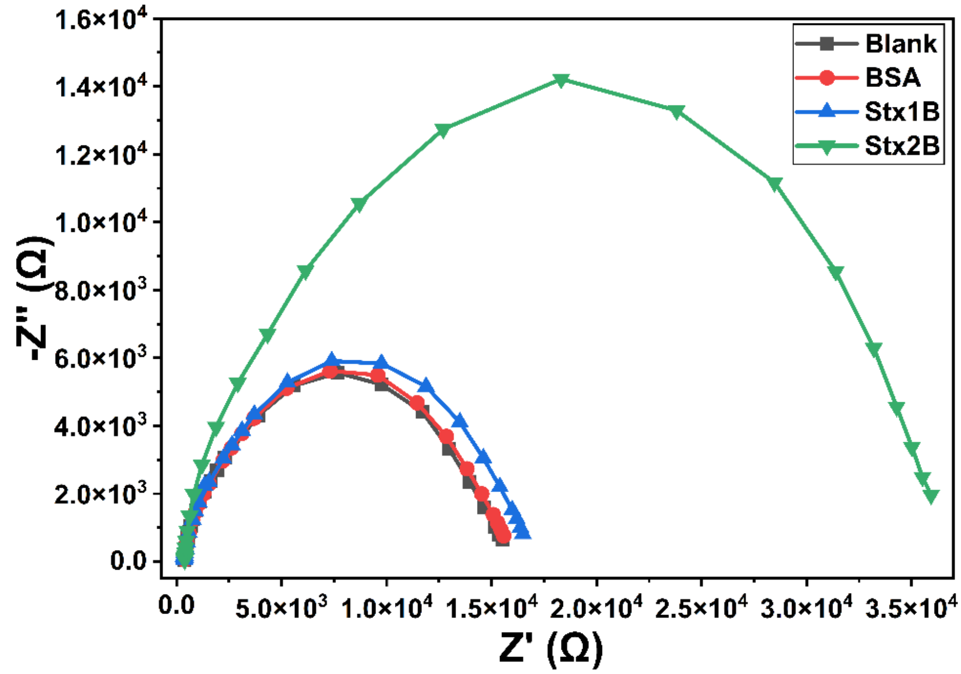

Figure 6.7: Nyquist plot of selectivity analysis of the Stx2B aptasensor.

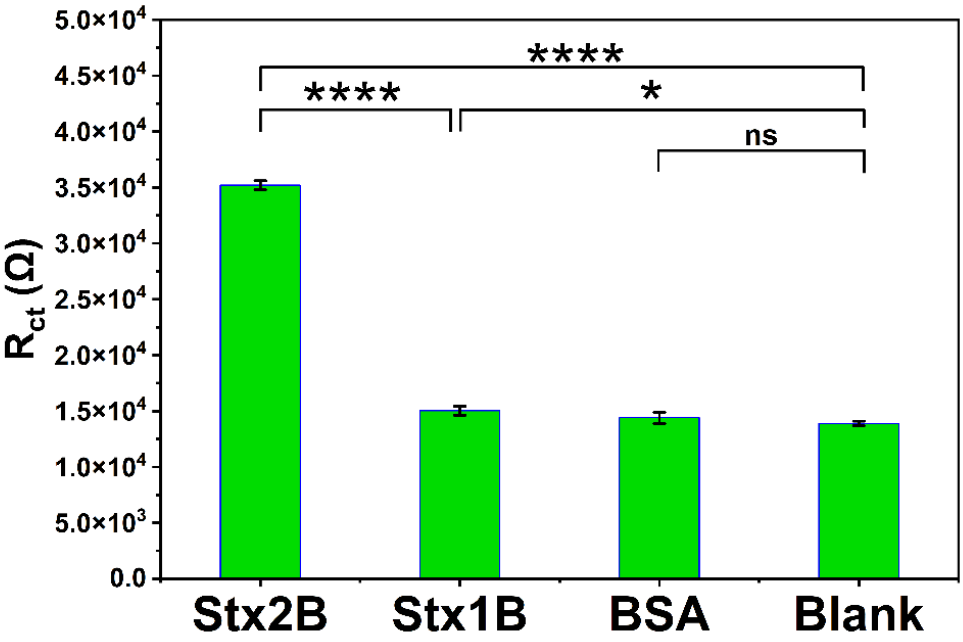

Figure 6.8: R_{ct} value of the aptasensor incubated with 150 pM of Stx2B, Stx1B, and BSA, and without any molecule, i.e., the blank aptasensor. Error bars represent the SD (n = 3). Statistical analysis by one-way ANOVA followed by Tukey's test. ****$p < 0.0001$, *$p < 0.05$, ns = not significant.

Long-term stability is a critical parameter for the practical application of biosensors. The storage stability of the developed aptasensor was evaluated over a period of 20 days. EIS measurements were performed on the blank aptasensor (i.e., aptamer and MCH immobilized IDWμE) at five-day intervals. During the study period, the sensors were stored at 4 °C in 1× PBS (pH 7.4). The R_{ct} values measured on the 20th day retained 95.6% of the initial response for the blank aptasensor, with a relative standard deviation (RSD) of 2.43%. The absence of significant signal degradation over the testing period indicates excellent storage stability of the aptasensor. This stability can be attributed to the strong Au–S covalent bonding between the gold electrode surface and the thiolated aptamer, which ensures robust surface immobilization (**Figure 6.9**).

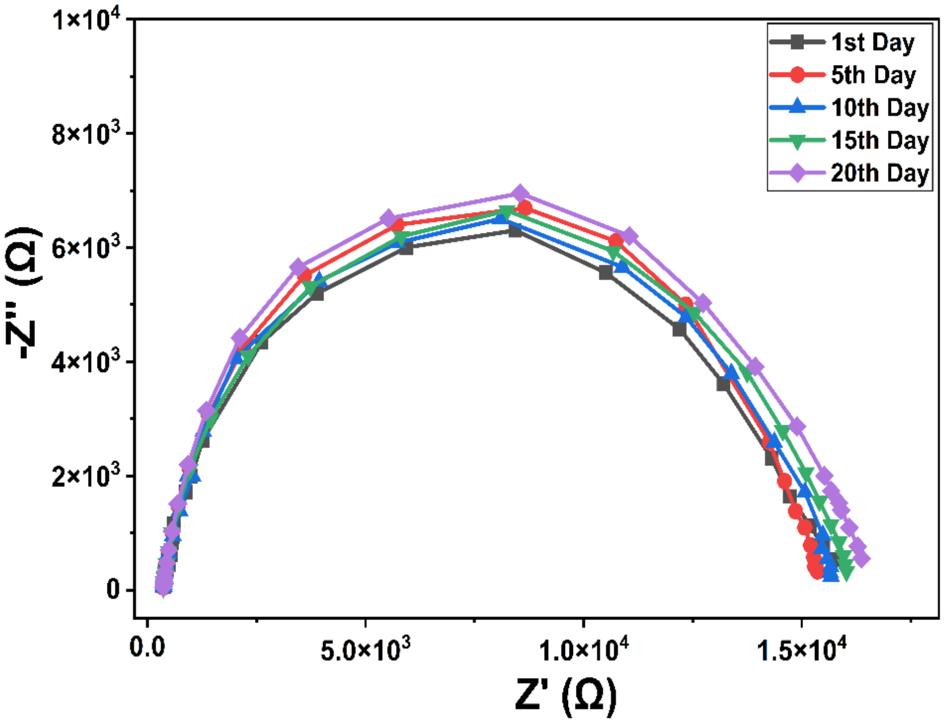

Figure 6.9: Stability analysis of the developed aptasensor over 20 days.

The reproducibility of the developed aptasensor was assessed through both intra-assay and inter-assay measurements by evaluating the relative standard deviation (RSD) of the charge transfer resistance values. For intra-assay reproducibility, the R_{ct} values were measured in triplicate using a single aptasensor incubated with 200 pM Stx2B. Inter-assay reproducibility was evaluated by incubating 50 pM Stx2B with three independently fabricated aptasensors under identical experimental conditions. The calculated RSD values were 0.47% for the intra-assay and 2.93% for the inter-assay measurements, indicating high measurement consistency and fabrication reliability. These results demonstrate that the developed aptasensor exhibits satisfactory reproducibility, supporting its suitability for practical and real-world applications.

6.3.5. Performance evaluation of the aptasensors in real sample analysis.

To assess the practical applicability of the developed aptasensor, EIS measurements were carried out using commercially available milk samples spiked with different concentrations of Stx2B. The real sample analysis results (**Table 6.2**) exhibited high recovery of the target protein, with recovery values exceeding 93.06% and a maximum relative standard deviation (RSD) of 2.08%. These findings demonstrate the reliability, accuracy, and reproducibility of the aptasensor for analysis in complex food matrices.

Spiked (pM)	Detected (pM)	Recovery (%)	RSD (%)
10	10.8	108.4	1.25
100	106	106	1.84
200	214.9	107.45	1.37
300	287.04	95.68	2.08
400	372.24	93.06	1.73

Table 6.2: Recovery study of Stx2B from spiked milk sample.

6.4. Conclusion.

Chapter 6 experimentally validates the *in-silico* developed aptamer, A330 as the recognition element for the detection of Stx2 using an impedance-based signal in a wave type interdigitated microelectrode as the transducing platform. The developed aptasensor exhibited a limit of detection (LOD) of 4.63 pM and a high analytical sensitivity of 97.03 Ω pM^{-1}, values that are comparable to those reported for aptamers obtained through conventional experimental selection methods. These findings provide strong experimental evidence supporting the reliability and effectiveness of computational approaches for aptamer design.

The aptasensor further demonstrated excellent analytical performance, exhibiting high selectivity toward Stx2B over structurally similar and non-specific proteins, strong reproducibility with intra- and inter-assay RSD values of 0.47% and 2.93%, respectively, and robust storage stability, retaining over 93% of its initial response after 20 days. Importantly, its applicability in complex matrices was validated through recovery studies in spiked milk samples, which yielded recovery values above 93.06% with a maximum RSD of 2.08%.

Overall, the findings of this chapter confirm the successful integration of a computationally designed aptamer into a high-performance electrochemical sensing platform, underscoring its potential for sensitive Stx2 detection and paving the way for future validation in clinical and field-deployable diagnostic applications.

Chapter 7

Conclusion and future outlook

Conclusion and future outlook.

7.1. Conclusion

This thesis presents a comprehensive and integrated strategy for the development of highly sensitive and selective aptamer-based electrochemical biosensors for the detection of Shiga toxins, specifically Stx1 and Stx2. The work systematically combines recombinant protein engineering, experimental and computational aptamer development, and electrochemical sensor fabrication to address the critical need for rapid, sensitive, and reliable detection platforms for food safety and public health monitoring.

Following the introduction and literature review in chapter 1, chapter 2 describes the successful cloning, heterologous expression, and purification of the B subunits of Shiga toxin 1 and 2, thereby establishing a strong experimental foundation for the subsequent chapters. Recombinant Stx1B and Stx2B proteins were expressed in optimized *E. coli* host systems and purified using Ni–NTA affinity chromatography. Structural characterization using MALDI-TOF mass spectrometry and circular dichroism spectroscopy confirmed the molecular integrity and proper folding of the proteins. The β-sheet–rich secondary structure observed for both proteins is consistent with the known architecture of Shiga toxin B subunits, validating their suitability as functional targets for aptamer selection and biosensor development.

Chapter 3 focused on the development of high-affinity ssDNA aptamers against Stx1B using the Systematic Evolution of Ligands by Exponential Enrichment (SELEX) process. The incorporation of negative SELEX using Stx2B and Ni–NTA beads significantly enhanced aptamer selectivity. Following twelve rounds of selection, cloning, and sequencing, dominant aptamer candidates were identified. Isothermal titration calorimetry revealed that the aptamer sT3 exhibited nanomolar binding affinity toward Stx1B, substantially outperforming other candidates. The high affinity and specificity of sT3 demonstrated the robustness of the SELEX strategy and justified its selection as the biorecognition element for sensor fabrication.

In Chapter 4, the SELEX-derived sT3 aptamer was successfully integrated into an impedimetric biosensor using a chain-shaped interdigitated gold microelectrode. The thiol-mediated immobilization of the aptamer enabled stable and reproducible sensor fabrication. Electrochemical impedance spectroscopy measurements showed a clear and concentration-dependent increase in charge transfer resistance upon Stx1B binding, yielding a wide linear detection range in the picomolar regime. The sensor exhibited excellent specificity, stability, and reproducibility, and demonstrated reliable performance in spiked milk samples, highlighting its applicability in complex biological matrices.

Chapter 5 introduced a complementary *in-silico* approach for aptamer development targeting Stx2B. A large ssDNA library was computationally designed, and then screened based on thermodynamic stability, molecular docking, and molecular dynamics simulations. This rational design strategy significantly reduced experimental time and resource requirements. Among the screened candidates, aptamer A330 exhibited the most favourable binding free energy and stable interaction with Stx2B. Experimental validation using circular dichroism spectroscopy and isothermal titration calorimetry confirmed the predicted interaction, demonstrating good agreement between computational and experimental results.

Chapter 6 translated the *in-silico* designed aptamer A330 into a functional electrochemical aptasensor using a wave-type interdigitated microelectrode. The sensor achieved a low limit of detection in the picomolar range and exhibited high specificity, reproducibility, and stability. Successful recovery of Stx2B from spiked milk samples further validated the practical applicability of the developed sensing platform. The use of distinct electrode geometries for Stx1 and Stx2 detection also emphasized the influence of microelectrode design on sensor sensitivity.

Overall, this thesis demonstrates that both experimental SELEX and rational *in-silico* design approaches can generate high-affinity aptamers suitable for biosensor development. The successful integration of these aptamers with interdigitated microelectrode platforms resulted in sensitive, selective, and matrix-tolerant biosensors for Shiga toxin detection. The outcomes collectively contribute to advancing aptamer-based diagnostics and offer promising alternatives to conventional antibody-based assays.

7.2. Future outlook.

While the present work establishes a robust and foundational framework for Shiga toxin detection, several avenues exist for further advancement of the current work.

One important future direction is the integration of the developed aptasensors into portable and miniaturized point-of-care (PoC) diagnostic devices. Coupling the sensor platform with compact potentiostat could enable on-site detection of Shiga toxins in food products and clinical samples without the need for specialized laboratory infrastructure.

Further optimization of the *in-silico* aptamer design pipeline also represents a valuable future goal. Incorporating machine learning–based sequence prediction, enhanced force-field models, and longer molecular dynamics simulations could improve the accuracy of affinity prediction and reduce false positives during computational screening. In addition, applying the developed *in-silico* design strategy to generate aptamers against other target molecules would further validate the general applicability of the computational approach. Such advancements would minimize experimental iterations and significantly accelerate aptamer discovery.

From a sensor performance standpoint, future studies may focus on improving long-term storage stability, regenerability, and reusability of the aptasensors. Surface chemistry optimization and antifouling strategies could enhance sensor durability during repeated use and prolonged storage.

Finally, clinical and field-level validation using real-world samples such as patient stool samples, environmental water, and food processing samples will be essential for regulatory acceptance and commercialization. Comparative studies against standard diagnostic methods would further establish the reliability and practical relevance of the developed biosensors.

In conclusion, the work presented in this thesis lays a strong scientific and technological foundation for aptamer-based electrochemical detection of Shiga toxins. The methodologies developed herein are versatile and can be readily adapted to other toxins and biomarkers, thereby contributing broadly to the fields of biosensing, food safety, and public health diagnostics.

Bibliography

Abraham, M. J., Murtola, T., Schulz, R., Páll, S., Smith, J. C., Hess, B., & Lindah, E. (2015). Gromacs: High performance molecular simulations through multi-level parallelism from laptops to supercomputers. *SoftwareX*, *1–2*, 19–25. doi.org/10.1016/j.softx.2015.06.001

Adasme, M. F., Linnemann, K. L., Bolz, S. N., Kaiser, F., Salentin, S., Haupt, V. J., & Schroeder, M. (2021). PLIP 2021: Expanding the scope of the protein-ligand interaction profiler to DNA and RNA. *Nucleic Acids Research*, *49*(W1), W530–W534. doi.org/10.1093/nar/gkab294

Alexander, G., Forest, D., Tanis, M., Nicholas, P., Xiong, W., Elizabeth, C., Flemming, S., Kelly, W., Burton, B., & Catherine, C. (2022). Characterization of Atypical Shiga Toxin Gene Sequences and Description of Stx2j, a New Subtype. *Journal of Clinical Microbiology*, *60*(3), e02229-21. doi.org/10.1128/jcm.02229-21

Alhadlaq, M. A., Aljurayyad, O. I., Almansour, A., Akeel, S. I. Al, Alzahrani, K. O., Alsalman, S. A., Yahya, R., Hindi, R. R. Al, Hakami, M. A., Alshahrani, S. D., Alhumeed, N. A., Moneea, A. M. Al, Seghayer, M. S. Al, Alharbi, A. L., Reshoodi, F. M. A. L., & Alajel, S. (2024). Overview of pathogenic Escherichia coli , with a focus on Shiga toxin - producing serotypes , global outbreaks (1982 – 2024) and food safety criteria. *Gut Pathogens*, *16*(57). doi.org/10.1186/s13099-024-00641-9

Amatore, C., Savéant, J. M., & Tessier, D. (1983). Kinetics of electron transfer to organic molecules at solid electrodes in organic media. *Journal of Electroanalytical Chemistry*, *146*(1), 37–45. doi.org/10.1016/S0022-0728(83)80111-9

Bachu, V., Mili, M., Dutta, A., Thungon, P. D., & Goswami, P. (2024). Electrochemiluminescence-Based Lateral Flow Assay for Detection of Cardiac Troponin T Using Aptamers Developed through a Modified SELEX Technique. *ACS Applied Optical Materials*, *2*(8), 1688–1698. doi.org/10.1021/acsaom.4c00258

Bai, X., Mernelius, S., Jernberg, C., & Einemo, I. (2018). Shiga Toxin-Producing Escherichia coli Infection in Jönköping County , Sweden : Occurrence and Molecular Characteristics in Correlation With Clinical Symptoms and Duration of stx Shedding. *Frontiers in Cellular and Infection Microbiology*, *8*(May), 1–8. doi.org/10.3389/fcimb.2018.00125

Bai, X., Scheutz, F., Dahlgren, H. M., Hedenström, I., & Jernberg, C. (2021). Characterization of Clinical Escherichia coli Strains Producing a Novel Shiga Toxin 2 Subtype in Sweden and Denmark. *Microorganisms*, *9*(11), 2374. doi.org/10.3390/microorganisms9112374

Bast, D. J., Banerjee, L., Clark, C., Read, R. J., & Brunton, J. L. (1999). The identification of three biologically relevant globotriaosyl ceramide receptor binding sites on the Verotoxin 1 B subunit. *Molecular Microbiology*, *32*(5), 953–960. doi.org/10.1046/j.1365-2958.1999.01405.x

Bélanger, S. D., Boissinot, M., Christian, M., J., P. F., & G., B. M. (2002). Rapid Detection of Shiga Toxin-Producing Bacteria in Feces by Multiplex PCR with Molecular Beacons on the Smart Cycler. *Journal of Clinical Microbiology*, *40*(4), 1436–1440. doi.org/10.1128/jcm.40.4.1436-1440.2002

Bell, D. R., Weber, J. K., Yin, W., Huynh, T., Duan, W., & Zhou, R. (2020). In silico design and validation of high-affinity RNA aptamers targeting epithelial cellular adhesion molecule dimers. *Proceedings of the National Academy of Sciences of the United States of America*, *117*(15), 8486–8493. doi.org/10.1073/pnas.1913242117

Bielaszewska, M., Idelevich, E. A., Zhang, W., Bauwens, A., Schaumburg, F., Mellmann, A., Peters, G., & Karch, H. (2012). Effects of antibiotics on Shiga toxin 2 production and bacteriophage induction by epidemic Escherichia coli O104:H4 strain. *Antimicrobial Agents and Chemotherapy*, *56*(6), 3277–3282. doi.org/10.1128/AAC.06315-11

Brown, A., Brill, J., Amini, R., Nurmi, C., & Li, Y. (2024). Development of Better Aptamers: Structured Library Approaches, Selection Methods, and Chemical Modifications. *Angewandte Chemie International Edition*, *63*(16), e202318665. doi.org/10.1002/anie.202318665

Chan, Y. S., & Ng, T. B. (2016). Shiga toxins: from structure and mechanism to applications. *Applied Microbiology and Biotechnology*, *100*(4), 1597–1610. doi.org/10.1007/s00253-015-7236-3

Chen, M., Yu, Y., Jiang, F., Zhou, J., Li, Y., Liang, C., Dang, L., Lu, A., & Zhang, G. (2016). Development of Cell-SELEX Technology and Its Application in Cancer Diagnosis and Therapy. *International Journal of Molecular Sciences*, *17*(12), 2079. doi.org/10.3390/ijms17122079

Ching, K. H., He, X., Stanker, L. H., Lin, A. V., McGarvey, J. A., & Hnasko, R. (2015). Detection of shiga toxins by lateral flow assay. *Toxins*, *7*(4), 1163–1173. doi.org/10.3390/toxins7041163

Chinnadayyala, S. R., Park, J., Abbasi, M. A., & Cho, S. (2019). Label-free electrochemical impedimetric immunosensor for sensitive detection of IgM rheumatoid factor in human serum. *Biosensors and Bioelectronics*, *143*(June), 111642. doi.org/10.1016/j.bios.2019.111642

Christine, B., Richard, D., Gabriele, A., Maximilian, M., Michael, B., & Erwin, M. (2003). Identification and Characterization of a New Variant of Shiga Toxin 1 in Escherichia coli ONT:H19 of Bovine Origin. *Journal of Clinical Microbiology*, *41*(5), 2106–2112. doi.org/10.1128/jcm.41.5.2106-2112.2003

Chui, L., Laura, P.-F., Julie, K., Vincent, L., & Valerie, B. (2015). Evaluation of Enzyme Immunoassays and Real-Time PCR for Detecting Shiga Toxin-Producing Escherichia coli in Southern Alberta, Canada. *Journal of Clinical Microbiology*, *53*(3), 1019–1023. doi.org/10.1128/jcm.03288-14

Chushak, Y., & Stone, M. O. (2009). In silico selection of RNA aptamers. *Nucleic Acids Research*, *37*(12), e87–e87. doi.org/10.1093/nar/gkp408

Ciszkowska, M., & Stojek, Z. (1999). Voltammetry in solutions of low ionic strength. Electrochemical and analytical aspects. *Journal of Electroanalytical Chemistry*, *466*(2), 129–143. doi.org/10.1016/S0022-0728(99)00141-2

Creuzburg, K., Ko, B., Hempel, H., Schreier, P., Jacobs, E., Schmidt, H., & Schmidt, H. (2005). Genetic structure and chromosomal integration site of the cryptic prophage CP-1639 encoding Shiga toxin 1 Printed in Great Britain. *Microbiology*, *151*, 941–950. doi.org/10.1099/mic.0.27632-0

D'Avino, A., Milano, A., Marchesano, V., Guilcapi, B., Sagnelli, D., Rippa, M., Zhou, L., Rossi, G., Consagra, L., Brigotti, M., Morabito, S., & Petti, L. (2025). Flexible gold nanoparticle SERS tape for rapid, label-free and ultrasensitive detection and differentiation of Shiga toxin variants. *Biosensors and Bioelectronics: X*, *27*, 100696. doi.org/10.1016/j.biosx.2025.100696

DeRosa, M. C., Lin, A., Mallikaratchy, P., McConnel, E. M., McKeague, M., Patel, R., & Shigdar, S. (2023). In vitro selection of aptamers and their applications. *Nature Reviews Methods Primers*, *3*(1), 55. doi.org/10.1038/s43586-023-00247-6

ECDC. (2024). *SURVEILLANCE REPORT Annual epidemiological report for 2022*. *April*, 1–10.

Elabbasy, M. T., Hussein, M. A., Algahtani, F. D., Abd El-Rahman, G. I., Morshdy, A. E., Elkafrawy, I. A., & Adeboye, A. A. (2021). MALDI-TOF MS Based Typing for Rapid Screening of Multiple Antibiotic Resistance E. coli and Virulent Non-O157 Shiga Toxin-Producing E. coli Isolated from the Slaughterhouse Settings and Beef Carcasses. *Foods*, *10*(4), 820. doi.org/10.3390/foods10040820

Elbehiry, A., Aldubaib, M., Abalkhail, A., Marzouk, E., ALbeloushi, A., Moussa, I., Ibrahem, M., Albazie, H., Alqarni, A., Anagreyyah, S., Alghamdi, S., & Rawway, M. (2022). How MALDI-TOF Mass Spectrometry Technology Contributes to Microbial Infection Control in Healthcare Settings. *Vaccines*, *10*(11), 1881. doi.org/10.3390/vaccines10111881

Ellington, A. D., & Szostak, J. W. (1990). In vitro selection of RNA molecules that bind specific ligands. *Nature*, *346*(6287), 818–822. doi.org/10.1038/346818a0

Fagerquist, C. K., & Sultan, O. (2010). Top-Down Proteomic Identification of Furin-Cleaved α-Subunit of Shiga Toxin 2 from Escherichia coli O157:H7 Using MALDI-TOF-TOF-MS/MS. *BioMed Research International*, *2010*(1), 123460. doi.org/10.1155/2010/123460

Fagerquist, C. K., Zaragoza, W. J., & Carter, M. Q. (2019). Top-Down Proteomic Identification of Shiga Toxin 1 and 2 from Pathogenic Escherichia coli Using MALDI-TOF-TOF Tandem Mass Spectrometry. *Microorganisms*, *7*(11), 488. doi.org/10.3390/microorganisms7110488

Fan, R., Shao, K., Yang, X., Bai, X., Fu, S., Sun, H., Xu, Y., Wang, H., & Li, Q. (2019). High prevalence of non-O157 Shiga toxin- producing Escherichia coli in beef cattle detected by combining four selective agars. *BMC Microbiology*, *19*(213), 1–9. doi.org/10.1186/s12866-019-1582-8

Fraser, M.E., Fujinaga, M., Cherney, M. M., Melton-Celsa, A. R., Twiddy, E. M., O’Brien, A. D., & James, M. N. G. (2004). Shiga toxin type 2. In *Worldwide Protein Data Bank*. doi.org/10.2210/pdb1r4p/pdb

Fraser, Marie E, Chernaia, M. M., Kozlov, Y. V, & James, M. N. G. (1994). Crystal structure of the holotoxino from Shigella dysenteriae at 2.5 Å resolution. *Nature Structural Biology*, *1*(1), 59–64. doi.org/10.1038/nsb0194-59

Freedman, S. B., Xie, J., Neufeld, M. S., Hamilton, W. L., Hartling, L., & Tarr, P. I. (2016). Shiga toxin-producing Escherichia coli infection, antibiotics, and risk of developing hemolytic uremic syndrome: A meta-analysis. *Clinical Infectious Diseases*, *62*(10), 1251–

1258. doi.org/10.1093/cid/ciw099

FSAI. (2019). Advice on Shiga toxin-producing Escherichia coli (STEC) detection in food. In *Report of the Scientific Committee of the Food Safety Authority of Ireland*.

Fuchs, G., Mobassaleh, M., Donohue-Rolfe, A., Montgomery, R. K., Grand, R. J., & Keusch, G. T. (1986). Pathogenesis of Shigella diarrhea: rabbit intestinal cell microvillus membrane binding site for Shigella toxin. *Infection and Immunity*, *53*(2), 372–377. doi.org/10.1128/iai.53.2.372-377.1986

Garred, Ø., Dubinina, E., Polesskaya, A., Olsnes, S., Kozlov, J., & Sandvig, K. (1997). Role of the Disulfide Bond in Shiga Toxin A-chain for Toxin Entry into Cells*. *Journal of Biological Chemistry*, *272*(17), 11414–11419. doi.org/10.1074/jbc.272.17.11414

Gavin, P. J., Peterson, L. R., Pasquariello, A., Joanna, B., G., H. M., J., K. K., & B., T. R. (2004). Evaluation of Performance and Potential Clinical Impact of ProSpecT Shiga Toxin Escherichia coli Microplate Assay for Detection of Shiga Toxin-Producing E. coli in Stool Samples. *Journal of Clinical Microbiology*, *42*(4), 1652–1656. doi.org/10.1128/jcm.42.4.1652-1656.2004

Gill, A., Huszczynski, G., Gauthier, M., & Blais, B. (2014). Evaluation of eight agar media for the isolation of shiga toxin—Producing Escherichia coli. *Journal of Microbiological Methods*, *96*, 6–11. doi.org/10.1016/j.mimet.2013.10.022

Goswami, P. (2020). *Advanced Materials and Techniques for Biosensors and Bioanalytical Applications* (P. Goswami (Ed.); 1st ed.). CRC PRESS. doi.org/10.1201/9781003083856

Guy, P., J., R. D., J., D. T., & R., B. F. (1999). Sequence of Shiga Toxin 2 Phage 933W fromEscherichia coli O157:H7: Shiga Toxin as a Phage Late-Gene Product. *Journal of Bacteriology*, *181*(6), 1767–1778. doi.org/10.1128/jb.181.6.1767-1778.1999

Harkins, V. J., McAllister, D. A., & Reynolds, B. C. (2020). Shiga-Toxin E. coli Hemolytic Uremic Syndrome: Review of Management and Long-term Outcome. *Current Pediatrics Reports*, *8*(1), 16–25. doi.org/10.1007/s40124-020-00208-7

Herbert, S., Jürgen, S., Stefano, M., Alfredo, C., H., W. L., & Helge, K. (2000). A New Shiga Toxin 2 Variant (Stx2f) fromEscherichia coli Isolated from Pigeons. *Applied and Environmental Microbiology*, *66*(3), 1205–1208. doi.org/10.1128/AEM.66.3.1205-1208.2000

Hovde, C. J., Calderwood, S. B., Mekalanos, J. J., & Collier, R. J. (1988). Evidence that glutamic acid 167 is an active-site residue of Shiga-like toxin I. *Proceedings of the National Academy of Sciences*, *85*(8), 2568–2572. doi.org/10.1073/pnas.85.8.2568

Hu, B., Zhou, R., Li, Z., Ouyang, S., Li, Z., Hu, W., Wang, L., & Jiao, B. (2019). Study of the binding mechanism of aptamer to palytoxin by docking and molecular simulation. *Scientific Reports*, *9*(1), 15494. doi.org/10.1038/s41598-019-52066-z

Islam, S., & Wu, J. (2023). Optimization of Planar Interdigitated Microelectrode Array for Enhanced Sensor Responses. *Micro*, *3*(4), 763–774. doi.org/10.3390/micro3040054

Johannes, L., & Römer, W. (2010). Shiga toxins — from cell biology to biomedical applications. *Nature Reviews Microbiology*, *8*(2), 105–116. doi.org/10.1038/nrmicro2279

Juarez, A. E., Krüger, A., & Lucchesi, P. M. A. (2025). Shiga toxin-producing Escherichia coli , food contamination, and bacteriophages as a control strategy. *Microbiology and Molecular Biology Reviews*, *89*(3). doi.org/10.1128/mmbr.00244-25

Jürgen, R., & Herbert, S. (2002). The Nucleotide Sequence of Shiga Toxin (Stx) 2e-Encoding Phage φP27 Is Not Related to Other Stx Phage Genomes, but the Modular Genetic Structure Is Conserved. *Infection and Immunity*, *70*(4), 1896–1908. doi.org/10.1128/iai.70.4.1896-1908.2002

Kalita, N., Gogoi, S., Minteer, S. D., & Goswami, P. (2023). Advances in Bioelectrode Design for Developing Electrochemical Biosensors. *ACS Measurement Science Au*, *3*(6), 404–433. doi.org/10.1021/acsmeasuresciau.3c00034

Kaur, H., Shorie, M., & Sabherwal, P. (2020). Biolayer interferometry-SELEX for Shiga toxin antigenic-peptide aptamers & detection via chitosan-WSe2 aptasensor. *Biosensors and Bioelectronics*, *167*, 112498. doi.org/10.1016/j.bios.2020.112498

Kim, J. S., Lee, M. S., & Kim, J. H. (2020). Recent Updates on Outbreaks of Shiga Toxin-Producing Escherichia coli and Its Potential Reservoirs. *Frontiers in Cellular and Infection Microbiology*, *10*(June), 1–10. doi.org/10.3389/fcimb.2020.00273

Konowalchuk, J., Speirs, J. I., & Stavric, S. (1977). Vero response to a cytotoxin of Escherichia coli. *Infection and Immunity*, *18*(3), 775–779. doi.org/10.1128/iai.18.3.775-779.1977

Krieger, E., Joo, K., Lee, J., Lee, J., Raman, S., Thompson, J., Tyka, M., Baker, D., & Karplus, K. (2009). Improving physical realism, stereochemistry, and side-chain accuracy in homology modeling. In *Proteins: Structure, Function, and Bioinformatics* (Vol. 77, Issue S9, pp. 114–122).

Kristina, C., Jürgen, R., Volker, K., Sylvia, H., Michael, H., & Herbert, S. (2005). The Shiga Toxin 1-Converting Bacteriophage BP-4795 Encodes an NleA-Like Type III Effector Protein. *Journal of Bacteriology*, *187*(24), 8494–8498. doi.org/10.1128/jb.187.24.8494-8498.2005

Krüger, A., & Lucchesi, P. M. A. (2015). Shiga toxins and stx phages: Highly diverse entities. *Microbiology (United Kingdom)*, *161*(3), 1–12. doi.org/10.1099/mic.0.000003

Kubo, Y., Ueda, O., Nagamitsu, S., Yamanishi, H., Nakamura, A., & Komatsu, M. (2021). Novel strategy of rapid typing of Shiga toxin-producing Escherichia coli using MALDI Biotyper and ClinProTools analysis. *Journal of Infection and Chemotherapy*, *27*(8), 1137–1142. doi.org/10.1016/j.jiac.2021.03.002

Kypr, J., Kejnovská, I., Renčiuk, D., & Vorlíčková, M. (2009). Circular dichroism and conformational polymorphism of DNA. *Nucleic Acids Research*, *37*(6), 1713–1725. doi.org/10.1093/nar/gkp026

Lacher, D. W., Gangiredla, J., Patel, I., Elkins, C. A., & Feng, P. C. H. (2016). Use of the Escherichia coli Identification Microarray for Characterizing the Health Risks of Shiga Toxin–Producing Escherichia coli Isolated from Foods. *Journal of Food Protection*, *79*(10), 1656–1662. doi.org/10.4315/0362-028X.JFP-16-176

Lai, C. Y., Weng, J. H., Shih, W. L., Chen, L. C., Chou, C. F., & Wei, P. K. (2019). Diffusion impedance modeling for interdigitated array electrodes by conformal mapping and cylindrical finite length approximation. *Electrochimica Acta*, *320*, 134629. doi.org/10.1016/j.electacta.2019.134629

Lamoureux, L., Adams, P., Banisadr, A., Stromberg, Z. R., Graves, S., Montano, G., Moxley, R., & Mukundan, H. (2015). An optical biosensor for detection of pathogen biomarkers from Shiga toxin-producing Escherichia coli in ground beef samples. *Proc.SPIE*, *9310*, 931004. doi.org/10.1117/12.2079658

Le, H. T. N., Park, J., Chinnadayyala, S. R., & Cho, S. (2019). Sensitive electrochemical detection of amyloid beta peptide in human serum using an interdigitated chain-shaped electrode. *Biosensors and Bioelectronics*, *144*(July), 111694. doi.org/10.1016/j.bios.2019.111694

Le, H. T. N., Park, J., & Cho, S. (2020). A Probeless Capacitive Biosensor for Direct Detection of Amyloid Beta 1-42 in Human Serum Based on an Interdigitated Chain-Shaped Electrode. *Micromachines*, *11*(9), 791. doi.org/10.3390/mi11090791

Lee, C. Y., Canavan, H. E., Gamble, L. J., & Castner, D. G. (2005). Evidence of impurities in thiolated single-stranded DNA oligomers and their effect on DNA self-assembly on gold. *Langmuir*, *21*(11), 5134–5141. doi.org/10.1021/la0472302

Leung, P. H. M., Peiris, J. S. M., Ng, W. W. S., Robins-Browne, R. M., Bettelheim, K. A., & Yam, W. C. (2003). A Newly Discovered Verotoxin Variant, VT2g, Produced by Bovine Verocytotoxigenic Escherichia coli. *Applied and Environmental Microbiology*, *69*(12), 7549–7553. doi.org/10.1128/AEM.69.12.7549-7553.2003

Li, D., Yi, J., Han, G., & Qiao, L. (2022). MALDI-TOF Mass Spectrometry in Clinical Analysis and Research. *ACS Measurement Science Au*, *2*(5), 385–404. doi.org/10.1021/acsmeasuresciau.2c00019

Lin, H., Zhang, W., Jia, S., Guan, Z., Yang, C. J., & Zhu, Z. (2014). Microfluidic approaches to rapid and efficient aptamer selection. *Biomicrofluidics*, *8*(4), 41501. doi.org/10.1063/1.4890542

Lindsey, R. L., Prasad, A., Feldgarden, M., Gonzalez-Escalona, N., Kapsak, C., Klimke, W., Melton-Celsa, A., Smith, P., Souvorov, A., Truong, J., & Scheutz, F. (2023). Identification and Characterization of ten Escherichia coli Strains Encoding Novel Shiga Toxin 2 Subtypes, Stx2n as Well as Stx2j, Stx2m, and Stx2o, in the United States. *Microorganisms*, *11*(10), 2561. doi.org/10.3390/microorganisms11102561

Liu, D., Perdue, R. K., Sun, L., & Crooks, R. M. (2004). Immobilization of DNA onto Poly(dimethylsiloxane) Surfaces and Application to a Microelectrochemical Enzyme-Amplified DNA Hybridization Assay. *Langmuir*, *20*(14), 5905–5910. doi.org/10.1021/la049605p

Liu, Y., Thaker, H., Wang, C., & Xu, Z. (2023). Diagnosis and Treatment for Shiga Toxin-Producing Escherichia coli Associated Hemolytic Uremic Syndrome. *Toxins*, *15*(10), 1–28. doi.org/10.3390/toxins15010010

Longo, E., Wright, K., Caruso, M., Gatto, E., Palleschi, A., Scarselli, M., De Crescenzi, M., Crisma, M., Formaggio, F., Toniolo, C., & Venanzi, M. (2015). Peptide flatlandia: A new-concept peptide for positioning of electroactive probes in proximity to a metal surface.

Nanoscale, 7(37), 15495–15506. doi.org/10.1039/c5nr03549j

Lu, T., Zhu, K.-D., Huang, C., Wen, T., Jiao, Y.-J., Zhu, J., Zhang, Q., & Ding, S.-N. (2020). Rapid detection of Shiga toxin type II using lateral flow immunochromatography test strips of colorimetry and fluorimetry. *Analyst*, *145*(1), 76–82. doi.org/10.1039/C9AN01996K

Marques, L. R. M., Peiris, J. S. M., Cryz, S. J., & O'Brien, A. D. (1987). Escherichia coli strains isolated from pigs with edema disease produce a variant of Shiga-like toxin II. *FEMS Microbiology Letters*, *44*(1), 33–38. //doi.org/10.1111/j.1574-6968.1987.tb02237.x

Maruyama, K., Ohkawa, H., Ogawa, S., Ueda, A., Niwa, O., & Suzuki, K. (2006). Fabrication and Characterization of a Nanometer-Sized Optical Fiber Electrode Based on Selective Chemical Etching for Scanning Electrochemical/Optical Microscopy. *Analytical Chemistry*, *78*(6), 1904–1912. doi.org/10.1021/ac0502549

Mclean, K., Palarea-Albaladejo, J., Currie, C. G., Imrie, L. H. J., Manson, E. D. T., Fraser-Pitt, D., Wright, F., Alexander, C. J., Pollock, K. G. J., Allison, L., Hanson, M., & Smith, D. G. E. (2018). Rapid and robust analytical protocol for E. coli STEC bacteria subspecies differentiation using whole cell MALDI mass spectrometry. *Talanta*, *182*, 164–170. doi.org/10.1016/j.talanta.2018.01.055

Melton-Celsa, A. R. (2014). Shiga Toxin (Stx) Classification, Structure, and Function. *Microbiology Spectrum*, *2*(4), 10.1128/microbiolspec.ehec-0024–2013. doi.org/10.1128/microbiolspec.ehec-0024-2013

Menge, C. (2020). Molecular Biology of Escherichia coli Shiga Toxins' Effects on Mammalian Cells. *Toxins*, *12*(5), 345. doi.org/10.3390/toxins12050345

Milano, A., D'Avino, A., Marchesano, V., Sagnelli, D., Rippa, M., Guilcapi, B., Zhou, L., Varrone, E., Rossi, G., Brigotti, M., Ardissino, G., Morabito, S., & Petti, L. (2025). Advancing Medical Diagnostics: Rapid, Label-Free Detection and Differentiation of Shiga Toxin Variants in Human Serum Using a Cost-Effective PCA-Assisted SERS Platform. *ACS Applied Materials & Interfaces*, *17*(46), 63237–63252. doi.org/10.1021/acsami.5c18171

Mili, M., Bachu, V., Kuri, P. R., Singh, N. K., & Goswami, P. (2024). Improving synthesis and binding affinities of nucleic acid aptamers and their therapeutics and diagnostic applications. *Biophysical Chemistry*, *309*(November 2023), 107218. doi.org/10.1016/j.bpc.2024.107218

Min, J., & Baeumner, A. J. (2004). Characterization and optimization of interdigitated ultramicroelectrode arrays as electrochemical biosensor transducers. *Electroanalysis*, *16*(9), 724–729. doi.org/10.1002/elan.200302872

Mirsaleh-Kohan, N., Bass, A. D., & Sanche, L. (2010). X-ray photoelectron spectroscopy analysis of gold surfaces after removal of thiolated DNA oligomers by ultraviolet/ozone treatment. *Langmuir*, *26*(9), 6508–6514. doi.org/10.1021/la9039804

Moyano, A., Serrano-Pertierra, E., Salvador, M., Martínez-García, J. C., Rivas, M., & Blanco-López, M. C. (2020). Magnetic Lateral Flow Immunoassays. *Diagnostics*, *10*(5), 288. doi.org/10.3390/diagnostics10050288

Nagatsuka, T., Uzawa, H., Sato, K., Kondo, S., Izumi, M., Yokoyama, K., Ohsawa, I., Seto, Y., Neri, P., Mori, H., Nishida, Y., Saito, M., & Tamiya, E. (2013). Localized Surface Plasmon Resonance Detection of Biological Toxins Using Cell Surface Oligosaccharides on Glyco Chips. *ACS Applied Materials & Interfaces*, *5*(10), 4173–4180. doi.org/10.1021/am4002937

Nebling, E., Grunwald, T., Albers, J., Schäfer, P., & Hintsche, R. (2004). Electrical Detection of Viral DNA Using Ultramicroelectrode Arrays. *Analytical Chemistry*, *76*(3), 689–696. doi.org/10.1021/ac0348773

Nichols, B. J., Kenworthy, A. K., Polishchuk, R. S., Lodge, R., Roberts, T. H., Hirschberg, K., Phair, R. D., & Lippincott-Schwartz, J. (2001). Rapid Cycling of Lipid Raft Markers between the Cell Surface and Golgi Complex. *Journal of Cell Biology*, *153*(3), 529–542. doi.org/10.1083/jcb.153.3.529

Nüesch-Inderbinen, M., Morach, M., Cernela, N., Althaus, D., Jost, M., Mäusezahl, M., Bloomberg, G., & Stephan, R. (2018). Serotypes and virulence profiles of Shiga toxin-producing Escherichia coli strains isolated during 2017 from human infections in Switzerland. *International Journal of Medical Microbiology*, *308*(7), 933–939. doi.org/10.1016/j.ijmm.2018.06.011

Ohnishi, M., Terajima, J., Kurokawa, K., Nakayama, K., Murata, T., Tamura, K., Ogura, Y., Watanabe, H., & Hayashi, T. (2002). Genomic diversity of enterohemorrhagic Escherichia coli O157 revealed by whole genome PCR scanning. *Proceedings of the*

National Academy of Sciences, *99*(26), 17043–17048. doi.org/10.1073/pnas.262441699

Palma-Martínez, I., Guerrero-Mandujano, A., Ruiz-Ruiz, M. J., Hernández-Cortez, C., Molina-López, J., Bocanegra-García, V., & Castro-Escarpulli, G. (2016). Active Shiga-Like Toxin Produced by Some Aeromonas spp., Isolated in Mexico City. *Frontiers in Microbiology*, *7*, 1522. doi.org/doi.org/10.3389/fmicb.2016.01522

Park, J., Lee, Y., Hwang, Y., & Cho, S. (2020). Interdigitated and Wave-Shaped Electrode-Based Capacitance Sensor for Monitoring Antibiotic Effects. *Sensors*, *20*(18), 5237. doi.org/10.3390/s20185237

Parsons, B. D., Zelyas, N., Berenger, B. M., & Chui, L. (2016). Detection, characterization, and typing of shiga toxin-producing Escherichia coli. *Frontiers in Microbiology*, *7*(APR), 1–12. doi.org/10.3389/fmicb.2016.00478

Patel, D., Hansen, M., Lambert, C., Hegde, S., Jayamohan, H., Gale, B. K., & Sant, H. J. (2023). Characterizing a Silver Nanoparticle-Based Electrochemical Biosensor for Shiga Toxin Detection. *ACS Omega*, *8*(43), 40898–40903. doi.org/10.1021/acsomega.3c06083

Paton, A W, & Paton, J. C. (1996). Enterobacter cloacae producing a Shiga-like toxin II-related cytotoxin associated with a case of hemolytic-uremic syndrome. *Journal of Clinical Microbiology*, *34*(2), 463–465. doi.org/10.1128/jcm.34.2.463-465.1996

Paton, Adrienne W, Paton, J. C., Heuzenroeder, M. W., Goldwater, P. N., & Manning, P. A. (1992). Cloning and nucleotide sequence of a variant Shiga-like toxin II gene from Escherichia coli OX3:H21 isolated from a case of sudden infant death syndrome. *Microbial Pathogenesis*, *13*(3), 225–236. doi.org/10.1016/0882-4010(92)90023-H

Paton, J. C., & Paton, A. W. (2006). Shiga toxin ‘goes retro’ in human primary kidney cells. *Kidney International*, *70*(12), 2049–2051. doi.org/10.1038/sj.ki.5001954

Pellino, C. A., S., K. S., Suman, P., & A., W. A. (2016). AB5 Preassembly Is Not Required for Shiga Toxin Activity. *Journal of Bacteriology*, *198*(11), 1621–1630. doi.org/10.1128/jb.00918-15

Peruzzi, C., Battistoni, S., Montesarchio, D., Cocuzza, M., Marasso, S. L., Verna, A., Pasquardini, L., Verucchi, R., Aversa, L., Erokhin, V., D’Angelo, P., & Iannotta, S. (2021). Interfacing aptamers, nanoparticles and graphene in a hierarchical structure for highly selective detection of biomolecules in OECT devices. *Scientific Reports*, *11*(1), 1–

11. doi.org/10.1038/s41598-021-88546-4

Pettersen, E. F., Goddard, T. D., Huang, C. C., Couch, G. S., Greenblatt, D. M., Meng, E. C., & Ferrin, T. E. (2004). UCSF Chimera - A visualization system for exploratory research and analysis. *Journal of Computational Chemistry*, *25*(13), 1605–1612. doi.org/10.1002/jcc.20084

Pollard, D. R., Johnson, W. M., Lior, H., Tyler, S. D., & Rozee, K. R. (1990). Rapid and specific detection of verotoxin genes in Escherichia coli by the polymerase chain reaction. *Journal of Clinical Microbiology*, *28*(3), 540–545. doi.org/10.1128/jcm.28.3.540-545.1990

Ren, K., Duan, M., Su, T., Ying, D., Wu, S., Wang, Z., & Duan, N. (2024). A colorimetric and SERS dual-mode aptasensor for the detection of Shiga toxin type II based on Mn/Fe-MIL(53)@AuNSs. *Talanta*, *270*(December 2023), 125636. doi.org/10.1016/j.talanta.2024.125636

Riley, L. M., Veses-garcia, M., Hillman, J. D., Handfield, M., Mccarthy, A. J., & Allison, H. E. (2012). Identification of genes expressed in cultures of E . coli lysogens carrying the Shiga toxin-encoding prophage F 24 B. *BMC Microbiology*, *12*(42). doi.org/doi.org/10.1186/1471-2180-12-42

Rippa, M., Sagnelli, D., Vestri, A., Marchesano, V., Munari, B., Carnicelli, D., Varrone, E., Brigotti, M., Tozzoli, R., Montalbano, M., Morabito, S., Zhou, J., Zyss, J., & Petti, L. (2022). Plasmonic Metasurfaces for Specific SERS Detection of Shiga Toxins. *ACS Applied Materials & Interfaces*, *14*(4), 4969–4979. doi.org/10.1021/acsami.1c21553

Roberts, P. H., Davis, K. C., Garstka, W. R., & Bhunia, A. K. (2001). Lactate dehydrogenase release assay from Vero cells to distinguish verotoxin producing Escherichia coli from non-verotoxin producing strains. *Journal of Microbiological Methods*, *43*(3), 171–181. doi.org/10.1016/S0167-7012(00)00222-0

Rodriguez-Rubio, L., Haarmann, N., Schwidder, M., & Muniesa, M. (2021). Bacteriophages of Shiga Toxin-Producing Escherichia coli and Their Contribution to Pathogenicity. *Pathogens*, *10*(404), 1–23. doi.org/10.3390/pathogens10040404 1

Sandvig, K., Olsnes, S., Brown, J. E., Petersen, O. W., & van Deurs, B. (1989). Endocytosis from coated pits of Shiga toxin: a glycolipid-binding protein from Shigella dysenteriae 1. *Journal of Cell Biology*, *108*(4), 1331–1343. doi.org/10.1083/jcb.108.4.1331

Sarzynska, J., Popenda, M., Antczak, M., & Szachniuk, M. (2023). RNA tertiary structure prediction using RNAComposer in CASP15. *Proteins: Structure, Function and Bioinformatics*, *91*(12), 1790–1799. doi.org/10.1002/prot.26578

Saxena, S. K., O'Brien, A. D., & Ackerman, E. J. (1989). Shiga Toxin, Shiga-like Toxin II Variant, and Ricin Are All Single-site RNA N-Glycosidases of 28 S RNA When Microinjected into Xenopus Oocytes. *Journal of Biological Chemistry*, *264*(1), 596–601. doi.org/10.1016/S0021-9258(17)31302-9

Schägger, H. (2006). Tricine-SDS-PAGE. *Nature Protocols*, *1*(1), 16–22. doi.org/10.1038/nprot.2006.4

Schmidt, H., Montag, M., Bockemühl, J., Heesemann, J., & Karch, H. (1993). Shiga-like toxin II-related cytotoxins in Citrobacter freundii strains from humans and beef samples. *Infection and Immunity*, *61*(2), 534–543. doi.org/10.1128/iai.61.2.534-543.1993

Schmitt, C. K., McKee, M. L., & O'Brien, A. D. (1991). Two copies of Shiga-like toxin II-related genes common in enterohemorrhagic Escherichia coli strains are responsible for the antigenic heterogeneity of the O157:H- strain E32511. *Infection and Immunity*, *59*(3), 1065–1073. doi.org/10.1128/iai.59.3.1065-1073.1991

Scotland, S. M., Rowe, B., Smith, H. R., Willshaw, G. A., & Gross, R. J. (1988). Vero cytotoxin-producing strains of Escherichia coli from children with haemolytic uraemic syndrome and their detection by specific DNA probes. *Journal of Medical Microbiology*, *25*(4), 237–243. doi.org/10.1099/00222615-25-4-237

Seidah, N. G., Donohue-Rolfe, A., Lazure, C., Auclair, F., Keusch, G. T., & Chrétien, M. (1986). Complete amino acid sequence of Shigella toxin B-chain. A novel polypeptide containing 69 amino acids and one disulfide bridge. *Journal of Biological Chemistry*, *261*(30), 13928–13931. doi.org/https://doi.org/10.1016/S0021-9258(18)66961-3

Sherif, S., Ghallab, Y. H., AbdelRaheem, O., Ziko, L., Siam, R., & Ismail, Y. (2023). Optimization design of interdigitated microelectrodes with an insulation layer on the connection tracks to enhance efficiency of assessment of the cell viability. *BMC Biomedical Engineering*, *5*(1), 4. doi.org/10.1186/s42490-023-00070-w

Shraim, A. S., Abdel Majeed, B. A., Al-Binni, M. A., & Hunaiti, A. (2022). Therapeutic Potential of Aptamer–Protein Interactions. *ACS Pharmacology & Translational Science*, *5*(12), 1211–1227. doi.org/10.1021/acsptsci.2c00156

Singh, N. K., Jain, P., Das, S., & Goswami, P. (2019). Dye coupled aptamer-captured enzyme catalyzed reaction for detection of pan malaria and p. Falciparum species in laboratory settings and instrument-free paper-based platform. *Analytical Chemistry*, *91*(6), 4213–4221. doi.org/10.1021/acs.analchem.9b00670

Skinner, C., Patfield, S., Khalil, R., Kong, Q., & He, X. (2016). New Monoclonal Antibodies against a Novel Subtype of Shiga Toxin 1 Produced by Enterobacter cloacae and Their Use in Analysis of Human Serum. *MSphere*, *1*(1), 10.1128/msphere.00099-15. doi.org/10.1128/msphere.00099-15

Staples, M., Jennison, A. V, Graham, R. M. A., & Smith, H. V. (2012). Evaluation of the Meridian Premier EHEC assay as an indicator of Shiga toxin presence in direct faecal specimens. *Diagnostic Microbiology and Infectious Disease*, *73*(4), 322–325. doi.org/10.1016/j.diagmicrobio.2012.05.004

Stein, P. E., Boodhoo, A., Tyrrell, G. J., Brunton, J. L., & Read, R. J. (1992). Crystal structure of the cell-binding B oligomer of verotoxin-1 from E. coli. *Nature*, *355*(6362), 748–750. doi.org/10.1038/355748a0

Štulík, K., Amatore, C., Holub, K., Mareček, V., & Kutner, W. (2000). Microelectrodes. Definitions, characterization, and applications (Technical report). *Pure and Applied Chemistry*, *72*(8), 1483–1492. doi.org/10.1351/pac200072081483

Takahashi, M., Wu, X., Ho, M., Chomchan, P., Rossi, J. J., Burnett, J. C., & Zhou, J. (2016). High throughput sequencing analysis of RNA libraries reveals the influences of initial library and PCR methods on SELEX efficiency. *Scientific Reports*, *6*(1), 33697. doi.org/10.1038/srep33697

Tesh, V. L., Burris, J. A., Owens, J. W., Gordon, V. M., Wadolkowski, E. A., O'Brien, A. D., & Samuel, J. E. (1993). Comparison of the relative toxicities of Shiga-like toxins type I and type II for mice. *Infection and Immunity*, *61*(8), 3392–3402. doi.org/10.1128/iai.61.8.3392-3402.1993

Thevendran, R., Tang, T.-H., & Citartan, M. (2023). In-silico selection employing rigid docking and molecular dynamic simulation in selecting DNA aptamers against androgen receptor. *Biotechnology Journal*, *18*(4), 2200092. doi.org/10.1002/biot.202200092

Tóth, I., Sváb, D., Bálint, B., Brown-Jaque, M., & Maróti, G. (2016). Comparative analysis of the Shiga toxin converting bacteriophage first detected in Shigella sonnei. *Infection, Genetics and Evolution*, *37*, 150–157. doi.org/10.1016/j.meegid.2015.11.022

Tuerk, C., & Gold, L. (1990). Systematic evolution of ligands by exponential enrichment: RNA ligands to bacteriophage T4 DNA polymerase. *Science*, *249*(4968), 505–510. doi.org/10.1126/science.2200121

Valdés-Tresanco, M. S., Valdés-Tresanco, M. E., Valiente, P. A., & Moreno, E. (2021). Gmx_MMPBSA: A New Tool to Perform End-State Free Energy Calculations with GROMACS. *Journal of Chemical Theory and Computation*, *17*(10), 6281–6291. doi.org/10.1021/acs.jctc.1c00645

Vega-Figueroa, K., Santillán, J., Ortiz-Gómez, V., Ortiz-Quiles, E. O., Quinones-Colón, B. A., Castilla-Casadiego, D. A., Almodóvar, J., Bayro, M. J., Rodríguez-Martínez, J. A., & Nicolau, E. (2018). Aptamer-Based Impedimetric Assay of Arsenite in Water: Interfacial Properties and Performance. *ACS Omega*, *3*(2), 1437–1444. doi.org/10.1021/acsomega.7b01710

Verhaegen, B., De Reu, K., Heyndrickx, M., & De Zutter, L. (2015). Comparison of Six Chromogenic Agar Media for the Isolation of a Broad Variety of Non-O157 Shigatoxin-Producing Escherichia coli (STEC) Serogroups. *International Journal of Environmental Research and Public Health*, *12*(6), 6965–6978. doi.org/10.3390/ijerph120606965

Wagner, P. L., Livny, J., Neely, M. N., Acheson, D. W. K., Friedman, D. I., & Waldor, M. K. (2002). Bacteriophage control of Shiga toxin 1 production and release by Escherichia coli. *Molecular Microbiology*, *44*(4), 957–970. doi.org/10.1046/j.1365-2958.2002.02950.x

Wang, B., Park, B., Chen, J., & He, X. (2020). Rapid and Label-Free Immunosensing of Shiga Toxin Subtypes with Surface Plasmon Resonance Imaging. *Toxins*, *12*(5), 280. doi.org/10.3390/toxins12050280

Wang, J., Katani, R., Li, L., Hegde, N., Roberts, E. L., Kapur, V., & DebRoy, C. (2016). Rapid Detection of Escherichia coli O157 and Shiga Toxins by Lateral Flow Immunoassays. *Toxins*, *8*(4), 92. doi.org/10.3390/toxins8040092

Wang, X., Yu, D., Chui, L., Zhou, T., Feng, Y., Cao, Y., & Zhi, S. (2024). A Comprehensive Review on Shiga Toxin Subtypes and Their Niche-Related Distribution Characteristics in Shiga-Toxin-Producing E. coli and Other Bacterial Hosts. *Microorganisms*, *12*(4), 687. doi.org/10.3390/microorganisms12040687

Wei, Q., Hu, Q., Shi, F., Li, S., Sun, C., Zhang, H., Xue, L., Feng, Q., Dong, J., Jiao, Y., & Zhou, L. (2020). Rapid and quantitative detection of Shiga toxin1 and Shiga toxin2 based on multiple targets UPT-LF assay. *Engineering in Life Sciences*, *20*(11), 494–503. doi.org/10.1002/elsc.202000031

Weinstein, D. L., Jackson, M. P., Samuel, J. E., Holmes, R. K., & O'Brien, A. D. (1988). Cloning and sequencing of a Shiga-like toxin type II variant from Escherichia coli strain responsible for edema disease of swine. *Journal of Bacteriology*, *170*(9), 4223–4230. doi.org/10.1128/jb.170.9.4223-4230.1988

Wenlan, Z., Martina, B., Thorsten, K., & Helge, K. (2002). Identification, Characterization, and Distribution of a Shiga Toxin 1 Gene Variant (stx1c) in Escherichia coli Strains Isolated from Humans. *Journal of Clinical Microbiology*, *40*(4), 1441–1446. doi.org/10.1128/jcm.40.4.1441-1446.2002

WHO Report. (2019). *Attributing illness caused by Shiga toxin-producing Escherichia coli (STEC) to specific foods*.

Willshaw, G. A., Smith, H. R., Scotland, S. M., Field, A. M., & Rowe, B. (1987). Heterogeneity of Escherichia coli phages encoding Vero cytotoxins: Comparison of cloned sequences determining VT1 and VT2 and development of specific gene probes. *Journal of General Microbiology*, *133*(5), 1309–1317. doi.org/10.1099/00221287-133-5-1309

Wong CS, Jelacic S, Habeeb RL, Watkins SL, T. P. (2002). The risk of the hemolytic-uremic syndrome after antibiotic treatment of Escherichia coli O157:H7 infections. *The New England Journal of Medicine*, *342*(26), 1930–1936. doi.org/10.1056/NEJM200006293422601

Yan, Y., Zhang, D., Zhou, P., Li, B., & Huang, S. Y. (2017). HDOCK: A web server for protein-protein and protein-DNA/RNA docking based on a hybrid strategy. *Nucleic Acids Research*, *45*(W1), W365–W373. doi.org/10.1093/nar/gkx407

Yang, L., Li, Y., & Erf, G. F. (2004). Interdigitated Array Microelectrode-Based Electrochemical Impedance Immunosensor for Detection of Escherichia coli O157:H7. *Analytical Chemistry*, *76*(4), 1107–1113. doi.org/10.1021/ac0352575

Yang, X., Bai, X., Zhang, J., Sun, H., Fu, S., Fan, R., He, X., Scheutz, F., Matussek, A., & Xiong, Y. (2020). Escherichia coli strains producing a novel Shiga toxin 2 subtype circulate in China. *International Journal of Medical Microbiology*, *310*(1), 151377.

doi.org/10.1016/j.ijmm.2019.151377

Yang, X., Liu, Q., Sun, H., Xiong, Y., Matussek, A., & Bai, X. (2022). Genomic Characterization of Escherichia coli O8 Strains Producing Shiga Toxin 2l Subtype. *Microorganisms*, *10*(6), 1245. doi.org/10.3390/microorganisms10061245

Yara, D. A., Greig, D. R., Gally, D. L., Dallman, T. J., & Jenkins, C. (2020). Comparison of Shiga toxin- - encoding bacteriophages in highly pathogenic strains of Shiga toxin- - producing Escherichia coli O157 : H7 in the UK. *Microbial Genomics*, *6*(3), e000334. doi.org/10.1099/mgen.0.000334

Yokoyama, S., Suzuki, T., Kawai, K., Ohishi, N., Yagi, K., Itoh, S., & Mori, H. (2000). Nucleotide Sequence Analysis of Shiga(-like) Toxins from an Enterohemorrhagic Escherichia coli Isolated from the Gifu, Japan, Outbreak. *Journal of Clinical Biochemistry and Nutrition*, *28*(2), 53–58. doi.org/10.3164/jcbn.28.53

Yolande, B., Karima, B., Nathalie, P., Valerie, L., & Christine, M. (2001). Stx2 Subtyping of Shiga Toxin-Producing Escherichia coli Isolated from Cattle in France: Detection of a New Stx2 Subtype and Correlation with Additional Virulence Factors. *Journal of Clinical Microbiology*, *39*(9), 3060–3065. doi.org/10.1128/jcm.39.9.3060-3065.2001

Yosief, H. O., Iyer, S. S., & Weiss, A. A. (2013). Binding of Pk-Trisaccharide Analogs of Globotriaosylceramide to Shiga Toxin Variants. *Infection and Immunity*, *81*(8), 2753–2760. doi.org/10.1128/iai.00274-13

Zahner Analysis software. (2023).

Zhang, H. L., Lv, C., Li, Z. H., Jiang, S., Cai, D., Liu, S. S., Wang, T., & Zhang, K. H. (2023). Analysis of aptamer-target binding and molecular mechanisms by thermofluorimetric analysis and molecular dynamics simulation. *Frontiers in Chemistry*, *11*(May), 1–12. doi.org/10.3389/fchem.2023.1144347

Zhang, H., Sun, Z., Sun, K., Liu, Q., Chu, W., Fu, L., Dai, D., Liang, Z., & Lin, C.-T. (2025). Electrochemical Impedance Spectroscopy-Based Biosensors for Label-Free Detection of Pathogens. *Biosensors*, *15*(7), 443. doi.org/10.3390/bios15070443

Zhang, W., Martina, B., Andreas, B., Angelika, F., Alexander, M., & Helge, K. (2012). Real-Time Multiplex PCR for Detecting Shiga Toxin 2-Producing Escherichia coli O104:H4 in Human Stools. *Journal of Clinical Microbiology*, *50*(5), 1752–1754.

doi.org/10.1128/jcm.06817-11

Zhang, Y., Xiong, Y., Yang, C., & Xiao, Y. (2024). 3dRNA/DNA: 3D Structure Prediction from RNA to DNA. *Journal of Molecular Biology*, *436*(17), 168742. doi.org/10.1016/j.jmb.2024.168742

Zuker, M. (2003). Mfold web server for nucleic acid folding and hybridization prediction. *Nucleic Acids Research*, *31*(13), 3406–3415. doi.org/10.1093/nar/gkg595

APPENDIX

Table A1: PCR reaction mixture

Component	Volume
2× Master mix	2 µL
Forward primer	1 µL
Reverse primer	1 µL
DNA template	20 - 30 ng
Nuclease-free water	To make final volume of 10 µL

Table A2: PCR reaction conditions

PCR Steps	Temperature and Time for Stx1	Temperature and Time for Stx2	Cycles
Initial Denaturation	95 °C for 10 min	95 °C for 10 min	1
Denaturation	95 °C for 0.5 min	95 °C for 0.5 min	35
Annealing	48 °C for 0.5 min	50 °C for 0.5 min	35
Extension	72 °C for 0.5 min	72 °C for 0.5 min	35
Final extension	72 °C for 10 min	72 °C for 10 min	1
Store	4 °C for ∞	4 °C for ∞	

Table A3: Primers used for cloning

Name	Sequence
Stx1B (Forward Primer)	CATGCCATGGATATGAAGAAAACCC
Stx1B (Reverse Primer)	CCGCTCGAGACGAAAAATAACC
Stx2 (Forward Primer)	CATGCCATGGCGGACTGCG
Stx2 (Reverse Primer)	CCGCTCGAGGTCGTTGTTAAATTG

Table A4: Double digestion reaction mixture

Components	**Volume**
NcoI	1 µL
XhoI	1 µL
10× G2P buffer	5 µL
DNA Template	1 µg
MQ	To 50 µL

Table A5: Ligation reaction mixture

Components	**Volume**
pET28 (a)	50 ng
PCR product	50 ng
Ligation buffer	1 µL
T4 DNA ligase	1 µL
MQ	To 10 µL

Table A6: Buffers for protein purification

Buffer	**Composition**
Binding buffer	1×PBS, 30 mM Imidazole, pH 7.4
Washing buffer	1×PBS, 100 mM Imidazole, pH 7.4
Elution buffer	1×PBS, 500 mM Imidazole, pH 7.4

Table A7: Primers used in SELEX

Name	Sequence
Forward Primer	CACCTAATACGACTCACTATAG
Biotinylated Reverse Primer	Biotin-GCAAGCTTGTTCGAGCCAG

Table A8: PCR reaction conditions for SELEX

PCR Steps	Temperature and Time for Stx1	Cycles
Initial Denaturation	95 °C for 10 min	1
Denaturation	95 °C for 15 Sec	20
Annealing	48 °C for 15 Sec	20
Extension	72 °C for 10 Sec	20
Final extension	72 °C for 15 min	1
Store	4 °C for ∞	

List of Publications

A. In peer-reviewed journals:

1. **M. Mili**, H. Mog, S. R. Chinnadayyala, S. Cho and P. Goswami, Structure-Guided Computational Design and Electrochemical Validation of a DNA Aptamer for Impedimetric Detection of Shiga-like Toxin 2, Langmuir, (May) 2026. 10.1021/acs.langmuir.6c0099
2. **M. Mili**, S. R. Chinnadayyala, S. Cho and P. Goswami, Development of an impedimetric aptasensor for Shiga-like toxin 1 using a DNA aptamer and an interdigitated microelectrode, RSC Advances, 16 (2026) 4590. http://dx.doi.org/10.1039/D5RA09084A.
3. **M. Mili**, V. Bachu, P.R. Kuri, N.K. Singh, P. Goswami, Improving synthesis and binding affinities of nucleic acid aptamers and their therapeutics and diagnostic applications, Biophys. Chem. 309 (2024) 107218. https://doi.org/10.1016/j.bpc.2024.107218.
4. V. Bachu, **M. Mili**, A. Dutta, P.D. Thungon, P. Goswami, Electrochemiluminescence-Based Lateral Flow Assay for Detection of Cardiac Troponin T Using Aptamers Developed through a Modified SELEX Technique, ACS Appl. Opt. Mater. 2 (2024) 1688–1698. https://doi.org/10.1021/acsaom.4c00258.

B. Manuscript communicated:

1. **M. Mili**, P. Goswami, Shiga Toxin Producing *Escherichia coli*: From Toxin Biology to Modern Detection Approaches.

C. Conference attended:

1. DST-SERB Sponsored International Conference on Devices, Sensors and Systems (CoDSS) 2024. Organized by Dept. of ECE, Tezpur University. (Best poster)
2. North East Research Conclave and Assam Biotech Conclave 2022 (NERC), IIT Guwahati. (Poster presented)

D. Workshop attended:

1. Nanobiotechnology Workshop on NanoBioTech Workshop: Integrating Biosensors and Nanotechnology for Advanced Diagnostics”, 29th to 31st January, 2024.

2. Host-pathogen interaction: Present and future perspective”, 24th to 25th September, 2020. Organized by Dept. of Life Science, NIT Rourkela.
3. in Rural Healthcare Hackathon, 2022. Organized by Bionest IIT Guwahati. (3rd prize)

Front Page of the Papers Published in International Journals

LANGMUIR

pubs.acs.org/Langmuir Article

Structure-Guided Computational Design and Electrochemical Validation of a DNA Aptamer for Impedimetric Detection of Shiga-like Toxin 2

Malaya Mili, Hritushree Mog, Somasekhar R. Chinnadayyala, Sungbo Cho, and Pranab Goswami*

Cite This: https://doi.org/10.1021/acs.langmuir.6c00991 Read Online

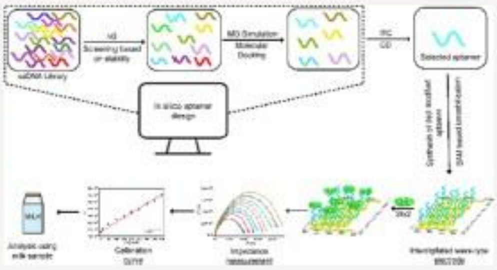

ABSTRACT: The extensive application potential of nucleic acid aptamers in biosensing and therapeutic domains necessitates the development of cost-effective, time-efficient, and technically simpler synthesis protocols compared with conventional SELEX methods. In this study, an *in silico*-based *de novo* approach has been proposed to design an aptamer targeting the B subunits of Shiga-like toxin 2 (Stx2-B) protein, intended for use as a recognition element in biosensors for detecting Stx2. A single-stranded DNA library comprising 5000 sequences was generated and ranked based on their Gibbs free energy (ΔG) of the 2D structures. The top 100 sequences with the lowest ΔG values were modeled in 3D and individually docked with the Stx2 protein. Sequences exhibiting the highest docking scores were further analyzed through molecular dynamics simulations. Among the analyzed candidates, sequence A330 demonstrated the highest stability, rigidity, and compactness in complex with Stx2B, as indicated by root-mean-square deviation, root-mean-square fluctuation, radius of gyration, and hydrogen-bond analysis over 100 ns simulation trajectories. The strong binding affinity of A330 for the target (K_d = 459 ± 7 nM) was confirmed through circular dichroism and isothermal titration calorimetry analyses. This aptamer was subsequently employed as a recognition element in the fabrication of an electrochemical impedimetric aptasensor for Stx2 detection, utilizing a microscale interdigitated wave-type electrode. The developed sensor exhibited high sensitivity, a limit of detection of 4.63 pM, and a linear detection range of 10−400 pM (R^2 = 0.99). The aptasensor's practical applicability was validated in milk samples, achieving a detection recovery of >93.06%. Overall, the proposed aptasensor shows strong potential for the sensitive and reliable monitoring of Shiga toxin-producing *Escherichia coli* contamination in real samples.

■ INTRODUCTION

The rational design of high-affinity and high-specificity aptamers remains a fundamental challenge in biosensor development. Although nucleic acid aptamers possess remarkable structural versatility and binding capabilities, identifying sequences that fold into stable three-dimensional conformations capable of selective target recognition is inherently complex. Conventional discovery relies primarily on Systematic Evolution of Ligands by Exponential Enrichment (SELEX), an iterative in vitro selection process that screens vast oligonucleotide libraries (10^{13}−10^{15} unique sequences).[1] While SELEX has been widely successful, it is labor-intensive, time-consuming, and susceptible to PCR amplification bias, which may lead to the loss of rare but high-affinity binders during enrichment. Moreover, the stochastic nature of library evolution limits precise control over the structural features that govern target recognition. These limitations have motivated increasing interest in structure-guided computational strategies that can rationally narrow the sequence space and accelerate aptamer discovery.

In this context, computational modeling provides a powerful framework to integrate thermodynamic stability, structural folding prediction, and molecular interaction analysis prior to experimental validation. Structure-guided in silico screening enables the preselection of candidate sequences based on predicted Gibbs free energy (ΔG), secondary structure stability, and binding interactions with specific target epitopes. Such approaches significantly reduce the experimental workload while enhancing the probability of identifying high-performance aptamers. However, most reported computational studies focus on truncation or point mutation of previously known aptamers rather than de novo identification of pristine sequences tailored to defined structural motifs on target proteins.[2,3]

Received: February 20, 2026
Revised: April 21, 2026
Accepted: April 22, 2026

RSC Advances

ROYAL SOCIETY OF CHEMISTRY

PAPER

Check for updates

Cite this: *RSC Adv.*, 2026, 16, 4590

Development of an impedimetric aptasensor for Shiga-like toxin 1 using a DNA aptamer and an interdigitated microelectrode

Malaya Mili,[a] Somasekhar R. Chinnadayyala,[†b] Sungbo Cho[bc] and Pranab Goswami[*a]

The life-threatening diarrheal disease caused by Shiga toxin-producing *Escherichia coli* (STEC) necessitates rapid, sensitive, portable, and low-cost diagnostic tools to strengthen on-field food safety monitoring, improve disease prognosis, and guide timely therapeutic interventions. In this study, an impedimetric aptasensor was developed against Shiga like toxin-1 produced by STEC using a 71-mer ssDNA aptamer (sT3), enriched from an initial library (~10^{14} sequences) through the Systematic Evolution of Ligands by Exponential Enrichment (SELEX) technique, and an interdigitated chain-type microelectrode fabricated by depositing Ti and Au layers on a glass substrate *via* electron-beam deposition, photolithography, and wet-chemical etching. The aptamer exhibited a strong binding affinity with a dissociation constant (K_d) of 273 ± 0.03 nM, as determined by isothermal titration calorimetry. The resulting aptasensor achieved a detection limit of 2.88 pM, a linear dynamic range of 10–450 pM, and a sensitivity of 107.02 Ω pM^{-1}, underscoring its strong analytical performance. It retained 97.6% of its initial response after 25 days with five intermittent operations and showed high reproducibility, with only 3.9% standard deviation across five independently fabricated sensors. These stable performances were attributed to the strong aptamer–surface coupling enacted by covalent immobilization through a self-assembled monolayer strategy. The aptasensor further demonstrated high selectivity and practical applicability by reliably detecting the toxin protein in spiked milk samples. Overall, the developed aptasensor offer a great prospect for its practical application as a diagnostic device for rapid and reliable detection of Shiga toxin-induced gastroenteritis at point-of-care settings.

Received 24th November 2025
Accepted 13th January 2026

DOI: 10.1039/d5ra09084a

rsc.li/rsc-advances

1. Introduction

Shiga toxin-producing *E. coli* (STEC) has caused numerous outbreaks worldwide, resulting in significant mortality and morbidity.[1] Infection with STEC leads to gastroenteritis, causing bloody diarrhea, hemorrhagic colitis, and hemolytic uremic syndrome. Children under 5 years of age and elderly people over 65 years of age are more susceptible to infection by STEC. The Shiga toxins produced by STEC are considered the primary virulence factor. They produce two types of toxin, Shiga-like toxin 1 (Stx1) and Shiga-like toxin 2 (Stx2). Both Stx1 and Stx2 are responsible for the pathogenicity of STEC, but they differ in their amino acid sequences with sequence similarity of ~56%,[2] receptor affinities, and immunological characteristics.[3] The Shiga toxins have an AB_5 structure, with one A subunit bearing the enzymatic active site and a pentameric B subunit, used for binding to the glycolipid globotriaosylceramide (Gb_3) on the target cells. The catalytic A subunit exhibits *N*-glycosidase activity, which removes an adenine residue at position 4324 of the 28S rRNA, thereby halting the protein synthesis mechanism at the target cell.[4] The molecular weight of the A subunit of the Shiga toxins is ~32 kDa, and each B subunit is ~7.7 kDa.

Multiple routes of transmission for STEC are known, such as contaminated food and water, contact with animals, and person-to-person interactions.[5] The source of most STEC outbreaks has been identified as cattle meat and its dairy products, tap water (including well water), fruits and vegetables, and their products.[6] Currently, treatment for STEC infection involves palliative care, which includes prompt fluid replacement, management of electrolyte imbalances, and control of elevated blood pressure.[7] Treatment with antibiotics is generally not recommended for STEC-infected patients, as studies have reported conflicting outcomes. While some investigations indicate an increased risk of hemolytic uremic syndrome,[8]

---

[a] *Department of Biosciences and Bioengineering, Indian Institute of Technology Guwahati, Guwahati 781039, Assam, India. E-mail: pgoswami@iitg.ac.in*

[b] *Department of Electronic Engineering, Department of Semiconductor Engineering, Gachon University, Seongnam-si, Gyeonggi-do, 13120, Republic of Korea*

[c] *Gachon Advanced Institute for Health Science & Technology, Gachon University, Incheon 21999, Republic of Korea*

† Current address: Transdermal Diagnostics Ltd, Science Creates, Old Market, Midland road, Bristol, BS2 0NS, England, UK.

Biophysical Chemistry 309 (2024) 107218

Contents lists available at ScienceDirect

Biophysical Chemistry

journal homepage: www.elsevier.com/locate/biophyschem

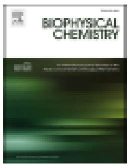

Review

Improving synthesis and binding affinities of nucleic acid aptamers and their therapeutics and diagnostic applications

Malaya Mili[a], Vinay Bachu[a], Pooja Rani Kuri[a], Naveen Kumar Singh[b], Pranab Goswami[a,*]

[a] Department of Biosciences and Bioengineering, IIT Guwahati, 781039, Assam, India
[b] Centre for Biomedical Engineering, IIT, Delhi 110016, India

ARTICLE INFO

Keywords:
SELEX
Biosensors
Biorecognition
Clinical diagnosis
Database
ssDNA
RNA

ABSTRACT

Nucleic acid aptamers have captivated the attention of analytical and medicinal scientists globally due to their several advantages as recognition molecules over conventional antibodies because of their small size, simple and inexpensive synthesis, broad target range, and high stability in varied environmental conditions. These recognition molecules can be chemically modified to make them resistant to nuclease action in blood serum, reduce rapid renel clearance, improve the target affinity and selectivity, and make them amenable to chemically conjugate with a support system that facilitates their selective applications. This review focuses on the development of efficient aptamer candidates and their application in clinical diagnosis and therapeutic applications. Significant advances have been made in aptamer-based diagnosis of infectious and non-infectious diseases. Collaterally, the progress made in therapeutic applications of aptamers is encouraging, as evident from their use in diagnosing cancer, neurodegenerative diseases, microbial infection, and in imaging. This review also updates the progress on clinical trials of many aptamer-based products of commercial interests. The key development and critical issues on the subject have been summarized in the concluding remarks.

1. Introduction

Nucleic acid aptamers are synthetic single-stranded oligonucleotides that can assume a three-dimensional shape by virtue of intra-strand base pairing, and thereby exhibit conformational specificity and high affinity to a target ligand. Aptamers were introduced first by two independent groups, Ellington and Szostak, 1990: Tuerk and Gold, 1990 [1,2]. Conventionally, these oligonucleotide molecules are generated in vitro by a process called Systematic Evolution of Ligands by Exponential enrichment (SELEX). It is an iterative process whereby an oligonucleotide library is exposed to the target of interest against which specific aptamer is generated by the general steps of binding, elution and amplification. Over the last decade, many modifications of the SELEX technique have been proposed to reduce its operational time and technical complexity.

Aptamers can bind to a wide variety of targets such as metal ions, simple inorganic and organic molecules, proteins, and microorganisms. This binding process involves various non-covalent interactions such as hydrogen bonding, π–π stacking, London dispersion forces, ion-ion interactions, and dipole-dipole interactions between the binding pockets in their organized three-dimensional (3-D) structure with that of its corresponding target. The 3-D structures with various motifs e.g., hairpins, bulges, loops and pseudo-knots of the aptamers are generated in the interacting ionic environment that facilitate its binding with the target entities [3]. Aptamers assumes these 3-D structures through the processes of secondary and tertiary structures [4]. The intra-strand base-pairing between nucleotides causes the formation of aptamer secondary structures including stems and loops. The nucleotide regions of stems and loops further undergo sequence-dependent complementarity with nucleotide regions of other stems and loops of the same aptamer, resulting in the formation of tertiary structure. These 3-D landscapes of biding interactions between an aptamer and its specific ligand are analogous to those involved between an antibody and its specific antigen. Both aptamers and antibodies bind to their specific targets with high selectivity and affinity. However, aptamers, as a recognition element offer some advantages over antibodies such as, their simple chemical synthesis-based production process, low production cost, low batch-to-batch variation, high stability, amenability to chemical modifications to improve their functionality, and low immunogenicity [5]. Consequently, aptamers, sometimes called "chemical antibodies", have

---

[*] Corresponding author.
E-mail address: pgoswami@iitg.ac.in (P. Goswami).

https://doi.org/10.1016/j.bpc.2024.107218
Received 21 November 2023; Received in revised form 21 February 2024; Accepted 17 March 2024
Available online 21 March 2024

ACS APPLIED OPTICAL MATERIALS

pubs.acs.org/acsaom Article

Electrochemiluminescence-Based Lateral Flow Assay for Detection of Cardiac Troponin T Using Aptamers Developed through a Modified SELEX Technique

Vinay Bachu, Malaya Mili, Arup Dutta, Phurpa Dema Thungon, and Pranab Goswami*

Cite This: *ACS Appl. Opt. Mater.* 2024, 2, 1688−1698 Read Online

ACCESS | Metrics & More | Article Recommendations | Supporting Information

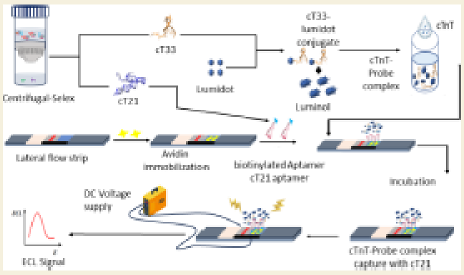

ABSTRACT: Rapid and sensitive detection of cardiac troponin T (cTnT) through a portable device holds immense significance for the early diagnosis of acute myocardial infarction in point-of-care settings. Herein, an electrochemiluminescence-based lateral flow assay (LFA) on a microfluidic hybrid platform for cTnT detection was developed using an aptamer sandwich assay. Aptamers specific to cTnT were enriched from a library through a new centrifugal-systematic evolution of ligands by exponential enrichment (c-SELEX) technique. Two high-affinity aptamers, cT21 (K_d = 10.7 μM) and cT33 (K_d = 13.1 μM), with K_d values determined by isothermal titration calorimetry, were used respectively as capture and detection probes in the assay. In the assay, cT33 was labeled with Lumidot, while cT21 was immobilized on the LFA strip to capture the cTnT−cT33−Lumidot complex. The reaction solution containing luminol and cT33−Lumidot conjugate generated ECL signals under an applied potential of 1.4 V through an electrode pair screen printed on a nitrocellulose membrane of the device. The ECL intensity correlated linearly with the concentration of cTnT in the range of 100 pM to 10 nM and offered a limit of detection of 142.71 pM. This developed sensor exhibits high prospects for practical applications in diagnosing acute myocardial infarction in point-of-care settings.

KEYWORDS: *Lumidot, luminol, diagnosis, myocardial infarction, sandwich assay, microfluidics*

1. INTRODUCTION

Cardiovascular diseases (CVDs) are the leading cause of mortality around the globe. The primary reason for CVD-led death is acute myocardial infarction (AMI).[1] Hence, a rapid and reliable diagnosis method for MI is crucial to initiate a timely therapeutic intervention and save lives. The conventional laboratory-based analytical methods used for its diagnosis are time-consuming and involve sophisticated instruments. Moreover, these methods are difficult to perform onsite and in point-of-care (POC) settings due to their bulky nature and requirement of skilled manpower for operations. Hence, there is a demand to develop rapid, reliable, portable, simple, and inexpensive diagnostic tools for MIs. Biosensors may be the right choice to address this critical issue, as there are numerous success stories with these analytical tools in diverse sectors, including clinical and environmental applications. To develop a suitable biosensor, a reliable biomarker is essential for an unambiguous diagnosis of the ailment. Many biomarkers have been reported for AMI, among which cardiac troponin T (cTnT) has been acclaimed as the gold standard biomarker for the diagnosis.[2,3] cTnT, the tropomyosin-binding subunit of troponin, plays a vital role in Ca^{2+}-mediated regulation of cardiomyocyte contractions. The release of troponins into the circulation from the cardiomyocytes occurs in the first few hours following the necrosis or ischemia conditions. The cytoplasm of the cardiomyocytes contains around 6−8% cTnT and 2.8−4.1% cardiac troponin I (TnI), which are released initially. This event is followed by the breakdown and release of the bound myofibrillar troponin components.[4] A biphasic pattern of the release of cTnT is observed. The concentration increased at 4−6 h following injury and attains optimal levels by 12−24 h. The level may remain stable for 2 weeks.[5]

There have been many reports of developing biosensors targeting troponins, and most of these reports utilized antibody as a biorecognition element.[6−11] However, antibody-based sensors encounter many hurdles, among which the low stability of these protein-based recognition elements and their cross-

Received: June 3, 2024
Revised: July 26, 2024
Accepted: August 4, 2024
Published: August 13, 2024

https://doi.org/10.1021/acsaom.4c00258
ACS Appl. Opt. Mater. 2024, 2, 1688−1698

Copyright permissions

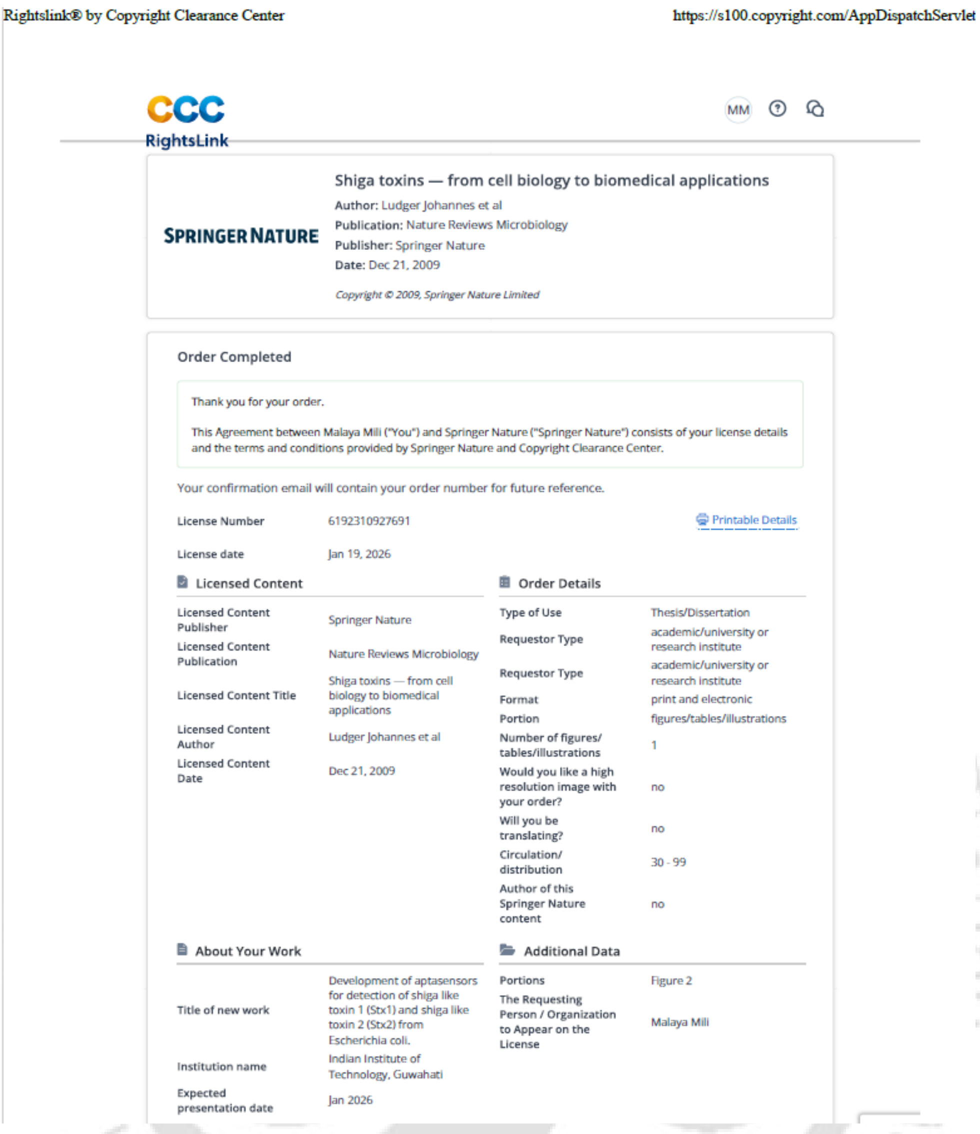

Rightslink® by Copyright Clearance Center https://s100.copyright.com/AppDispatchServlet

SPRINGER NATURE

Shiga toxins — from cell biology to biomedical applications

Author: Ludger Johannes et al
Publication: Nature Reviews Microbiology
Publisher: Springer Nature
Date: Dec 21, 2009

Copyright © 2009, Springer Nature Limited

Order Completed

Thank you for your order.

This Agreement between Malaya Mili ("You") and Springer Nature ("Springer Nature") consists of your license details and the terms and conditions provided by Springer Nature and Copyright Clearance Center.

Your confirmation email will contain your order number for future reference.

License Number	6192310927691
License date	Jan 19, 2026

Licensed Content

Licensed Content Publisher	Springer Nature
Licensed Content Publication	Nature Reviews Microbiology
Licensed Content Title	Shiga toxins — from cell biology to biomedical applications
Licensed Content Author	Ludger Johannes et al
Licensed Content Date	Dec 21, 2009

Order Details

Type of Use	Thesis/Dissertation
Requestor Type	academic/university or research institute
Requestor Type	academic/university or research institute
Format	print and electronic
Portion	figures/tables/illustrations
Number of figures/ tables/illustrations	1
Would you like a high resolution image with your order?	no
Will you be translating?	no
Circulation/ distribution	30 - 99
Author of this Springer Nature content	no

About Your Work

Title of new work	Development of aptasensors for detection of shiga like toxin 1 (Stx1) and shiga like toxin 2 (Stx2) from Escherichia coli.
Institution name	Indian Institute of Technology, Guwahati
Expected presentation date	Jan 2026

Additional Data

Portions	Figure 2
The Requesting Person / Organization to Appear on the License	Malaya Mili

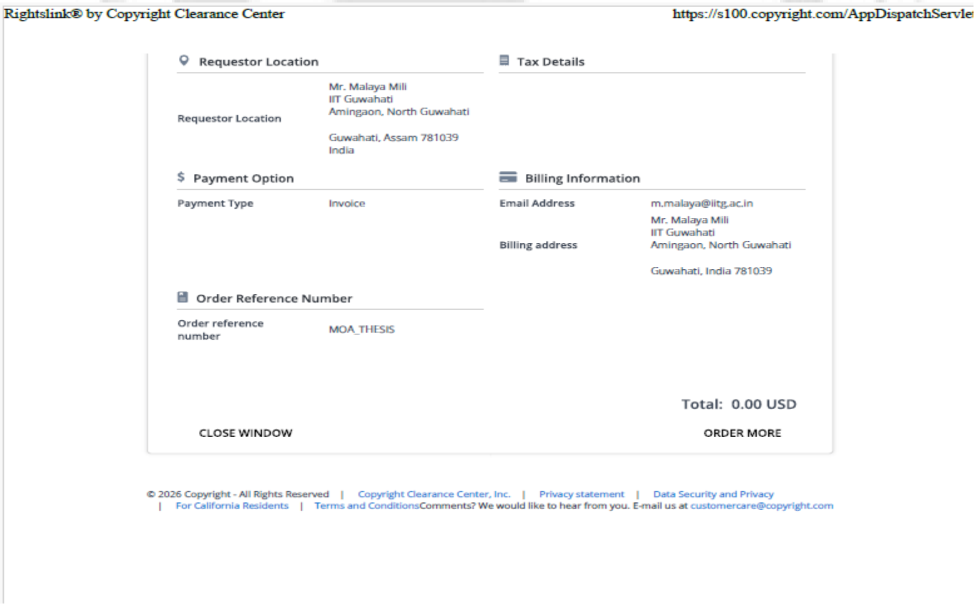

Rightslink® by Copyright Clearance Center https://s100.copyright.com/AppDispatchServle

Requestor Location

Requestor Location	Mr. Malaya Mili IIT Guwahati Amingaon, North Guwahati Guwahati, Assam 781039 India

Tax Details

Payment Option

Payment Type	Invoice

Billing Information

Email Address	m.malaya@iitg.ac.in
Billing address	Mr. Malaya Mili IIT Guwahati Amingaon, North Guwahati Guwahati, India 781039

Order Reference Number

Order reference number	MOA_THESIS

Total: 0.00 USD

© 2026 Copyright - All Rights Reserved | Copyright Clearance Center, Inc. | Privacy statement | Data Security and Privacy | For California Residents | Terms and ConditionsComments? We would like to hear from you. E-mail us at customercare@copyright.com

Similarity report

DrillBit

The Report is Generated by DrillBit Plagiarism Detection Software

Submission Information

Author Name	Malaya Mili
Title	Development of aptasensors for detection of shiga like toxin 1 (Stx1) and shiga like toxin 2 (Stx2) from Escherichia coli.
Paper/Submission ID	5187468
Submitted by	m.malaya@iitg.ac.in
Submission Date	2026-01-26 23:40:35
Total Pages, Total Words	174, 42507
Document type	Thesis

Result Information

Similarity **9 %**

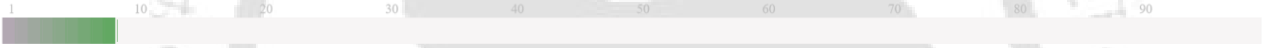

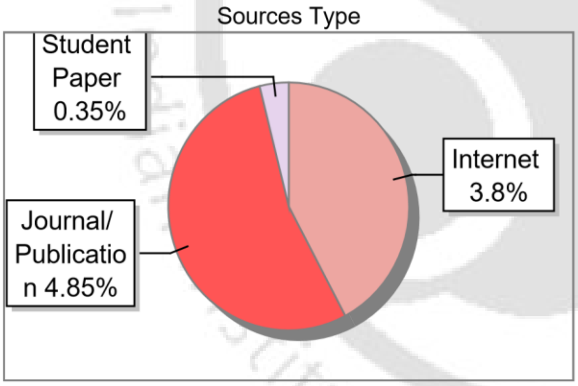

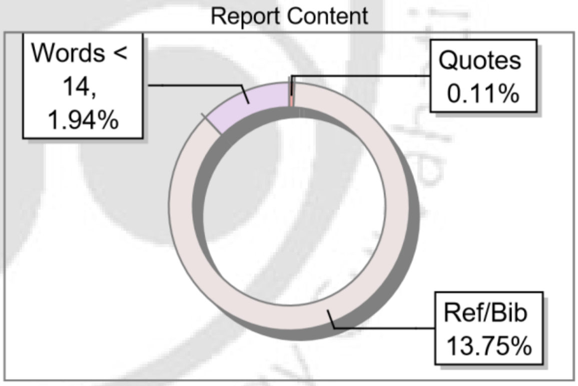

Exclude Information

Quotes	Not Excluded
References/Bibliography	Not Excluded
Source: Excluded < 14 Words	Not Excluded
Excluded Source	**0 %**
Excluded Phrases	Not Excluded

Database Selection

Language	English
Student Papers	Yes
Journals & publishers	Yes
Internet or Web	Yes
Institution Repository	Yes

A Unique QR Code use to View/Download/Share Pdf File